



**HAL**  
open science

# Nanoscale structure of actin filaments probed by polarized super-resolution microscopy

Caio Vaz Rimoli

► **To cite this version:**

Caio Vaz Rimoli. Nanoscale structure of actin filaments probed by polarized super-resolution microscopy. Optics / Photonics. Aix Marseille Université (AMU), Marseille, FRA., 2020. English. NNT: . tel-03039674

**HAL Id: tel-03039674**

**<https://hal.science/tel-03039674>**

Submitted on 4 Dec 2020

**HAL** is a multi-disciplinary open access archive for the deposit and dissemination of scientific research documents, whether they are published or not. The documents may come from teaching and research institutions in France or abroad, or from public or private research centers.

L'archive ouverte pluridisciplinaire **HAL**, est destinée au dépôt et à la diffusion de documents scientifiques de niveau recherche, publiés ou non, émanant des établissements d'enseignement et de recherche français ou étrangers, des laboratoires publics ou privés.

## THÈSE DE DOCTORAT

Soutenue à Aix-Marseille Université  
le 30 Novembre 2020 par

**Caio VAZ RIMOLI**

**Titre de la thèse:**

**Nanoscale structure of actin filaments probed by  
polarized super-resolution microscopy**

**Discipline**

Physique et Sciences de la Matière

**Spécialité**

Biophysique

**École doctorale**

ED352 : Physique et sciences de la matière

**Laboratoire/Partenaires de recherche**

Institut Fresnel

(Aix Marseille Université, CNRS, Centrale  
Marseille)

**Composition du jury**

Prof. Cristina KURACHI      Rapporteuse

IFSC-USP, Brésil

Prof. María GARCÍA-PARAJÓ      Rapporteuse

ICFO, Espagne

Dr. Bassam HAJJ      Examineur

Institut Curie-CNRS, France

Prof. Paulo B. MIRANDA      Président du jury

IFSC-USP, Brésil

Dr. Sophie BRASSELET      Directrice de thèse

Institut Fresnel-AMU, France

Dr. Manos MAVRAKIS      Co-directeur de thèse

Institut Fresnel-AMU, France

# Affidavit

Je soussigné, Caio VAZ RIMOLI, déclare par la présente que le travail présenté dans ce manuscrit est mon propre travail, réalisé sous la direction scientifique de Sophie BRASSELET et Manos MAVRAKIS, dans le respect des principes d'honnêteté, d'intégrité et de responsabilité inhérents à la mission de recherche. Les travaux de recherche et la rédaction de ce manuscrit ont été réalisées dans le respect à la fois de la charte nationale de déontologie des métiers de la recherche et de la charte d'Aix-Marseille Université relative à la lutte contre le plagiat.

Ce travail n'a pas été précédemment soumis en France ou à l'étranger dans une version identique ou similaire à un organisme examinateur.

Fait à Piracicaba (Brésil), le 10/Octobre/2020



Cette œuvre est mise à disposition selon les termes de la [Licence Creative Commons Attribution - Pas d'Utilisation Commerciale - Pas de Modification 4.0 International](https://creativecommons.org/licenses/by-nc-nd/4.0/).

# Affidavit

I, undersigned, Caio VAZ RIMOLI, hereby declare that the work presented in this manuscript is my own work, carried out under the scientific direction of Sophie BRASSELET and Manos MAVRAKIS, in accordance with the principles of honesty, integrity and responsibility inherent to the research mission. The research work and the writing of this manuscript have been carried out in compliance with both the French national charter for Research Integrity and the Aix-Marseille University charter on the fight against plagiarism.

This work has not been submitted previously either in this country or in another country in the same or in a similar version to any other examination body.

Place Piracicaba (Brazil), date 10/October/2020



Cette œuvre est mise à disposition selon les termes de la [Licence Creative Commons Attribution - Pas d'Utilisation Commerciale - Pas de Modification 4.0 International](https://creativecommons.org/licenses/by-nc-nd/4.0/).



## Résumé

Les filaments d'actine sont des éléments structurels clés qui affectent le comportement et la fonction des cellules. Bien qu'ils soient largement étudiés, des questions restent ouvertes sur la manière dont leur organisation à l'échelle nanométrique influence la morphologie et les processus cellulaires. Un assemblage d'actine important est celui des fibres de stress, qui sont des faisceaux supramoléculaires constitués de filaments de F-actine et de réticulants qui jouent un rôle important dans l'adhésion et la motilité des cellules. Les fibres de stress de l'actine supportent des forces cellulaires et peuvent être subdivisées en différentes catégories, en particulier celles qui sont contractiles et celles qui ne le sont pas. La manière dont les filaments d'actine sont organisés en différentes catégories de fibres de stress à l'échelle nanométrique est un sujet encore mal compris. À cette fin, les techniques de microscopie à fluorescence polarisée (PFM) peuvent être très utiles dès lors qu'elles peuvent fournir des informations quantitatives de sous-diffraction de l'organisation moléculaire avec une grande spécificité dans les cellules. Dans cette thèse, nous construisons un système de microscope optique capable de réaliser deux méthodes PFM différentes pour étudier l'organisation des filaments d'actine à l'échelle nanométrique. La première méthode PFM, est une réplique d'un système précédemment construit dans notre groupe, qui est une technique de résolution de polarisation moyenne d'ensemble. Cette dernière utilise une rotation rapide de la polarisation effectuée par une cellule de Pockels placée dans le trajet d'excitation, et un balayage confocal parallèle multi-focal pour une imagerie rapide (disque rotatif). La seconde méthode PFM est une nouvelle méthode de super-résolution polarisée que nous avons appelée 4polar-dSTORM. Cette méthode est basée sur la méthode de microscopie à reconstruction optique stochastique directe (dSTORM) qui divise les signaux de fluorescence monomoléculaire en 4 canaux de polarisation projetés. Avec ce dernier, nous avons pu mesurer chaque orientation moyenne d'un fluorophore unique (le long d'un filament) indépendamment de l'ondulation du fluorophore (fluctuations angulaires). Grâce à cela, nous avons pu effectuer la première quantification 2D non biaisée de l'ordre statique du filament d'actine à l'échelle nanométrique avec une résolution optique allant jusqu'à environ 20 nm. Grâce à ces techniques, nous avons pu conclure que l'organisation des filaments d'actine est assez constante (avec des écarts angulaires d'environ 20° à 30°) le long de toutes les catégories de fibres de stress et qu'il s'agit de structures très stables en cas de perturbation de la contractilité ou de stimuli. Il est intéressant de noter que, puisque la méthode 4polar-dSTORM est basée sur une seule molécule, d'autres structures complexes d'actine telles que des maillages de filaments d'actine très denses à l'échelle nanométrique (par exemple dans les lamellipodes) pourraient être étudiées, ce qui illustre le potentiel de la méthode pour étudier des organisations inconnues.

Mots clés: Filaments d'actine, Polarisation, Nano-échelle, Microscopie ultra-résolue, Microscopie polarisée, Structure biomoléculaire.

# Abstract

Actin filaments are key structural building blocks that affects cell behavior and function. Although they are extensively studied, open questions still arise on how their organization at the nanoscale influences cell morphology and processes. An important actin assembly is stress fibers, which are supramolecular bundles made of F-actin filaments and crosslinkers that have an important role in cell adhesion and motility. Actin stress fibers bear cellular forces, and can be subdivided into different categories, in particular those which are contractile and those which are not. How actin filaments are organized in different stress fiber categories at the nanoscale is a topic still not well understood. To that end, polarized fluorescence microscopy (PFM) techniques can be very useful once they can provide subdiffraction quantitative information of the molecular organization with high specificity in cells. In this thesis, we build up an optical microscope system capable of performing two different PFMs methods to study the organization of actin filaments at the nanoscale. The first PFM method, is a replica of a previously built system in our group, which is an ensemble averaged polarization resolved technique. The latter uses a fast polarization rotation performed by a Pockels cell placed in the excitation path, and a multi-focus parallel confocal scanning for fast imaging (spinning disk). The second PFM method is a novel polarized super-resolution method that we named 4polar-dSTORM. The method is based on direct Stochastic Optical Reconstruction Microscopy (dSTORM) method that splits single-molecule fluorescence signals into 4 projected polarization channels. With the latter, we were able to measure each single-fluorophore mean orientation (along a bundle) independently of the fluorophore wobbling (angular fluctuations). Thanks to that, we were able to perform the first 2D unbiased quantification of the actin filament static order at the nanoscale with an optical resolution up to approximately 20nm. With these techniques, we were able to conclude that actin filament organization is quite constant (within angular deviations of about 20° to 30°) along all stress fiber categories and they are highly stable structures upon contractility perturbation or stimuli. Interestingly, since 4polar-dSTORM is a single-molecule based method, other actin complex structures such as very dense nanoscale actin filament meshworks (e.g., in lamellipodia) could be studied, illustrating the potential of the method to investigate unknown organizations.

Keywords: Actin filaments, Polarization, Nanoscale, Super-Resolution Microscopy, Polarized Microscopy, Biomolecular structure.

## Acknowledgments

Here I would like to acknowledge all the people that gave me support to do this PhD thesis work. From the very beginning to the very end (jury), I am very thankful to all of you.

First, a very special acknowledgement to my two *super* supervisors: Sophie Brasselet and Manos Mavrikis. I am deeply thankful for the opportunity of being your PhD Student in Fresnel. You two transmitted me a very strong passion to work with the optics and the biological part of the thesis. It was very exciting and to learn so many things from you both. I could not be more motivated to work in such warm and inspiring environment. It was my first time I have been abroad for a very long time, and you both took care of me – from the beginning to the very end. It is difficult to find the right words that demonstrate such level of gratitude I am. This work would be impossible to be done without you. Thank you so much for your kind attention, patience, and for making this happen. A dream coming true.

I would like to acknowledge Hilton Barbosa de Aguiar for presenting me to Sophie. Without you, I would not have this great experience of doing my PhD studies at Institut Fresnel. Besides, I would like to acknowledge Herve Rigneault for accepting me in the group.

I very special acknowledgement to César Augusto Valadés Cruz, a former PhD student that developed the Matlab code for 4polar-dSTORM. Thank you for all the discussions about your code, and for giving us your support during this PhD work. Besides, I would like to thank another former student, Xiao Wang, for his insightful PhD thesis.

I would like to acknowledge Louwrens Van Dellen (engineer) for interfacing the Labview part of the polar-spinning disk experiment and the autofocus system in 4polar-dSTORM. Besides, I would like to thank Serge Monneret for lending us the autofocus Labview code for the 4polar-dSTORM setup.

I would like to acknowledge my office and lab partner Valentina Curcio (PhD student), that developed the bias simulations that I displayed in this thesis. Thank you for our friendship and partnership.

I would like to acknowledge Sanjay Kumar (Berkeley, USA) and K. Rottner (Univ. Braunschweig Germany) for donating CA-MLCK U2OS cell line and B16 (skin cancer) melanoma cells respectively for our experiments.

I would like to acknowledge all my Fresnel colleagues and friends. Thank you for our friendship, scientific discussions, and help with French translations and bureaucracies. You all made my stay in Marseille much warmer, productive, and lovely. Thank you so much, Matthias, Sid, Raju, Viktor, Barbara, Vasyl, Valentina, Carla, Alberto, Sandro, Dmitry, Miguel, Anna, Camille, Simon, Hadrien, Satyajit, and so many others that were present during my stay in Marseille.

I would like to acknowledge all Fresnel workers (computer technicians, secretaries, etc). A very special thanks to the two Freds that helped me with all the computer bugs I got during the PhD.

I would like to acknowledge CNRS for providing me the funding during my stay in Marseille.

I would like to acknowledge the jury that accepted to read and evaluate this detailed thesis. Thank you for your patience and scientific discussions (during the Thesis defense).

I would like to acknowledge Felipe Nadai and Sophie Exbrayat for my psychiatric treatment in the last years. Thank to you I manage to recover and finish the writing of the thesis in Brazil. Likewise, I would like to thank Luci Abraão for the psychological treatment.

Finally, I would like to acknowledge my family. Their kindness and love supported me in all moments during this thesis.

# Table of Contents

Résumé	i
Abstract	ii
Acknowledgements	iii
Table of Contents	v
General Introduction	xi
<b>Chapter 1 - Actin Filament Structures and Function</b>	<b>1</b>
Introduction: actin is an important biomolecule present in almost all organisms	1
I. 1 Structure of actin and actin networks	1
I.1.1 Structure and properties of a single actin monomer (G-actin)	1
I.1.2 The structure and properties of a single actin filament (F-actin)	2
I.1.3 Actin binding proteins fine regulate the F-actin formation and degradation	3
I.1.4 The contractility with myosin motors (the muscle model)	6
I.2 Actin role at the cell scale	7
I.2.1 Cell shape and movement are provided by actin filaments	7
I.2.2 Actin filaments linked to plasma membranes induces cell shape and movement	8
I.2.3 Cell shape and movement can be regulated via membrane signaling	8
I.2.4 Filopodia, lamellipodia and stress fibers studied by Electron Microscopy	10
I.3 The actin stress fibers	11
I.3.1 Actin stress fiber types	11
I.3.2 The biomechanics of actin stress fibers	18
I.3.3 Cell geometry and biomechanics is dependent of stress fiber organization	23
I.4 Final considerations: the main differences between sarcomeres and stress fibers	30
I.5 Open questions on actin stress fibers organization: a motivation for this PhD work	32
Conclusion of Chapter 1	33

<b>Chapter 2 - Principles of polarization resolved fluorescence microscopy</b>	<b>35</b>
<b>II.1 Light polarization</b>	<b>35</b>
II.1.1 Light: the basic concepts	35
II.1.2 Light can be polarized, unpolarized or partially polarized	36
<b>II.2 Fluorescence light properties</b>	<b>37</b>
II.2.1 Fluorescence: introduction	37
II.2.2 Fluorescence is a radiative relaxation process	38
II.2.3 Fluorescence lifetime and quantum yield are important properties of the fluorophores	40
<b>II.3 Fluorescence light polarization properties</b>	<b>41</b>
II.3.1 The efficiency of radiative transitions is orientation sensitive	41
II.3.2 Transition dipole moment ( $\vec{\mu}$ ) of a fluorophore and its interaction with light	41
II.3.3 The absorption probability and its orientation sensitivity	43
II.3.4 The emission probability and its orientation sensitivity	44
II.3.5 Orientation sensitivity of the absorption-emission fluorescence process	46
<b>II.4 Fluorescence anisotropy in isotropic media</b>	<b>47</b>
<b>II.5 Fluorescence polarized response in anisotropic media</b>	<b>49</b>
II.5.1 Modelling the orientation distribution of fluorophores in ordered samples – the cone model	49
II.5.2 Polarized fluorescent response from a cone distribution of fluorophores	53
II.5.2.1 The microscopic frame coordinates related to the fluorophores' mean orientation $\vec{\mu}$	54
II.5.2.2 Aligning the microscopic frame onto the laboratory (macroscopic) frame	54
II.5.2.3 Reducing the geometry to a 2D problem	56
II.5.3 The cone model at the single-molecule level	56
II.5.3.1 What can we learn from single molecule polarized approaches?	58
<b>II.6. Experimental approaches for polarization resolved fluorescence microscopy</b>	<b>58</b>
II.6.1 Different polarized microscopy geometries	61
<b>Conclusion of Chapter 2</b>	<b>62</b>

<b>Chapter 3 - Polarized Fluorescence Microscopy Methods</b>	<b>63</b>
<b>Introduction</b>	<b>63</b>
<b>Nonlinear (multi-photon) vs linear (one-photon) optical methods, a brief discussion about why we keep using fluorescent probes</b>	<b>63</b>
<b>III.1 Polarized fluorescence microscopy in ensemble molecular organizations</b>	<b>64</b>
<b>III.1.1 Fluorescence anisotropy microscopy – conventional ensemble emission dipole mapping</b>	<b>64</b>
<b>III.1.2 Linear dichroism microscopy</b>	<b>66</b>
<b>III.1.2.1 The conventional ensemble absorption dipole mapping</b>	<b>66</b>
<b>III.1.2.2 Angular resolved linear dichroism (confocal) microscopy</b>	<b>67</b>
<b>III.1.3 Fast angular resolved linear dichroism (spinning disk) microscopy</b>	<b>72</b>
<b>III.1.4 Biological applications of ensemble polarization resolved microscopies</b>	<b>76</b>
<b>III.2 Ensemble vs single-molecule polarized fluorescence: why go to the single-molecule level?</b>	<b>82</b>
<b>III.3 Single-molecule approaches</b>	<b>83</b>
<b>III.3.1 Principle of dSTORM imaging</b>	<b>84</b>
<b>III.3.2 Adequate buffer for dSTORM imaging</b>	<b>85</b>
<b>III.3.3 Retrieving quantitative parameters from dSTORM single-molecule fluorescence events</b>	<b>86</b>
<b>III.4 The polar-dSTORM method</b>	<b>88</b>
<b>III.4.1 The current state of the art of single-molecule and super-resolution polarization resolved microscopy</b>	<b>88</b>
<b>III.4.2 Limitations of the polar-dSTORM method</b>	<b>91</b>
<b>III.5 The 4polar-dSTORM: 4 polarized analyzer channels</b>	<b>96</b>
<b>III.5.1 The state of the art in 4 polarized-split detection for polarized fluorescence imaging</b>	<b>96</b>
<b>III.5.2 The 4polar-dSTORM setup</b>	<b>97</b>
<b>III.5.3 The 4polar detection unit</b>	<b>100</b>
<b>III.5.4 The autofocus system</b>	<b>102</b>
<b>III.5.5 The 4polar-dSTORM method: retrieval of orientation and wobbling parameters from a single molecule</b>	<b>103</b>
<b>III.5.6 The 4polar-dSTORM: overcoming the polar-dSTORM limitations</b>	<b>108</b>
<b>III.6 Conclusions of Chapter 3</b>	<b>109</b>

<b>Chapter 4 - Ensemble Polarized Fluorescence Microscopy applied to Actin Stress Fibers</b>	<b>111</b>
Introduction	111
IV.1 - Materials and methods	113
IV.1.1 Cell preparation	113
IV.1.2 Imaging conditions of ensemble-PFM	113
IV.2 Preliminary calibrations of the setup	114
IV.2.1 Control of the excitation polarization: polarimetry measurements	114
IV.2.2 Data representation and correction procedure of the polarization distortions for the data processing	115
IV.3 Interpretation of the measured $\Psi$ value in SFs	119
IV.4 Comparing molecular order in different SFs: data processing	122
IV.4.1 Choice of cell shapes	122
IV.4.2 Stress fiber segmentation	123
IV.4.3 Stress fibers selection and classification	125
IV.4.4 Polarized image processing and molecular order parameters retrieval	129
IV.5 Comparing molecular order in different SFs and conditions: results	132
IV.5.1 Comparison among SF types in naïve U2OS cells	133
IV.5.2 Comparison among cell shapes and sizes in naïve U2OS cells	135
IV.5.3 Comparison among different contractile conditions	136
IV.5.4 Comparison among different cell morphologies in CA-MLCK U2OS cells	144
IV.5.5 Comparison between different spreading times in CA-MLCK U2OS cells	148
IV.6 Conclusions of Chapter 4	153
<b>Chapter 5 - Polarized Single-molecule Super-resolution Fluorescence Microscopy applied to Actin Stress Fibers</b>	<b>157</b>
Introduction	157
V.1. 4polar-dSTORM setup: calibration and correction of spatial distortions	157
V.1.1. Calibration factors	157
V.1.2. Spatial distortions can be corrected with Fluorescent beads	161
V.2. 4polar-dSTORM processing and analysis software: principle	163
V.2.1 Principle of the polar-dSTORM data processing software	164



V.2.1.1 Polar-dSTORM data processing overview	164
V.2.1.2 Vector estimation and pair identification	168
V.2.1.3 Single molecules' pairs parameters retrieval	169
V.2.2 The 4polar-dSTORM data processing principle	170
V.2.2.1 Orientation parameters retrieval and expected precision	173
<b>V.3 4polar-dSTORM setup: validation</b>	<b>175</b>
<b>V.4 Effect of the illumination and detection aperture conditions</b>	<b>176</b>
V.4.1 The illumination condition (normal incidence versus total internal reflection) affects the detection efficiency	176
V.4.2 Other parameter potentially affecting the detection efficiency	179
V.4.3 The illumination condition affects the retrieved wobbling parameter ( $\delta$ )	179
V.4.4 Minimizing the bias on fluorophore's wobbling ( $\delta$ ) under TIRF conditions	180
<b>V.5 Quantitative estimation of orientation and wobbling in SF regions in a fixed cell</b>	<b>183</b>
V.5.1 Retrieved detection and orientation quantities	183
V.5.2 Correlations between retrieved quantities	185
V.5.3 Results after filtering detection parameters	187
V.5.4 Effect of post-processing filtering on the 4polar-dSTORM polarimetry images	190
<b>V.6 Qualitative comparison of actin organization in different SFs regions of a fixed cell</b>	<b>192</b>
V.6.1 Focal adhesions regions	192
V.6.2 Dorsal SF regions	196
V.6.3 Summary of the qualitative SF regions analysis	198
<b>V.7 Quantitative comparison of different stress fibers and their sensitivity to contractility perturbations</b>	<b>199</b>
V.7.1 Comparison of F-actin degree of alignment in different SFs	199
V.7.2 F-actin alignment at the nanoscale is robust to perturbations	200
<b>V.8 Application of 4polar-dSTORM in complex and dense actin regions: cell lamellipodia</b>	<b>203</b>
<b>V.9 Conclusions of Chapter 5</b>	<b>205</b>
<b>Chapter 6 – Conclusion and prospectives</b>	<b>207</b>

<b>Appendix A – Sample preparation materials and protocols</b>	<b>211</b>
<b>Appendix B – dSTORM acquisition parameters</b>	<b>217</b>
<b>Appendix C – Examples of CYTOO patterned cells</b>	<b>219</b>
<b>Bibliography</b>	<b>229</b>

## General introduction

Biological processes within the cell can be complex in chemistry, structure, and behavior (dynamics). Biomolecular interactions at the nanoscale might trigger whole cell changes, and, in some cases, even multicellular scale responses (e.g., muscle contraction). To investigate such complex processes, fluorescence microscopy (FM) techniques are powerful tools due to their high specificity, versatility, and wide range of tailored applications. Moreover, one of the most important advantages of FM is that it can be extended to live cell imaging and provide insights about dynamic processes, elucidating complex behaviors in real time. For example, they can afford a good contrast to multiple and specific molecular targets simultaneously (e.g., multicolor), and observe how do these targets spatially distribute at different scales (from tissues to subcellular level). In particular, FM tools could be adapted to afford quantitative information about cells. For example, structural information of macromolecules could be probed by using fluorescent probes in polarized microscopy and in FRET microscopy. On the other hand, different chemical environment of the cell could be probed by tracking the energy states dynamics of the fluorescent probes (e.g., using FLIM microscopy).

In the last 20 years, there has been a remarkable development on new methods of fluorescence microscopy thanks to three major breakthroughs in the field of fluorescence imaging: the capacity to overcome the optical diffraction resolution, the possibility to probe single-molecules, and the ability to tailor fluorescent protein tags for live cell imaging. Such advances have already made it possible to investigate nanoscale structural heterogeneities and behaviors previously hidden in ensemble averaging methods, giving scientists unprecedented details of their system of interest at the nanoscale. For example, interferometric photoactivated localization microscopy (iPALM) showed that focal adhesions molecules have a sub-diffraction stratified organization along z-direction, and single particle tracking PALM (sptPALM) could monitor spatial maps of diffusion coefficients in cell compartments and in live cells membranes.

In parallel, another class of FM technique that exploit the anisotropic properties of the fluorescent labels has been converging to this very multidisciplinary field: polarization resolved imaging methods such as linear dichroism and fluorescence anisotropy microscopy. These methods use polarized light to decode orientation information of the fluorophores, thus adding a new dimension to the fluorescence images. With polarized FM, the angular orientation and local organization (angular distribution) of the fluorophores can be quantitatively estimated. Since such fluorophores are linked to the biological structure of interest, the latter structural organization can be indirectly quantified and displayed on the image, pixel by pixel. However, all polarized FM techniques developed so far have their own limitations, and cannot investigate any random supramolecular biological structure. The major limitation is that fluorophores undergo thermal motion at room temperature, which affects the orientation readout. Thus, because ensemble techniques averages the orientation over many molecules, ensemble approaches are not capable of disentangling such dynamic contribution, therefore biasing the organization map.

The main goal of this thesis is to develop a setup capable of measuring ensemble and single-molecule orientation and order of fluorophores, and therefore providing for the first time a consistent study of instrumentation limitations in the imaging of structural organization maps. The chosen biological structure of interest was filamentous actin in actin bundles Stress Fibers (SF). This choice was made because these structures are well referenced and well known. Additionally as the reader will see in the following chapter (Chapter 01), stress fibers can be

subdivided into classes that are contractile and not contractile depending on their composition, thus they are a very interesting model to test if polarization resolved methods can detect orientation alignment changes related to biological or mechanical functions.

This thesis is organized as follows:

In *Chapter 1 – Actin Filament Structures and Function*, we introduce the biological system probed in this thesis and we show that some relevant questions are still open due to the lack of suitable microscopy techniques to probe the system at the nanoscale in cells.

In *Chapter 2 – Principles of polarization resolved fluorescence microscopy*, we detail the principles of polarized fluorescence microscopy and theoretically show how experimental conditions might affect the polarization readout.

In *Chapter 3 – Polarized Fluorescence Microscopy Methods*, we make a literature review of the PFM methods, and we show how each technique improved the polarization parameters readout until we reach the current ensemble and single-molecule state-of-the-art methods.

In *Chapter 4 – Ensemble Polarized Fluorescence Microscopy applied to Actin Stress Fibers*, we describe the fast ensemble-PFM setup we have built, and its application to probing actin filament organization at different stress fiber types taking account their different natures.

In *Chapter 5 – Polarized Single-Molecule Super-Resolution Fluorescence Microscopy applied to Actin Stress Fibers*, we finally show our novel polarized single-molecule setup, and apply it to investigate the nanoscale organization of actin filaments in stress fibers in an unbiased manner in 2D.

In *Chapter 6 – Conclusions and perspectives*, we summarize all the work done, give general conclusions related to the results of chapters 4 and 5, and give a few prospective for this work.

# Chapter 1

## Actin Filament Structures and Function

### Introduction: actin is an important biomolecule present in almost all organisms

Actin is one of the main building blocks of the cellular cytoskeleton. It is the most abundant protein in eukaryotic cells (5%-10% of total protein content, reaching 20% in muscle cells) [1]. Actin is also highly conserved through the species. In particular, its sequence is 90% conserved in eukaryotic cells [2]. For example, the protozoan *Acanthamoeba* differs from mammalian actin by only 15 out of 375 amino acid residues, and a comparison among different skeletal muscle actin from many warm-blooded vertebrates reveal 100% amino acid sequence conservation [1]. Actin isoforms exist, they are six in mammals, and are mainly divided in three classes by electrophoretic 2D SDS PAGE:  $\alpha$ -actin (found only in muscle cells), and  $\beta$ - and  $\gamma$ -actin (found in almost all non-muscle cells) [2-5]. These six actin isoforms might be expressed in different tissues, but even these differ at the maximum by around 23 out of 375 residues [1]. These numbers only highlight the importance of actin in the eukaryotic cell life, and demonstrate that actin must keep a very similar 3D structure throughout different cells, tissues and species.

In this chapter, the main properties of actin are described. A very general overview is given to explain the motivation of this PhD work for measuring actin organization at the nanoscale in cells.

### I. 1 Structure of actin and actin networks

#### I.1.1 Structure and properties of a single actin monomer (G-actin)

The actin molecule is a globular protein composed in general by 375 amino acid residues (374 in some cases [5]), with a molecular weight of around 42 kDa, and isoelectric point around pH=5.5 [1, 2, 5]. In particular, Collins J.H, and Elzinga M. (1975), estimated that  $\alpha$ -actin skeletal muscle of rabbits had an isoelectric point around pH=4.8 yielding a net charge of  $q = -7$  at neutral pH [6]. Actin molecule is oftentimes called globular actin (G-actin). It can polymerize in vitro and in vivo into filamentous actin (F-actin). G-actins are divided in 4 main sub-domains (see Figure 1.1)

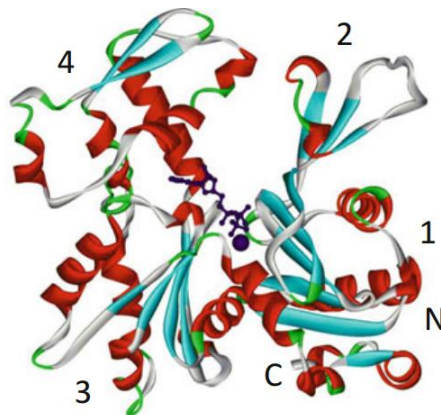


Figure 1.1 – Actin monomer (G-actin) in ribbon representation. Alpha-helices are in red, beta-strands are in blue, beta-turns are in green, and loops are in gray. In purple in the center it is the ATP enzymatic site for polymerization.

Actin needs a covalent cofactor ATP (or ADP), and an ionic  $\text{Ca}^{+2}$  cofactor to work [1]. The numbers 1, 2, 3, and 4 are the four subdomains of G-actin. C, N stands for C- and N- terminus end. The odd subdomains (1 and 3) points to the filament plus end, whereas the even subdomains (2 and 4) points to the minus end. Figure taken from [3].

### I.1.2 The structure and properties of a single actin filament (F-actin)

When single filaments are formed, the G-actin subunits point to the same direction and the actin filament is said to be polarized. At one end, named plus end (or barbed end), it polymerizes 10x faster in vitro than the minus end (also named pointed end) (see, Figure 1.2). [1, 2] Therefore there is a preferential orientation of polymerization, and the single filament can be thought to hold a specific orientation. Single actin filaments have a left-handed helicoidal rotation of 74 nm pitch, and around 8 nm thickness (Figure 1.2). Actin filaments can be as long as the size of a cell, spanning from a few nm to whole cell scale (i.e., tens to hundred of  $\mu\text{m}$  scale).

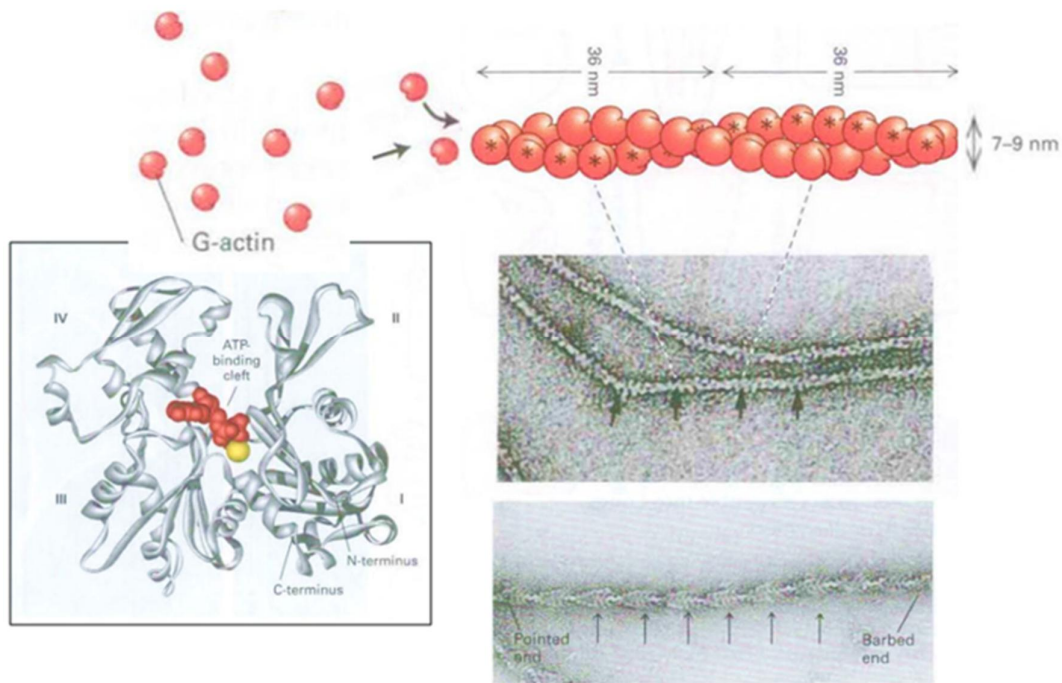


Figure 1.2 – Illustration of actin polymerization into a single filament, and its polarity (barbed (+) end, and pointed (-) ends). The electron micrograph on the top shows (black arrows) the helical periodicity of 74nm of the left handed spiral F-actin structure. The bottom micrograph shows F-actin decorated with myosin highlighting the pointed and barbed ends geometry. Figure adapted from [7].

### **I.1.3 Actin binding proteins fine regulate the F-actin formation and degradation**

What makes actin so extraordinary is the incredible amount of different molecules (more than 60) that can interact with it in order to control actin filament formation or degradation [1]. Actin binding proteins (ABP) are responsible for the fine control of actin polymerization and orientation in space, in time and in quantity within cells. For example, capping proteins can bind to one of the filament edges (termini) allowing the polymerization at one specific orientation. For example, Formin dimer and CapZ protein bind specifically to actin filament (+) end, and Tropomodulin protein binds to (-) end. Other proteins bind alongside of actin filaments. For example, accessory proteins such as Tropomyosin stabilizes actin filament making a few regions of F-actin available for interaction with myosin, an important motor protein that generates forces by pulling actin. Another side-binding proteins are from the Gelsolin superfamily, which a model suggests to break actin filament from their neighbors. Proteins such as Gelsolins and Severins induce actin filament depolymerization, making stiff and large bundles, and some 3D actin gels become more fluid, affecting the mechanical properties of their local environment of the cell. Other proteins can also destabilize actin filaments by inducing a tighter twist in actin filament conformation. That is the case of Cofilin, an actin depolymerization factor. The actin helicoidal pitch when bound to Cofilin is reduced to 57nm from the wild type 74 nm. As we may expect, some ABP compete against each other. That is the case of Cofilin and Tropomyosin, which compete for the same actin sites for filament stability. Stability here is the capacity to keep F-actin properties, such as filament length.

ABP can also crosslinks two actin filaments in different fashions for different purposes see Figure 1.3. For example, actin filaments can be bundled and oriented with parallel (e.g., with Fimbrins in filopodial structures, see Figure 1.4) or anti-parallel (e.g., with  $\alpha$ -actinin in stress fibers structures, see Figure 1.4). Sometimes, the cell needs to induce crossed filaments in different fashions, and not aligned ones. For example, Arp2/3 complex and Filamin dimers induces a formation of different actin networks. The former induces the formation of a dendritic network with actin filament branches oriented with specific angle among each other (close to 70°), and the latter induces a more loose and viscous network that resembles a gel (with actin crossings of around 90°). Both are often present in the front edge of the cell, in an actin structure named Lamellipodia (see Figure 1.4). The way the actin filaments are crosslinked also affect their packing degree. For example, Fimbrin in filopodia are short crosslinkers and induces actin filaments to bundle in a very aligned and paralleled fashion (see bundling protein in Figure 1.3). On the other hand, Filamins are longer and more flexible crosslinkers compared to Fimbrins, and induces a loosen actin network formation (see example of cross-linking protein in cell cortex in Figure 1.3).

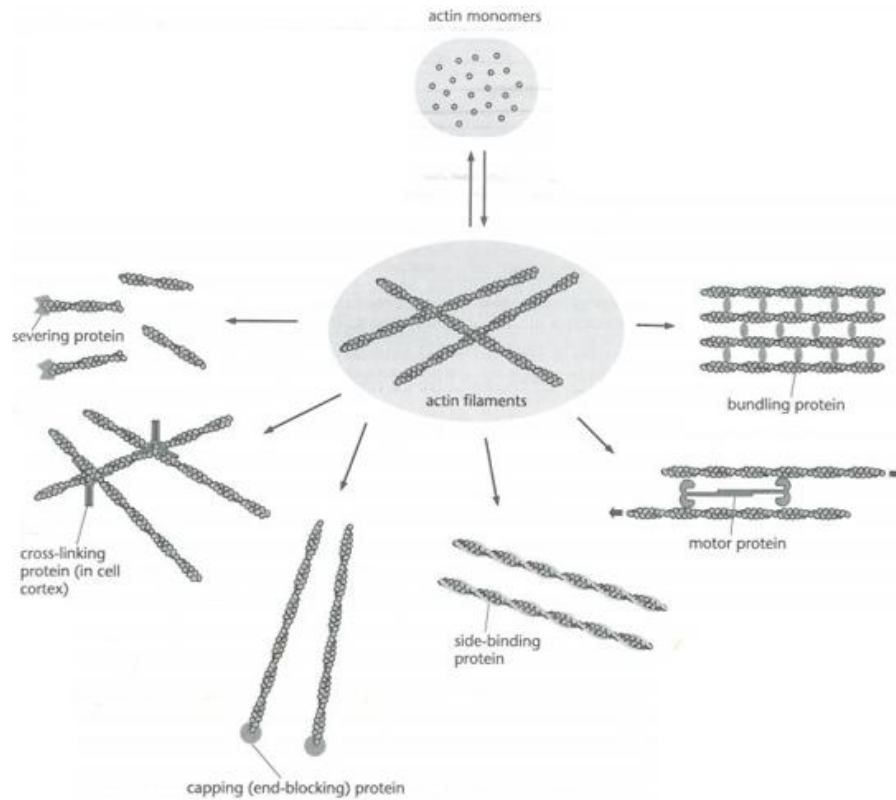


Figure 1.3 – Illustration of some possible actin binding proteins (ABP) function and how they control the organization of actin filaments. Adapted from [1].

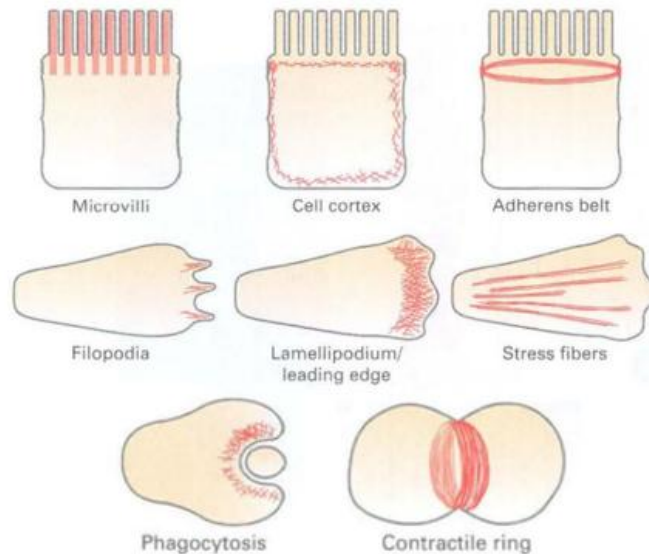


Figure 1.4 – Examples of higher order structures built with actin filaments (in red). In epithelial cells (three squared cells above), the whole geometry of the cells, including the microvilli, are supported by actin filaments. The three cells in the center exemplifies the migrating cells on a planar substrates, such as green monkey kidney cells (COS-7) and human osteosarcoma (U2OS) cells. Note that, filopodia (surface spikes), lamellipodia (leading edge network) and large actin filament bundles (stress fibers) are structures often present in migrating cells. In particular, stress fibers of U2OS cells were used in this thesis as the main model for study actin filament organization. Other important cell processes such as phagocytosis and cell division are dependent on structures built with actin filaments. Note that to study a specific structure of interest, it depends on the cell type, cell regions, cell environment, and cell cycle moment. Adapted from [7].



The goal of this section was to give a glimpse of how actin filament might interact with other proteins, and what are the effects of their interaction with actin filaments. Actin filaments are therefore highly controlled in different fashions and geometries. Besides, each higher order structure built with actin filaments, such as stress fiber bundles (for cell movement and mechanically sense the environment), actin rings (in cell division), Z-disk (in muscle contraction), etc, has a specific set of actin binding proteins that are more present in loci, which tightly regulates actin filament function and their location within cells accordingly. For more details, we invite the reader to read textbooks of Bruce Alberts (Molecular Biology of the Cell, 6<sup>th</sup> ed.), and Dennis Bray (Cell movements, from molecules to motility, 2<sup>nd</sup> ed.). All the examples given above were taken from these textbooks. In the next section, we will present in more detail the most studied actin structure that generates forces in the presence of myosin motors.

### I.1.4 The contractility with myosin motors (the muscle model)

Actin binding proteins (ABP) can also have active roles such as force generation in actin filament bundles. The most studied case are the myosin motors in sarcomeric structures in striated muscle cells (see Figure 1.5).

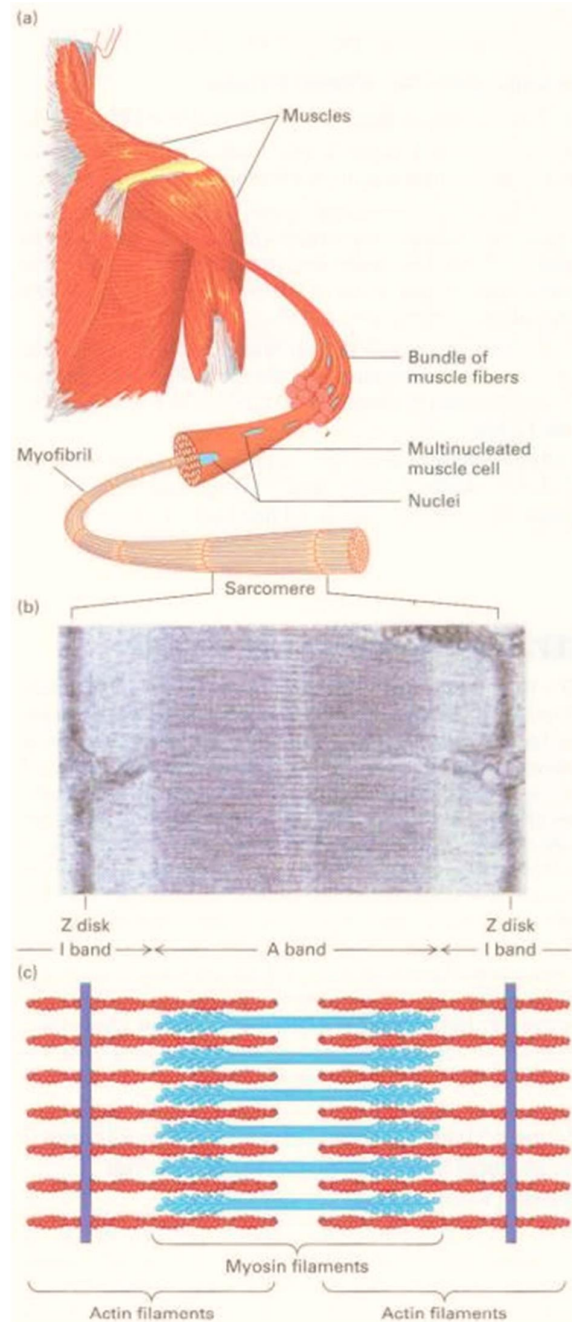


Figure 1.5 – The sarcomeric actin structure present in striated muscle cells. (a) Illustration of muscle fibers and their elongated cells (myofibrils). Myofibrils expel their nuclei to the lateral edges the cell, and their intracellular content is mainly composed by actin structures named sarcomeres. (b, c) Sarcomeres are repeated contraction units mainly composed by 3 components: actin filaments (in red), molecular motors (myosin filaments or A band, in blue) and rigid wall structures (named Z-disks, containing  $\alpha$ -actinin and other molecules, the I band in purple). Figure taken from [7].

A sarcomere is a contraction unit between two Z-disks that provide a framework to myosin filaments (motors) to slide on actin filaments by pulling actin filaments of opposite polarities (see Figure 1.5). The latter means that the myosin heads of myosin filaments *only* slide on actin filaments from the (-, pointed) end to the (+, barbed) end (see Figure 1.6). In this sense,  $\alpha$ -actinin is the crosslinker rigidly situated on Z-disks that is responsible to rearrange actin filaments with different polarities on the both sides of the Z-disk wall. Since the sarcomeres are bound aligned to each other and to the edges of the muscle cell, when multiples sarcomeres contract, the whole cell (myofibril) contracts accordingly (see Figure 1.6).

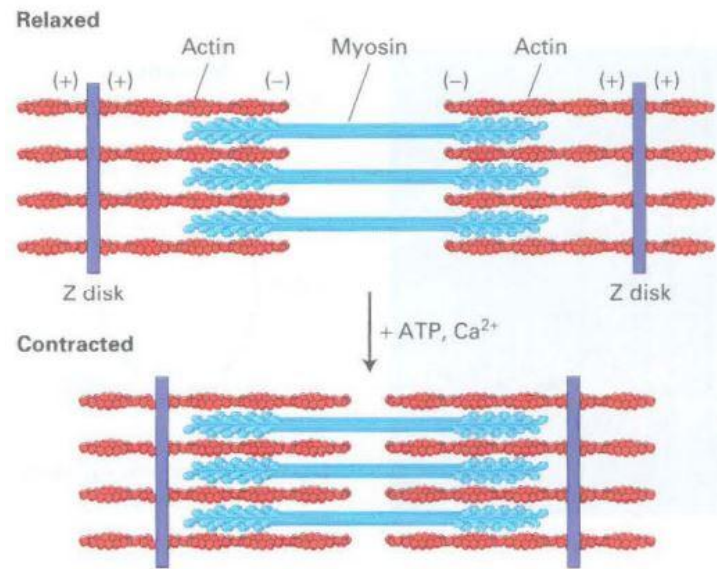


Figure 1.6 – The contraction process in sarcomeres. On the top, the relaxed state, on the bottom the contracted state. Note that upon the injection of +ATP and Ca<sup>2+</sup> stimuli in the system it induces the myosin heads (in blue) to pull actin filaments, thus coming closer to the Z-disks (in purple) during contraction process. Figure taken from [7].

Such model in striated muscle cells suggests that for effective contraction, actin filaments of opposite polarities must be well aligned to make the myosin filaments easily slide on them. In striated muscle cells, such sarcomeres have a local crystalline order, which represents one of the main ordered structures built with actin filaments in cell biology. The knowledge of the main building blocks for contraction in muscle cells helps us to understand better how other actin filament structures contract, such as stress fibers, the main studied structure of this thesis.

## 1.2 Actin role at the cell scale

### 1.2.1 Cell shape and movement are provided by actin filaments

Actin filaments are needed for cell shape and movement in non-muscle cells. The cell morphology and motility are key features for proper cell function. For example, a neuron must keep its stellar shape to access different parts in the brain, and white blood cells must migrate

to search for pathogens in the body. Besides, cell migration is an important behavior in wound healing and in cancerous tumors (e.g., metastasis). In particular, filopodia, lamellipodia, and stress fibers (see Figure 1.4) are examples of important actin higher order structures for cell shape and motility on 2D solid substrates. The main non-muscle cells used in the literature for studying such actin structures are COS-7 cells (green monkey kidney), U2OS cells (human osteosarcoma), fish keratocytes, fibroblasts, and melanoma cells [8, 9]. Among them, we chose U2OS cells in this PhD work because they display a large variety of stress fibers and have a rich literature about these structures. Many important questions about how stress fibers assemble and how they contract (or bear tension) have been tackled by using U2OS cells as a model. As it is going to be explained in the next sections, although some stress fibers contain actin and myosin filaments, they lack the same crystalline organization seen in muscle sarcomeres. How actin filaments, myosin filaments and other actin binding structures are organized in different stress fibers is a topic still under investigation.

### **1.2.2 Actin filaments linked to plasma membranes induces cell shape and movement**

Actin is mostly concentrated at the cell cortex (regions close to the plasma membrane of around 200nm to 500nm thick), although it is present throughout the cell. Such layer of actin filaments provide enough mechanical strength for the cell surface, enabling it to change its shape and move. Important processes such as pinocytosis and phagocytosis (engulfing particles), cell crawling (motility), and cell division, depends on the capacity of the cell cortex to produce such membrane protrusions. Actin can be linked to the plasma membrane in different ways. Actin can be linked directly through an integral protein embedded into plasma membrane (e.g., proteins such as cortaxillin, ponticulin, calpactin, or lipocortin), or indirectly linked via crosslinkers such as  $\alpha$ -actinin and Filamin [1]. Another important protein group that indirectly binds actin to the plasma membrane, and stimulates cell cortex changes are the ERM proteins (stands for Ezrin, Radixin, and Moesin). The ERM proteins are present in vertebrate cells, and link actin filaments to integral membrane proteins. They are present in two ON/OFF states: they can be switched on (open conformation, that binds to actin filaments), and switched off (closed conformation, that does not bind actin filaments). It is believed that the ERM proteins can switch ON via phosphorylation by small GTP-binding proteins (e.g., Rho kinases), from a large family of membrane proteins named Ras superfamily, responsible for many cell signaling processes.

### **1.2.3 Cell shape and movement can be regulated via membrane signaling**

Membrane signaling via GTP-binding proteins (i.e., G proteins, such as Rho, Rac and Cdc42 kinases) changes the cell surface morphology by interacting with actin filaments present in the cell cortex. A few examples are illustrated in Figure 1.7. The G proteins are self-inactivating switches, i.e. when they are active (i.e., when GTP is bound), they trigger a downstream signaling cascade of events in the cell. One of the most prominent G proteins are the Rho kinases. The Rho kinases regulate the association of actin filaments with cell surface receptors, like ERM proteins. It is believed that that ERM phosphorylation by Rho kinases induces the formation supramolecular anchorage structures named focal adhesions (FA). These structures are of a few  $\mu\text{m}$  long present at the ventral part of the cell. They are responsible to make the contact between the cell to the substrate, and they also sense the substrate stiffness. Focal adhesions form clusters with transmembrane proteins named Integrins. The latter bind to components of the extracellular matrix (e.g., fibronectin, laminin, and collagen), attached to the substrate.

Integrins are a very important and diverse family of transmembrane protein that are responsible to transmit to local mechanical tension from the focal adhesions to the actin cytoskeleton. In general, the focal adhesions are bound to F-actin bundles named stress fibers (SF), that endure cell tension (see Figure 1.7 and Figure 1.8).

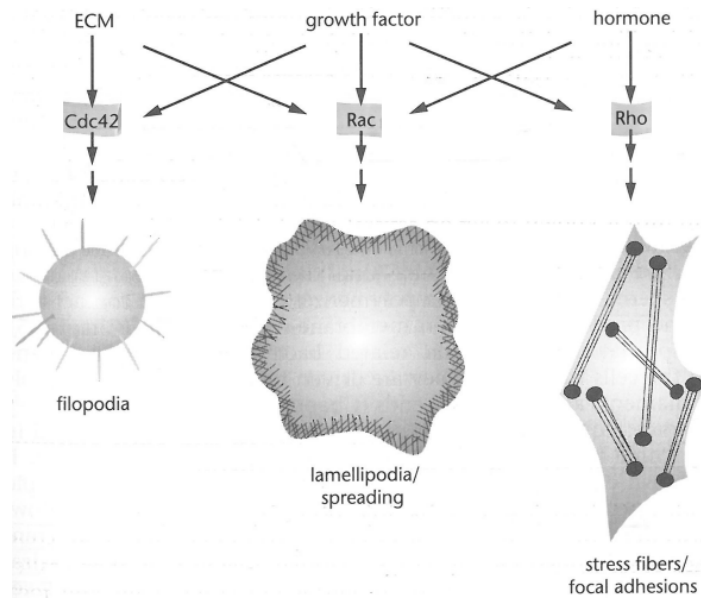


Figure 1.7 – Illustration of different cell surface morphologies induced by different G-proteins. On the left, Cdc42 kinases induce the formation of filopodial structures. On the center, Rac kinases induce cell spreading by the formation of cell cortex protrusion named lamellipodia. On the right, Rho kinases stimulate the formation of focal adhesions and stress fibers. Possible crosstalk might occur between the signaling pathways (represented by arrows in diagonal). ECM, extracellular matrix. Figure adapted from [1].

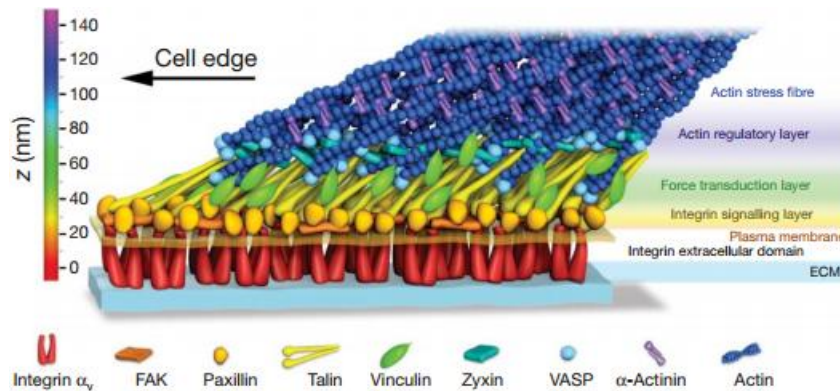


Figure 1.8 – Focal adhesion structure model suggested by interferometric super-resolution microscopy (iPALM). Focal adhesions contain hundreds of proteins that assemble together forming an anchorage complex between the cell and the extracellular matrix (ECM). The study of Kanchanawong, P. et al (2010) demonstrated many functional layers along z direction corresponding to different focal adhesion molecules (Integrin, FAK, Paxillin, Talin, Vinculin, Zyxin, VASP,  $\alpha$ -actinin and F-actin). Figure taken from [10].

#### 1.2.4 Filopodia, lamellipodia and stress fibers studied by Electron Microscopy

Electron Microscopy (EM) techniques use a beam of electrons to create imaging contrast. Electron microscopes have a higher resolving power than light microscopes (capable of viewing the cellular ultrastructure with nm resolution), but with limited applications (only applied to fixed samples). It needs a high vacuum tube to guide the electrons to the sample, and these must be accelerated in a kilovolt range to properly interact with the sample. Oftentimes, biological samples need a coating with electron dense materials such as gold or platinum to increase the contrast. As light microscopes, one could make an EM image by transmission, scanning or scattering, depending on the properties under investigation (e.g., scanning electron microscope to investigate the surface topology of materials). One could also label cellular structures with immunoglobulins (e.g., immunogold) to provide chemical specificity, but when it is performed, the morphological readout is affected. For proper contrast in biology, very thin sections (typically of 50nm thick) must be achieved by using an ultramicrotome or equivalent sectioning strategy.

Actin filaments are very difficult structures to be imaged via EM, because they are very thin (~8nm thick) and delicate. The sample preparation for EM is in general long (few days), and it can be relatively harsh for the sample, thus possibly affecting the morphology of delicate structures, creating artifacts in the image. Although challenging, actin structures such as Filopodia, Lamellipodia and Stress Fibers have already been evaluated by Electron Microscopy (EM) techniques by different research groups [8, 9, 11]. In Tatyana Svitkina group, for example, they optimized the sample preparation procedure for imaging actin filaments in cultured cells (see Figures 1.9-1.10).

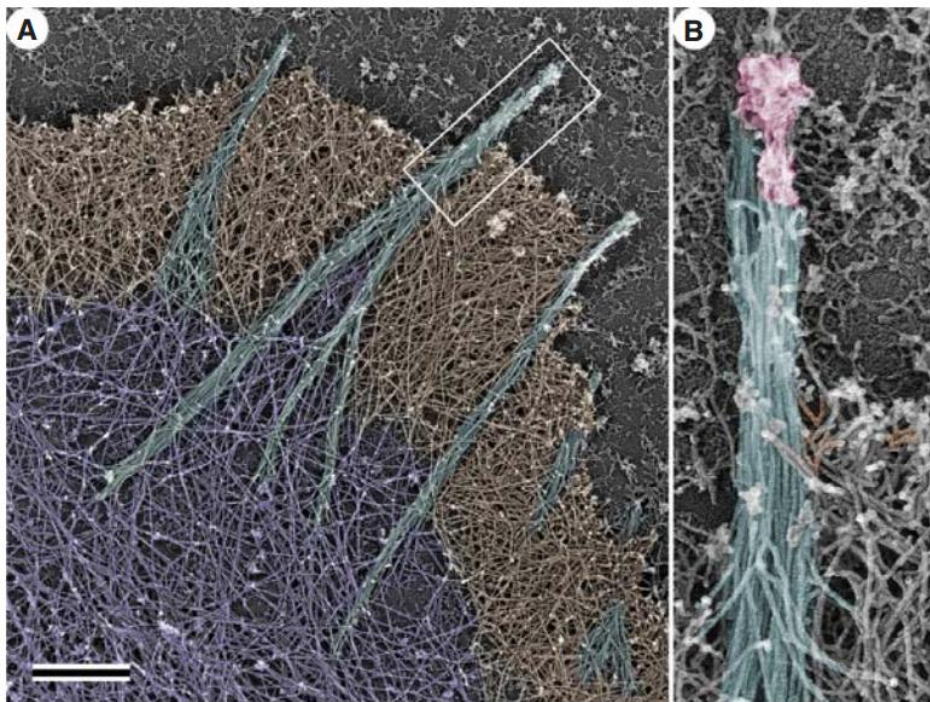


Figure 1.9 – Electron micrographs of mouse melanoma cell. (a) The leading edge of the cell. In cyan, actin filament bundles (filopodia), in yellow, the dense actin network of lamellipodia, and in purple the sparse network (lamella). (b) Enlarged ROI of the filopodium from (a). In pink, regulatory proteins at the tip of the filopodium (in cyan). Figure taken from [11].



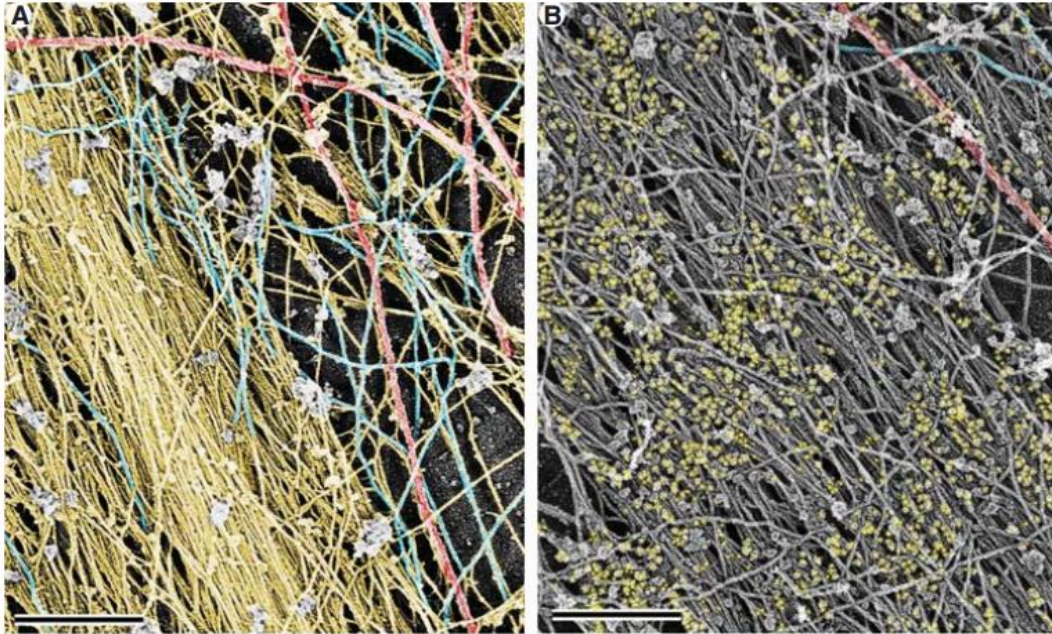


Figure 1.10 – Electron micrographs of stress fibers from rat fibroblasts. Color code in (a): yellow, actin filaments; cyan, intermediate filaments; red, microtubules. (b) Immuno gold staining with antibody to nonmuscle myosin II. Color code in (b) : yellow, gold particles; red, microtubules; cyan, intermediate filaments. Scalebar: 500nm. Figure taken from [11].

### **1.3 The actin stress fibers**

#### **1.3.1 Actin stress fiber types**

Actin stress fibers (SF) are bundles of 10-30 actin filaments in general (reaching up to 300 filaments in very thick bundles) of around 0.2 $\mu$ m to 1.5 $\mu$ m thick, and a few to tens of  $\mu$ m long that play a role in many important non-muscle cell functions (see Figure 1.10 and 1.11) [12-15]. In general, SFs participate in processes related to cell adhesions, sensing and exchanging mechanical forces with the environment (ECM), guaranteeing morphological stability, and allowing cell motility (e.g., crawling). Such cell processes are important in embryogenesis, tissue regeneration and in pathological conditions such as metastatic cancer [12]. The typical biochemical composition with their corresponding function in SF is listed in Table 1.1.

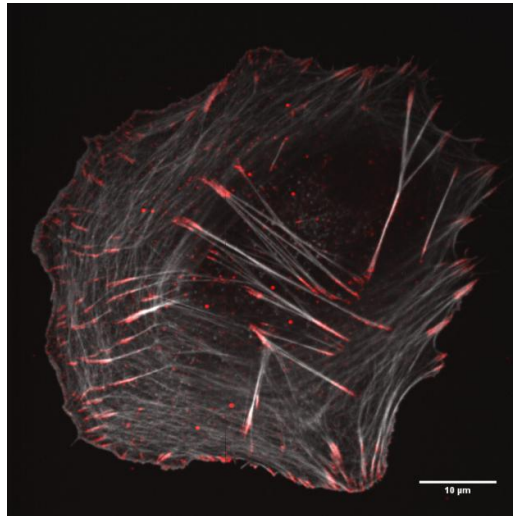


Figure 1.11 – Actin stress fibers in human osteosarcoma (U2OS) cell. In gray, phalloidin-AlexaFluor488 staining for actin filaments; in red, immune labelled phosphorylated focal adhesion kinase (phospho-FAK sites) for staining focal adhesions. Scale bar: 10 $\mu$ m. Figure elaborated by the author (see Chapter 4).

Stress fiber component	Function
$\alpha$ -Actinin	Filament crosslinking, signal transduction
Caldesmon	Regulation of contractility, cell motility and stress fiber stability
Calponin	Regulation of contractility, motility, stability of actin-based structures, signal transduction
Serine/threonine protein kinase 35 (CLIK1 or STK35)	Signal transduction
Coactosin	F-actin binding
Cysteine-rich protein 1 (CRP1)	Actin filament bundling
Fascin	Actin filament bundling
FH1/FH2 domain-containing protein 1 (FHOD1)	Stress fiber stabilization
Filamin	Filament crosslinking, mechanosensing
Myosin phosphatase Rho-interacting protein (MPRIIP)	Control of MLC phosphorylation through MLCP
Myosin II	Stress fiber contraction
NUAK family SNF1-like kinase 1 and 2 (NUAK1 and NUAK2)	Regulation of MLC phosphorylation
Palladin	Actin crosslinking, cytoskeletal scaffold
PDZ-LIM proteins	Signal transduction
Rho-associated protein kinase (ROCK)	MLC phosphorylation
Septin2 (SEPT2)	Regulation of myosin II activity
Transgelin	Stabilization of stress fibers, regulation of contraction and cell motility
Tropomyosin	Stabilization of stress fibers, myosin recruitment, regulation of contraction
Vasodilator-stimulated phosphoprotein (VASP)	Stress fiber assembly
Zyxin	Stress fiber stability and repair

Table 1.1 – Typical actin stress fibers components and function. Table taken from [13].

Although Table 1.1 lists the typical biomolecules present in actin stress fibers (SF), the composition of all actin stress fibers are not the identically same. In fact, there are many ways one could categorize actin SF bundles. They are generally classified into a few subtypes depending on their composition, localization, signaling pathways and interaction with focal adhesions. Conventionally, stress fibers are subdivided into 3 main classes: dorsal SF, ventral SF, and transverse arcs (T-arcs), see Figure 1.12.



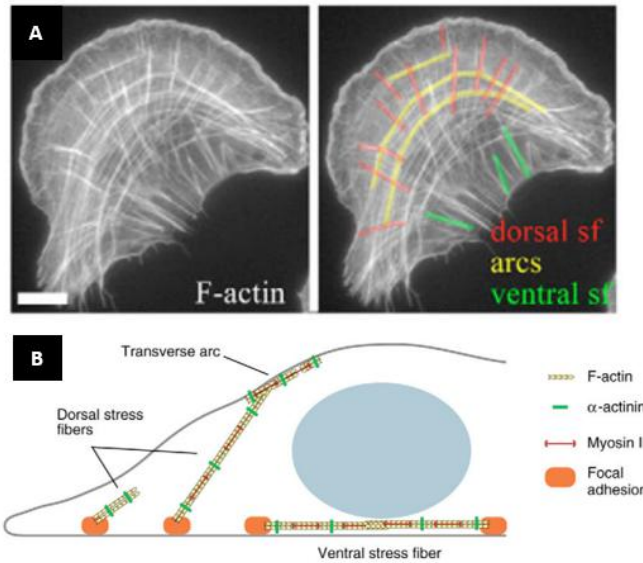


Figure 1.12 – Human osteosarcoma (U2OS) cell stained for F-actin and the conventional classification actin SF bundles. (A) Actin stress fibers. Color code: gray, F-actin; red, dorsal SF; yellow, transverse arcs; green, ventral SF. (B) Typical localization and geometry of actin SFs. Dorsal SF have a tilted orientation, and are attached by a single focal adhesion to the substrate. Ventral SFs are at the ventral part of the cell, close to the substrate, and are connected by two focal adhesion sites. Transverse arcs are at the dorsal part of the cell, aligned with the dorsal plasma membrane and form circumferential arcs around the nucleus. Figure adapted from [14].

Dorsal stress fibers are bundles that are continuously elongated from the focal adhesions (leading edge, ventral part of the cell) until they reach transverse arcs (top, dorsal part). Quantification of GFP-actin labeled stress fibers resulted in a growth rate of  $0.3\mu\text{m}/\text{min}$  [16]. The mean growth rates of different dorsal SF were similar among each other and also similar to the transverse arcs centripetal flow (see Figure 1.13a-b). Fluorescence recovery after photobleaching (FRAP) analysis demonstrated that the actin polymerization emerged from focal adhesions. A rearward flow of bleached region ( $\sim 2.5\mu\text{m}$  wide) followed the dorsal SF elongation (see Figure 1.13c). The quantification of the rate of the newly form actin filament from focal adhesion was very similar ( $0.25\mu\text{m}/\text{min}$ ) to the dorsal bundle elongation ( $0.3\mu\text{m}/\text{min}$ ), suggesting that the latter was mainly caused by actin filament polymerization at the focal adhesions (see Figure 1.13a-c). Such live cell imaging and photobleaching studies suggests that dorsal SF assemble with uniform polarity from newly formed focal adhesions. Besides, Fascin, which is an actin crosslinker that binds to bundled actin filaments with uniform polarity, is only found in focal adhesions and stress fiber termini [15]. Consequently, dorsal SF bundles might be not contractile, since the presence actin filament with bi-directional polarity are expected for contraction with myosin (like sarcomeres). Accordingly, live cell imaging studies with non-muscle myosin-II did not detect amounts of myosin II in dorsal stress in regions close to the focal adhesions (see Figure 1.13d). However, myosin spots were visible in distal regions of dorsal SF of several  $\mu\text{m}$  long, already connected with transverse arcs (i.e., under a conversion process to ventral SF, explained below) [16].

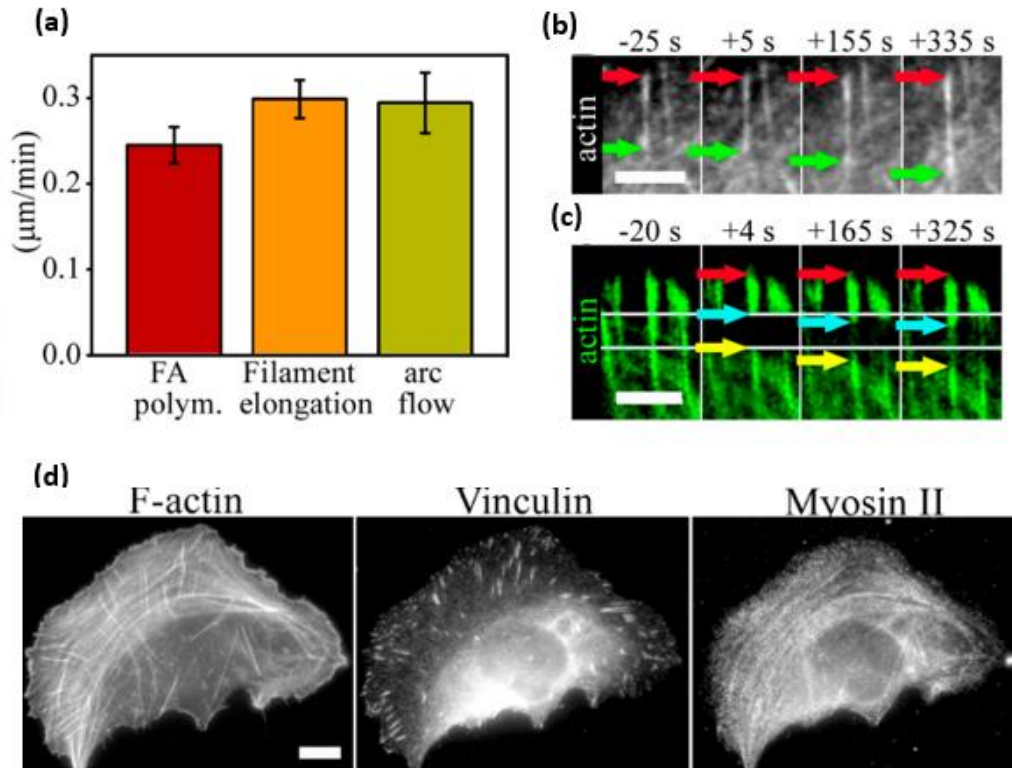


Figure 1.13 – Dorsal stress fiber elongation and composition. (a) Rates of live cell actin elongation at focal adhesion, dorsal bundle, and transverse arc centripetal flow. (b) Live cell experiment of dorsal SF elongation. Red arrow, focal adhesion tip (nascent); Green arrow, dorsal bundle end. (c) Filament elongation close to focal adhesion by FRAP ( $2.5\mu\text{m}$  wide bleaching, highlighted by white lines). (d) U2OS cell stained with F-actin, vinculin (focal adhesion marker), and myosin II (contractility sites). Note that dorsal actin filaments (orthogonal to transverse arcs) do not have in general myosin II. On the other hand, transverse arcs and ventral SF do have myosin II. Scale bar:  $10\mu\text{m}$ . Figure adapted from [16].

Transverse arcs (T-arcs) are curved bundles that are formed in the lamellar region of the cell and flows upwards and centripetally along the dorsal membrane of the cell. Both transverse arcs and dorsal stress fibers are subjected to continuous formation and disassembly. Nevertheless, instead of being elongated in one defined direction, T-arcs are generated by condensation of small filament fragments at the leading edge, in a constant flow towards cell center of around  $0.3\mu\text{m}/\text{min}$  (see Figure 1.13a) [16]. Another contrast in relation to dorsal SF is that T-arcs contain myosin II along its whole bundle. In addition, a periodical rearrangement of  $\alpha$ -actinin and myosin II is observed in transverse arcs (see Figure 1.14), which resembles a sarcomeric organization for contractility. Moreover, the periodical rearrangement of  $\alpha$ -actinin-myosin-II during transverse arc assembly gets clearer with time (maturation process), suggesting that the formation of T-arcs is followed by an increase in contractility capacity. Besides, myosin inhibition experiments lead to disappearance of transverse arcs, followed by the delayed disappearance of dorsal SF due to focal adhesions disassembly [16]. Thus, such evidences suggests that transverse arcs are contractile bundles, in contrast to dorsal SF, that are mainly non-contractile bundles generated under focal adhesion tension.

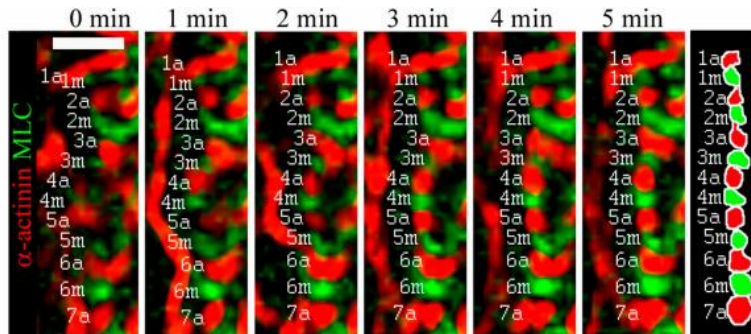


Figure 1.14 – Transverse arcs assembly in live cell experiment using U2OS cell. Color code: red,  $\alpha$ -actinin (a); green, myosin light chain (MLC or m). The U2OS cell was expressing  $\alpha$ -actinin tagged with cyan fluorescent protein (CFP), and MLC tagged with yellow fluorescent protein (YFP). Cell edge is on the left side of the arc. From this time lapse, we can see that green and red spots get more defined (periodically separated) within minutes. Scale bar  $5\mu\text{m}$ . Figure taken from [16].

Ventral stress fibers are considered contractile bundles that can be assembled by the conversion of transverse arcs and dorsal stress fibers into a single bundle (see Figure 1.15). They hold periodical  $\alpha$ -actinin-myosin-II features, like transverse arcs. Ventral SF are located at the ventral part of the cell and typically are defined as bundles in between two focal adhesions (see Figure 1.12b). The formation of ventral SF is dependent on the centripetal flow of transverse arcs. While some transverse arcs centripetally move upwards the cell being disassembled in the perinuclear region, other T-arcs get annealed together with two opposite oriented dorsal SFs, being transferred to the ventral part of the cell (close to the substrate surface) (see Figure 1.15).

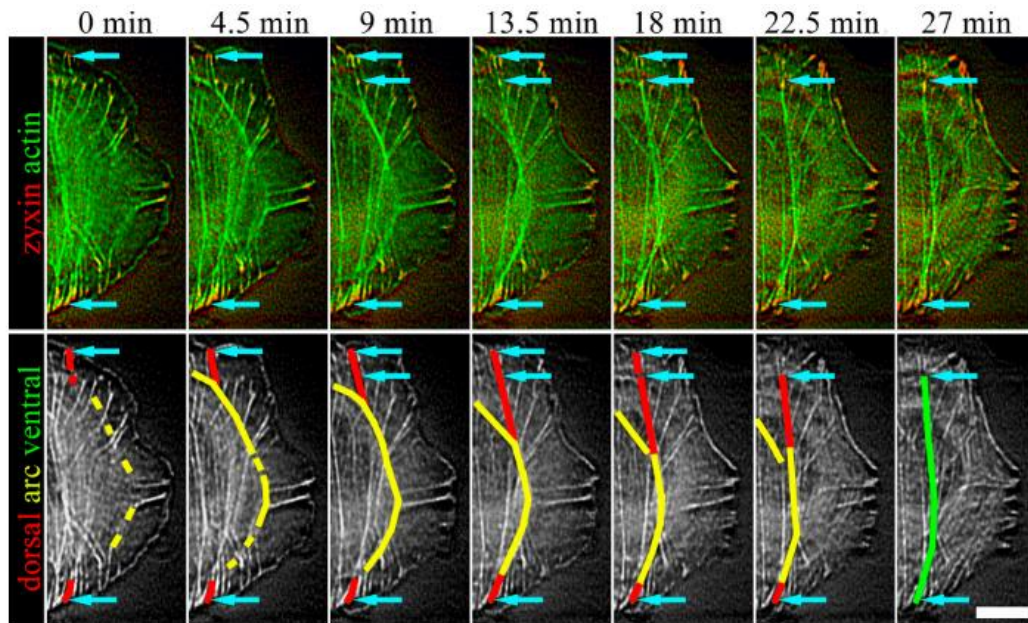


Figure 1.15 – Ventral stress fiber assembly within minutes. On the top, F-actin (in green, tagged with YFP) and a focal adhesion marker (zyxin in red, tagged with CFP). On the bottom, the same time lapse, but highlighting the stress fibers in different colors. Color code: dorsal SF, in red; transverse arcs, in yellow; ventral SF, in green. Blue arrows are focal adhesion sites. Note that as some transverse arcs flow centripetally, they might connect with dorsal SF from opposite regions, thus generating ventral SFs. Scale bar:  $10\mu\text{m}$ . Figure taken from [16].

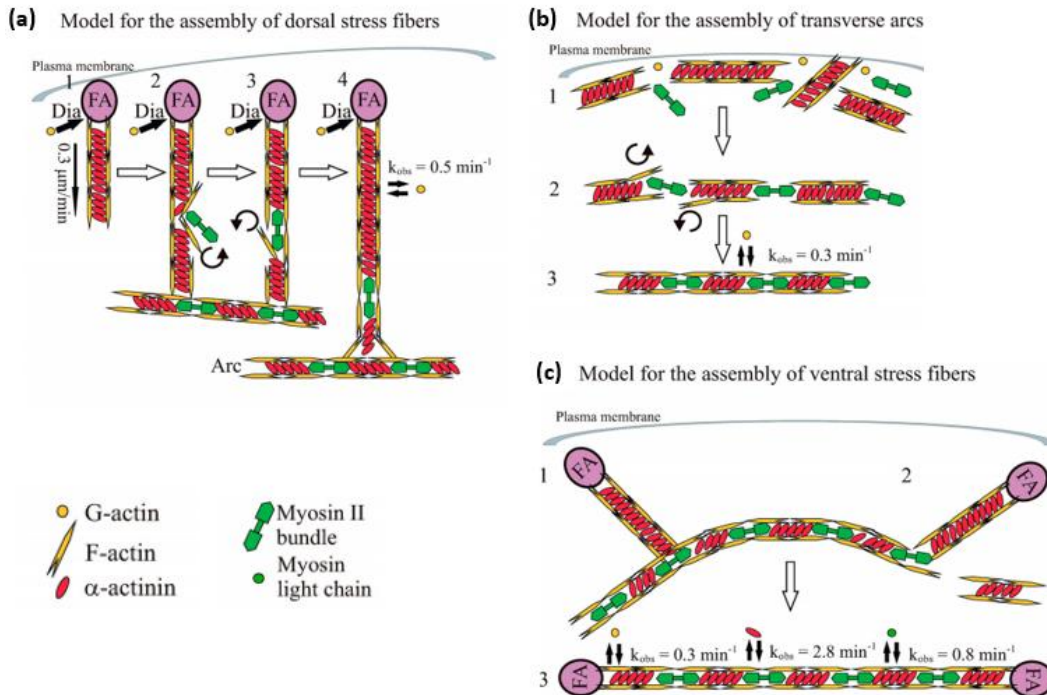


Figure 1.16 – Stress fiber assembly models suggested by Hotulainen, P. and Lappalainen, P. (2006). The numbers 1,2,3 and 4 dictates the steps of stress fiber assembly. (a) Dorsal SF assembly, with unidirectional polymerization with delayed incorporation of myosin II at distal end (close to transverse arcs). FA, focal adhesion. Dia, formin that promotes actin assembly. (b) Transverse arcs assembly from F-actin fragments crosslinked with  $\alpha$ -actinin during centripetal flow. (c) Ventral SF formation from transverse arcs and dorsal SFs. FRAP rates of actin (yellow circle),  $\alpha$ -actinin (red ellipse), and myosin light chain (green circle) are displayed. Figure adapted from [16].

Notably, Tojkander S. et al (2015) showed that dorsal stress fibers that were under conversion process to ventral SF were more aligned to transverse arcs and were more long lived, while dorsal stress fibers orthogonal to transverse arcs were more rapidly disassembled (Figure 1.17). Their data show that actomyosin tension regulates actin stress fiber assembly and disassembly.

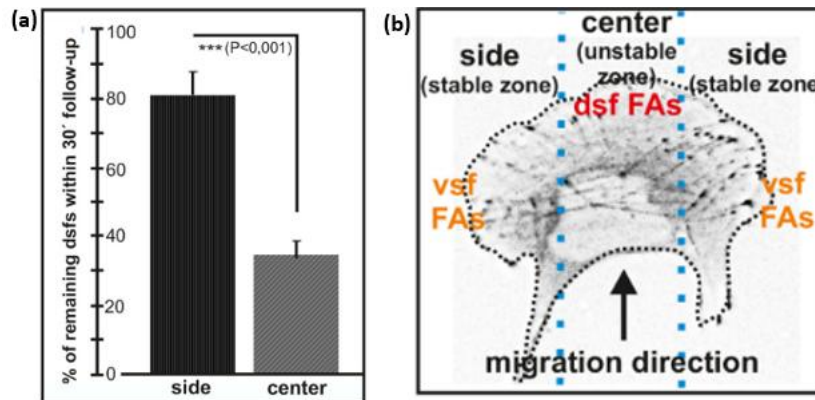


Figure 1.17 – Dorsal SF (dsf) aligned to T-arcs (side, stable zone) are longer lived than dorsal SF orthogonally oriented to transverse arcs (center, unstable zone). (a) the percentage of remaining dorsal SF in 30 min of observation comparing side and center population of dorsal SF. (b) The blue dots separates the stable zones (side, ventral SF (vsf) and focal adhesions (FA) in orange), from the unstable zone (center, dorsal SF (dsf) and focal adhesions, in red). Figure adapted from [17].



Cell signaling studies demonstrated that different ventral SFs might be modulated by different signaling pathways. Therefore, they could be further subdivided into two classes: peripheral SF (located at the cell periphery) and central ventral SF (not peripheral) [18-20]. For example, a seminal study showed that Myosin Light Chain Kinase (MLCK) activity induces a fast contraction (2 to 7 times more rapidly) at peripheral SF bundles than does Rho-A Kinase (ROCK) at central ventral SF of fibroblasts [18]. In particular, ROCK seems to control the direct phosphorylation of MLC and the inhibition of MLC phosphatase activity at central ventral SF in a smooth and more diffuse manner compared to MLCK (more rapid and specific to peripheral bundles, see Figure 1.18).

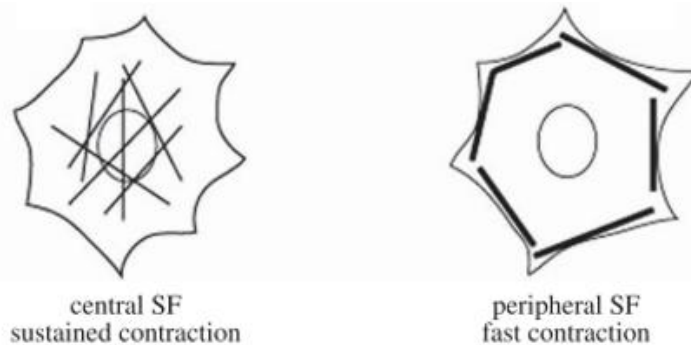


Figure 1.18 – Ventral SF can be subdivided into two populations: central SF and peripheral SF. Both populations respond differently to contractility stimuli and drug inhibitors. Figure taken from [20].

Peripheral and central ventral SFs have different drug sensitivity. The central SF are more sensitive to Rho-kinase inhibitors (e.g., Y-27632 and HA1077) than MLCK inhibitors (e.g., ML-7, ML-9, and KT5926) [19]. On the other hand, peripheral SFs are more sensitive to MLCK and Calmodulin (e.g., W-5, W-7) inhibitors. For example, when cells were treated for 1h with Rho-kinase inhibitors, peripheral SF were almost not affected, meanwhile central ventral SF and focal adhesions were greatly reduced (see table 1.2).

Inhibitors	Concentration, $\mu$ M	Peripheral SF	Central SF	Focal Adhesion	Cell Rounding	Lamellipodium
Rho-kinase inhibitors						
Y-27632	10	+	-	-	-	+
HA1077	30	+	-	-	-	+
MLCK inhibitors						
ML-7	25	-	+	+	+	-
ML-9	100	-	+	+	+	-
KT5926	15	-	+	+	+	-
Calmodulin inhibitors						
W-5	100	-	+	+	+	-
W-7	100	-	+	+	+	-

Table 1.2 – Effects of different inhibitors on human foreskin fibroblasts (FS-133). (+) when SF characteristics were not greatly affected; (-) when SFs were absent or greatly affected in the presence of the inhibitors. Table taken from [19]

Interestingly, stress fiber models made with triton extraction showed that, in the presence of  $Ca^{+2}$  and Mg-ATP, the contraction of central SF only occurs after the almost full contraction of peripheral SFs. Although these SFs contracted at different times, the speed of contraction of each type was almost identical. Such evidences are in accordance that peripheral and central ventral SF might be regulated by two different signaling pathways: MLCK/Calmodulin and ROCK [19, 20]. Moreover, kinetics analysis of isolated stress fibers suggests that Rho-kinase system induces a slow and continuous contraction, whereas MLCK/Calmodulin contractility

system induces a transient and rapid contraction [20]. For both cases, the major factor responsible for stress fiber contraction is the phosphorylation of myosin light chain (MLC), but with different signaling pathways that reflects in different ventral SF locations within the cell [20].

Other differences between peripheral and central ventral SF appear when studying their mechanics in vivo, e.g. tension probed by laser nanosurgery. Tanner, K. et al (2010) severed peripheral and central ventral SF using laser ablation and observed bundle kinetics and mechanics in vivo. When photodisrupting peripheral SF, a dramatic contraction of the whole cell was observed (15-20% reduction in cell area) in a timescale of minutes, suggesting that the shape of the cell is highly dependent on peripheral SF bundles. Moreover, the ablation of peripheral SF followed by disengagement of terminal focal adhesions, suggesting the release of tension in the whole peripheral bundle. On the other hand, severing central ventral SF did cause the same drastic morphological changes. In this case, a reduction of only 5% of cell area was observed when ablating central SF [21].

A more recent paper correlated laser nanosurgery results with biomolecular tools such as Western blotting [22]. They were able to quantify constitutively active (CA) proteins (MLCK and ROCK) with different degree of phosphorylation, and correlate these with the mechanical properties and spatial localization of peripheral and central ventral SF. In particular, they showed that CA-MLCK U2OS cell line increased the myosin regulatory light chain (RLC) monophosphorylation (p-RLC) in a dose dependent manner. Moreover, the latter were spatially localized on peripheral SFs. On the other hand, CA-ROCK U2OS cell line increased the diphosphorylation of RLC (pp-RLC) of central SFs in a graded manner. In particular, the authors expect that the CA-MLCK monophosphorylation (p-RLC) occurs on the Serine 19 amino acid residue of RLC, whereas the diphosphorylation (pp-RLC) due to CA-ROCK occurs at both Threonine18 and Serine19 residue sites of RLC. The phosphorylation of RLC is important to allow non-muscle myosin II (NMII) to assemble into thick myosin filaments and perform acto-myosin contraction. Such work was important to connect molecular sources that distinguish both peripheral and central ventral SF pools. Other differences appear when analyzing the biomechanics of SF bundles, better summarized in the following section.

### **1.3.2 The biomechanics of actin stress fibers**

The biomechanics of actin SF have been reviewed by Kassianidou, E. and Kumar, S. (2015) [23] giving focus on the different techniques to probe actin stress fibers and whole cell mechanics. Here we will discuss the main works of the review, adding to it a few other works that were not present there. We will focus on the quantitative values of the mechanical properties of actin stress fibers. In most cases, only ventral SF were studied, and peripheral and central ventral SF were pooled together into a single class. In the next section, we will comment on other works about whole cell biomechanics, whose stress fiber organization is dependent on the adhesive substrate stiffness and geometry.

The expected transmitted force that stress fiber transmit to focal adhesion is estimated to be of around  $5.5 \text{ nN}/\mu\text{m}^2$ , and it is generally accepted that the larger the focal adhesions and thicker the stress fibers, the higher the myosin content, therefore, the higher the local tension [24].

The mechanical properties of isolated stress fibers were studied using microcantilevers. The longitudinal elastic modulus (capacity to resist to elastic deformation) of isolated stress

fibers were nonlinear, and it increased with strain. For example, for “de-roofed” smooth muscle cell, the average value of elastic modulus of isolated SF was around 1.45 MPa, while for endothelial cells it was 0.3 MPa, considering uniform SF structure and constant cross sectional area of  $0.05\mu\text{m}^2$ . In addition, the force needed to stretch a single SF from its length of zero stress to its original length was approximately 10nN (comparable to traction forces of single adhesion sites) [23].

Maybe the most detailed work about the mechanical properties of stress fibers was performed in living cells using atomic force microscopy (AFM) with nanoindentations (contact-mode) [25]. The nanoindentations were done with a hemispherical pyramidal tip, and the contact area was a square of  $200\times 200\text{nm}^2$ , with 200nm depth. An array of  $8\times 6$  indentations was used to probe in the same experiment the stress fiber and of the cytosol around it ( $600\times 300\text{nm}$  spacing). The authors demonstrated that, in the same SF, its stiffness increased upon increasing the contractility level with of Calyculin A (a serine/threoninephosphatase inhibitor), and decreased when decreasing contractility level with of Blebbistatin (which inhibits actomyosin contractility). Such result highlights the link between contractility and SF stiffness: the higher the contractility, the higher will be the SF stiffness, and vice-versa. For example,  $10\mu\text{M}$  Blebbistatin induced around 30% decrease in SF stiffness (from  $\sim 12\text{kPa}$  to  $\sim 8\text{kPa}$ , Figure 1.19a) within minutes, whereas 2nM of Calyculin A induced an increase of almost 40% of stiffness (from  $\sim 13.7\text{kPa}$  to  $\sim 19.1\text{kPa}$ , Figure 1.19b). Importantly, the authors were able to compare SF stiffness at different SF regions (termini and center) under different conditions (contractile and control). In this sense, they demonstrated that under contractile condition (i.e., presence of Calyculin A), the changes in SF stiffness were higher at regions close to focal adhesions (terminus, within  $20\mu\text{m}$  from FA) than from regions far from focal adhesions (center, more than  $45\mu\text{m}$  from FA). For example, at regions close to FA, the presence of Calyculin A increased the stiffness in 34% (from  $11.7\text{kPa}$  to  $15.7\text{kPa}$ ), whereas at the center of the bundle Calyculin A increased the SF stiffness in 6% (from  $9.7\text{kPa}$  to  $10.3\text{kPa}$ ), see Figure 1.19c. The differences in stiffness from the terminus ( $11.7\text{kPa}$ ) to the center ( $9.7\text{kPa}$ ) under control conditions were not significantly different. Such results imply that heterogeneities in stiffness along the bundle mainly arises under SF contraction, whereas under control conditions they are not significantly different.

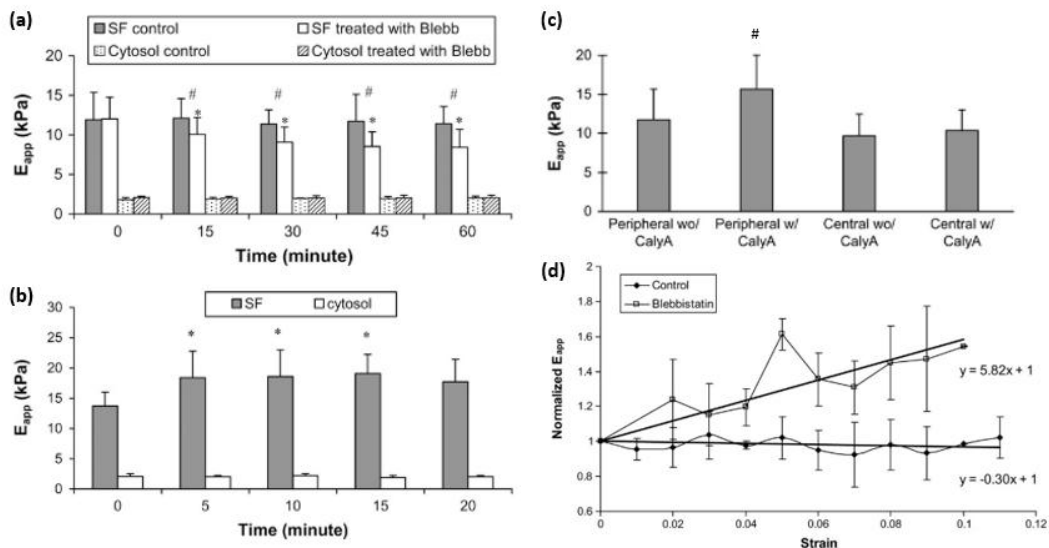


Figure 1.19 – Ventral stress fiber stiffness in human aortic endothelial cells. (a) Time lapse of SF stiffness decreasing upon decreasing contractility levels using Blebbistatin (Blebb), whereas the stiffness of the cytosol is unchanged. #, significantly difference between treated and untreated SFs. \*, significantly difference from the value at the time 0. (b) Time lapse of SF stiffness increasing upon SF contraction stimulation with Calyculin A, whereas the stiffness of the cytosol is unchanged. Note, after 20 min of Calyculin A, the SF stiffness is slightly decreased. (c) Stiffness of the terminus (peripheral) and of the central regions of ventral SFs upon the presence or not of Calyculin A. Note that, regions mainly close to focal adhesion changed their stiffness. (d) Stress fibers under Blebbistatin treatment does not hold the linear behavior as untreated cells upon increasing strain of the stretchable substrate (silicone membrane). Figure adapted from [25].

As commented before, another way to probe SF stiffness in living cells is by laser nanosurgery. With the latter, a strong focused beam (typically fs pulsed laser of 1-2nJ with  $0.5\mu\text{m}^2$  area) is used to ablate the SF and what is measured are the bundle retraction parameters. A mathematical model (e.g., Kelvin-Voigt) is used to fit retraction dynamics and extract mechanical parameters. Tanner, K. et al (2010) induced laser ablations comparing peripheral and central ventral SFs behavior under different drug treatment (ROCK and MLCK inhibitors, see Figure 1.20) [21]. First, peripheral SF retract with lower effective elasticities than central SF, but they do show a higher final retraction length (overall elastic energy dissipation, tension). Drugs that inhibits ROCK and MLCK decreased the tension level of peripheral SF, demonstrated by an overall decrease in retraction length (Figure 1.20a). However, an interesting result arose from central SF. Although inhibiting central SF via ROCK inhibitor a decrease in central SF tension was also observed, the behavior of central SF was different when perturbing peripheral SF contractility. When inhibiting peripheral SF contractility with ML-7 (via MLCK inhibition), central SF were more tensioned (longer retraction length than naïve cells), demonstrating that central SF can bear peripheral SF tension load when the latter is compromised (see Figure 1.20b).

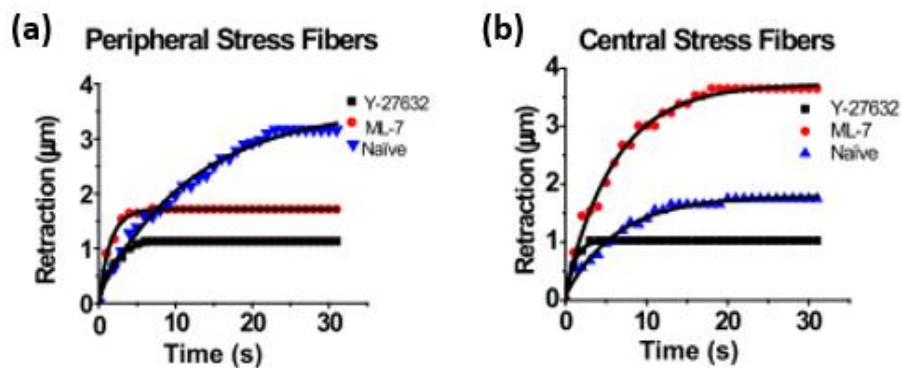


Figure 1.20 – Retraction length (elastic energy dissipation) dynamics of peripheral (a) and central (b) ventral SF. Note that, both ROCK (Y-27632) and MLCK (ML-7) inhibitors decreased the tension of peripheral SF. On the other hand, inhibition of peripheral SF via ML-7, increased the tension load in central SF (red curve in b). Figure adapted from [21].

Another important work with laser nanosurgery applied on SFs tackled how the connectivity of SF and the adhesive pattern geometry affect SF tension [26]. Kassianidou, E. et al (2017) plated U2OS cells onto rectangular U-shaped patterns of different sizes (aspect ratios), and they showed that longer peripheral SF (main bundle across the gap of coated regions with U-pattern) had a longer retraction length (more tensioned), whereas its viscoelastic properties remained constant. Besides, they were able to quantify the influence of other SF connections to the main peripheral SF of U-shaped cells. The number of SF connections had no difference in SF



retraction length, but the orientation angle by which the connections make with the main peripheral SF bundle contributes to the SF retraction length. For example, average angles higher than  $90^\circ$  had smaller retraction length ( $L_0$ ) than average angle smaller than  $90^\circ$ , probably due to opposite force direction of retraction. In addition, the retraction was maximum for angles in between  $20^\circ$ - $40^\circ$ , whereas it was minimum at angles higher than  $120^\circ$  (see Figure 1.21). Finally, the geometry of the cells (e.g. their aspect ratio) affects how much tension the side bundles influences the main peripheral SF tension. This study emphasizes the role of the SFs connectivity in their mechanical behavior.

In addition, they also developed a mechanical network model to quantify the forces transmitted from the side bundles to the main (ablated) SF. They assumed the SF network as a series of connected elastic cables. With the simulation, they had the following results. First, both force components ( $x$  and  $y$ ) of side bundles contributes to the main SF tension (contributing to the bundle prestress). Second, they could quantitatively estimate the forces and string parameters of SFs using the model. They could convert the forces retrieved from the model to the obtained experimental retraction length by using a simple spring model (with spring constant of  $k=3\text{nN}/\mu\text{m}$ ). They estimated that connecting SF to the main bundle (the one to be ablated) adds  $5\text{nN}$  of force, considering SF stiffness of  $EA=500\text{nN}$ . Moreover, the total force at the center of the SF when ablated is around  $25\text{nN}$ . Besides, they concluded that SF are both stiffer and more contractile at higher aspect ratio. For example, for U-shaped cells with aspect ratio of 3.0, the pulling force was  $F_0=7\text{nN}$ , and the bundle stiffness was  $EA=80\text{nN}$ , whereas for cells with aspect ratio of 1.9,  $F_0=4\text{nN}$ , and  $EA=40\text{nN}$ . Moreover, they applied such quantitative values to a cell monolayer system, where peripheral SFs were the borders among cells. Using such simulations, they showed that the effect of connectivity is amplified in the presence cell-cell adhesions. Finally, they showed that the tension released by a given cell is felt within distant cells tens of microns away.

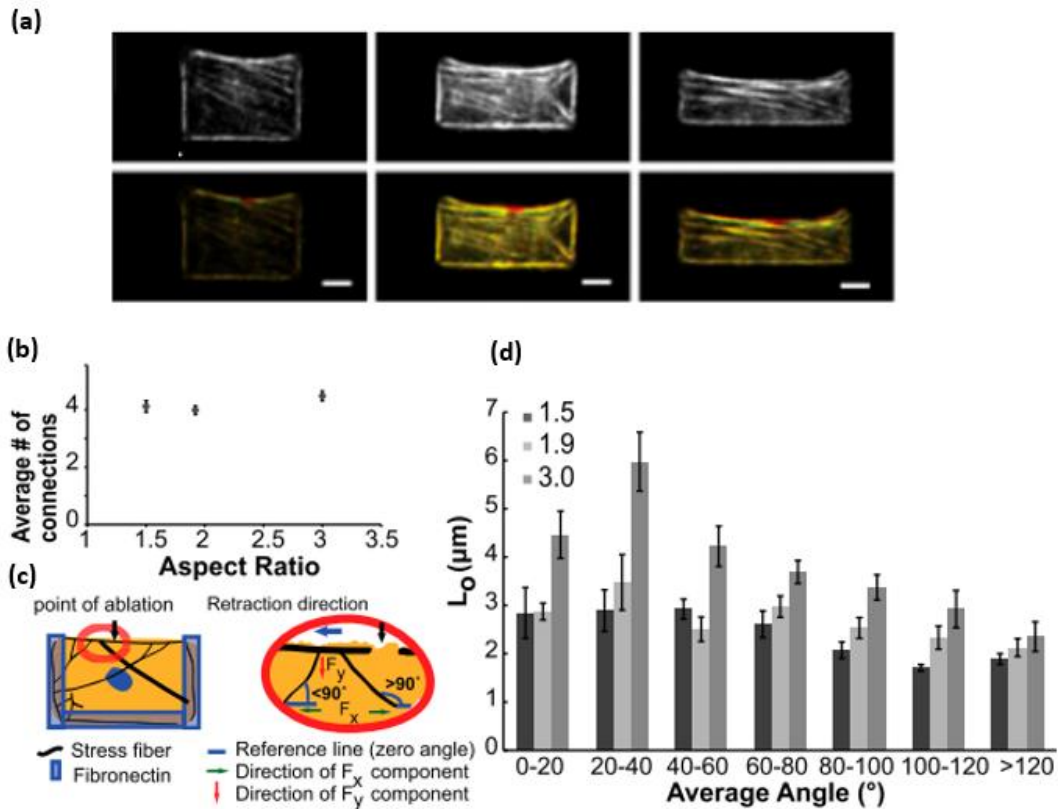


Figure 1.21 – The effects of cell geometry and SF connectivity on SF tension. (a) Rectangular U-shaped micropatterned cells with different aspect ratios (1.5, 1.9 and 3.0). The main SF is the peripheral SF on the top side of the cell that is probed with laser nanosurgery. Images in grayscale, cells before ablation. Colored cells (red before ablation, green after ablation). (b) The number of connected fibers to the main peripheral SF per aspect ratio does not change (N= 66, 94 and 103 cells for each aspect ratio). (c) Illustration of point of ablation and retraction direction showing when the angles are higher and lower than  $90^\circ$  of the connected side bundles. (d) A peak (maximum) in retraction length (named  $L_0$ ) is observed when side bundles make  $20^\circ$ - $40^\circ$  angles with the main peripheral SF. Note that, the higher the aspect ratio (gray colors), the higher the final retraction length. Figure adapted from [26].

At last, another way to map cellular forces is by the use of traction force microscopy (TFM). With TFM, the displacement of fluorescent beads in the extra-cellular matrix (ECM) can be traced before and after the presence of the cell. Soiné, J. R. D. et al (2015) fluorescent labelled focal adhesions (paxillin) and F-actin of U2OS cells in order to segment the SFs [27]. The authors overlapped these images with TFM displacements micrographs. By doing so, they estimated the force applied onto the substrate by ventral SF, transverse arcs, and dorsal SF. They found out that the distribution of forces was wide for each stress fibers, but ventral SF were the ones that applied more tension onto the substrate, followed by transverse arcs and dorsal SF (see Figure 1.22). Note that the order of magnitude of the estimated forces were very similar compared to other works (a few nN to 15nN), that estimated transmitted force that stress fiber transmit to focal adhesion [24].

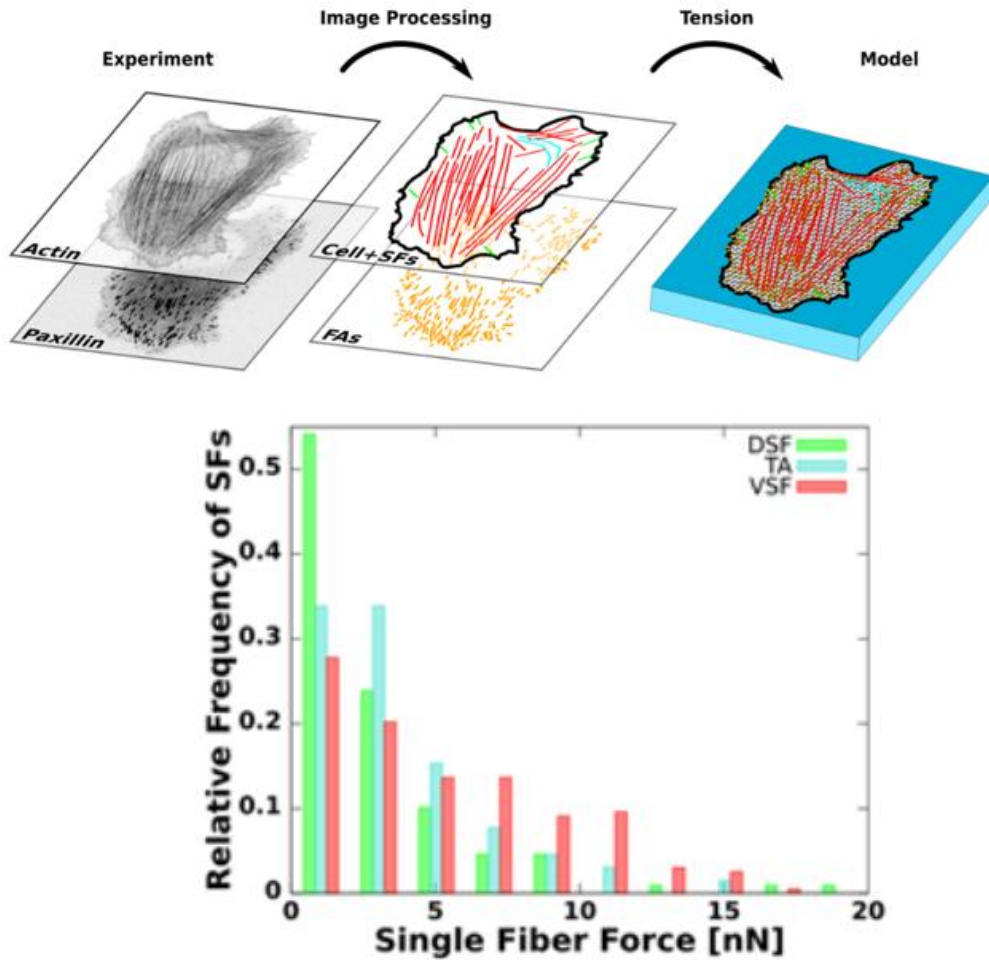


Figure 1.22 – Dorsal SF (DSF, in green), Transverse arcs (TA, in blue), and Ventral SF (VSF, in red) statistical distribution of forces in U2OS cells. Note that ventral SF are the bundles that most applied force onto the substrate, whereas most of dorsal SF presented no force. Figure taken from [27].

### 1.3.3 Cell geometry and biomechanics is dependent of stress fiber organization

One could choose what stress fibers type to be more present in a cell population by selecting the substrate stiffness and geometry. Indeed, the cells senses its substrate stiffness and adapts its geometry via the stress fibers. For example, around 89% of U2OS cells plated on a stiff substrate (64kPa) contains ventral SF, whereas the latter is only present in 10% of the cells plated on a soft (0.5kPa) substrate [17]. In this sense, it is possible that the mechanical tension might regulate dorsal SF elongation, and the generation of ventral SF for example. Tojkander, S. et al (2015) discussed about topic and their results suggests that weak forces exerted by retrograde actin flow might be needed for dorsal SF polymerization at focal adhesions [17]. On the other hand, strong forces exerted by non-muscle myosin II system might inhibit dorsal SF polymerization, and simultaneously be needed for ventral SF maturation. Tojkander, S. et al (2012) discuss about environmental mechanosensing role of SF, being a crucial factor for lineage determination of stem cells [13].

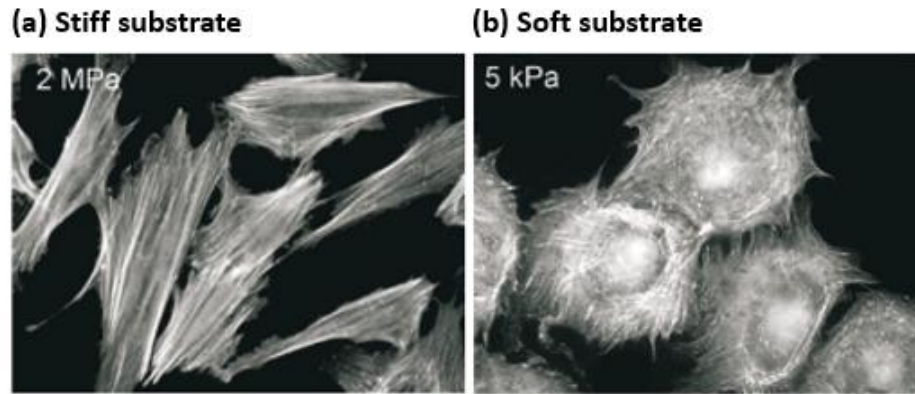


Figure 1.23 – The effect of substrate stiffness on fibroblasts stress fiber organization. Controllable substrate stiffness is obtained with the same polymer poly(dimethylsiloxane) (PDMS). (a) fibroblasts plated on 2MPa stiff PDMS. The cells are mainly populated by well oriented ventral SF. Note that the cell borders are mainly constituted by straight and concave edges (resembling straight polygons). (b) Fibroblasts plated on soft 5kPa PDMS substrate. Note that the morphology is more convex, having a more diverse population of stress fibers (e.g., dorsal SF crossing transverse arcs). Note that the cellular shape is different from (a), with cell borders mainly concave, typical of well spread cells. Figure adapted from [13].

Since the cell morphologies in a population plated on a 2D homogeneous substrate can be very complex, one way to study geometrical factors is by plating cells on micropatterned substrates to obtain reproducible cellular shapes [28-31]. It is generally accepted that the brighter and larger are focal adhesions and the ventral stress fibers, the higher their acto-myosin content, and therefore the higher the tension in the bundles. They, M. (2006) confirmed that trend based on micropatterned cells on different adhesive patterns (for example,  $\nabla$ , V, T, Y, see Figure 1.24) [28].

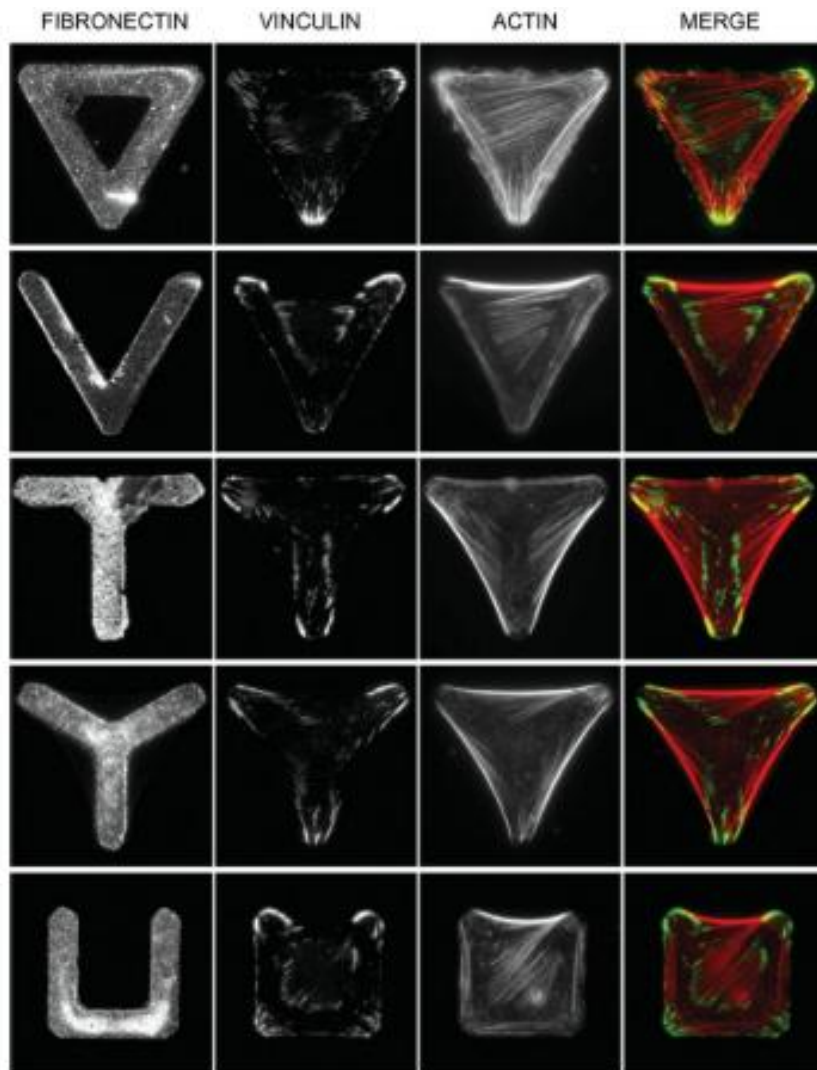


Figure 1.24 – Micropatterning as a tool to obtain reproducible cell shapes. Note that the focal adhesions (vinculin) show the regions of attachment of stress fibers, and they follow the geometry of the coated pattern (fibronectin). The stress fibers, on the other hand, defines and keeps the geometry of the cell (e.g., triangular shape for fibronectin patterns of [∇], [V], [T], and [Y], and square shape for [U]). The triangle edge length is 46μm. Figure taken from [28].

By using such approach, the authors were able to draw a few conclusions. Stress fibers that bridge the gap between two-adherent regions are thicker and brighter, and their focal adhesions were larger and brighter (see average intensity of F-actin and vinculin, a focal adhesion marker, in Figure 1.24). Such results suggest that F-actin bundles are reinforced (thicker) to bear a higher tension in order to hold the cell geometry when it lacks adhesive attachment over a region in the substrate. In addition, they performed drug perturbation essays on such patterns and evaluated cell convexity before and after drug treatment. Cells became more concave after the addition of Y-27632 (Rho-kinase inhibitor). Interestingly, SF that bridge adherent regions became more concave, demonstrating that upon contractility inhibition they were the ones most affected (see Figure 1.25), whereas SF lying over a coated region were more robust upon drug treatment.

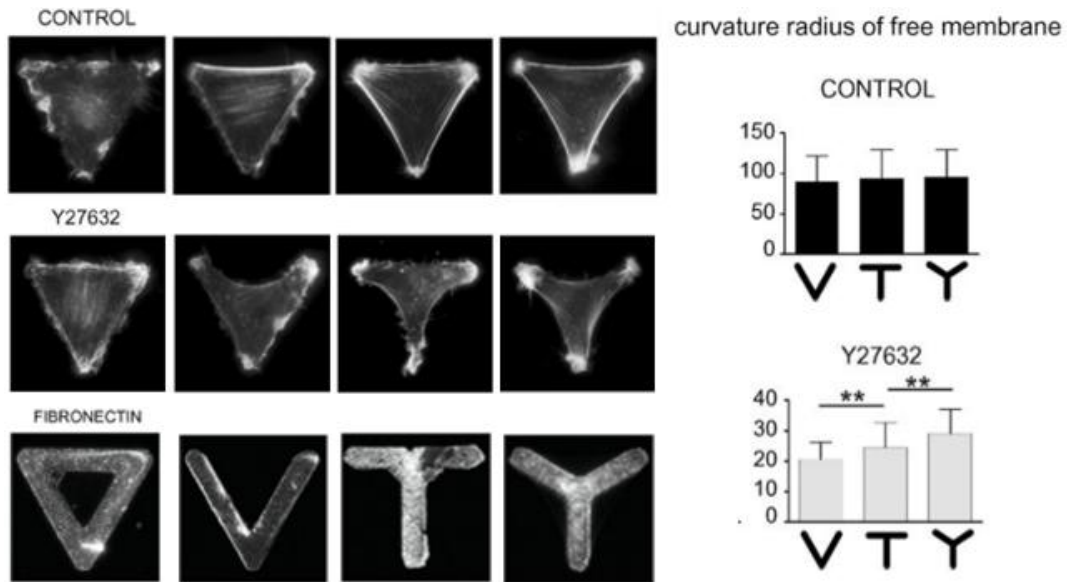


Figure 1.25 – Cell convexity study of [∇], [V], [T], and [Y], showing that stress fibers over a non adherent gap were more tensioned. Drug treatment with a contractility inhibitor (Y-27632) demonstrated the vulnerability of stress fiber when myosin II activity was blocked. The concave peripheral SFs after the drug treatment are the ones lying over fibronectin coating gaps. The peripheral SF's curvature radius decreased with Y-26732, and it was shorter for the [V] case (holding higher tension). Figure adapted from [28].

Micropatterned cells have already been probed by atomic force microscopy (AFM) [29]. The obtained elasticity map (Young's moduli) could be overlapped with the cell topography. Retinal pigment epithelial (RPE1) cells were grown on fibronectin coated [∇], [T], and [Y] patterns. Their results were in agreement with Théry, M. (2006) [28]. Stress fibers over adherent regions were thinner than non-adherent borders. Moreover, they obtained quantitative values about cell stiffness and concluded that cells with concave borders have higher tension, with higher heterogeneity in the stiffness values. On the other hand, SF over borders with fibronectin coating were less tensioned, more stable, and with more homogeneous stiffness (see Figure 1.26).

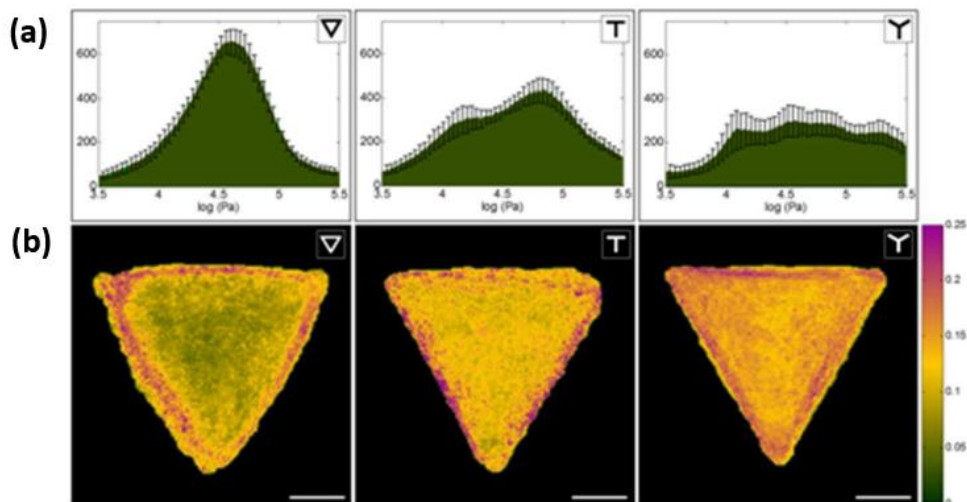




Figure 1.26 – Elasticity heterogeneity of RPE1 cells plated on [∇], [T], and [Y] patterns. (a) Young’s modulus histograms showing a single lognormal distribution for cells plated on [∇] pattern, whereas it becomes more heterogeneous (more peaks) for [T], and [Y] patterns. (b) Young’s modulus deviation mapping (the red, the higher heterogeneity). Note that, regions close to the borders have a more heterogeneous stiffness. Figure adapted from [29].

At patterns with non-adherent borders ([T] and [Y]), the stiffness was higher at regions on top of stress fibers rather than over the nuclei, suggesting that the increase in the stiffness was mainly due the presence of thick actin stress fiber bundles. For example, in [Y] shaped patterns, the stiffness range of non-adherent edges were mainly in between 40kPa and 63kPa. That is not the case for patterns where the cell periphery was fully coated with fibronectin, with thinner SF bundles. In such case, the stiffness of the cell borders maintained as low as the nuclear region, mainly in the range between 25kPa and 40kPa, see Figure 1.27. The latter result suggests that the stiffness of the cell borders are directly affected by the tension provided by stress fibers and focal adhesions, and the nuclear region elasticity is less affected. Accordingly, drug perturbation experiments performed with Latrunculin-A and Blebbistatin reduced the cell stiffness (10 and 5 fold respectively), particularly clear at the cell borders of [T] and [Y] patterns, where they became concave. The nuclear region was less affected. Besides, the highest elasticity values (40kPa to 100kPa) were found at the cell boundary. Upon drug perturbation, the very stiff peripheral regions of 100kPa collapsed to 10kPa in stiffness. In addition, the more non adherent borders the patterns had, the higher the median stiffness values was observed. The median Young’s modulus of cells were: 32kPa for [∇], 34kPa for [T], and 41kPa for [Y] pattern, see Figure 1.27.

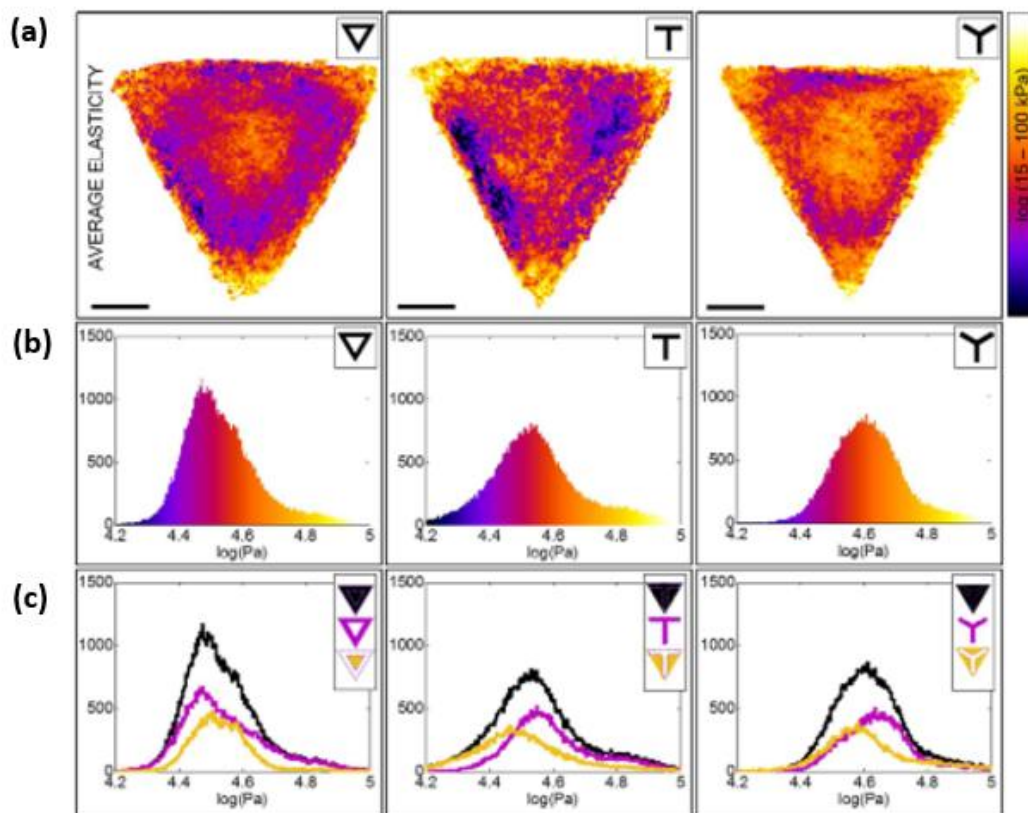


Figure 1.27 – Average stiffness in RPE1 cells plated on [∇], [T], and [Y] patterns. (a) Young’s modulus mapping. Note that at the cell borders the stiffness is gradually higher (yellow) the more non adhesive edges the coating pattern has,

i.e., stiffness of [Y] > [T] > [∇]. (b) Young's modulus histograms. (c) Histogram profile of different cell regions of each pattern (whole cell in black; on top of the coated region, in pink; and on top of non coated regions, in yellow). Note that only cells plated on [∇] had similar stiffness profile of different regions. Figure adapted from [29].

Traction force microscopy (TFM) can be combined with micropatterning to obtain reproducible cell shape together with the ability to measure forces onto the substrate. Mandal, K. et al (2014) plated mouse embryonic fibroblasts (MEF) onto patterns of [H], [U], and [arrow] that resulted in cells with overall squared shape [31]. They showed that local geometry of the micropatterns can trigger more or less stress fiber alignment, and the latter is correlated with force orientation. For example, a sharp peak in the horizontal orientation of stress fibers is observed in [H] pattern, which is in agreement with a high value in the polarization degree of the TFM force maps. On the other hand, in other patterns the stress fibers were more diagonal, and the force polarization degree along the main axis was lower. In addition, they performed perturbation experiments with Rho-kinase inhibitor Y-26732. Upon myosin contractility inhibition, the ability of the patterns to align the bundles in one direction is weakened, since the orientation of SF were more variable. On the other hand, when contractility was stimulated upon treatment with LPA, the bundles were locally more clearly oriented. Such results suggests that Rho-A pathway can modulate the degree of cell mechanical polarization.



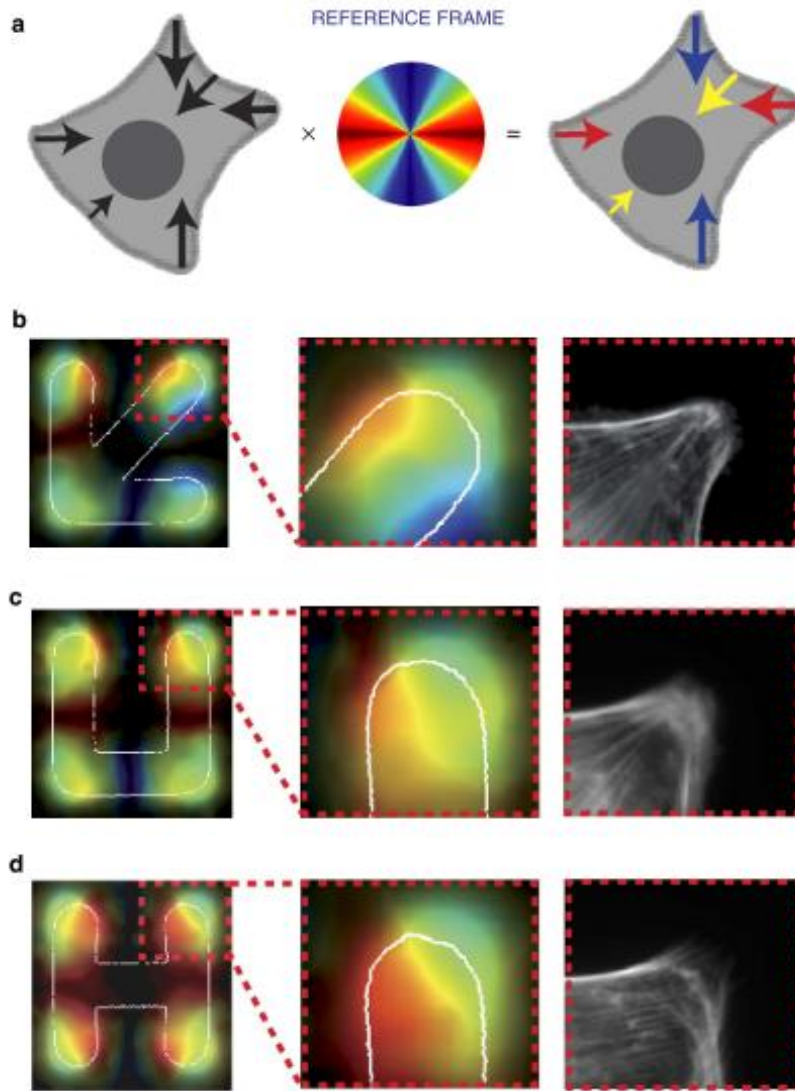


Figure 1.28 – Traction force mapping with MEF cells plated on [arrow], [U], and [H] micropatterns. (a) illustration and colorcode of the possible force orientations within the cells (blue is vertical, and red is horizontal). Note that, the force orientation is very horizontal (red) in (d) with [H] pattern, and these display very horizontal stress fiber orientation compared to cells plated on (b) [arrow] and (c) [U] shaped patterns. Figure taken from [31].

Finally, the degree of cell spreading also affect the cell tension transmitted to the substrate. By using a bed of microneedles as a substrate (i.e., microfabricated arrays of elastomeric microneedle-like posts), Tan, J. L. et al (2002) demonstrated that cells with larger spreading area tilted more the microneedles posts, therefore more tension per post is transmitted to the substrate [32]. For example, for cells with low spreading area ( $140\mu\text{m}^2$ ), the estimated mean force/post is less than 10nN, whereas for well spread cells ( $1520\mu\text{m}^2$ ), the force/post was around 25nN in average.

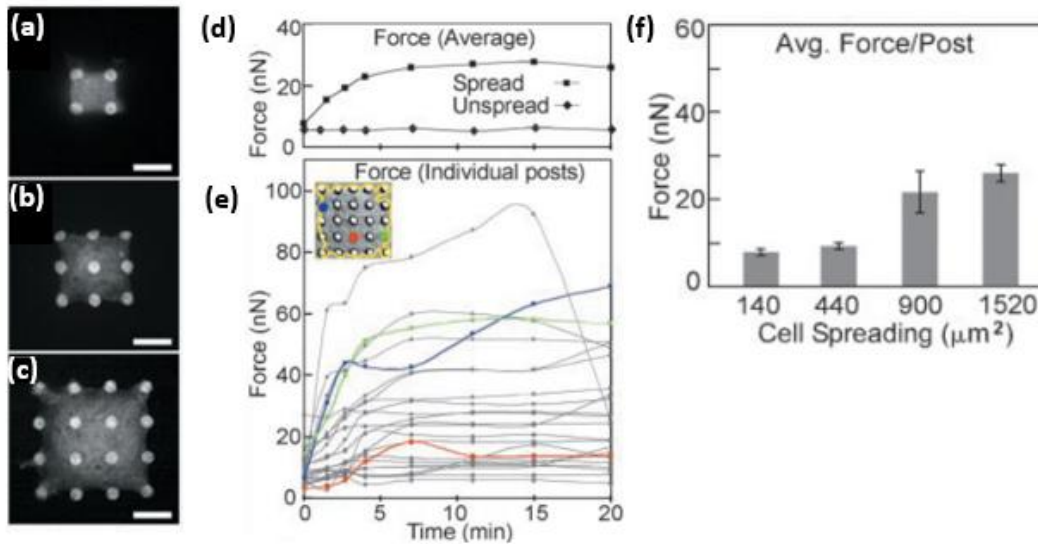


Figure 1.29 – Cell forces exerted on substrate made elastomeric microneedle-like posts increases upon spreading area and time. (a-c) Different cell spread areas on the posts. (d) The average force per post as a function of cell spreading time. Note that unspread cells keep low tension onto the substrate, while spread cells increase the tension to the substrate. (e) Individual force per post as a function of spreading time. (f) Average force/post as a function of cell spreading area. Figure adapted from [32].

#### 1.4 Final considerations: the main differences between sarcomeres and stress fibers

The sarcomeres are the molecular units responsible to exchange mechanical forces with the surrounding environment in muscle cells (Figure 1.5 and Figure 1.6). They might be the most studied model for cell contractility, and thus they are a reference to understand stress fiber force generation. As we commented previously, muscle sarcomeres are very ordered structures with clear contractile behavior. The presence of  $\text{Ca}^{2+}$  and ATP induces the myosin filaments to slide on actin filaments of opposite polarities, generating contraction in sarcomeres. On the other hand, although stress fibers contain many actin binding proteins similar to sarcomeres (e.g., myosin filaments,  $\alpha$ -actinin, tropomyosins, etc), stress fibers are not always clearly contractile, but under isometric tension (i.e., tension without changing the structure length). An important study made by Peterson, L. J. et al (2004) shed light on the isometric tension performed by stress fibers in non-muscle cells, highlighting many differences of SF compared to muscle sarcomeres, that work under isotonic tension (i.e., tension with contraction) [33]. In the study, the stress fibers force generation units are named “sarcomeric” units, and are defined as intercalated fluorescent bands of myosin II and  $\alpha$ -actinin along ventral SF. Besides, they compared the periodicity and size of those bands at the terminus of stress fibers (within 5-7  $\mu\text{m}$  of a focal adhesion), to the bands localized at the center of SFs (within 10 $\mu\text{m}$  segment either side of the bundle midpoint). For example, in untreated cells, the periodicity was higher at regions close to focal adhesions (avg. distance of  $1.1 \pm 0.3 \mu\text{m}$ ) compared to the center (avg. distance of  $1.25 \pm 0.35 \mu\text{m}$ ). After contractility stimulus with 5nM of calyculin A, a phosphatase inhibitor that enhances the myosin light chain (MLC) phosphorylation, the MLC bands decreased in 30% in terminal regions of ventral SF, whereas at central regions it increased to nearly 125% of their original length. When analyzing  $\alpha$ -actinin bands, similar behavior was observed. The “sarcomeric” units shortened by 30-40% at edge regions, whereas central unit stretched to more than 150% of their original length (see Figure 1.30). In particular, terminal “sarcomeric” units shortened at a rate of  $\sim 0.017 \mu\text{m}/\text{min}$ , whereas central “sarcomeric” units lengthened by

$\sim 0.024\mu\text{m}/\text{min}$ . Moreover, the width of the bands were also quantified before and after the treatment with calyculin A. In untreated cells, the MLC band width at central regions were larger compared to the termini of the bundles. At central regions, the avg. width size was  $0.78\pm 0.13\mu\text{m}$ , whereas at the SF terminus it was  $0.60\pm 0.11\mu\text{m}$ . Upon the addition of calyculin A, the MLC central bands became even larger ( $0.85\pm 0.14\mu\text{m}$ ), and the terminal bands became even smaller ( $0.48\pm 0.10\mu\text{m}$ ). The same trend was observed on  $\alpha$ -actinin bands. Before treatment: central regions were larger ( $0.63\pm 0.12\mu\text{m}$ ) than terminal regions ( $0.51\pm 0.08\mu\text{m}$ ), and the differences between both became more evident upon contraction: central regions increased width to  $0.71\pm 0.13\mu\text{m}$ , and terminal regions decreased the band width to  $0.43\pm 0.07\mu\text{m}$ . Besides, the authors noticed that phosphorylated-serine19-MLC localized at cell termini after stimulation with calyculin A. The latter suggest that there is a preferential phosphorylation sites at different regions of the same ventral SF bundle.

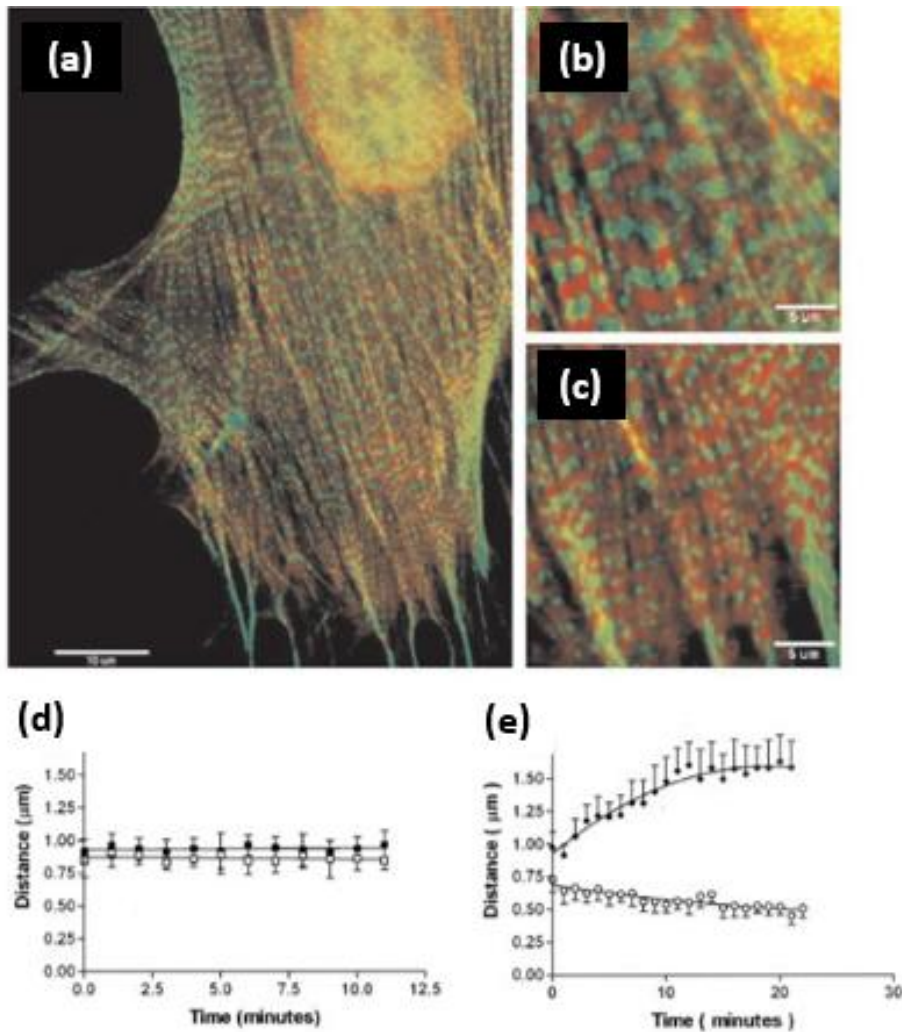


Figure 1.30 – The stress fibers “sarcomeric” units in gerbil fibroblast cell with 5 min of calyculin A contractile stimulation. (a) Stress fiber “sarcomeric” units (green,  $\alpha$ -actinin band; red, MLC bands). (b) Large bands at central regions of ventral SF. (c) SF regions close to focal adhesions (terminus). (d) Time lapse of central (black) and terminal (white square) regions distance between  $\alpha$ -actinin bands in untreated cells. (e) Time lapse of central (black) and terminal (white square) regions distance between  $\alpha$ -actinin bands in cells treated with 5nM calyculin A. Scale bar: (a)  $10\mu\text{m}$ , (b,c)  $5\mu\text{m}$ . Figure taken from [33].

These results show that ventral SF have non homogeneous distribution of “sarcomeric” bands along the bundle, and they become even more heterogeneous upon contractility stimulus. In other words, in ventral SF is observed a simultaneous stretching and contractile behavior at different regions of the bundle, and the quantity of molecules (band dimensions) is also non-homogeneously distributed upon contraction. These results suggest that the “sarcomeric” units in SF apply or resist to tension in a different fashion depending on the region of the bundle. This isometric tension behavior in SF is quite different from what happens in isotonic contraction of muscles. The muscle cells (myofibrils, see Figure 1.5 and Figure 1.6) are extended cylindrical structures, spanning the entire length of the muscle (a few millimeters to tens of centimeters in skeletal muscle). They are composed of  $10^2$ - $10^5$  sarcomeres precisely aligned to each other from one end to the other of the myofibril. The sarcomeres only contract upon contractility stimulus (i.e., do not stretch), and the actin binding proteins are evenly distributed along the many muscle sarcomeres, suggesting same contractility efficiency [15, 24, 33]. In this sense, the sarcomeres have homogeneous size ( $\sim 2\mu\text{m}$  long), and are able to shrink by  $\sim 30\%$  at the peak of the muscle contraction [15]. On the other hand, in stress fibers “sarcomeric” units can behave independently along the same bundle, suggesting different force generation efficiency. Moreover, the activation dynamics is different. Skeletal muscle cells can repeatedly shorten and relax in 10-100ms by action potential of  $\text{Ca}^{+2}$ , whereas the stress fiber contraction takes minutes to reach the peak amplitude, with almost no change in stress fiber length.

Other differences arise at the molecular composition level. For example, the key molecular components such as  $\alpha$ -actinin, myosin II, and other actin binding proteins (ABP) have different isoforms in muscle cells in relation to stress fibers [15]. Another difference arises when analyzing the activation of contractility. In striated muscles cells, a troponin switching is responsible for sarcomeric activation, whereas in stress fibers is the phosphorylation of myosin light chain (MLC) [15]. Besides, the myofibril machinery is permanently assembled to guarantee efficient response to the action potential, whereas actin stress fibers are continuously being assembled and disassembled.

### **1.5 Open questions on actin stress fibers organization: a motivation for this PhD work**

Many interesting open questions arise when trying to understand how F-actin structures exchange forces at the molecular level [15]. Although a lot is known about F-actin structures and their organization at the microscale, little has been reported in terms of nanoscale molecular organization within cells. How these structures are assembled and are regulated are constantly being probed by optical microscopy tools. We, in particular, are mainly interested in understanding if/how F-actin nanoscale alignment affects the stress fibers organization, and if that has any correlation with function and with mechanical forces. For example, how is F-actin organized in different stress fiber “sarcomeric” units? Is there any difference in F-actin alignment among different stress fiber types? Does contractility play a role in F-actin alignment in stress fibers? If yes, do the filaments become more or less aligned? Do/how other actin binding proteins (crosslinkers) affect F-actin alignment in stress fibers? How is F-actin alignment close to focal adhesions compared to in the middle of a bundle? Correlating information on actin organization with the results obtained on the mechanical properties of SFs described in this chapter, could bring important insight into the role of actin in such functions.

As we already commented in this chapter, one way to probe F-actin organization at the nanoscale is by electron microscopy (EM). However EM has some limitations (specificity, sample preparation) that makes it inappropriate in live cells investigations. Particularly, when using EM without marking the structures, we typically obtain an *unspecific* morphological map of the cell at the nanoscale. The lack of chemical specificity might be problematic when analyzing complex structures such as the molecular content of a stress fiber bundle or focal adhesion structures. On the other hand, if immune specific markers are added, the morphological readout might be affected by the presence of the immunoglobulins markers. In this context, super-resolution optical microscopy techniques might help, because they can probe nanoscale structures keeping high specificity of the fluorescent markers. However, super-resolution microscopy techniques offer a localization map, but not a direct way to quantify F-actin filament alignment. To overcome this limitation, in this thesis we developed two polarized optical microscopy techniques able to tackle the F-actin degree of alignment (e.g. organization) within cells. As we will described in this manuscript, polarized fluorescence microscopy (PFM) are very interesting tools because they add orientational information on top of the localization map. In particular, we developed a novel super-resolution microscopy technique which provide quantitative parameters to evaluate the actin filaments organization in 2D at the nanoscale, based on single molecule level orientation imaging.

## **Conclusion of Chapter 1**

In this chapter, we presented an introduction about actin filament structures, with a focus on actin stress fibers. The geometrical organization and the biomechanics of actin structures (e.g., stress fibers) are closely related to the cell morphology, motility, and therefore cell function. Although there are similarities between actin stress fibers and muscle sarcomeres, many striking differences appear when analyzing their contractility behavior. Besides, the scientific community is highly interested in understanding how actin stress fibers build up and exchange forces with the environment, and how cells regulate them. Since the topic involves many different biochemical signaling pathways that coordinate the assembly of supramolecular complexes of hundreds of molecules at the nanoscale, simple questions such as to understand how actin filament alignment play a role on them are still elusive. To tackle such questions, we have developed a fluorescence polarization resolved microscope as well as a novel quantitative super-resolution optical microscopy technique based on the monitoring of fluorescence light polarization. These techniques will be described in the next chapters.



## Chapter 2

# Principles of polarization resolved fluorescence microscopy

### II.1 Light polarization

#### II.1.1 Light: the basic concepts

Light is a complex quantum mechanical wave-particle entity. Sometimes light is better described by a discrete particle-like units named photons, sometimes better understood as a continuous orthogonal electromagnetic wave, i.e., an electric ( $\vec{E}$ ) and magnetic ( $\vec{B}$ ) oscillatory fields that lies orthogonally to their propagation direction  $\vec{k}$  (see Figure 2.1). The energy that one photon carries is encoded in a wave-like parameter: the wavelength  $\lambda$ . The lower the wavelength, the more energy the photon carries and vice-versa:

$$E_{\text{photon}} = \frac{hc}{\lambda} = h\nu \quad \text{Eq. 2.1}$$

where  $c$  is the speed of light in the dielectric medium,  $\nu$  is the light frequency (units s<sup>-1</sup>),  $\lambda$  is the wavelength of the light,  $h$  the Planck constant.

The electric and magnetic fields can be described by the propagation equations in the far field:

$$\nabla^2 \vec{E} = \frac{1}{c^2} \frac{\partial^2 \vec{E}}{\partial t^2}; \nabla^2 \vec{B} = \frac{1}{c^2} \frac{\partial^2 \vec{B}}{\partial t^2}$$
$$\text{with } c = \frac{c_0}{n} = \frac{\omega}{k} = \frac{\lambda \omega}{2\pi n} = \lambda \nu \quad \text{Eq. 2.2}$$

where  $c_0$  is the speed of light in the vacuum,  $n$  is the refractive index of the medium,  $t$  is time,  $\nabla^2$  is the Laplacian operator in 3D,  $\omega$  is the angular frequency (units rad.s<sup>-1</sup>),  $k$  is the wavenumber (typical units cm<sup>-1</sup>),  $\vec{r}$  is the position in 3D space,  $\vec{k}$  is the wave-vector, with magnitude  $|\vec{k}| = k$ , and it points to the propagation direction of the wave (along  $\vec{z}$  in the far field).

Henceforth, we will focus only on the oscillatory electric field vector of the light,  $\vec{E}$ , whose has major importance in our context. Besides, whenever describing the behavior of the light in the far field (at distances from the emitter much longer than the light wavelength), we can approximate  $\vec{E}$  by a planar wave which propagates in one specific direction  $\vec{k} // \vec{z}$ . In such cases, the electric field vector is lying on the 2D transverse plane to its propagation along  $\vec{E} \perp \vec{k} // \vec{z}$  (see Figure 2.1) [34]. Any more complex geometry such as focused beams can be described by a sum over planar waves.

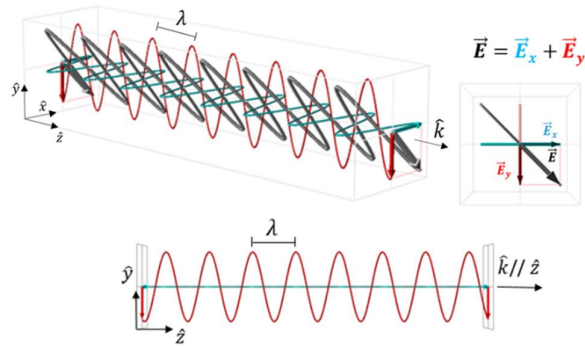


Figure 2.1 - Optical wave with wavelength  $\lambda$ . The propagation of the electric field ( $\vec{E}$ ) and its components orthogonal ( $\vec{E}_x$  in blue, and  $\vec{E}_y$  in red) that lie transverse to its propagation ( $\vec{k}$ ) direction. On the right side, the transverse plane illustrating the projection of  $E$  into  $\vec{E}_x$  (blue) and  $\vec{E}_y$  (red) components. On the bottom, a side view projection of the plane wave showing that " $\vec{k} // \hat{z}$ " direction. Adapted from EMANIN free software [35].

### II.1.2 Light can be polarized, unpolarized or partially polarized

Light can be polarized, unpolarized or partially polarized (e.g. the combination of polarized and unpolarized components). Figure 2.1 shows a representation of linearly polarized light. Unpolarized light is occurring when the two orthogonal components of the electric field vector are independent to each other, therefore the oscillations of the *net electric field vector*  $\vec{E}(t)$  are randomly oriented in 2D over time throughout the wave propagation (see Figure 2.2). This happens for example when the phase relation between  $\vec{E}_x$  and  $\vec{E}_y$  components of  $\vec{E}$  is random. In other words, there is no constant phase delay between x and y component in time.

$$\nexists \varphi = \text{constant} \mid \varphi = \varphi_x - \varphi_y, \quad t \in (-\infty, \infty) \quad \text{Eq. 2.3}$$

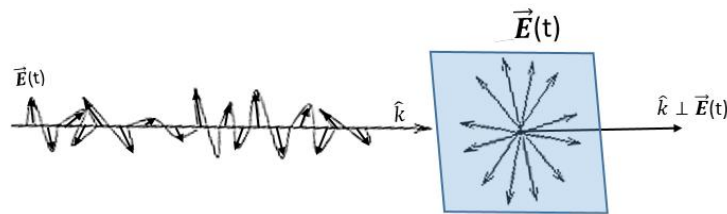


Figure 2.2 – Illustration of unpolarized light propagated in time along  $k$  direction, and the 2D projections of the electric field vector. The transverse plane (represented in blue) is perpendicular to the planar wave propagation. Adapted from [36].

Conversely, the light is said to be polarized when the oscillations in 2D are *not random* over time. Mathematically, it is when  $\vec{E}_x$  and  $\vec{E}_y$  components of  $\vec{E}$  have a constant phase dependence between each other,  $\varphi = \varphi_x - \varphi_y$  :

$$\exists \varphi = \text{constant} \mid \varphi = \varphi_x - \varphi_y, \quad t \in (-\infty, \infty) \quad \text{Eq. 2.4}$$



Consequently, the electric field oscillations projected on the horizontal axis is phase shifted in a synchronized way with respect to the vertical projection. Due to this synchronization, the net  $\vec{E}$  vector performs a periodical movement on the 2D transverse plane that can draw a line, an ellipse or a circle over time. Such light states are named linear, elliptical or circular polarized light respectively (see Figure 2.3).

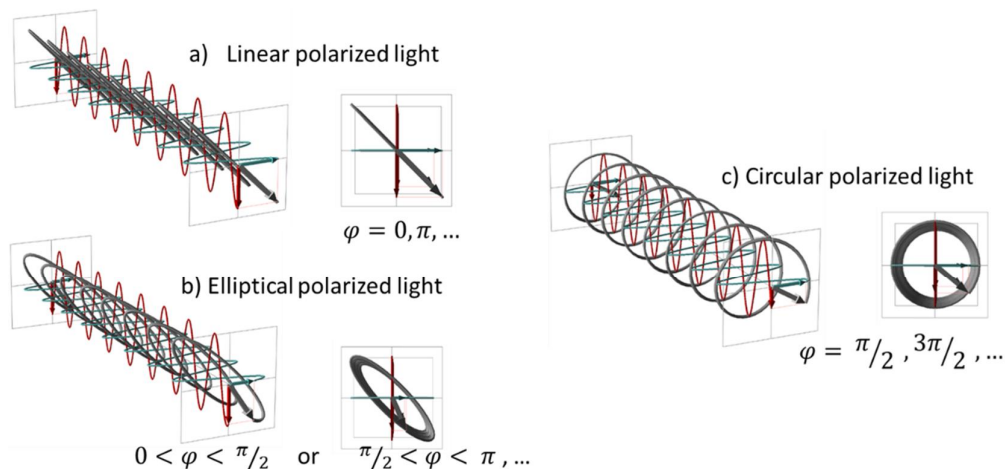


Figure 2.3 – Polarization states of the light (plane-wave). (a) Linear polarized, (b) elliptical polarized, (c) circularly polarized. On the left, the propagated wave and vectors, and on the right the transversal projection and their phase between two orthogonal electric field transverse components. When light is linear polarized, both electric field components increase and decrease together and the phase between them is a multiple of  $\pi$ . On the other hand, when it is circularly polarized, both components are dephased by a multiple of  $\pi/2$ . Adapted from EMANIN free software [35].

## II.2 Fluorescence light properties

### II.2.1 Fluorescence: introduction

Fluorescence is the optical process that consists in the emission of light from a molecule (fluorophore) or atomic arrangement (if this is a nanoparticle), that has been previously excited with an incoming light with higher energy photons (lower wavelength). Fluorescence has been extensively used as a readout of countless experiments mainly because fluorescent molecules can be highly specific markers, providing a good contrast in very complex environments (e.g., inside cells) [37-39]. Thanks to the developments on new fluorescent probes, properties such as color, brightness, binding specificity, chemical stability, solubility, etc, can be tailored to one's need [38-42], and this makes fluorescence methods very versatile. The fluorescence process itself was first explained by Aleksander Jablonski in 1935 [43], and it can be clearly illustrated by an energy level diagram named Jablonski diagram (see Figure 2.4). Nowadays, there are whole textbooks on photophysics and photochemistry detailing how such phenomenon and other related ones can happen [43-45]. In the next section, we will brief describe the main features of the fluorescence process.

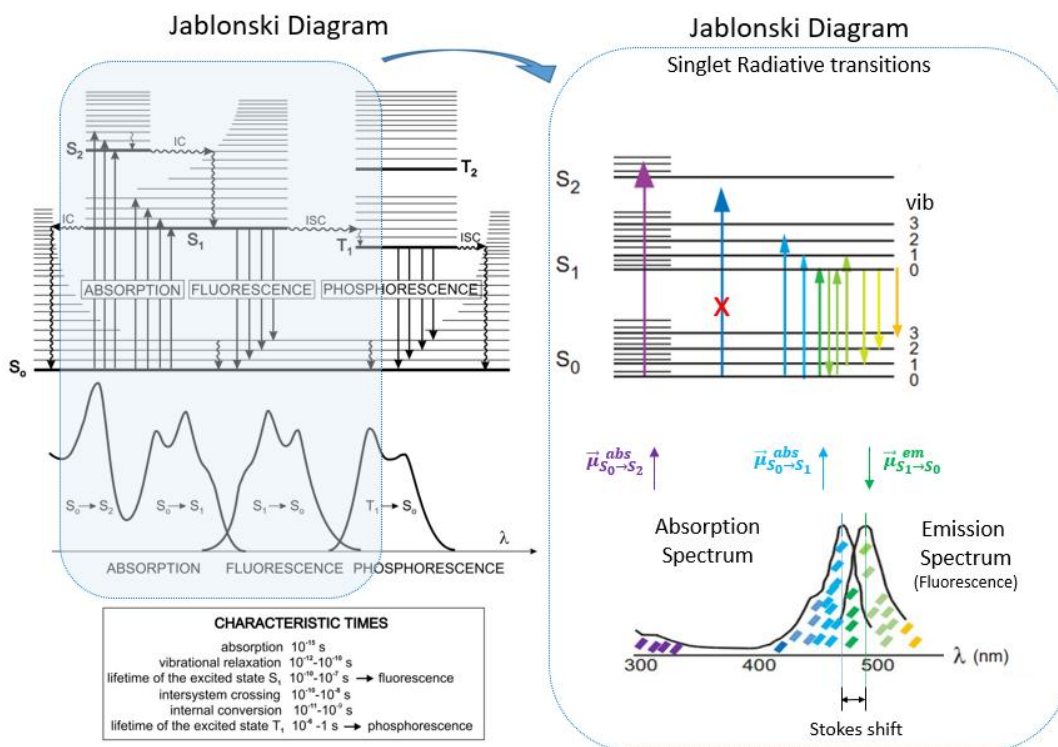


Figure 2.4 – Jablonski diagram is a potential energy diagram used to illustrate many energy transfer processes, including the absorption and fluorescence emission optical processes (singlet radiative processes). It also explains the absorption and emission spectra of fluorophores. Each potential *energy state* is described by horizontal *lines*, and each *photophysical phenomenon* is described by *arrows* (wavy or not). Straight arrows (radiative pathways), wavy arrow (non-radiative pathways). Photophysical phenomena are also called *transitions* between states, and their have their own characteristic life time (see the box). Each horizontal line with position along the vertical axis represents the quantity of potential energy that the molecule holds on that electronic configuration state. For example, the closer the line is to the bottom, the lower in energy that state has, and the more stable the molecule should be (oftentimes correlated with longer lifetimes). Here,  $S_0$  is the layer of energy levels that represent the molecule without excitation (i.e.,  $S_0$  is the *ground state* level).  $S_1$  and  $S_2$  represents the first two excited *singlet* state layers.  $T_1$  and  $T_2$  represents the first two excited *triplet* state layer. Singlet and Triplet states are energy states of the molecule that the valence electrons differ in the spin multiplicity/configurations. The spin configuration play a crucial role on the fluorophore reactivity/stability with its surrounding environment, and therefore, affects their excited state lifetime. On the selected Radiative Transitions of the Jablonski diagram (right side) we illustrate the connection between the energy states  $S_0$ ,  $S_1$ ,  $S_2$ , with the absorption (straight arrows pointing up) and fluorescence emission (straight arrows down), with their related optical spectra. The absorption and emission transitions are mediated by the transition dipole moment (TDM,  $\vec{\mu}$ ). Other abbreviations: IC stands for *internal crossing*, and is related to vibrational motions and non-radiative relaxations *without* changing the spin multiplicity. In solution, any excess of vibrational energy is mostly dissipated by collisions with the surrounding solvent molecules. ISC stands for *intersystem crossing*, and it is related to vibrational motions and non-radiative relaxations when changing spin multiplicity. Figure adapted from [44, 46].

## II.2.2 Fluorescence is a radiative relaxation process

Fluorescence is the process that releases the excess of energy (excitation) by emission of photons. To better understand it, we will use the Jablonski energy diagram (see Figure 2.4). The molecule (fluorophore) instantaneous state can be depicted as point on a determined energetic level (that represents the amount of potential energy it has). Depending on the

interaction with light, this point in the diagram could perform a trajectory along the energy levels (i.e., through the potential energy landscape), absorbing and releasing energy until it gets back to its ground state (lowest and most stable energy level). Importantly, these energy levels are the energy fingerprint of the molecule under specific physicochemical condition (that takes into account the type of solvent, temperature, pressure, etc). We cannot exactly predict which photophysical pathway (i.e., the sequence of transitioned levels) a single-fluorophore will take, but sometimes one could control and bias a possible transition (radiative or not), making it more or less probable. This could be done by changing thermodynamic parameters of the system or by changing the chemistry of the molecules/atoms involved in the desired transition (e.g., fluorescence in our case). Hence, the local environment that surrounds the fluorophore can also affect the probability for the fluorescence pathway to occur [43, 45]. Experimentally, the energy levels are measured by different spectroscopic methods. The spectra are the plots related to the energy level gaps (transitions) in between states. Oftentimes the spectra are plotted in wavelength scale of the light used in the experiment, and the plot profile represents the energy gaps between the energy state levels probed in the system under investigation (see Figure 2.4).

From the Jablonski diagram, we can readily infer many important features of fluorescence and other related processes, but here we will briefly comment only on two. First, the fluorescent photon (transition  $S_1 \rightarrow S_0$ ) has generally lower energy (longer wavelength) than the excitation/absorbed one (transition  $S_0 \rightarrow S_1$  or  $S_0 \rightarrow S_2$ ), because energy was lost in the vibrational levels of the excited state ( $S_1$  levels, the most common case). Such shift in energy is named *Stokes shift*, and it can be visualized as the *spectral shift* between the absorption and emission peak profiles [43]. Thanks to the Stokes shift, fluorescent photons can be experimentally filtered out from the excitation photons, providing a good imaging contrast (low background), if proper optical filters are chosen to block only the excitation beam. Second important inference from Jablonski diagram: the more vibrational states in the excited and in the ground state levels, the bigger is the stokes shift and the longer is the photophysical path that the excited molecule travels through the potential energy landscape before reaching back to the ground state [44, 45]. In solution, such vibrational modes imply on molecular movements that dissipate the energy via collision with the solvent molecules and/or radiating in other longer wavelengths (e.g., mid-IR).

Although there are exceptions for every rule, from the length of the photophysical path, it is reasonable to expect a few important consequences. First, the longer the photophysical paths, the longer in time the excited fluorophore takes to emit the fluorescent photon. A competition among different pathways (radiative or not) will be important in the super-resolution method employed in this thesis: the dSTORM, and it will be detailed later (Chapter 3). Second, the higher the chances of the fluorophore had changed its orientation many times before its emission due to thermal movements. This has relevant consequences for their orientation determination. For example, fluorophores at room temperature are never static in solution. Even at their ground state (i.e., without any excitation laser beam), the heat of the room is enough to excite the ground state vibrational modes of both fluorophore and solvent (e.g., water) molecules. Thus, the nanoscopic picture one should have in mind during a fluorescence microscopy experiment is that the fluorophore molecules are vibrating, bending, rotating, wobbling and colliding constantly in their local environment (independently of the excitation beam). Such random movements are generally quite fast (ranging from picoseconds

to tens-hundreds of nanoseconds in general). Besides, in principle, the higher the temperature, the more numerous conformational states the fluorophore have access, and therefore, more isotropically distributed in space the fluorophore *could* get. The latter depends on how tightly bound the fluorophore is to the biomolecular structure of interest (SOI). The less tightly bound, the higher the angular freedom available for the fluorophore to be exploited via rotational Brownian movements. In polarization resolved microscopy methods, our group has modelled (and simplified) such complex stochastic thermal movements into just one type of movement: fluorophore wobbling. The wobbling approximation will be more detailed when discussing how to model the orientation distribution in ordered samples (e.g., cone model).

### II.2.3 Fluorescence lifetime and quantum yield are important properties of the fluorophores

One can evaluate fluorophore emission by two major properties: fluorescence lifetime and quantum yield. Fluorescence lifetime ( $\tau_f$ ) is the characteristic decay time related to the fluorophore relaxation to the ground state (in a determined thermodynamic condition). Although the decay time of a single-fluorophore from its excited state is a stochastic process, we can statistically quantify an ensemble parameter that tells the average time that the fluorophores spend in the excited state. Hence, in the simplest case (mono-exponential), the lifetime can be written as the inverse relation of the sum of all the relaxation transition rates (radiative or not) that remove the fluorophore from its excited state [43]:

$$\tau_f = \frac{1}{k_r + k_{nr}} \quad \text{Eq. 2.5}$$

where  $\tau_f$  is the fluorescence lifetime decay,  $k_r$  is the radiative (fluorescence) rate and  $k_{nr}$  is the non-radiative processes rate.

The fluorescence lifetime is an important parameter for many reasons. It can be used to define the lowest acquisition time window to detect most ( $\approx 63\%$ ) of the emitted photons (e.g., minimum integration time), and it can tell information about the fluorophore interactions with its local environment. For example, one could evaluate how the local environment improves or hampers the fluorescence stability (or the contrary: blinking) by measuring the fluorescence lifetime. In addition, as we will see in the following sections, the fluorescence lifetime dictates what type of polarization resolved experiments one could apply, because rotational Brownian movements of the fluorophore might be faster, equivalent, or slower than the fluorescence lifetime. Depending on their relative timescales, the outcome and the interpretation of the acquired data change in polarization resolved methods. This is because the fluorophores might be very dynamic (“~ wobbling quite a lot”) or not during the process of photon emission.

Another important fluorophore property is the fluorescence quantum yield ( $Q_f$ ), that estimates how bright a fluorophore is. The quantum yield is a statistical value that quantifies the average number of emitted photons for a given number of incident photons. One way to define it is to consider the ratio between two transition rates: the fluorescence emission rate by the sum of all relaxation rate transitions. In the simplest case [43]:

$$Q_f = \frac{k_r}{k_r + k_{nr}} \quad \text{Eq. 2.6}$$

As the fluorescence lifetime, the quantum yield also depends on the local thermodynamical properties and molecular interactions between the fluorophore with the surrounding solvent molecules. Typically, the higher the number of collisions with the solvent, intermolecular vibrations, and rotations, the more favored (higher  $k_{nr}$ ) are the non-radiative relaxation paths, therefore the less bright the fluorophores becomes.

## II.3 Fluorescence light polarization properties

### II.3.1 The efficiency of radiative transitions is orientation sensitive

A very important aspect that *cannot* be inferred from Jablonski diagram is that radiative transitions such as photo-absorption and photo-emission (e.g., fluorescence) are orientation sensitive processes in respect to the incoming/emitting light. Their orientation sensitivity is very well characterized by the transition dipole moment (TDM =  $\vec{\mu}_{(i \rightarrow f)}$ ) between the initial ( $i$ ) and final ( $f$ ) states of the transition [34, 43]. From the quantum mechanical theory point of view,  $\vec{\mu}_{(i \rightarrow f)}$  is a vectorial property of the fluorophore that describes the optical transition from the initial state  $i$  to the final state  $f$  [43]. For example, in the case of one photon absorption transition, the absorption dipole moment is described by  $\vec{\mu}_{abs} = \vec{\mu}_{(S_0 \rightarrow S_1)}$ . The TDM quantifies how similar the molecular electronic density distribution (i.e., the electron “cloud”, or “orbital”) on the excited state (final, S1 state) of the molecule is in relation to the distorted ground state electron “cloud” (initial, S0 state) after being perturbed by the presence of the photon (with specific  $\lambda$  and polarization/orientation). One way to imagine such optical perturbation is to think that, in quantum mechanics, the molecular electronic states are described by wave functions that have wave-like features. Hence, when waves (electronic “clouds”) are put together, they can interact via resonance if they are similar, forcing strong interactions in the whole system, and therefore allowing energy to be *exchanged* between states. The energy transfer between states can be represented as an energy transition between them on the Jablonski diagram. For example, energy can be transferred in form of light (i.e., oscillatory electric field: excitation, fluorescence emission, etc), or by any other form of electric field modulation/propagation: movements of single charges (e.g., radicals), electron pairs (e.g., bonds), or excitons (e.g., electron-hole dipoles), etc. To conclude: the light-induced perturbation is orientation sensitive because the *net density of charges* on each molecular state has its own spatial density configuration (i.e., with characteristic net charge density gradient direction: the molecular dipole direction). Thus, fluorophores at a different initial energy states have different sensitivity to the light polarization, and therefore are described by different transition dipole vectors  $\vec{\mu}_{(i \rightarrow f)}$ .

### II.3.2 Transition dipole moment ( $\vec{\mu}$ ) of a fluorophore and its interaction with light

A fluorophore is a molecule sensitive to *visible* light (whose wavelength is approximately in between  $400\text{nm} < \lambda < 700\text{nm}$ ). Nevertheless, not all of atoms of the fluorophore participate directly on such radiative processes. Within the fluorophore molecule, the molecular framework (atoms) that encloses the electrons that are sensitive to visible light is called *chromophore*. Thus, the chromophore regulates the fluorophore’s optical transitions in the visible range, such as

absorption and fluorescence, and therefore it is the structural framework whose is sensitive to the orientation of the *visible* light polarization [43]. Generally, we illustrate the molecular dipole vector,  $\vec{\mu}$ , on top of the chromophore region (see Figure 2.5). In the idealistic cases, the magnitude of  $\vec{\mu}$  vector represents the dipole intrinsic strength of interaction, and it is qualitatively related to the distance that the positive and negative charge densities are separated. The orientation of the vector  $\vec{\mu}$  points to the direction of maximum gradient in charge density. For chemists, the convention is that  $\vec{\mu}$  points to the highest electron density (+  $\rightarrow$  -) (see Figure 2.5). For physicists, the  $\vec{\mu}$  points to the maximum positive charge density(-  $\rightarrow$  +). For us, it does not matter to where it points; what really matters is only the *angular orientation* of  $\vec{\mu}$  axis related to the reference x-axis. In a chromophore, the direction of  $\vec{\mu}$  axis generally also coincide with the direction of the conjugation in the molecular structure, e.g. the direction that  $\pi$ -electrons are likely to follow under the effect of an incident electric field. Since charges are sensitive to electric field, the probability to any optical transition occur under light illumination depends on the relative orientation between the molecular transition dipole  $\vec{\mu}_{(i \rightarrow f)}$  between a given initial *i*-state and its final *f*-state, and the orientation of electromagnetic field (polarization) of the light with a given  $\lambda$ . The more aligned the electric field to the molecular transition vector  $\vec{\mu}_{(i \rightarrow f)}$ , the higher the light-matter interaction, consequently the higher the probability for the transition to the final *f*-state will occur. In the Figure 2.5 below, we show the example of a typical fluorophore used in this work, phalloidin linked with Alexa Fluor 488 dye.

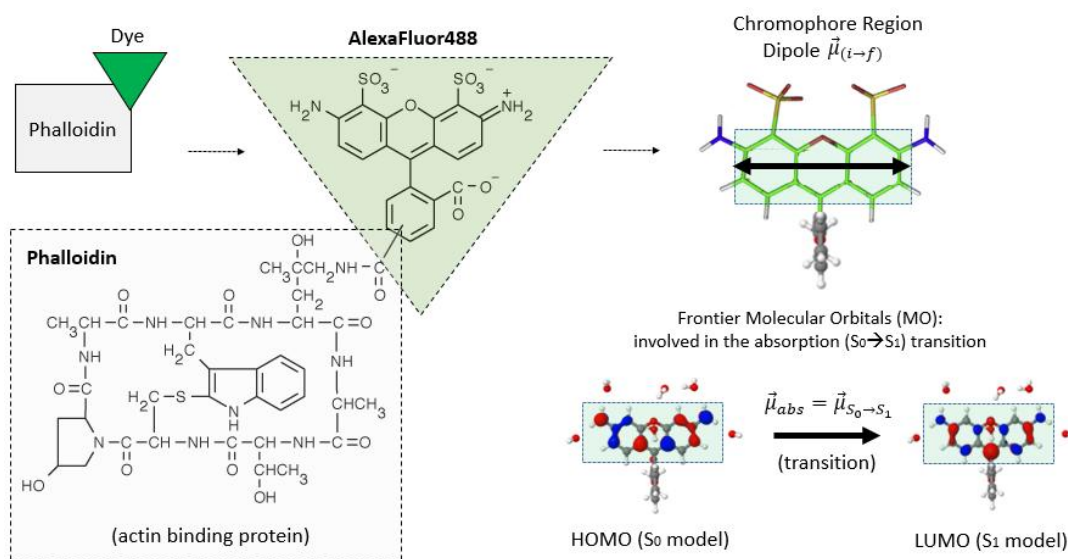


Figure 2.5 – Examples of state dipoles and transition dipoles. Chemical structure of Phalloidin-AlexaFluor488 fluorophore, the fluorescent label we used in this thesis. Phalloidin is a non-fluorescent drug that binds and stabilizes actin filaments. The linkage of Alexafluor488 Dyes to phalloidin drug yields optical sensitivity to the drug in the visible range. The dye AlexaFluor488 is a Rhodamine derivative dye whose chromophore region (green rectangle) encompasses the optical transition dipole moments, whose are sensitive to the light polarizations. The chromophore region consists on 3 electron-conjugated xanthene planar rings due to electronic resonance. Below, the simulation of the idealistic ground state ( $S_0$ ) and excited state ( $S_1$ ) molecular electronic density using Rhodamine A (simplified model of AlexaFluor488). The simulations illustrate some spatial difference in electron phase (red-blue colors) and density (volume), that can be used to estimate the transition dipole moments. Figure adapted from [47, 48].

### II.3.3 The absorption probability and its orientation sensitivity

One can estimate from quantum mechanics (first order perturbation theory formalism [49]) the one photon absorption transition probability,  $P_{S_0 \rightarrow S_1}$ , that is the probability of a fluorophore on its ground state  $S_0$  to absorb the energy of a photon and then reaches the first excited state  $S_1$  energy level. It can be shown that  $P_{S_0 \rightarrow S_1}$  is proportional to the square of the dot product (vectorial projection) of the electric field orientation,  $\vec{E}_{exc}$ , with the molecular transition dipole  $\vec{\mu}_{(S_0 \rightarrow S_1)}$ . In what follows, we will name this transition dipole “absorption dipole”  $\vec{\mu}_{abs}$  [49]. For the case of linear excitation (1PE, one photon excitation), we could write the absorption probability as [50]:

$$P_{abs} = P_{S_0 \rightarrow S_1} \propto |\vec{E}_{exc} \cdot \vec{\mu}_{abs}|^2 \propto |E \cdot \mu_{abs} \cdot \cos\theta_{E,\mu}|^2 \quad \text{Eq. 2.7}$$

where,  $\theta_{E,\mu}$  is the angle between  $\vec{E}_{exc}$  and  $\vec{\mu}_{abs}$ .

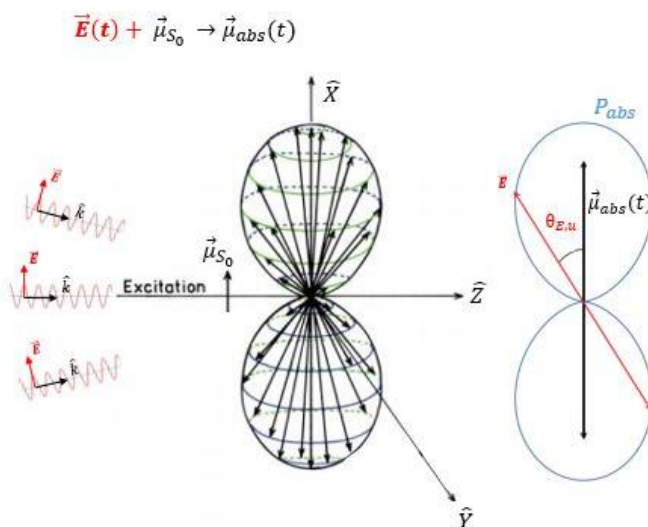


Figure 2.6 – The orientation dependence profile of photo-absorption. Here, the different excitation light vectors ( $\vec{E}(t)$ , in red), incidence on the fluorophore dipole vector at the ground state, ideally represented by  $\vec{\mu}_{S_0}$ . The light interacts with the molecule at the ground state inducing electronic movements of the valence electrons. An absorption dipole moment ( $\vec{\mu}_{abs}$ ) can be defined with orientation aligned with the highest absorption probability of the fluorophore to absorb a photon ( $P_{abs}$ ). Note that, different excitation orientation in relation to the absorption dipole moment yields different absorption probabilities, represented in a blue curve profile on the right. The highest alignment between the excitation field with the absorption dipole moment yields the highest absorption probability. Conversely, when the excitation orientation is perpendicular to the absorption dipole moment, no interaction with the light occurs, and ideally no photon is absorbed by the fluorophore.

As we see in Figure 2.6, there is zero probability of excitation when the vector of the electric field is orthogonal to the absorption dipole moment. On the other hand, the absorption probability is maximum when both are perfectly aligned between each other. The property of photo-selection can be used or not (wanted or avoided) in polarization resolved experiments, as we will describe in more details later when detailing the methods (Chapter 3).

### II.3.4 The emission probability and its orientation sensitivity

In the emission process, the radiated field (e.g., fluorescence generated by one oscillating dipole) propagates in space in a very anisotropic way. This is because the propagation of the emitted photons is identical to that of a radiating dipole, named emission dipole moment  $\vec{\mu}_{em}$ . This dipole can be associated to the transition dipole moment from the lowest excited S1-state to the ground S0-state, during the relaxation process :  $\vec{\mu}_{(S1 \rightarrow S0)}$ . This emitted angular pattern happens mainly radially (see Figure 2.7). Since light can be described by an oscillating electric field that lies transverse to its propagation ( $\vec{k}$ ), the emitted electromagnetic field  $\vec{E}_{em}$  is mainly oriented parallel to the axis of the emission dipole (see Figure 2.7 and Figure 2.8). It follows the equation [51, 52]:

$$|\vec{E}_{em}(\vec{k})| \propto |\vec{k} \times (\hat{k} \times \vec{\mu}_{em})| \propto k \cdot \mu_{em} \cdot \sin\theta_{k,\mu} \quad \text{Eq. 2.8}$$

where  $\hat{k}$  is the unitary propagation direction of the emitted light,  $\vec{\mu}_{em}$  is emission dipole, and  $\theta_{k,\mu}$  is the angle between  $\vec{k}$  and  $\vec{\mu}$  vectors.

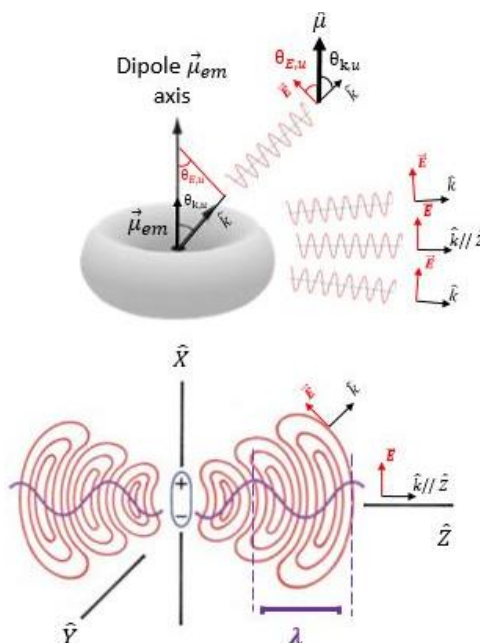


Figure 2.7 – Diagram describing qualitatively how oscillating dipoles generate light of wavelength  $\lambda$ . Note that, when the dipole oscillates, the red arrows along the radial direction display a sinusoidal form projected on X -direction, which is orthogonal to the wave propagation ( $k//Z$ ). In other words, dipole oscillations parallel to X-direction generate fluorescence (electric field oscillations) mainly along X-direction, and the light propagates mainly radially (along Y and Z direction, generating a donut profile). On the top, the anisotropic 3D geometry (donut shaped) of the emitted photons: light propagating mainly along Y and Z axis, but not parallel to the dipole oscillation (X direction). On the bottom, the electric field on the plane-X,Z generated by an oscillating dipole along X direction. Adapted from [34, 53].

Thus, to detect an emitted photon at distances much longer than its wavelength (in the far field), it is reasonable to expect the highest probability, i.e.,  $P_{em} = max$ , along a polarization direction parallel to the emission dipole axis. In other words, the polarization of the detected photon is essentially parallel to the orientation of the emission dipole. In practice, when placing



a polarizer in the far field along the direction  $\vec{u}_i$  (see Figure 2.8), the emission probability in the propagation direction  $\vec{k}$  writes:

$$P_{em,u_i}(\vec{k}) \propto |\vec{E}_{em}(\vec{k}) \cdot \vec{u}_i|^2 \propto |E_{em}(\vec{k}) \cdot \cos\theta_{E,u_i}|^2 \quad \text{Eq 2.9a}$$

where  $\vec{E}_{em}$  is emitted fluorescence electric field vector (see Figure 2.9),  $\vec{u}_i$  is the unitary vector parallel to the analyzer detection,  $\theta_{E,u_i}$  is the angle between the analyzer orientation  $\vec{u}_i$  and the fluorescence emitting field  $\vec{E}_{em}$ . In the far field  $\vec{k}$  direction the probability to detect a photon is proportional to the projection of  $\vec{\mu}_{em}$  on the transverse plane of propagation (called  $\vec{\mu}_{em,\perp}$ , perpendicular to  $\vec{k}$  vector, see Figure 2.9), therefore in relation to an arbitrary transverse detection direction  $\vec{u}_i$ :

$$P_{em,u_i}(\vec{k}) \propto |\vec{\mu}_{em,\perp} \cdot \vec{u}_i|^2 \quad \text{Eq. 2.9b}$$

Usually the detection is collected using an objective with a given numerical aperture NA, therefore the total emission probability is written:

$$P_{em,u_i} = \int_{k \in NA} P_{em,u_i}(\vec{k}) d\vec{k} \quad \text{Eq. 2.10}$$

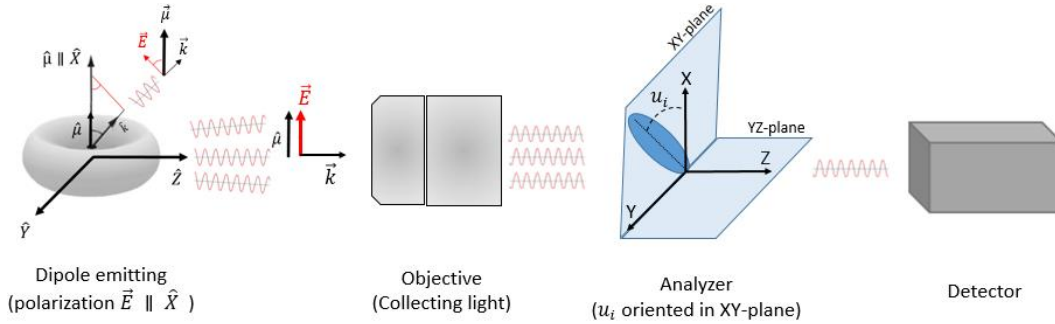


Figure 2.8 – The anisotropic emission of single dipoles and their detection in the far field. On the left, an illustration showing that the propagation of light is higher at radial directions (YZ), while the propagation at orientations close to the dipole orientation ( $\vec{\mu}$ ) are minimum. Thus most of the emitted light has YZ directions. Consequently, the main polarization (direction of  $\vec{E}$  field) is parallel to the dipole. The objective lens collect light according to its numerical aperture (NA). When probing the polarization of the emission, an analyzer (e.g., polarizer) is used at a given orientation ( $u_i$ ) in the XY-plane. Changing the orientation of the analyzer in the XY-plane modulates the detected signal, allowing us to retrieve the orientation of the polarization. The highest detected signal would be aligned to the polarization of the emitted light, which is also the mean orientation of the dipole.

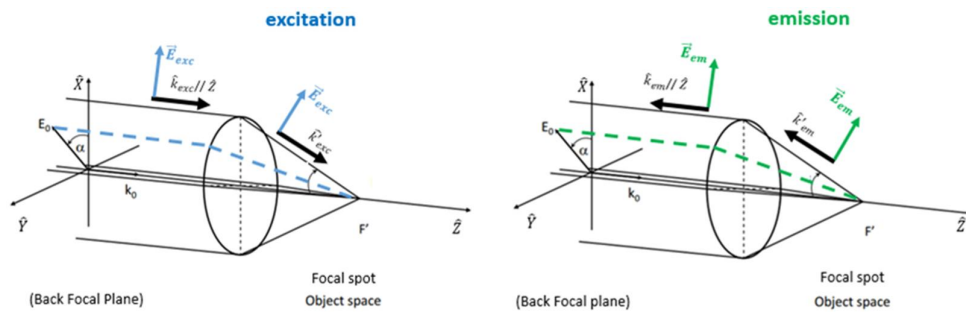


Figure 2.9 – Definition of the vectors to calculate the polarization sensitivity to both excitation (left) and emission (right) processes.  $\vec{k}$  and  $\vec{k}'$  vectors are the propagation vectors,  $\vec{E}_{exc}$  and  $\vec{E}_{em}$  vectors of the excitation and emission respectively. In the back focal plane of the objective, the alpha angle denotes the polarization orientation of a linearly

polarized incident light (left) or that of the emission light at a point on the optical axis. Note that the higher the objective NA, the wider would be the light cone aperture, and therefore, higher polarization mixing is induced (see text below). Only light propagating aligned in the center of the beam (i.e.,  $E_0$  field with  $K_0$  perfectly aligned to z-axis) does not have mixed components after focusing with the objective NA.

### II.3.5 Orientation sensitivity of the absorption-emission fluorescence process

Due to the Stokes shift, the fluorescence light is not in phase with the absorption light, i.e., the fluorescence light is randomly emitted after a certain time (random phase delay). Stochastically emission leads to temporal incoherence between the absorption and the emission events. Consequently, fluorescence and absorption processes can be understood as two *consecutive and temporal independent (incoherent)* optical processes. Based on that, the steady-state probability to detect fluorescence on an analyzer with a specific orientation  $\vec{u}_i$  ( $I_{u_i}$ ) is proportional to the *product* of both events: absorption and emission probabilities. Mathematically, we can write the detected fluorescence intensity as:

$$I_{u_i} \propto P_{abs} \cdot P_{em, u_i} \quad \text{Eq. 2.11}$$

For example, if we want to detect the fluorescence intensity in the far field direction Z in a analyzer directions "parallel" to the "X-axis" ( $I_{\parallel}$  or  $I_x$ , projection on the laboratory X-axis orientation  $\vec{u}_x$ ) and "orthogonal" or "Y-axis" ( $I_{\perp}$  or  $I_y$ , projected on the laboratory Y-axis orientation  $\vec{u}_y$ ), the plane wave approximation *per se* would yield:

$$I_{\parallel} = I_x \propto P_{abs} \cdot P_{em, X} \propto |\vec{E}_{exc} \cdot \vec{\mu}_{abs}|^2 \cdot |\vec{\mu}_{em, Z} \cdot \vec{u}_x|^2 \quad \text{Eq. 2.12a}$$

$$I_{\perp} = I_y \propto P_{abs} \cdot P_{em, Y} \propto |\vec{E}_{exc} \cdot \vec{\mu}_{abs}|^2 \cdot |\vec{\mu}_{em, Z} \cdot \vec{u}_y|^2 \quad \text{Eq. 2.12b}$$

For many polarized fluorescence methods in isotropic media, the latter equations are enough to describe the outcome of the experiments if proper frame axes and excitation polarization conditions are chosen. Nevertheless, as we will detail more later, in polarization resolved *microscopy* experiments, the high numerical aperture of the objective lens mixes the electric field components in the 3D space, due to the integration visible in Eq. 2.10.

Therefore both analyzer channels have components of all X, Y, and Z directions in different, but complementary proportions. The integration performed over the NA of the detection objective (see Eq. 2.10) leads to a mixture of polarized terms with weights  $\kappa_1, \kappa_2, \kappa_3$  that have been calculated in [54]. It can be shown that we can then rewrite the detected fluorescence emission equation in a more generalized form by using the J modified intensity components, which describe the polarization mixing:

$$J_X \propto \kappa_1 |\vec{\mu}_{em} \cdot \vec{u}_x|^2 + \kappa_2 |\vec{\mu}_{em} \cdot \vec{u}_y|^2 + \kappa_3 |\vec{\mu}_{em} \cdot \vec{u}_z|^2 \quad \text{Eq. 2.13a}$$

$$J_Y \propto \kappa_2 |\vec{\mu}_{em} \cdot \vec{u}_x|^2 + \kappa_1 |\vec{\mu}_{em} \cdot \vec{u}_y|^2 + \kappa_3 |\vec{\mu}_{em} \cdot \vec{u}_z|^2 \quad \text{Eq. 2.13b}$$

where  $\kappa_1, \kappa_2, \kappa_3$  are normalized coefficients that weights the polarization mixture on the 3 main axes. [54].

## II.4 Fluorescence anisotropy in isotropic media

Techniques that probe the orientation state of the emission dipole in isotropic environments are generally named fluorescence anisotropy techniques (see figure Figure 2.10). Fluorescence anisotropy is usually performed under linearly polarized excited light (unpolarized or circular polarized light). The polarized emission (fluorescence) orientation can be retrieved by splitting the emission wave on different orthogonal analyzer components. The latter can be done by different means: absorption (e.g., polarizer), reflection (e.g., polarized beam splitter) or refraction (e.g., Wollaston prism). In general, the difference of the detected intensity on each analyzer channels normalized by the total intensity defines the fluorescence anisotropy, which is sensitive to how the dipoles are oriented in space.

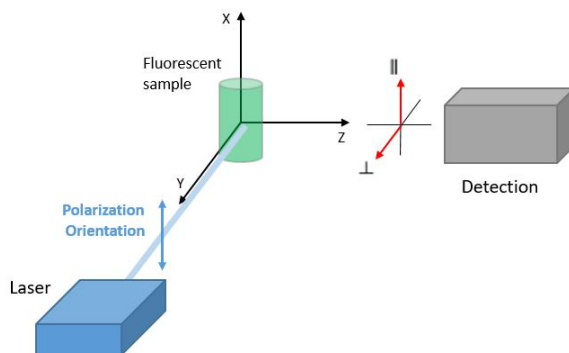


Figure 2.10 – Schematic illustration of a fluorescence anisotropy setup. The X-polarized laser excites the fluorescent sample, which emits lights mainly in the YZ directions. A detector is placed typically orthogonally to the excitation in order to avoid background signal due to the laser light. An analyzer is placed just before the detection, being capable of measuring the polarization parallel and/or orthogonal to the excitation beam. Adapted from [52].

In the geometry displayed in Figure 2.10, the incident polarization is along X.  $I_{\parallel}$  stands for the intensity measured for a polarizer along X, while  $I_{\perp}$  is measured for a polarizer along Y. The fluorescence anisotropy  $r$  is defined as :

$$r = \frac{I_{\parallel} - I_{\perp}}{I_T} \quad \text{Eq. 2.14}$$

where  $I_T = I_X + I_Y + I_Z = I_{\parallel} + 2I_{\perp}$  is the total intensity.

Fluorescence anisotropy experiments using linearly polarized light are powerful, because since both excitation and detection polarizations are controlled, depolarization mechanisms can be quantified such as difference between absorption and emission dipoles, rotational diffusion, or energy transfer between fluorophores. For example, in a static isotropic media such as a very viscous/cold and diluted fluorescent-labelled sample, the relative angle  $\beta$  between the absorption dipole  $\vec{\mu}_{abs}$  and the emission dipole  $\vec{\mu}_{em}$  of the fluorophore can be determined (Eq. 2.15) (see Figure 2.11). In such cases, the fluorophores are assumed to be immobile and enough distant to each other (in order to avoid energy transfer). Thanks to the linear absorption, photo-selection and to a randomly distributed spatial configuration of the fluorophores, it can be shown that the values of the anisotropy varies always in between the

range of 0.4 and -0.2 [43]. In such conditions, the ‘static’ anisotropy ( $r=r_0$ ) can be calculated to deduce  $\beta$ , as follows:

$$r = r_0 = \frac{2}{5} \left( \frac{3 \cos^2 \beta - 1}{2} \right) \Leftrightarrow \beta = \cos^{-1} \left( \sqrt{\frac{5r_0 + 1}{3}} \right) \quad \text{Eq. 2.15}$$

Once knowing the static fluorescence anisotropy value of a fluorophore, the  $\beta$  angle between  $\mu_{\text{abs}}$  and  $\mu_{\text{em}}$ , is oftentimes assumed a *constant* parameter in follow up experiments. Table 2.2 lists typical  $\beta$  and  $r_0$  values measured in different fluorophores.

Angle between $\mu_{\text{abs}}$ and $\mu_{\text{em}}$	$\beta$ (degrees)	$r_0$	References
Ideally aligned (max value)	0°	0.400	[43]
Fluorescein (+ correction)	6.63°	0.392	[55]
Fluorescein (- correction)	11.04°	0.378	
Rhodamine & Xanthene derivatives	$\approx 10^\circ$	$\approx 0.38$	[50]
<b>AlexaFluor488</b>	<b>11.54°</b>	<b>0.376</b>	<b>[56]</b>
Rhodamine B	14.16°	0.364	[55]
Ideally 45°	45.0°	0.100	[43]
Magic angle	54.7°	0.000	[43]
Ideally orthogonal (min value)	90.0°	-0.200	[43]

Table 2.2 – Static anisotropy ratio values and the related  $\beta$  angle between  $\mu_{\text{abs}}$  and  $\mu_{\text{em}}$ . Note: values using long excitation wavelengths,  $\lambda_{\text{abs}} \geq 450\text{nm}$

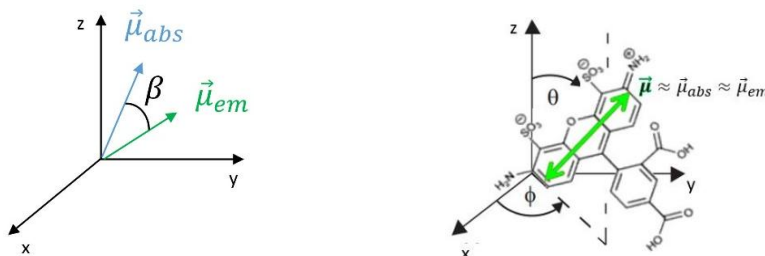


Figure 2.11 – Illustration of the beta angle in between the absorption and the emission dipole (left). On the right side, an illustration when the beta angle is very small so that we can approximate the dipoles by a single one on a determined orientation (defined by the angles  $\theta, \phi$  in a microscopic frame  $x, y, z$ ). Adapted from [52].

In the literature, it has been shown that fluorophores that have  $\beta < 20^\circ$  are relevant to be used on most polarization resolved microscopy experiments [57]. Hence, if one is interested in finding new probes for such methods, one could start first by evaluating  $\beta$  of the new probes. For example, Rhodamine derivative dyes can be employed because their  $\beta$  angle fit within this range, and therefore yields good polarization-sensitive signals when both incident and detected polarizations are controlled. Particularly, in our case, the AlexaFluor488 exhibits  $\beta_{AF488} = 11.5^\circ$ . Nevertheless as we will see in Chapter 3, in fluorescence polarized microscopy experiments, the value of  $\beta$  does not appear in the data analysis, because the excitation is performed under circular polarized light (or any other homogeneous excitation), so that there is no photo-selection *bias* affecting the measurement.

Once the angle  $\beta$  is known, further anisotropy experiments in liquid solutions (non-immobile fluorophores cases) which are sensitive to other depolarization processes such as rotational diffusion and resonance energy transfer (RET) can be carried out. Typical depolarization experiments allow the study of the rotational mobility of proteins and other biomolecules under different conditions. For example, the presence of different ligands, different medium viscosity (e.g., cytosol vs membranes), temperature and/or pH, etc. One could evaluate the depolarization changes using the Perrin's equation and the rotational correlation time equation (Eq 2.16). Consequently, it is possible to quantify protein conformational changes (e.g., denaturation), formation of protein complexes (dimerization, aggregation, polymerization, etc), and binding affinity between ligands (e.g., in antibody-binding domains of immunoglobulins, etc). Moreover, thanks to RET, it is possible to study how short-range interactions (i.e., within distances less than 10nm) affects the biomolecular structure of interest (SOI), among others applications [43]. In conditions where the molecular rotational diffusion time  $\tau_{rot}$  is comparable or faster than the fluorescence lifetime  $\tau_f$ , the fluorescence anisotropy  $r$  follows :

$$\frac{1}{r} = \frac{1}{r_0} \left( 1 + \frac{\tau_f}{\tau_{rot}} \right) \quad \text{Eq. 2.16}$$

where  $\tau_{rot} = \frac{\eta V}{RT}$ . Here,  $r$  is the measured anisotropy (e.g., in aqueous isotropic medium),  $r_0$  is the fundamental anisotropy of the label (constant, see Eq. 2.15),  $\tau_f$  is the fluorescence lifetime,  $\tau_{rot}$  is the rotational diffusion time,  $\eta$  is the viscosity of the solvent,  $V$  is the hydrodynamic volume (related to the size and shape of the SOI-fluorophore complex),  $R$  is the thermodynamic gas constant and  $T$  is the temperature.

## II.5 Fluorescence polarized response in anisotropic media

### II.5.1 Modelling the orientation distribution of fluorophores in ordered samples – the cone model

In the previous section, the fluorophores were distributed within an isotropic angular distribution. In microscopy in general, fluorophores are rather distributed in more complex angular distributions, which complexifies the fluorescence polarized response. In what follow, we describe a simple way to model the orientation distribution of fluorophores. It has been shown that when using one-photon fluorescence responses, one can simplify any orientation distribution by a simple cone angular aperture (e.g. angles explored by the molecules in space and time) oriented in the sample frame [57], as depicted in Figure 2.12. The reason is that polarized paraxial one-photon fluorescence depends on the square of absorption/emission dipoles projections, and is therefore limited to the determination of two parameters only defining their distribution [57]. We will therefore use a cone model to represent the orientation distribution function of the fluorophores. Two parameters can be used to define this distribution in 2D: their mean orientation in the sample plane (Figure 2.13) and its angular aperture (sometimes called angular organization, or order) [52, 57-58] (Figure 2.12 and Figure 2.13). In 3D, an additional orientational angle is required (Figure 2.13), which we will address in more details in Chapters 3 to 5. The order represents the extent of angles explored by all

molecules (present in a focal volume) during the integration time of the measurement, making this quantity an average in time (over the integration time) and space (over the spatial resolution limit).

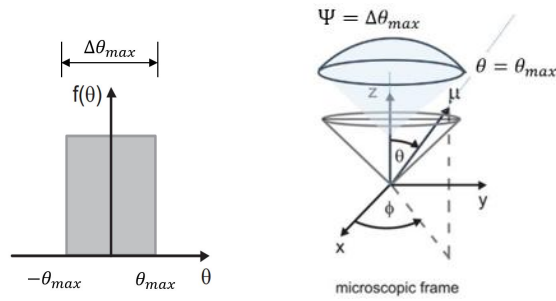


Figure 2.12 – The microscopic frame  $(x,y,z)$  and the cone model parameters. In this illustration the orientation of the cone is aligned with the microscopic  $z$ -axis, that represents the mean orientation of the fluorophores, and the cone aperture is defined as  $\Psi = \Delta\theta_{max} = 2|\theta_{max}|$ , where  $\theta_{max}$  is the maximum angle of the fluorophores that deviates from the mean (the microscopic  $z$ -axis, the center). The cone aperture  $\Psi$  is also called order parameter in ensemble techniques. The cone encloses all the integrated fluorophore orientations of the fluorophores on a determined focus spot. Adapted from [52, 58].

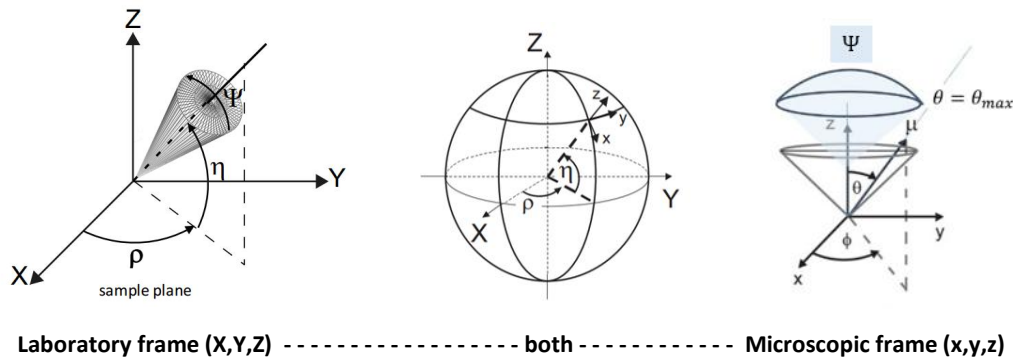


Figure 2.13 – The laboratory frame (left) and the microscopic frame (right), and the connection between both (central scheme). The laboratory frame is a macroscopic frame where the setup is built, and its frame axes are defined by capital letters  $X,Y,Z$ . Typically,  $X$  and  $Y$  axes define a plane that is parallel to the sample plane, and  $Z$  to the propagation of the light in the far field. Conversely, the microscopic frame is defined by the letters  $x,y,z$ , where  $z$ -axis is the mean orientation of the fluorophores on a determined  $X,Y$  spot. Note that the microscopic  $z$ -axis defines the orientation of the cone, which is defined by two macroscopic angles  $(\rho, \eta)$ , see central scheme. Each orientation of the fluorophores (different  $\mu_s$ ) can be defined in the microscopic frame by two angles  $(\theta, \phi)$ . Figure adapted from [52].

Denoting  $(\theta, \phi)$  the orientation angles of each molecule belonging to the cone distribution within its microscopic frame (Figure 2.12), we can define our microscopic angular conical distribution function  $f_{cone} = f_c(\theta, \phi)$  to be a cone shaped function such as:

$$f_c(\theta, \phi) \equiv \begin{cases} \frac{1}{\int_0^{2\pi} d\phi' \int_0^{\frac{\Psi}{2}} \sin\theta' d\theta'} & \text{if } |\theta| \leq \frac{\Psi}{2} \\ 0 & \text{otherwise} \end{cases} \quad \text{Eq. 2.17}$$

where  $\Psi$  is the full aperture of the cone (Figure 2.12). Thanks to the *homogeneous integration* over  $\phi$ , we obtain a distribution function dependent only on  $\theta$ :

$$f_c(\theta) \equiv \begin{cases} \frac{1}{4\pi \sin^2\left(\frac{\Psi}{4}\right)} & \text{if } |\theta| \leq \frac{\Psi}{2} \\ 0 & \text{otherwise} \end{cases} \quad \text{Eq. 2.18}$$

The cone model can be thought as a simplification of a more realistic and complicated angular stochastic distribution function described by all possible fluorophore orientations at thermal equilibrium. The static orientations of different fluorophores, plus each explored orientation of their dynamic stochastic rotational behavior would contribute to the real stochastic aperture. Whenever considering an ensemble of fluorophores within a focal spot region at thermal equilibrium at room temperature  $T$ , such stochastic aperture could be described as an orientational distribution function  $f_m(\theta, \phi)$  by Boltzmann statistics if we consider that the thermal fluctuations are confined by a defined energy potential  $U(\varphi, \theta)$ . In such cases, we can expect:

$$f_m(\theta, \phi) \propto e^{-\left(\frac{U(\theta, \phi)}{k_b T}\right)} \quad \text{Eq. 2.19}$$

From Eq2.19, we see that, the higher the temperature, the wider would be the aperture of the distribution function. The problem of using such equation in polarimetry is that the energy potential is not easily mathematically defined for every region of the sample.

Even though the cone model is a simplified model for a distribution which real shape is unknown, it provides the essential parameters that can be accessed via a fluorescence polarized measurement. In this sense, in ordered and anisotropic biomolecular structures, fluorescence anisotropy could also be applied to quantify the angular distribution of fluorophores attached to such biomolecular structures. In Figure 2.14 we show a schematic representation of the molecular order projected in 2D (in the sample plane), which could be probed by fluorophores attached to biological filaments. The wider the  $\Psi$  angle (cone aperture), the more isotropically distributed the orientations of the probed labels, and therefore the higher the local filaments' disorder. Conversely, if the labels are well aligned, more anisotropic will be the detected signal, and thus such response could be interpreted as a higher filament order at the molecular scale. The cone model has many positive aspects. First, it is a simple model to be computationally programmed and implemented, because it is based on simple geometrical parameters. Second, it affords a clear geometric perspective of the molecular order, so that it is more intuitive to visualize. Finally, it can be used on a wide range of applications, including different polarization resolved microscopy methods, such as angular resolved linear dichroism microscopy [52] and on single-molecule super-resolution fluorescence anisotropy measurements [59-60], which will be described below and in Chapter 3. Particularly, it has already been successfully used to quantitatively image the organization of lipids in membrane models (e.g., giant unilamellar vesicles), and other biomolecules in fixed cells, such as lipids in real cell membranes, DNA, amyloid fibers, actin filaments, microtubules and septins [52, 54, 57-63]. Note that in the most of the cases in microscopy, only 2D structures are probed, since the polarization state is manipulated in 2D (in the sample plane). The case of 3D orientations will be addressed in the next chapters. Note that in certain situations the rotational probability of the fluorophore is not along a cone direction but perpendicular to an axis of symmetry. In this case, the distribution to consider is rather of donut-shape [58]. In what follows, we derive all equations for a cone

distribution, which can be directly exchanged for a donut-shape distribution in this other type of geometry.

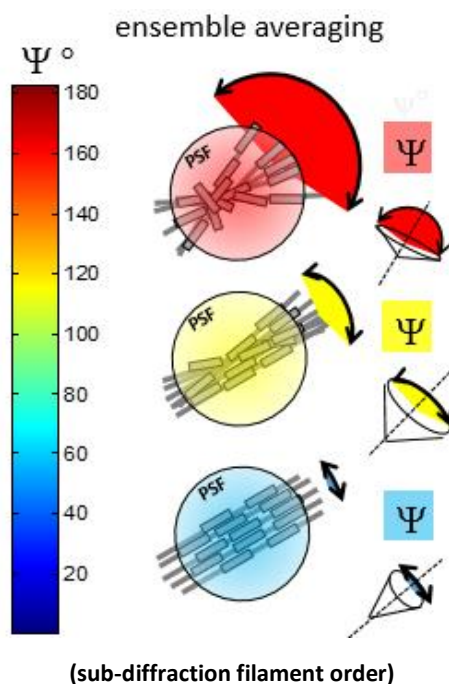


Figure 2.14 – The ensemble angular aperture is called order parameter ( $\Psi$ ). The order parameter probes the total angular aperture of the labels within the point spread function size (PSF), which defines the diffraction limit size. Since the probes are aligned along the structure (such as in the case of phalloidin-AlexaFluor488), measuring the orientations of the probes on each focal spot gives information about the sub-diffraction molecular organization of the filaments. On the right side, the cone model representation of each aperture angle. The wider the cone aperture, the more isotropically distributed are the fluorophores orientations, therefore more disorganized are the molecular structure of the filaments, and vice-versa. On the left side, the cone aperture angle scale in colorcode. The red color corresponds to higher the disorder. The blue color corresponds to higher molecular order of the filaments.

Note that in Figure 2.14, and important factor is not represented: the angular mobility of each single fluorophore during the integration time of the image. Even though we will try to minimize this mobility to report proteins' orientations using fluorescence labels, many linkers leave some degree of flexibility between the protein of interest and its fluorescent label. We therefore need to keep in mind that in ensemble fluorescence imaging, the focal volume encompasses many labels which can have their own rotational mobility. In particular in the context of F-actin filaments assemblies, the detected aperture angle ( $\Psi$ ) encompasses not only the single molecule's orientations from all labels in a focal spot (called  $\rho$  in Figure 2.15), which are a signature of filament's disorder, but also their rotational flexibility (called  $\delta$  in Figure 2.15). This aspect will be discussed in more detail in the next chapters.



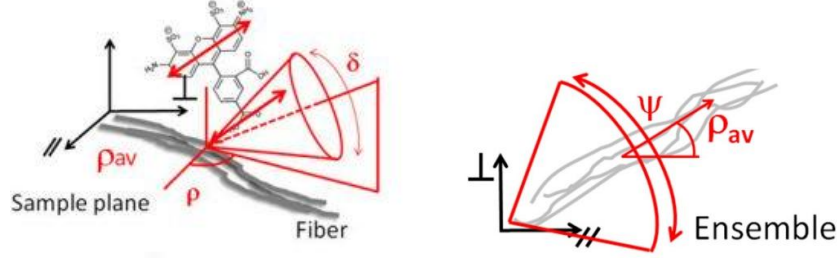


Figure 2.15 – On the left, the biological filaments are the structure of interest (SOI). They are lying on a 2D plane. There, we show a single fluorophore bound to the filaments has its 3D orientation (given by  $\rho$ ) and thermal fluctuation aperture angle, which is approximated by a wobbling conical angle ( $\delta$  – described in more detail in single molecule methods, Chapter 5). On the right, when an ensemble of fluorophores are probed in any arbitrary focal spot, many static and dynamic ( $\sim$ wobbling) orientations are integrated in the same signal, so the total aperture angle ( $\Psi$ ) is typically wider compared to each wobbling angle of isolated fluorophores ( $\delta$ ). On the right image, we only showed the 2D projection of the 3D cone of an ensemble of fluorophores, which follows an averaged mean orientation  $\rho_{av}$ . Adapted from [59].

## II.5.2 Polarized fluorescent response from a cone distribution of fluorophores

In what follows, we derive the specificities of polarized fluorescence intensities in a microscope, accounting for the angular distribution of fluorophores within cone distributions. When considering an ensemble of fluorophores within an angular distribution, the resulting intensity is the incoherent sum of intensities from each fluorophores embedded in the orientation distribution function  $f_m(\theta, \phi)$ . Considering that  $f_m(\theta, \phi)$  is the orientation distribution function of all labels in a focal spot (that can be approximated in our case to a cone model,  $f_c(\theta, \phi)$ ), the resulting intensity measured along analyzers in directions X and Y leads to:

$$I_X \propto \int_0^{2\pi} \int_0^\pi |\vec{E}_{exc} \cdot \vec{\mu}(\theta, \phi)|^2 \cdot J_X(\vec{\mu}(\theta, \phi)) \cdot f_m(\theta, \phi) \cdot \sin(\theta) d\theta d\phi \quad \text{Eq. 2.20a}$$

$$I_Y \propto \int_0^{2\pi} \int_0^\pi |\vec{E}_{exc} \cdot \vec{\mu}(\theta, \phi)|^2 \cdot J_Y(\vec{\mu}(\theta, \phi)) \cdot f_m(\theta, \phi) \cdot \sin(\theta) d\theta d\phi \quad \text{Eq. 2.20b}$$

Together with Eq. 2.13:

$$J_X(\vec{\mu}(\theta, \phi)) \propto [\kappa_1 |\vec{\mu}(\theta, \phi) \cdot \vec{u}_X|^2 + \kappa_2 |\vec{\mu}(\theta, \phi) \cdot \vec{u}_Y|^2 + \kappa_3 |\vec{\mu}(\theta, \phi) \cdot \vec{u}_Z|^2] \quad \text{Eq. 2.21a}$$

$$J_Y(\vec{\mu}(\theta, \phi)) \propto [\kappa_2 |\vec{\mu}(\theta, \phi) \cdot \vec{u}_X|^2 + \kappa_1 |\vec{\mu}(\theta, \phi) \cdot \vec{u}_Y|^2 + \kappa_3 |\vec{\mu}(\theta, \phi) \cdot \vec{u}_Z|^2] \quad \text{Eq. 2.21b}$$

Note that this expression supposes that both absorption and emission dipoles have the same orientation at a given time, which is true if one supposes that the rotational diffusion time within the cone is slower than the fluorescence life time. If it is not the case, a more complex equation needs to be written [54], which we will not display here since this is not used in our methods where excitation and emission will be decoupled.

In what follows, we will detail the principle of the calculation of this intensity as a function of the fluorophore's order and mean orientation parameters. It consists of two steps.

### II.5.2.1 The microscopic frame coordinates related to the fluorophores' mean orientation $\bar{\mu}$

Here, we will enter in more detail about the microscopic orientations of the fluorophore's dipoles. For the sake of simplicity, we will use the term "fluorophore orientation" to describe its transition dipole orientation. Besides, we will assume that the absorption and emission transition dipoles have the same orientation  $\vec{\mu}$ , whose magnitude is normalized to unity (the following equations can be extended to a more general case):

$$\vec{\mu} \approx \vec{\mu}_{abs} \approx \vec{\mu}_{em} \quad \text{Eq. 2.22}$$

This dipole orientation can be written at any time t using an instantaneous orientation  $(\theta, \phi)$ , defined by its polar and azimuthal angles respectively. We denote  $\vec{\mu}'(\theta, \phi)$  this instantaneous dipole :

$$\vec{\mu}' = \vec{\mu}'(\theta, \phi) = \begin{bmatrix} \mu_x'(\theta, \phi) \\ \mu_y'(\theta, \phi) \\ \mu_z'(\theta, \phi) \end{bmatrix} = \begin{bmatrix} \sin(\theta)\cos(\phi) \\ \sin(\theta)\sin(\phi) \\ \cos(\theta) \end{bmatrix} \quad \text{Eq. 2.23}$$

In Eq. 2.23 the coordinates of the dipole are written in the microscopic frame carried by the cone explored by the fluorophore (see Figure 2.12). When averaged in time and space, the observation is an averaged quantity. Since the cone distribution is of cylindrical symmetry, it is convenient to define the theta and phi angles with respect to its symmetry axis (called z, see Figure 2.13) and orient later the cone in the macroscopic frame to define its interaction with light polarizations orientation of the dipoles  $(\theta, \phi)$ :

$$\text{Microscopic mean orientation} = \bar{\mu} \parallel \hat{z} \Rightarrow \bar{\theta}\bar{\phi} = 0.$$

$$\text{Microscopic angular distribution function} = f_m(\theta, \phi) \text{ centered around } \hat{z} \quad \text{Eq. 2.24}$$

### II.5.2.2 Aligning the microscopic frame onto the laboratory (macroscopic) frame

The microscopic reference frame is dependent on the microscopic volume probed in sample, so that it changes its orientation depending on how the fluorophores are distributed, because  $\hat{z}$  must be  $\parallel$  to  $\bar{\mu}$ , the mean probed orientation (Eq 2.24). Since the interaction with the light polarization  $\vec{E}_{exc}$  is defined in the macroscopic frame, it is important to know how the laboratory frame relates to it and vice-versa. For simplicity, both the microscopic  $(\hat{x}, \hat{y}, \hat{z})$  and the macroscopic laboratory  $(\hat{X}, \hat{Y}, \hat{Z})$  reference frame can be defined as two orthonormal coordinates frames (see Figure 2.13), so that we can find a single transformation matrix (M) that performs two rotations around particular main axes, whose can align both reference frames, Macroscopic (M) to microscopic (m) :

$$\vec{M}_{XYZ \rightarrow xyz} = \vec{M}_{M \rightarrow m} \quad \text{Eq. 2.25}$$

where  $\vec{M}_{M \rightarrow m}$  is a product of two 3D rotation matrix around the main axes. We depict here the essential rotations that are used in the formation of this matrix:

A positive (right hand) rotation of an angle  $a_x$  around x-axis:

$$R_x(a_x) = \begin{bmatrix} 1 & 0 & 0 \\ 0 & \cos(a_x) & -\sin(a_x) \\ 0 & \sin(a_x) & \cos(a_x) \end{bmatrix} \quad \text{Eq. 2.26}$$

A positive (right hand) rotation of an angle  $a_y$  around y-axis:

$$R_y(a_y) = \begin{bmatrix} \cos(a_y) & 0 & \sin(a_y) \\ 0 & 1 & 0 \\ -\sin(a_y) & 0 & \cos(a_y) \end{bmatrix} \quad \text{Eq. 2.27}$$

A positive (right hand) rotation of an angle  $a_z$  around z-axis:

$$R_z(a_z) = \begin{bmatrix} \cos(a_z) & -\sin(a_z) & 0 \\ \sin(a_z) & \cos(a_z) & 0 \\ 0 & 0 & 1 \end{bmatrix} \quad \text{Eq. 2.28}$$

Using the example of Figure 2.13, we want to represent/transform the mean orientation of the fluorophores  $\vec{\mu} \parallel \hat{z}$  that was detected at one specific focal spot in the microscopic frame ( $\hat{x}, \hat{y}, \hat{z} \parallel \vec{\mu}$ ) onto the laboratory reference system (e.g., aligned with the sample plane X,Y), whose is written in the laboratory frame coordinates ( $\hat{X}, \hat{Y}, \hat{Z}$ ). In other words, we have to transform the microscopic vector into the macroscopic vectors,

$$\vec{\mu}_m(\hat{x}, \hat{y}, \hat{z}) \rightarrow \vec{\mu}_M(\hat{X}, \hat{Y}, \hat{Z}) \quad \text{Eq. 2.29}$$

By the transformation matrix  $\vec{M}_{m \rightarrow M}$ :

$$\vec{\mu}_M = \vec{M}_{m \rightarrow M} \cdot \vec{\mu}_m \quad \text{Eq. 2.30}$$

This transformation necessitates to align the axes  $\hat{x} \parallel \hat{X}$ ,  $\hat{y} \parallel \hat{Y}$ , and  $\hat{z} \parallel \hat{Z}$ . To do so, we could start performing a left hand rotation of  $(\frac{\pi}{2} - \eta)$  around the microscopic y-axis until align both z axes (making  $\hat{z} \parallel \hat{Z}$ ), and then making another negative rotation around  $\hat{z} \parallel \hat{Z}$  until align all the main axes together, in other words:

$$\begin{aligned} \vec{M}_{xyz \rightarrow XYZ} &= \vec{M}_{m \rightarrow M} \\ \eta' &= -\left(\frac{\pi}{2} - \eta\right) \\ \vec{M}_{m \rightarrow M} &= \vec{R}_z(-\rho) \cdot \vec{R}_y(\eta') = \begin{bmatrix} \cos(\rho) & \sin(\rho) & 0 \\ -\sin(\rho) & \cos(\rho) & 0 \\ 0 & 0 & 1 \end{bmatrix} \begin{bmatrix} \cos(\eta') & 0 & \sin(\eta') \\ 0 & 1 & 0 \\ -\sin(\eta') & 0 & \cos(\eta') \end{bmatrix} \quad \text{Eq. 2.31} \end{aligned}$$

So finally:

$$\vec{M}_{m \rightarrow M} = \begin{bmatrix} \cos(\rho)\cos(\eta') & \sin(\rho) & -\sin(\eta') \\ -\sin(\rho)\cos(\eta') & \cos(\rho) & -\sin(\rho)\sin(\eta') \\ -\sin(\eta') & 0 & \cos(\eta') \end{bmatrix} \quad \text{Eq. 2.32}$$

Applying this matrix transformation to the dipole's expressions of Eq. 2.20 leads to a final intensity that depends on  $\vec{E}_{exc}$ , but also importantly on key parameters defining of the fluorophores distribution: its mean-orientation  $(\rho, \eta)$  and its aperture  $\Psi$ .

$$I_{X,Y} \propto \int_{\phi=0}^{2\pi} \int_{\theta=-\Psi/2}^{\Psi/2} |\vec{E}_{exc} \cdot \vec{\mu}(\theta, \phi, \rho, \eta)|^2 \cdot J_{X,Y}(\vec{\mu}(\theta, \phi, \rho, \eta)) \cdot \sin(\theta) d\theta d\phi \quad \text{Eq. 2.33}$$

The principle of polarization resolved microscopy is to control the incident linear polarization direction  $\vec{E}_{exc}$  in order to access the parameters mean-orientation and order  $(\rho, \eta, \Psi)$ , characteristics of  $f_m(\theta, \phi)$ . We will first show below, that the problem can be reduced to the determination of  $(\rho, \Psi)$  in some specific situations. The methodology of this approach will then be described in Chapter 3.

### II.5.2.3 Reducing the geometry to a 2D problem

As we will see in the next chapter, in fluorescence polarized microscopy experiments, the excitation field is often polarized in the plane of the sample, which reduces the photo-selection to molecules that are mostly aligned to the plane of the sample. In addition, since biological structures of interest are often lying down in the 2D (X,Y-plane), and fluorophores such as phalloidin-AlexaFluor488 are bound aligned to the structure, we therefore expect also to obtain projected light mostly lying in the X,Y-plane. As a consequence, we will often assume in this work that the detected dipoles are lying in the (X,Y) sample plane. A discussion on the effect of 3D orientations will be detailed in Chapters 3 and 4, where the bias in the order parameter will be discussed. As a consequence when using  $\eta \rightarrow 0$ , the mean orientation of the fluorophore dipoles lies along one direction *orthogonal* to  $\hat{Z}$ , and represents its real orientation on the 2D sample (Figure 2.13 becomes the following Figure 2.16). In other words,  $\bar{\mu} \parallel \hat{z} \perp \hat{Z}$  :

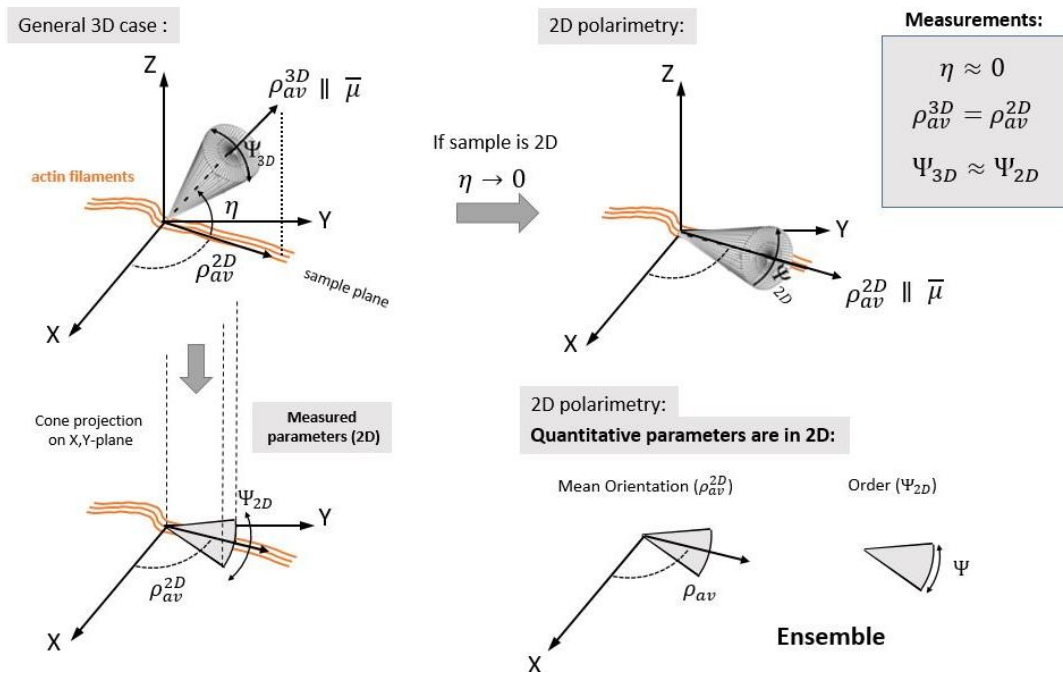


Figure 2.16 – Simplification of the 3D behavior when probing 2D structures. Note that the projection in 2D of the *mean orientation* in 3D is the same as a pure 2D scheme. However, the projection of the *angular aperture* might have an overestimated bias when  $\eta \neq 0$ . Such bias will be discussed in Chapter 3.

### II.5.3 The cone model at the single-molecule level

As we will describe in more details in Chapter 3, one could detect the fluorescence signal of single-molecules by sparsely labelling the sample or by fluorophore blinking, photoswitching, or photoactivation procedures. This is at the basis of the super-resolution imaging methods based on single molecule localization, such as Stochastic Optical Reconstruction Microscopy (STORM) and photo-activated localization microscopy (PALM) [38]. In what follows, we show that the equations derived above can also be adapted to single molecule situations, and used to measure orientational properties at the single fluorophore level.

At the single-molecule (SM) level, a fluorophore undergoes fast rotational movements which time scale  $\tau_{rot}$  is faster than the integration time of the recorded image. During the fluorescence

emission, a fluorophore can emit hundreds to thousands of photons per image, at a rate of about 10 kHz. Since the rotational diffusion time in cells and solutions is much faster than this rate, one could detect many different fluorophore orientations during the integration time: the fluorophores are considered homogeneously distributed in orientation within the local accessible or exploitable angular range. In such cases, we expect that the fluorophore has changed so many times its orientation that it exploits all *possible orientations* within a cone many times during each integration time of the camera. In such situation, the approximation of the cone model distribution  $f_c(\theta)$  also becomes reliable for single fluorophores. Indeed, at the single-fluorophore level, the fluorophore has explored its own orientation distribution function, that it is due to its own thermal fluctuations, which can be depicted by a cone whose aperture is the wobbling angle ( $\delta$ , see Figure 2.17) and whose mean orientation is the dipole mean orientation ( $\bar{\mu} = \rho$  in 2D). In other words, the equations shown above for an ensemble of fluorophores which time and space average lead to a cone of parameters ( $\rho_{av}, \Psi$ ), can be transposed to the case of a single molecule which time average lead to a cone ( $\rho, \delta$ ).

The specific optical setup required to measure such parameters from single molecules can differ from the one used in ensemble measurement, in particular when coupled to STORM/PALM single molecule detection scheme. This will be detailed in Chapter 3.

### Cone model at the single-molecule level

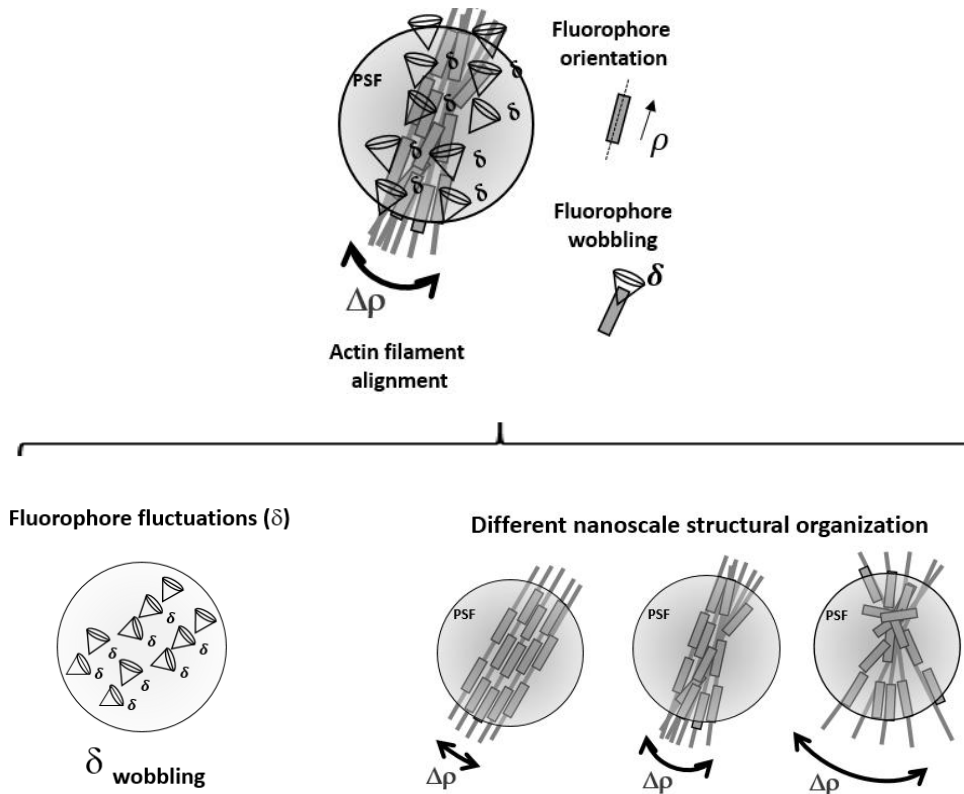


Figure 2.17 – Illustration of how the cone model will be used in Single-Molecule (SM) polarization microscopy methods. The mean orientation ( $\rho$ ) is the static mean orientation of isolated labels, meanwhile the cone aperture angle ( $\delta$ ) is the dynamic angular amplitude of the thermal fluctuations of each fluorophore (which we simplified by a wobbling angle). The nanoscale filament order can be retrieved by quantifying aperture  $\Delta\rho$  (the structural order) given by the many measured SM mean orientations along the filament, which is independent of the fluorophore thermal fluctuations at the single-molecule level.

### II.5.3.1 What can we learn from single molecule polarized approaches?

We emphasize here the difference in *notation* in both cone models, ensemble ( $\rho_{av}, \Psi$ ) and single-molecule ( $\rho, \delta$ ). As the main motivation of our experiments, we are generally interested to know how proteins or interest are organized, or their change in conformation. This is primarily given by the angle  $\rho$  and its distribution width:  $\Delta\rho$ , which we can name ‘biomolecular structural order’, see Figure 2.17. It is important to note that this parameter is not directly accessible via ensemble methods. As we can see from the equations above, the measured ensemble order parameter  $\Psi$  cannot directly tell  $\Delta\rho$ , because  $\delta$  is always summed up during the acquisition time and therefore appear as a intricated offset value. This means that care must be taken whenever interpreting  $\Psi$  from a polarized experiment in an ensemble, because it equally depends on the biomolecular structural order *and* on the fluorophore angular freedom accessible by their stochastic fluctuations around the mean (wobbling angle  $\delta$ ). Consequently, the outcome of the cone model might have different interpretation when evaluating the organization of the biomolecular structure of interest (SOI), depending if is an ensemble method or if it is a single-molecule method. In particular, the measurement of  $\Psi$  is not only biased by its offset value  $\delta$ , it is also bound to a lower value  $\delta$  that does not allow to probe high proteins disorders. Indeed variations around large  $\Psi$  values cannot be detected if since an apparent isotropy will be quickly reached if  $\delta$  is large.

On the other hand, if  $\delta$  is known and it is homogeneous within the probed volume, we can readily subtract its influence from the  $\Psi$  measurement. It is also possible to measure relative variations of  $\Psi$  within an ensemble, even though  $\delta$  is not known. This is the basis of all previously preformed polarization resolved studies, and has proven to be successful to evaluate the effect of drugs or mutations for instance [58, 62].

Another characteristics that single molecule measurements provide is that they allow to probe possible deviations from the ‘ensemble cone model’ described above. In particular, the distribution of fluorophores is assumed to be cylindrically symmetric, and its shape is assumed to be a cone. With the individual measurements of many fluorophores one at a time, it is possible to probe such assumptions.

## II.6. Experimental approaches for polarization resolved fluorescence microscopy

There are several ways one could perform polarization resolved fluorescence microscopy experiments. Here we just want to introduce the main basic concepts of how an objective lens can produce an *image* (i.e., how it provide a 2D map of localizations of fluorescence intensity) and how they can affect the polarization readout. In particular, there are two main ways one could provide light excitation to the sample: scanning a focus spot on the sample and to image the whole sample at once with a wide collimated laser beam.

In the first family scheme, one scans small focal volumes on the sample, delivering light and collecting fluorescence light point by point. The latter methods are classified as scanning point microscopy (e.g., confocal and spinning-disk microscopy). In conventional confocal microscopy (Figure 2.18a) the laser beam passes through the dichroic mirror and focused in a diffracted limited spot on the sample plane. Galvometric mirrors deflect the excitation beam in order to translate the focused spot on the sample plane. The emission of each translated spot is

collected by the objective lens and re-focused back into a pinhole detector (typically Avalanche Photodiodes (APDs) or photomultiplier tubes). The pinhole in the detection plane must be conjugated to the focused spots in the sample plane. Another way to retrieve confocal microscopy is by letting the system simultaneous confocal aligned for the excitation and for the detection (Figure 2.18b). This is done by placing the pinhole in the excitation path conjugating it to the sample plane and the image plane (detector). The advantage of this scheme is that it the excitation and the emission are intrinsically aligned. The drawback is that that probably less laser power is delivered into the sample due to addition to a pinhole in the excitation path. A very good compromise is when using parallel confocal (spinning disk microscopy). With the latter, many focused spots are imaged simultaneously on the sample plane like the case-b. In the case (Figure 2.18c), more power is delivered onto the sample, and faster acquisition time is obtained due to multiplexed scanning. The detection in the latter case is performed using a camera (full 2D chip of pixels), and not a pinhole detector (single pixel, or small array). The drawback compared to the previous techniques is that the z-sectioning is partially hampered, because it is possible that more out of focus light passes through many pinhole than by a single-one.

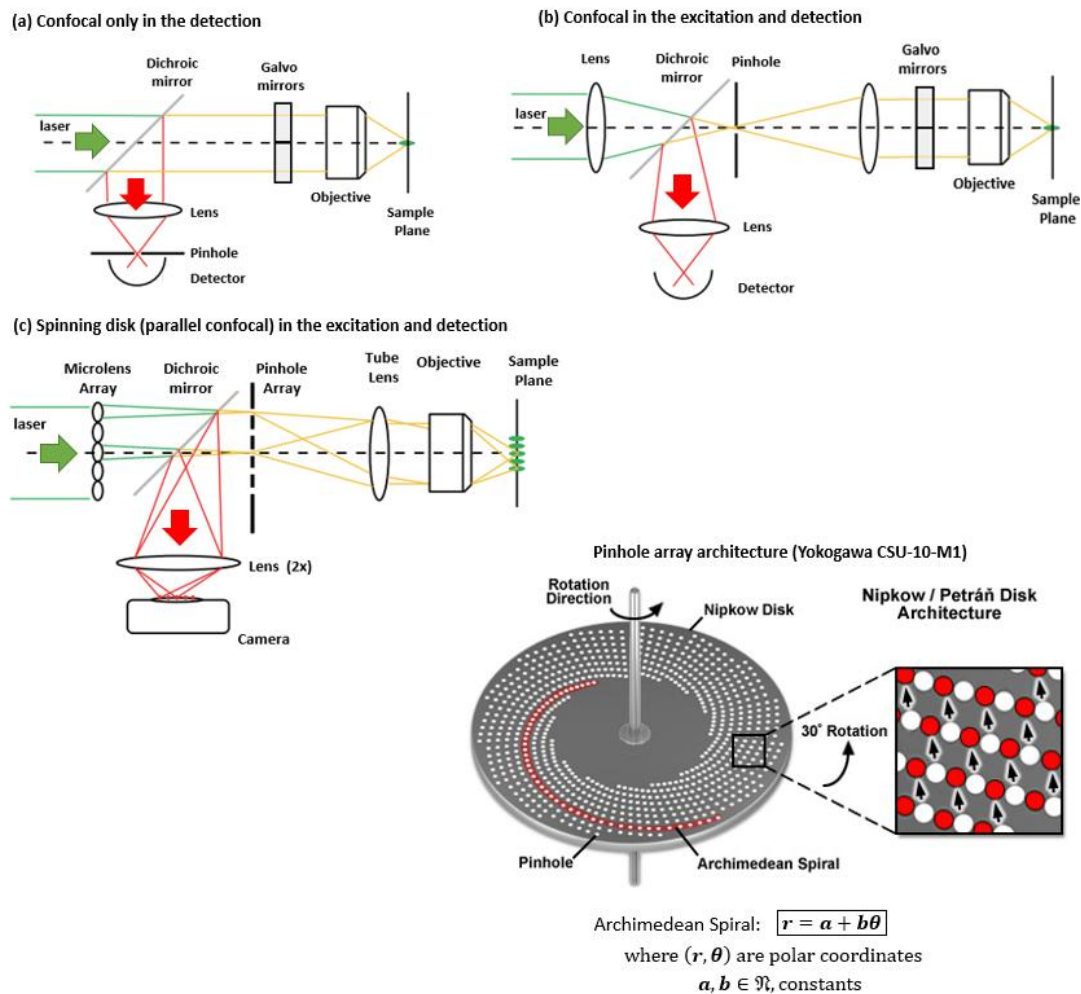


Figure 2.18 – Different point scanning microscopy approaches. (a) Conventional confocal microscopy, with a single pinhole only in the detection path. (b) The intrinsically aligned confocal microscopy, when the excitation and emission passes through the same pinhole. (c) Parallel confocal microscope is a variant of (b), with multiple pinholes. Figure adapted from [52, 64].

In the second family scheme, light is delivered in all points of the sample at the same time, and the objective lens could collect all the fluorescence light emitted from all points at the same time. In such cases, the methods are classified as wide-field, meaning the whole field of view (FoV) is illuminated at the same time. Examples include Epi (with normal incidence/collection), **h**ighly **i**nclined and **l**aminated **o**ptical sheet (HILO) microscopy and **t**otal **i**nternal **r**eflection **f**luorescence (TIRF) microscopy. Here, the difference between Epi, HILO and TIRF is how one inclines a collimated laser beam to excite the sample. The latter is performed thanks to different back focal plane (BFP) focus spot position (see Figure 2.19).

As we can see in Figure 2.19, the normal incidence (oftentimes also called Epi), is when the focus spot is formed at the center of the back focal plane (BFP) of the objective (see the dark blue beam). HILO configuration occurs when the focus spot at the BFP is not centered, but spatially displaced at the BFP so that the objective lens tilts the collimated beam on the sample (see the tilted blue beam). TIRF configuration occurs when the focus spot at the back focal plane is so displaced from the center that the angle of incidence is more inclined than the critical angle. Consequently, the beam is fully reflected back, and only a few nanometers of the sample receives the excitation of the evanescent light at the interface (light blue beam in Figure 2.19).

The reason why one would incline the beam is to minimize background by affording a sharper excitation volume sectioning. In the case of Epi, the laser beam excites the whole sample (all z-planes), meaning that out of focus z-planes also generates light that can be detected and yield background. In HILO, an optical sheet sections the sample in an inclined fashion. In principle, only a smaller portion of the sample is illuminated (in fact, it depends on how thick is the sample and how inclined is the beam). Last, if one incline the excitation beam more than the critical angle, TIR phenomenon occur at the surface glass of the sample. The generated evanescent wave can penetrate a few hundreds of nm deep above the surface. The intensity along Z decay exponentially, allowing a good optical sectioning for structures close to the sample plane.

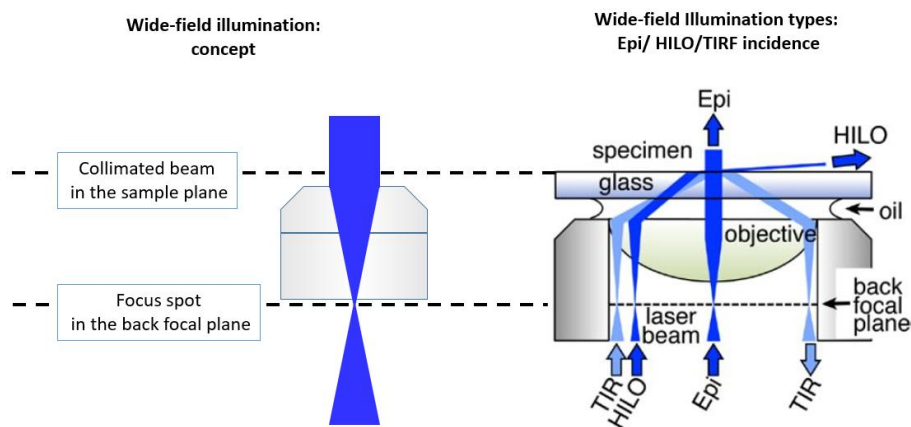


Figure 2.19 – The wide-field excitation configuration and variants. On the left, the concept on how to obtain a wide-field excitation: it requires to make a focus spot at the back focal plane (BFP) of the objective in order to retrieve a wide collimated beam on the sample plane. On the right, 3 possible variants of wide-field excitation (Epi or normal incidence, HILO, and TIRF). With Epi-configuration all Z –planes are illuminated, yielding a relative high background. The HILO and TIRF are schemes that attempt to minimize the background by improving the sectioning of the illumination. Figure adapted from [39].



### II.6.1 Different polarized microscopy geometries

As we saw, polarization resolved methods rely on the anisotropic behavior of fluorophore transition dipole moments (absorption and/or emission dipoles). Based on them, one could design the polarization resolved experiment to use. As we are going to see below, there are many ways one could design a polarimetry experiment (check reviews on [57, 65]): probing the excitation dipoles' orientation distribution, the emission dipole's orientation distribution, or both at the same time. Probing the excitation vs emission characteristics requires to add polarization sensitivity in the setup in the excitation vs emission path, respectively. One could retrieve orientation and order parameter readout by using polarized light when (1) exploring the absorption dipole moment of the fluorophore (e.g., modulating the excitation polarization, and detecting how the fluorescence *intensity* modulates accordingly); or when (2) investigating the emission dipole moment properties by analyzing how the emitted fluorescence is *polarized*.

Whenever we tune the polarization in the excitation path, for example by rotating a linear polarizer, we will probe how the fluorophore is sensitive to absorb the light on each given excitation polarization orientation. In other words, we are using the anisotropic properties of the absorption dipole moment to extract orientation and order information from the sample. This class of method is sometimes called linear dichroism. On the other hand, whenever we add a polarization analyzer in the emission path, we are measuring the fluorescence emission *polarization*. In other words, by projecting the emission field onto orthogonal analyzers, such as polarizers, polarizing beam splitter cubes, or Wollaston prism, we are exploiting the anisotropic properties of the emission dipole moment of the fluorophores. In the simplest cases, one could explore *only the absorption dipole moment* or *only the emission dipole moment properties* of the fluorophore independently. For that, we need to guarantee un-polarized detection (while polarization excitation orientation  $\alpha$  is modulated) or guarantee un-polarized excitation (while polarization emission orientation  $i$  is analyzed) during the integration time. Another one can consist of controlling both excitation and emission states of polarization: this approach is rather dedicated to the study of rotational dynamics or depolarization processes occurring in molecular isotropic environments, as displayed in Figure 2.10. In this work, we studied schemes where only excitation or emission polarizations were controlled, since what needs to be measured is an orientational steady state distribution. The general equations related to these methods, based on Eq. 2.33, are fairly simplified since only excitation or emission polarization matter. We considered that the explored angular aperture of fluorophores is  $(\Delta\theta = 2\theta_{max} = \Psi)$  for ensemble measurements and  $(\Delta\theta = 2\theta_{max} = \delta)$  for single molecules.

In the case of pure excitation polarization control, assuming an incident linear polarization rotating by an angle  $\alpha$  ( $\vec{E}_{exc}(\alpha)$ ), the intensity simplifies into:

unpolarized detection path:  $P_{em,2D} \rightarrow P_{em,2D}^{max} = constant$

$$I(\alpha) = C \cdot P_{em,2D}^{max} \int_0^{\theta_{max}} \int_0^{2\pi} |\vec{\mu}_{abs}(\theta', \phi') \cdot \vec{E}_{exc}(\alpha)|^2 \cdot f_c(\theta') \cdot \sin\theta' d\theta' d\phi' \quad \text{Eq. 2.34}$$

Here, the homogeneous detection (in all 2D orientations) makes the total detected intensity modulation only dependent on the excitation polarization orientation defined by alpha ( $\alpha$ ). In addition,  $\vec{\mu}_{abs}$  represent the mean fluorophore orientation of the whole set  $N_\mu$  of absorption dipoles in the focal volume integrated during the integration time, and  $f_c(\theta')$  is the

cone model distribution (the angular aperture) of all the instantaneous ( ' ) detected angles. C is a proportionality constant dependent on the fluorophore brightness and the system detection efficiency.

In the case of pure emission polarization control, assuming polarized detection along the direction  $\vec{u}_i$  the intensity simplifies into:

$$\text{unpolarized excitation: } P_{abs,2D} \rightarrow P_{abs}^{max} = \text{constant}$$

$$I_i(\vec{u}_i) \propto P_{abs,2D}^{max} \int_0^{\theta_{max}} \int_0^{2\pi} J_i((\theta', \phi')) \cdot f_c(\theta') \cdot \sin\theta' d\theta' d\phi' \quad \text{Eq. 2.35}$$

where  $J_i = \kappa_1 |\vec{\mu}_{em}(\theta', \phi') \cdot \vec{u}_i|^2 + \kappa_2 |\vec{\mu}_{em}(\theta', \phi') \cdot \vec{u}_j|^2 + \kappa_3 |\vec{\mu}_{em}(\theta', \phi') \cdot \vec{u}_z|^2$  and  $\vec{u}_j \perp \vec{u}_i$ .

Here, the homogeneous excitation (in both 2D orthogonal orientations) makes the detected intensity modulation only dependent on the polarized intensity in the analyzer unitary vector  $\vec{u}_i$  with orientation i. Here,  $\vec{\mu}_{em}$  represent the mean fluorophore emission dipole orientation of the whole set  $N_\mu$  of emission dipoles in the focal volume integrated during the integration time, and  $f_c(\theta')$  is the cone model (the angular distribution that includes all measured angular orientations). In addition,  $J_i$  is the detection factor that takes into account the polarization mixing (with the transverse orthogonal axis  $j$  in relation to  $i$ , and the axial component  $z$ ) due to the use of the objective lens. If  $i=X$ , then  $i_2=Y$ , and vice versa.

## Conclusion of Chapter 2

In this chapter, we introduced how light polarization can be used to retrieve biomolecular structural organization of biological filaments. We started by the simplest definitions of light, polarization and anisotropy. We defined fluorescence and how the anisotropic behavior of the absorption and the emission dipole can be used to track the fluorescent label alignment with the structure that they are bound to. We briefly introduced experimental variants of excitation and detection polarization control of light, and how these schemes could affect the equations of the detected intensities. In the next chapters, we will go into more experimental details of the setups used, which are based either on pure excitation polarization control, or detection polarization measurement.

## Chapter 3

# Polarized Fluorescence Microscopy Methods

### Introduction

Before giving the details of the setups we built, it is worth exploring the context in polarized fluorescence microscopy methods: we will briefly review the current state of the art of polarization resolved microscopy methods giving focus on one-photon excitation fluorescence.

### **Nonlinear (multi-photon) vs linear (one-photon) optical methods, a brief discussion about why we keep using fluorescent probes**

Nonlinear methods are very powerful approaches with superior image depth sectioning, and sometimes with label-free capabilities, meaning that they could directly retrieve biomolecular organization information without the usage of a label. The details of nonlinear methods are out of the scope of this thesis and will not be reviewed here. Nonetheless, it is worth to briefly discuss some pros and cons between linear and label-free nonlinear microscopy methods, justifying why we still use fluorescent labels and how we can still profit (a lot) from them.

Whenever probing structures within cells, nonlinear methods (*label-free*) generally rely on a scanning point excitation approach to trigger nonlinear light-matter interactions on the sample. The need of a scanning point is mostly because a high power is required to generate a nonlinear signal, since molecular cross-sections at the origin of nonlinearities are generally low. For this reason, single molecule nonlinear signals are extremely low and nonlinear microscopy generally implies ensemble averaging. The latter means that the generated nonlinear signal is created over an ensemble of nonlinear induced dipoles, created by many molecules (for harmonic generation processes or multiphoton fluorescence) or vibrational modes (for coherent Raman processes) present within the focal volume. [66]. Overall, *nonlinear label-free* microscopy methods are more often used to distinguish *classes of biomolecules* (RNA/DNAs, Lipids, Proteins in cells and of the extracellular matrix) in a context of cell-to-tissue level of organization [67, 68], due to their degree of selectivity and superior sectioning capability (required for tissues). Within cells, the selectivity of label-free methods is not very well adapted to address cell biology questions, in particular as compared to the methods that use fluorescent labels. This is because, within cells, the focal volume encompasses different, but similar chemical species, yielding a less specific signal *a priori* for label-free methods.

*Polarized* nonlinear microscopy methods (label-free or not) have already been developed successfully [69]. It has been shown in particular that the nonlinear nature of the interaction of light with molecules can provide refined information on molecular ensemble organization, a high order nonlinearity bringing in particular high order probing of orientational distributions of molecules.

On the linear regime side, fluorescence imaging is the most used method for biological imaging. Single-molecule sensitivity and subdiffraction resolution can be *easily achieved* by

various linear fluorescence methods (using fluorophores), even within complex environments like inside living cells [38, 42, 70]. Thanks to the last advances in super-resolution methods (dSTORM, PALM, etc) and fluorescent labelling technology, via novel biochemical linkers, fluorescent protein (FP), etc, fluorescent probes can distinguish biomolecules and their domains with higher degree of specificity.

A few different polarized microscopy methods have already been developed to probe biomolecular organization in fluorescence imaging, which have been applied to typical biomolecular systems: lipid and/or proteins in membrane models or in real membranes (using lipid probes and membrane proteins' GFP labelling), actin filaments (using phalloidin staining), microtubules and septins (using GFP labelling), DNA and amyloid fibers (using intercalants), etc [57, 59, 60]. In all cases, the biomolecular structure of interest (SOI) holds an ordered organization with an anisotropic behavior, i.e., along a preferential cylindrical axis that defines the main symmetry of the system (see Chapter 2).

In this chapter, we will start reviewing the polarization resolved *ensemble* techniques, we and later we will give focus on *single-molecule* approaches. In Section III.1, we review polarization resolved ensemble microscopy methods. There, we will end presenting the polar-spinning disk setup we built in this thesis. In Section III.2, we will discuss why it is interesting to develop and work with the single-molecule regime. In Section III.3 we will review how to obtain single-molecule fluorescence images, and we will present in Section III.4 one of the current polarization resolved single-molecule and super-resolution method based on polarization splitting: the polar-dSTORM approach. We will finish reviewing the state of the art in 4 polarized-split detection channels in Section III.5, which we used in our novel method: the 4polar-dSTORM. There, we will present our new setup, and discuss how this technique overcomes the limitations of the previously developed polar-dSTORM.

### III.1 Polarized fluorescence microscopy in ensemble molecular organizations

#### III.1.1 Fluorescence anisotropy microscopy – conventional ensemble emission dipole mapping

Conventional fluorescence anisotropy microscopy experiments generally use circularly polarized light to excite the sample (in order to provide an homogeneous photo-selection) and projects the emitted anisotropic fluorescence polarization onto 2 orthogonal analyzer channels (for example,  $I_{\parallel} = I_X$  and  $I_{\perp} = I_Y$ ), see Figure 3.1a below. One common way to perform fluorescence anisotropy microscopy is under wide field excitation, and the subsequent wide field emission field is split by polarizing optics such as polarizing splitting cubes or Wollaston prisms, projecting the light onto the camera(s) chip (Eq 2.35) [52]. In such configuration, the anisotropy measured writes:

$$r = \frac{I_{\parallel} - I_{\perp}}{I_T} \xrightarrow{\text{Anisotropic sample}} A = \frac{I_{\parallel} - I_{\perp}}{I_T} \xrightarrow{\text{homogeneous excitation}} A = \frac{I_{\parallel} - I_{\perp}}{I_{\parallel} + I_{\perp}} \quad \text{Eq. 3.1}$$

We note that this anisotropy factor for ordered media in microscopy is written slightly differently from the case of fluorescence anisotropy experiments in isotropic media (e.g., fluorescent solution) (Eq. 2.14). This is because what it is probed now (ordered sample) is within a 2D plane, hence the total intensity is defined as  $I_T = I_X + I_Y = I_{\parallel} + I_{\perp}$  (with  $\parallel$  denoting a

direction parallel to the excitation polarization while  $\perp$  a direction perpendicular to it). In solution, where the excitation and emission directions explore all 3D axes, we have access to all directions of polarizations and therefore  $I_T = I_X + I_Y + I_Z = I_{\parallel} + 2I_{\perp}$ . Hence, the total fluorescence term ( $I_T$ ) in the denominator of Eq. 2.14 and Eq. 3.1 differ, in a measured quantity called (depending on the publication) ‘fluorescence anisotropy’ or ‘fluorescence anisotropy factor’ or ‘fluorescence polarization factor’. By inserting the cone model introduced in Chapter 2 in the calculation of the corresponding intensities, the anisotropy factor (called A in Figure 3.1) described by Eq.3.1 can be calculated and used to retrieve information on the molecular organization at each measured pixel. An illustration of the dependence of this anisotropy factor with respect to the ensemble averaged orientation ( $\rho_{av}$ ) and molecular order ( $\Psi$ ) parameters is given in Figure 3.1b.

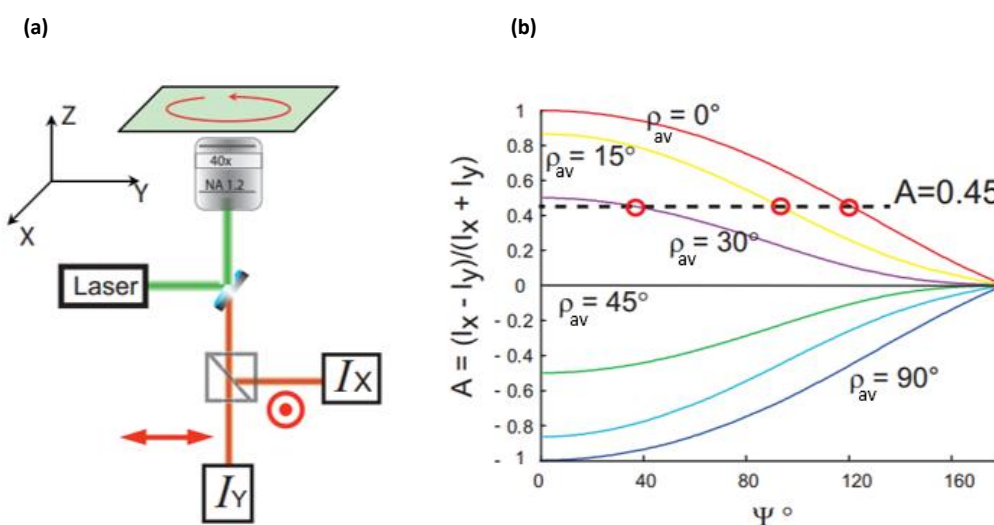


Figure 3.1 – Conventional fluorescence anisotropy microscopy setup scheme (a) and the anisotropy factor dependence to the molecular order parameters (b). On the left, the laser with circular polarized light excites the sample (green beam) and the emission (red beam) is split onto 2 orthogonal detectors  $I_x$  and  $I_y$ . On the right side, the anisotropy factor A is seen to depend on two parameters  $A=A(\rho_{av}, \Psi)$ . Note that for low  $\Psi$  values (higher order) values it is easier to distinguish the  $\rho_{av}$  values, meanwhile whenever fully isotropically organized (when  $\Psi$  is close to  $180^\circ$ ), the curves of different  $\rho_{av}$  yields similar values of anisotropy, close to  $A=0$ . Besides, note that for  $\rho_{av}=45^\circ$  (black horizontal line), the anisotropy value is the same independently of the value of the order  $\Psi$ , making it impossible to retrieve order parameter from structures aligned at  $45^\circ$ . Figure adapted from [52].

As we are going to explain next, this technique suffers from some limitations when it comes to determine molecular order information in an image. For example, for a given  $A=A'$  constant value, there are multiple possible solutions (combinations of  $\rho_{av}$  and  $\Psi$ ) that yields the same  $A=A'$  value (see the case of  $A=0.45$  dashed line in Figure 3.1). This means that, we need to know some a priori information of the sample to extract the order information  $\Psi$  from the system. For example, if we know the mean orientation  $\rho_{av}$  of the labels at certain region of interest (ROI), then we can use this constant orientation value to probe the order parameter ( $\Psi$ ) using Eq. 3.1. Thanks to that, such techniques have been used to probe the molecular organization of samples with known mean orientation, like lipids in membranes of red blood

cells [54], lipids in giant unilamellar vesicles [63], photosynthetic complexes in cell membranes [71], and cytoskeletal filaments [72]. Another limitation is that when using the quantity  $A$  to retrieve information on the mean orientation of an ensemble (supposing for instance  $\Psi$  known),  $\rho_{av}$  can only be determined with an arithmetic modulo  $\pi/2$ , which means that there is an ambiguous readout on supplementary angles ( $10^\circ$  and  $170^\circ$ ,  $20^\circ$  and  $160^\circ$ , ...). In other words, if one wants to retrieve orientational statistics along one given mean direction (e.g.:  $\rho_{av}=15^\circ$ ), supplementary angular values (e.g.:  $165^\circ$ ) give the same anisotropy value. Therefore, such techniques need to assume some extra hypothesis (for instance supposing that the orientation does never deviate much from the visual mean orientation of the structure). Besides, particularly at  $45^\circ$  or  $135^\circ$  angles, none order information can be retrieved (e.g.  $\Psi$  cannot be estimated) because  $I_{\parallel} = I_{\perp} \rightarrow A = 0$ . Other limitations include that fluorescence anisotropy experiments at the ensemble level can be biased by depolarization processes, such as fluorescence resonance energy transfer (homo-FRET) and fast re-orientation dynamics, as well as biases due to off-planes orientations of the fluorophores (since the information is projected in 2D).

### III.1.2 Linear dichroism microscopy

#### III.1.2.1 The conventional ensemble absorption dipole mapping

Linear dichroism (LD) techniques are less prone to depolarization bias, because they are based only on the absorption dipole photo-selection property of the fluorophores, and not on both absorption and emission processes. Here, the excitation beam is linearly polarized with a varied direction in the sample plane, and the fluorescence signal is, in the simplest case, detected without any specific polarization direction (see Eq.2.34). Consequently, LD microscopy techniques are more suitable to probe orientation and order behavior in structures where the biomolecular assembly is not a priori known [57, 58]. Nevertheless, in the simplest excitation schemes, when only 2 orthogonal polarization excitation angles are provided, there is still some ambiguity in between supplementary angles of the detected signal (e.g.,  $45^\circ$  and  $135^\circ$ ) [52]. Consequently, with only 2 polarization excitation angles, some a priori knowledge of the sample orientation is still needed for unambiguous parameter retrieval in the simplest cases. To circumvent such ambiguity, more than 2 excitation polarization angles have to be used. Next, we will detail the two linear dichroism methods developed by our lab that significantly improved the capacity of LD microscopy [58, 73]. Particularly, in this PhD thesis, we duplicated the most recent LD method developed by a former student Xiao WANG [73].

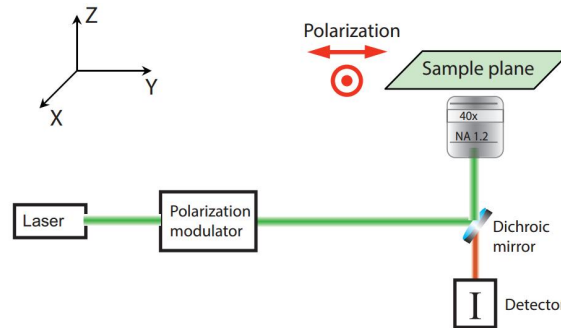


Figure 3.2 – Conventional linear dichroism setup scheme. Here, the excitation beam (in green) has its polarization modulated before reaching the sample. For each incident linear polarization (we show only two with the orthogonal red arrows), the average fluorescence intensity ( $I$ ) is detected without any polarization optics in the detection path (fluorescent beam in red). Figure taken from [52].

### III.1.2.2 Angular resolved linear dichroism (confocal) microscopy

It is possible to modulate the incident polarization in *many* different known angles and retrieve back the intensity modulation dependent on such controlled excitation. In the past years there has been a significant effort in this sense, particularly by our group, to improve parameter retrieval capacity of linear dichroism microscopy techniques by different forms (linear and nonlinear excitation microscopy methods)[58, 69, 73-75]. The modulation of incident excitation in many polarization orientations applied to microscopy was firstly developed in our lab, in 2009 by Alicja GASECKA et al [69]. Her setup was a two-photon excitation polarization resolved microscopy. The first linear microscopy with polarization excitation modulation was done by DeMay, B.S. et al, two years later, using 4 polarization angles in the excitation path [74]. However, in their work, they were more vulnerable to photobleaching artifacts because they chose a trans-illumination wide-field scheme to be less sensitive to polarization distortions caused by the dichroic mirrors. The first linear angle resolved point scanning method (confocal) microscopy setup that systematically took into account the polarization distortions in a robust manner was done by our group, in 2013, by Alla KRESS [58] and later by Xiao WANG [73], see Figure 3.3 below.

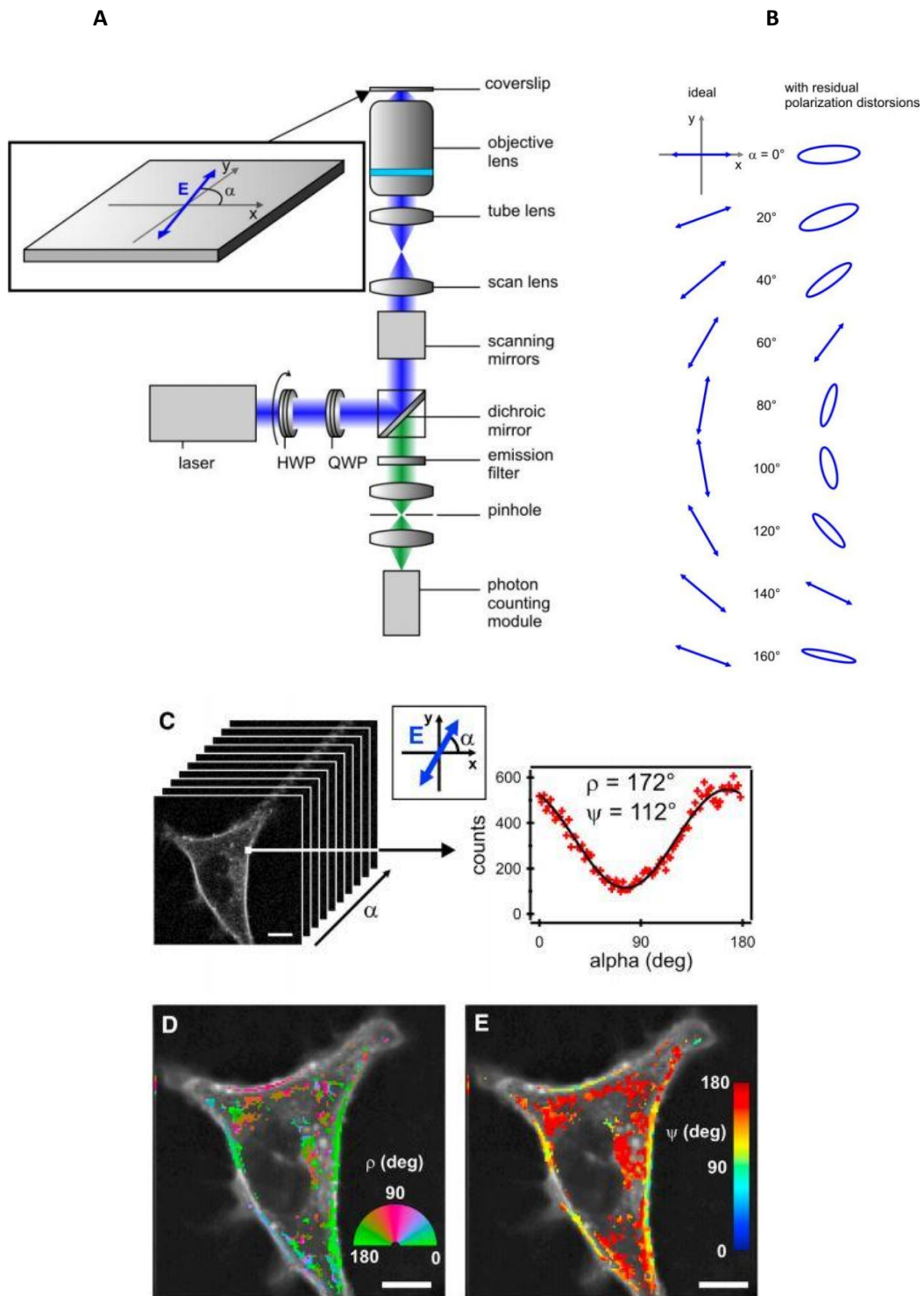


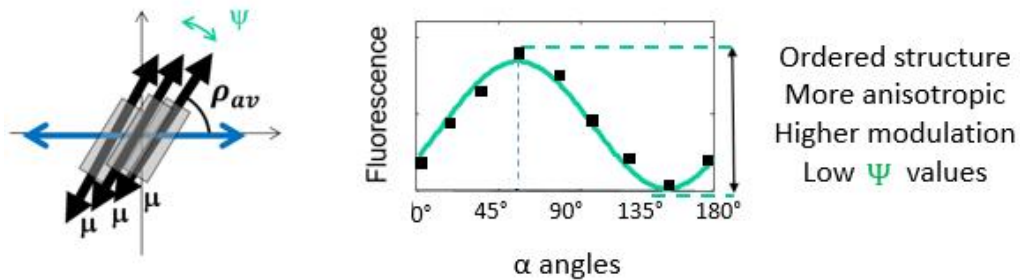
Figure 3.3 – Angle Resolved Linear Dichroism (ARLD) microscopy. (A) ARLD setup scheme. Note that QWP in the excitation path was added to compensate the polarization distortions mainly caused by the dichroic mirrors. (B) linear polarization rotation and their residual polarization distortions on each angle. (C) Illustration of the concept: a stack of images with different orientation excitation orientation (alpha angle) is collected. On each pixel along the polar stack, the intensity modulates proportionally to how the labels are oriented. (D) and (E) the orientation ( $\rho_{av}$ ) map and the order ( $\Psi$ ) map overlaid with the intensity profile respectively. Figure adapted from [58].



Here, a stack of images is collected under different linear polarization excitation orientations (alpha angles in Figure 3.3). For each incident linear polarization, the emitted fluorescence is collected without any polarization optics in the detection path. For example, by using a motorized half wave plate (HWP) in the excitation path, one could modulate the orientation of the incident linear polarization in an automatic fashion. Since each image frame of the stack represents the fluorescence signal recorded for a single linear polarization excitation angle ( $\alpha$ ), the anisotropic modulation information can be depicted pixel-by-pixel along the stack in a post-processing step. Such modulation curve contains information of both mean orientation ( $\rho_{av}$ ) and order parameter ( $\Psi$ ) per pixel. Indeed the pure anisotropy factor  $A$  measurement mentioned above was similar to having access to only 2 angles  $\alpha$  of this modulation, while here we add more information and hence we can access two parameters unambiguously. Hence, using such data we can use the cone model to extract both parameters (Chapter 2).

To get a qualitative idea of how the mean orientation and order parameter are encoded in such fluorescence modulation (Figure 3.3), we have to think on the underlying generation of this modulation, which relates how fluorophores interact with the incoming linear polarization (Figure 3.4). The maximum of the modulation is related to the mean orientation of the fluorophores within the PSF ( $\rho_{av}$ ), since this corresponds to the direction of the incident polarization that provides the maximum signal. The amplitude of the modulation is related to how anisotropic (ordered) the fluorophores are distributed within that PSF (see Figure 3.4). In particular, the more anisotropic (ordered) the fluorophore's distribution is, the higher will be the amplitude modulation and vice-versa. On the other hand, less ordered regions would yield a flatter polarization modulation, because the fluorophores are more isotropically distributed (see Figure 3.4). This supposes of course that the distribution of fluorophore's orientations is lying in the sample plane. This will be further discussed in Chapters 4 and 5.

**(a) More ordered structures**



**(b) More disordered structure**

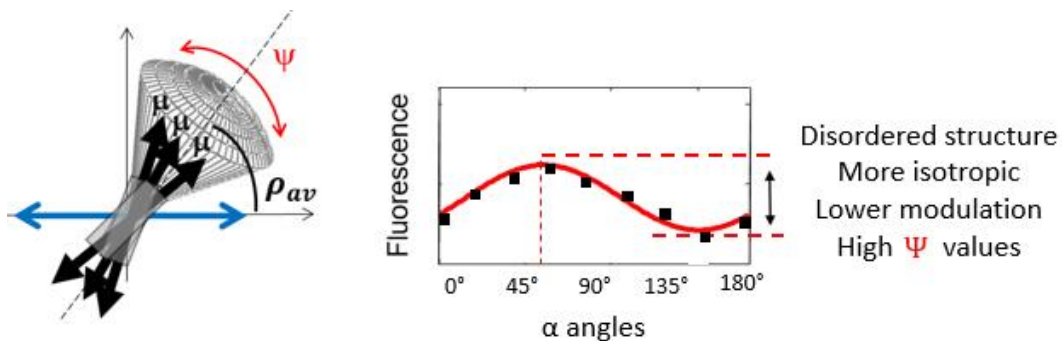


Figure 3.4 – Fluorescence modulation dependence on the orientational distribution of the fluorophore dipoles ( $\mu$ ) and its relation with the polarization resolved parameters ( $\rho_{av}$ ,  $\Psi$ ). On the left, hypothetical illustrations of the possible orientations dipoles measured in an arbitrary focal spot. In linear dichroism experiments (Figure 3.3) it is used a sequence of linear polarized excitation angles (here, alpha angles are in the abscissa of the plots). For each excitation angle, the total fluorescence intensity is detected, so that an image is made for each alpha angle. In the center, a plot of fluorescence modulation vs alpha excitation angles that is determined per pixel along the polar-stack (Figure 3.3 C). Note that, the maximum of the modulation coincides with the mean orientation of the fluorophores, meanwhile the amplitude of the modulation depends on how aligned (ordered) the fluorophore dipoles were organized on each pixel. Here, case (a) represents a focal volume whose labels have a higher order, and (b) higher disorder. The higher the amplitude of the modulation, the higher the probed anisotropy, therefore the higher the order, and *vice-versa*. Figure adapted from [76].

To retrieve mean orientation ( $\rho_{av}$ ) and order ( $\Psi$ ) from the measured modulation, we will have to use Eq.2.33 based on the cone model describing the fluorophore's angular distribution. Because we are working in the linear regime of excitation, the detected fluorescence intensity is proportional to the square of the incident electric field  $\vec{E}_{exc}(\alpha)$ , which linear incident polarization is set along the angle  $\alpha$  (with respect to X, horizontal in the sample plane). As seen in Eq. 2.33, which we recall here, the fluorescence intensity is proportional to the absorption probability of the molecular ensemble of orientations measured within the diffraction limit of the focal spot and within the integration time of the detector:

$$I_{X,Y}(\alpha) \propto \int_{\phi=0}^{2\pi} \int_{\theta=-\frac{\Psi}{2}}^{\frac{\Psi}{2}} |\vec{E}_{exc}(\alpha) \cdot \vec{\mu}(\theta, \phi, \rho, \eta)|^2 \cdot J_{X,Y}(\vec{\mu}(\theta, \phi, \rho, \eta)) \cdot \sin(\theta) d\theta d\phi \quad \text{Eq. 3.2}$$

Where (X,Y) denotes the sample plane axes,  $\vec{\mu}$  the fluorophore's absorption dipole, and  $J_{X,Y}$  the expression related to the emission probability of the fluorophores (see Chapter 2). ( $\rho, \eta$ ) denotes the 3D orientation of the cone distribution (Figure 2.13).

In the present experiment, the detection is not polarized, therefore the measured intensity is:

$$I(\alpha) = I_X(\alpha) + I_Y(\alpha) \quad \text{Eq. 3.3}$$

Note that we suppose here that there is no contribution from the longitudinal component of the incident electric field along Z ( $\vec{E}_Z(\alpha)$ ) in the focused incident beam: this effect has been studied in [77] and this component is seen to be negligible at the NA used (below 1.2), for distributions lying in the sample plane (which is the framework of this work). It appears therefore, from Eqs. 3.2 and 3.4, that  $I(\alpha)$  is a linear combination of the components  $\vec{E}_X(\alpha)^2$  and  $\vec{E}_Y(\alpha)^2$ . These components are respectively proportional to  $\cos^2(\alpha)$  and  $\sin^2(\alpha)$ , which can be linearized into  $(1 + \cos(2\alpha))$  and  $(1 + \sin(2\alpha))$  forms. Thus we must truncate the Fourier series for the terms k=0, 2:

$$I(\alpha) \propto A_0 + [A_2 \cos(2\alpha) + B_2 \sin(2\alpha)] \quad \text{Eq. 3.4}$$

It is visible that  $A_0$  represents the total intensity at a given pixel, and the coefficients of  $A_2$ ,  $B_2$  encode the orientation and order information, since they represent the amplitude contrast and offset of the intensity modulation  $I(\alpha)$ . Importantly, these coefficients are functions of ( $\rho_{av}, \Psi, \eta$ ), which characterize the complete 3D information of the molecular

distribution in 3D (mean orientation  $\rho_{av}$ , cone aperture/molecular order  $\Psi$ , off plane tilt angle  $\eta$ ). These parameters can be independently obtained by inverting the Fourier transform:

$$\begin{aligned}
 A_0(\rho_{av}, \Psi, \eta) &= \frac{1}{\pi} \sum_{k=1}^N I(\alpha_k) \\
 A_2(\rho_{av}, \Psi, \eta) &= \frac{2}{A_0 \pi} I(\alpha_k) \cos(2\alpha_k) \\
 B_2(\rho_{av}, \Psi, \eta) &= \frac{2}{A_0 \pi} \sum_{k=1}^N I(\alpha_k) \cdot \sin(2\alpha_k)
 \end{aligned} \tag{Eq. 3.5}$$

Where  $k = (1 \dots N)$  represents the index of the incoming polarization angle  $\alpha_k$ , tuned in  $N$  steps from  $0^\circ$  to  $180^\circ$ . In what follows we assume a distribution lying in the sample plane, therefore  $\eta \rightarrow 0$ . The consequences of the deviations from this assumption were briefly discussed in the section III.2.2 below, but a more detailed discussion will be done in Chapter 5. In such conditions, two unknown parameters ( $\rho_{av}, \Psi$ ) have to be determined from the two measured normalized parameters,  $A_2/A_0$  and  $B_2/A_0$ . Using the cone model as in Eq. 3.2, an analytical expression relating ( $A_2/A_0, B_2/A_0$ ) and the ( $\rho_{av}, \Psi$ ) parameters can even be expressed:

$$\begin{aligned}
 \frac{\sin \Psi}{\Psi} &= \frac{3}{2} \sqrt{\left(\frac{A_2}{A_0}\right)^2 + \left(\frac{B_2}{A_0}\right)^2} \\
 \rho_{av} &= \tan^{-1}\left(\frac{B_2}{A_2}\right)
 \end{aligned} \tag{Eq. 3.6}$$

In situations where polarization distortions are present in the incident field, the intensity equation takes a more complex form and it is necessary to use fitting or to numerically invert the problem, in order to retrieve ( $\rho_{av}, \Psi$ ) from the intensity modulation. In the results section, we use a method that relies on minimization with respect to a look-up table relating ( $A_2/A_0, B_2/A_0$ ) to ( $\rho_{av}, \Psi$ ), as developed in previous works [58, 73].

In addition, it is worth to briefly discuss the advantages when using confocal microscopy for polarimetry, and not wide-field, and they are the following. Confocal imaging has a better sectioning, therefore reduced background. Lower background improves not only image quality, but also the quality of the retrieval of orientation and order parameters, since less artifacts are introduced in the measured signals. Moreover, focused scanned illumination allows to reduce the incident power used on the useful field of view, reducing damage and bleaching issues. On the other hand, the drawback of using conventional confocal excitation is the need to use a single focal spot to scan the whole field of view (FoV), so that global acquisition time is dependent on the scanning parameters. The bigger the FoV and the smaller the pixel size, the longer is the global acquisition time, thus the higher the risks to bleach the sample and to face motion and dynamics issues and artifacts. Single spot scanning imposes to sequentially rotate

the incident polarization after each image is recorded, which is generally done using a rotation motor in which a half wave plate (HWP) is inserted [58]. Typical times to make one polar-confocal stack with  $N=18$  angles (separated by  $10^\circ$  each), scanning an ROI of  $100\mu\text{m} \times 100\mu\text{m}$  with pixel size of  $100\text{nm}$ , with integration time of  $50\mu\text{s}$  is of the order of a few minutes. Theoretically it is  $1.5\text{min}$ , but it is a bit more ( $\approx 2\text{min}$  almost) because of instrument communication delays. If one wishes to go for higher precision, for example, with finer angular steps (e.g., alpha angle on every  $5^\circ$  step) the motorized HWP, the global acquisition time of the polar-stack increases proportionally. Since the sample needs to be static along all the polar-stack images to guarantee the overlap of the same pixels, we see that this technique is mainly applicable to static fixed samples. For this reason, solutions have been developed based on faster scanning, by using a spinning-disk [52, 73] as described below.

### **III.1.3 Fast angular resolved linear dichroism (spinning disk) microscopy**

As commented in Chapter 2, spinning disk is a parallel (multiplexed) confocal method that allows the detection of a whole field of view using a camera (as opposed to a single detector such as photomultiplier (PMT) or avalanche photodiode (APD) in confocal microscopy), and keeps a good sectioning due to the use of a pinhole array. The advantages of using the spinning disk is higher temporal resolution in the acquisition, which is particularly more attractive for live-cell experiments [52]. To perform polarimetry using a spinning-disk, we also have to rotate faster the incident polarization; otherwise we would be limited by the speed of the motorized HWP. For this, an electro-optical modulator (EOM) is combined with a quarter-wave plate (QWP) (see Figure 3.5) [73] and synchronized with the camera. Using this combination, we can create a linear polarized light that can rotate as fast as the capacity of the EOM, which can reach MHz modulation rates. Therefore, our temporal resolution would be in principle limited by the camera acquisition time only, which is typically 10 to hundreds of ms times 10-18 polarization angles (in total about a second).

Our polar-spinning disk setup (see Figure 3.5) is described as follows. We used an inverted microscope (Nikon, Eclipse Ti-U) in epifluorescence mode. The spinning-disk unit (Yokogawa, CSU-X1 FW-06P-01) is connected to the left side-port of the microscope, so that the excitation and the emission beam pass through the same port.

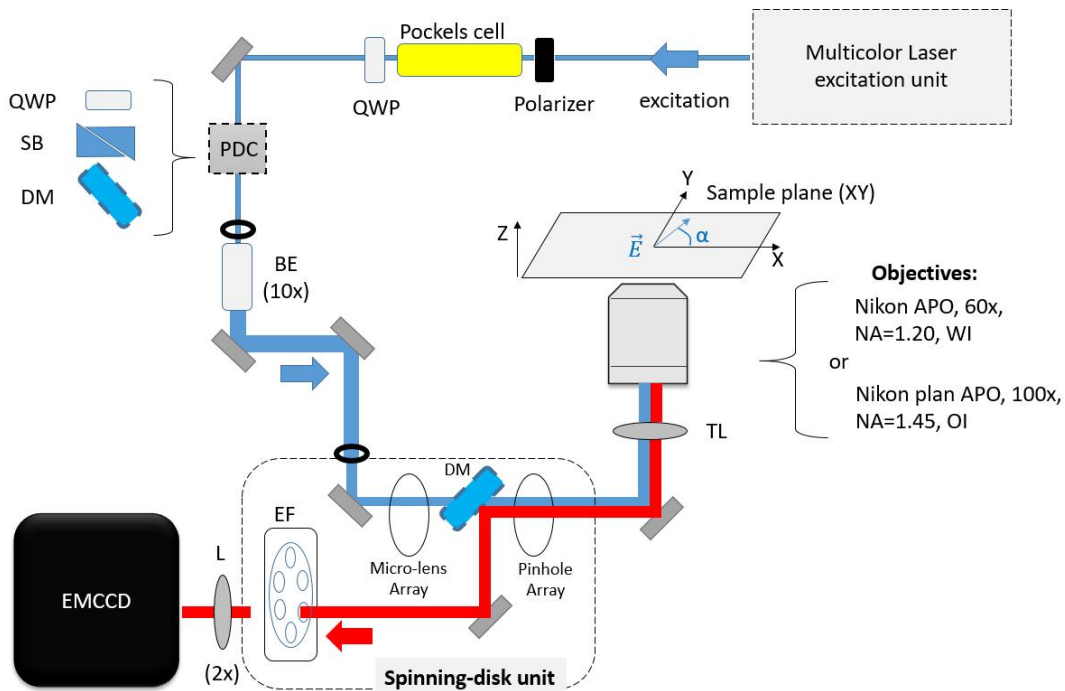


Figure 3.5 – The polar-spinning disk setup for fast ensemble polarimetry. PDC, polarization distortion compensator; QWP, quarter wave-plate; SB, Soleil Babinet compensator; DM, dichroic mirror (here, a multiband 405/488/561/640 nm dichroic mirror is used); BE, beam expander; EF, emission filter wheel (containing filters appropriate for 415/525/580/670nm emission wavelengths); TL, tube lens; L, lens; EMCCD, electron multiplier charged coupled device camera. The multicolor laser excitation unit is described in Figure 3.6.

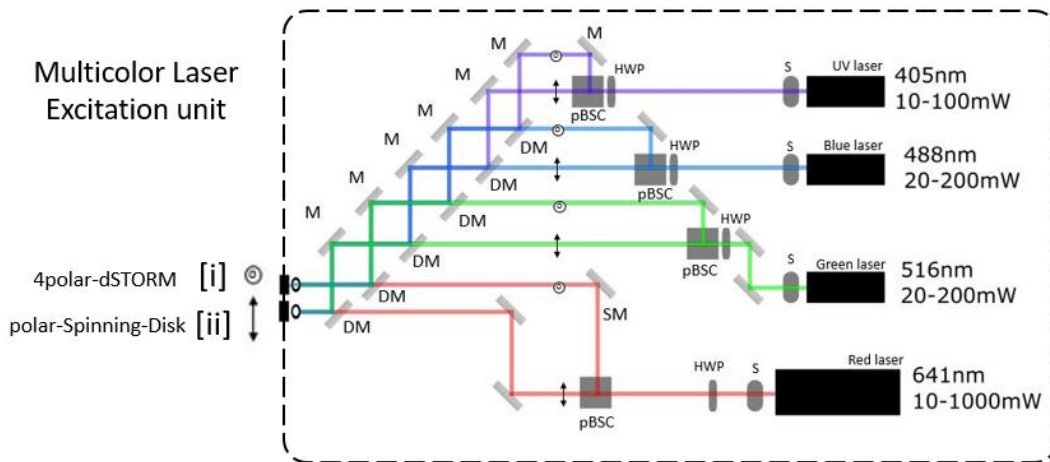


Figure 3.6 – The multicolor CW laser excitation unit. The 405nm (Coherent 405 OBIS, max power: 100mW), 488nm (Coherent Sapphire, max power: 200mW), 561nm (Coherent Sapphire, max power: 200mW), 641nm (Coherent Genesis-MX, max power 1W). For each beam, we added a power control unit consisting in an achromatic half-wave plate HWP (Thorlabs: AHWP05M-600) in combination with a polarizing beam-splitter cube (Thorlabs: PBS101, 10mm size). Particularly, for the UV laser, the HWP is adapted to the wavelength (Thorlabs: WPMH05M). As we see in Figure3.6, each pBSC splits the beam in two beam lines, and each of them is meant for different polarization controlled experiment (ensemble or single-molecule setup). By rotating a HWP, we could tune the amount of power to be delivered into the ensemble setup (polar-spinning disk) and into the single-molecule setup (4polar-dSTORM, see next sections). The lasers 405nm, 561nm, 641nm lasers we used mainly for tests on different dyes and co-stained cell samples.

The excitation beam used for polarimetry is generated by continuous-wave lasers for which different wavelengths are available (see multicolor laser excitation unit described in the Figure 3.6). In our work we used mainly the 488nm wavelength provided by a Coherent Sapphire 488nm (typical output power range 20-200mW). After adjusting the laser output power, the beam is filtered by a linear polarizer before entering in an electro optical modulator, EOM (transverse type Pockels Cell, 334-NP, Quantum Technology, Inc). The latter consists in potassium dideuterium phosphate (KDP) uniaxial crystals, for which the extraordinary refractive index depends on the voltage applied (in our Pockels cell, a phase shift of  $\pi$  between the ordinary and extraordinary axes is obtained for a typical range of input voltage between 300V and 500V, depending on the wavelength).

The Pockels Cell (Figure 3.5) is a voltage dependent wave retarder. Hence, it creates a linear voltage dependent phase shift of the transverse components of the light, therefore changing the light polarization in a controlled manner. Importantly, proper Pockels cell alignment in relation to the incoming light polarization is needed. The Pockels cell main axes (i.e., extraordinary or ordinary axes) must be oriented  $45^\circ$  (or  $135^\circ$ ) in relation to the incoming horizontal linear polarization of the light. On the exit of the Pockels cell, the voltage dependent phase shift will generate a variable elliptically polarized beam. To finally get a rotated linear polarization, a quarter wave plate (Thorlabs AQWP05M-600) must be placed right behind the exit of the Pockels cell, oriented parallel to the input horizontal polarization. The Pockels cell combined with a QWP can reach linear polarization rotation of in a timescale of microseconds [52, 73].

Before the excitation beam reaches the sample, it passes through some optical components that potentially distort the (linear) polarization state of the light. For example, the dichroic mirror (DM) inside the spinning disk unit (see Figure 3.5 and Figure 3.7) is a major perturbation for the incoming polarization. Thus, we typically add in the excitation path a polarization distortion compensator (PDC) unit (see Figure 3.5). The PDC unit can be another QWP (Thorlabs: WPQ05M-488 chromatic QWP [58]), or a Soleil Babinet Compensator, SB [73]. The QWP has been used in the past because the generated distortions were of the order of  $\pi/2$  in phase shift between orthogonal polarization components. The SB is more appropriate for a variable phase shift, however it is complex to align and re-adjust for multiple wavelengths. To circumvent this problem, we used rather a compensating DM, e.g. the same DM that is used inside the spinning disk unit, but with flipped transmission axis configuration. This scheme exchanges the roles of s and p polarizations in the propagation and thus naturally compensates the polarization distortions occurring for all wavelengths used. After the PDC, the laser passes through a beam expander (10x magnification) and through a diaphragm (with 1cm diameter) to spatially filter the beam before entering in the confocal spinning-disk unit (Yokogawa CSU-X1-FW06-01).

The Yokogawa CSU-X1 contains two coaxially aligned and synchronous rotating disk arrays (microlens disk and the Nipkow disk of pinholes). Each microlens focuses the light into its respective pinhole array. The pinhole array is conjugated with the sample plane, and with the EMCCD camera, generating thousands of simultaneous focused spots on the specimen, and on the camera chip (Andor Ixon-Ultra 888, 1024x1024 pixels, 13 $\mu$ m pixel size). Because the pinholes are spatially configured as an Archimedean spiral, the radial position of a single spot moves

proportionally with the rotated angle of the disk, sweeping thousands focused spots in the FoV in a spiral manner.

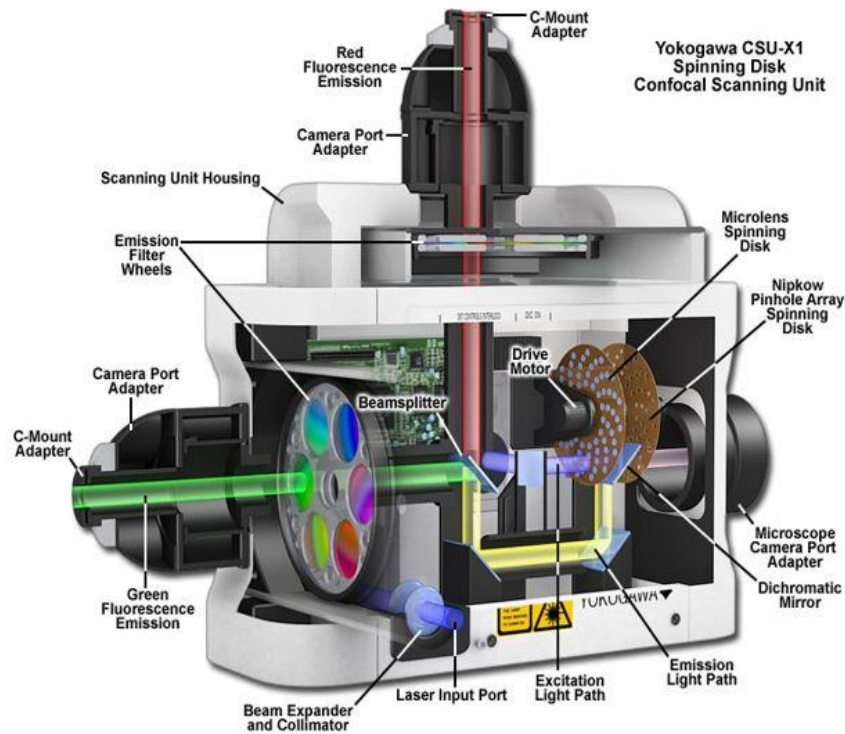


Figure 3.7 – The Yokogawa confocal spinning disk unit CSU-X1. In particular, the collimating and shaping optics of our Yokogawa spinning-disk were bypassed to avoid polarization distortions in the excitation path. Besides, the camera port for the “red” emission is closed, thus only the “green” fluorescence path is used in our setup. Figure taken from [64].

The Yokogawa CSU-X1 spinning-disk is the high-speed model of the CSU series. The number of microlenses in the first disk is the same of the number of pinholes in the Nipkow disk. The CSU-X1 Nipkow disk has approximately 20000 pinholes of 50 $\mu$ m diameter with 250 $\mu$ m spacing among each other. A simple spinning disk rotation of 30° is enough to sweep a full frame with the pinhole array pattern. A full 360° disk rotation sweeps 12 frames of the pinhole pattern. The maximum disk rotation speed of CSU-X1 is about 10000 rpm, yielding a theoretical frame rate of 2000 fps. In practice, we use a rotation speed of about 1800 rpm.

In between the two disk arrays, there is a dichroic mirror, DM (Semrock Di01-T405/488/568/647-13x15x0.5mm) that will transmit the excitation (typically 488nm) and reflect the emission beam (typically 520nm). The latter passes through an emission filter wheel (EF), and a focusing lens (L, 2x magnification) on the EMCCD.

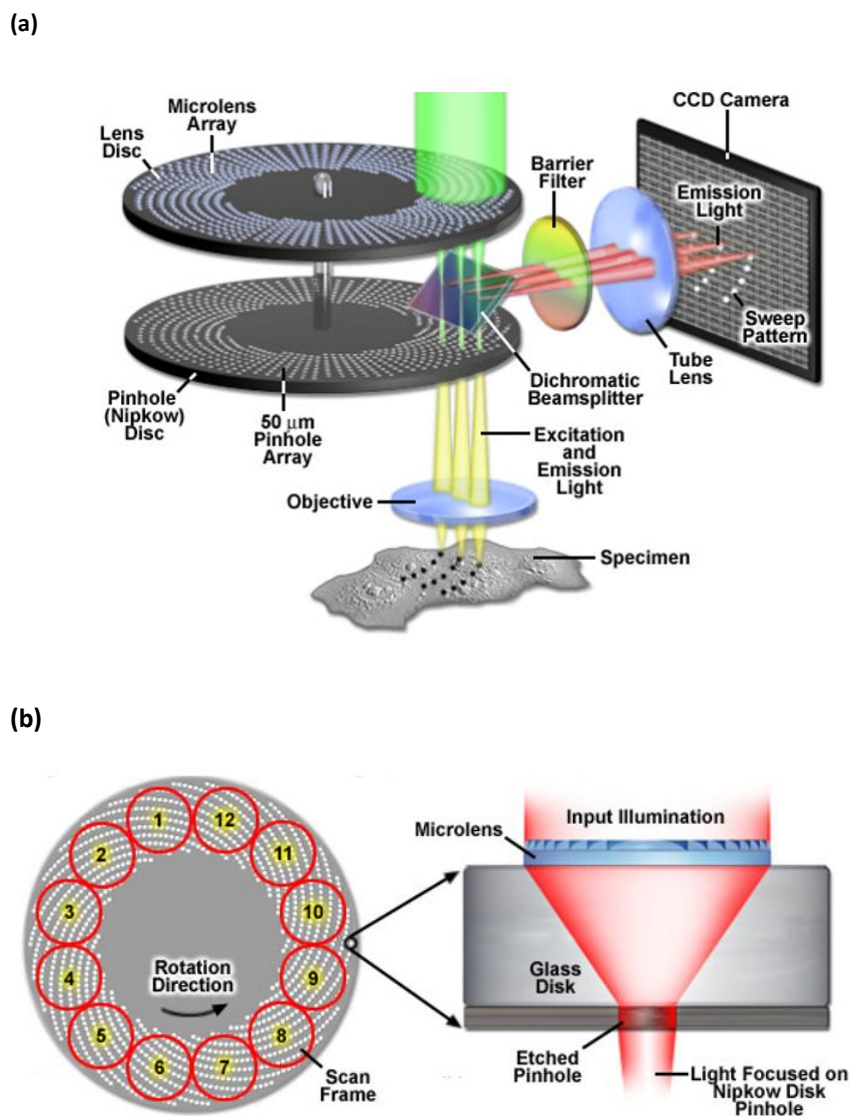


Figure 3.8 – Yokogawa confocal spinning disk unit (CSU-X1). (a) The two rotating disks (microlens and pinhole arrays) configuration, and the excitation (green) and emission (red) beam paths. (b) All 12 FoV scan frames of a single full rotation of the microlens disk array. Figure taken from [64].

### III.1.4 Biological applications of ensemble polarization resolved microscopies

Before moving to polarized single-molecule microscopy methods, it is worth to present a few biological applications of polarized ensemble methods. In this section, we will present the work done in proteins of the nuclear pore complex, cytoskeletal structures such as septins, actin filaments, integrins, and finally the applications on the organization of lipid membranes. Showing a few examples should emphasize the strengths and importance of developing polarization resolved microscopy methods.

Septins are cytoskeletal proteins that can form higher order structures particularly important in cell division, such as hourglass and ring shaped structures. It is believed that septins



build such higher order structures thanks to their polymerization into filaments *in vivo*, however the polymerization into filaments was only clearly shown in *in vitro* studies. Besides, because some septins contains some structural flexible regions, their whole structure is not easily obtained by X-ray crystallography. How such proteins interact with other cytoskeletal proteins or to each other to promote their assembly *in vivo* is highly unknown. In this sense, any information obtained about their organization and assembly, particularly *in vivo*, is clearly demanded. Vrabliou, A. M. and Mitchison, T. J. (2006, 2007) studied yeast septin organization in the bud neck of *Saccharomyces cerevisiae* cell division *in vivo* [78, 79]. The authors used fluorescence anisotropy microscopy to probe green fluorescent protein (GFP) rigidly linked to Septins (Cdc3, Cdc10, Cdc11 and Cdc12). They constrained the GFP by genetically engineering a continuous alpha-helix structure in a coiled coil region of the septins. In their work, they showed that the whole structure of septins changed in orientation by 90° during the hourglass transition to two independent rings *in vivo* (see Figure 3.9). The authors also showed that the structure of septins kept well organized throughout the cell division process, having their main orientations aligned with the main axis of system. Besides, it is worth to highlight the advantage of GFP tagging approach in the alpha-helix: in addition to obtain a rigid linkage needed for polarimetry, they profited from the knowledge that alpha-helices are periodical, and tagging the GFP in different sequence of aminoacids position would rotate the GFP around the main axis of the helix. Thanks to the symmetric properties (C2 symmetry) of hourglass and rings structures, they used the helix information to generate septin probes for in all main axis. Further work done by DeMay, B. S. et al (2011) explored the symmetry of such transition, also using septin-GFP constructs, but using another polarization resolved method: linear dichroism with four linear excitation angles controlled by a liquid crystal device. The main advantage of the latter is that it is robust against homo-fret process, thanks to the fact that the anisotropic signal is dependent only on the absorption dipole of the GFP. In their work, they demonstrated the polarization resolved method at that time, and detailed more the organization of the transition step of septins from hourglass structure to rings.

#### The septin transition from hourglass structure to rings

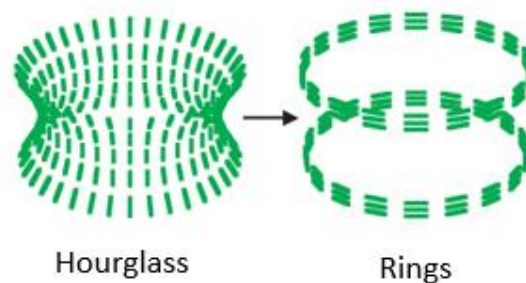


Figure 3.9 – The representation of hourglass to 2 rings septin transition in yeast bud neck. Note that the green stick (septins) is depicted changing in orientation during the transition. Figure taken from [78].

Nuclear pore complex (NPC) are proteic pores on the cell nucleus that selective mediates the transport of macromolecules between intranuclear region and the cytoplasm. They are embedded in the nuclear envelop and they are composed of approximately 30 distinct proteins, termed nucleoporins (nups). The nups appear in the NPC multiple times, having their own spatial

distribution in the NPC. Based on the available crystal structures and biochemical data, many models of how the nups mediates the selective transportation or even how they are organized in the NPC were proposed. Like septins, nups contains protein domains that are rigid and other that are flexible. Disordered regions are difficult to be studied by classical methods, but with polarimetric approach some information can still be accessible. Mattheyses, A. L. et al (2010) and Kampmann, M. (2010) et al mapped the orientation of nups and probed nups order in NPC in vivo with fluorescence anisotropy microscopy method (see proposed model in Figure 3.10). In their work, they profited from the circular geometry of the nuclear envelop in yeast [80] (and quasi circular shape in mammalian cells)[81] to define 32 sector regions in the FoV, therefore, sectioning the nuclear envelop periphery in 32 angles (11.25° equally spaced). The polarimetric probe were engineered GFP-nups, that were rigidly linked without any extra aminoacid between the GFP and the nup. Although their approach did not distinguish between a domain that is intrinsically rigidly held, and another that is flexible, their approach could distinguish which protein domains were structurally ordered from the ones that were disordered. Besides, when probing ordered domains, the authors managed to map the nup (Nic96, Nup133-Nup107 dimer) orientation in relation to the nuclear envelop in live cells. Finally, the authors have shown that their approach could work for other biological system in membranes such as ATPase complexes.

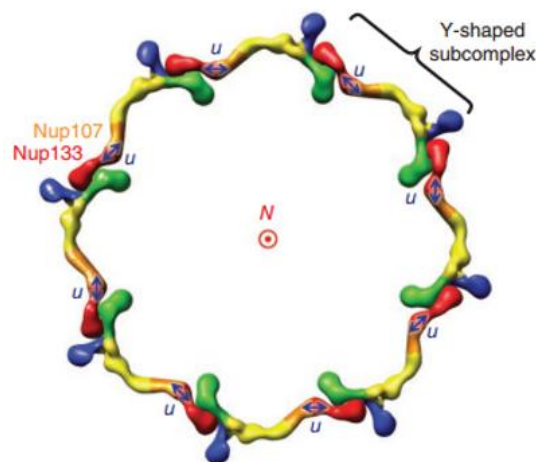


Figure 3.10 – The octameric nups organization model with proposed by Kampmann, M. et al (2011). With polarization resolved microscopy, they concluded that the angle between Nup107 - Nup133 complex should be closer to 90°, and not 0° (see the dipole u orientation in blue). Such condition supports the octameric symmetry rearrangement of nucleoporins. Figure taken from [81].

Integrins are a family of transmembrane cell adhesion proteins, mostly found in large supramolecular adhesion complexes named focal adhesions (but not only). It is generally accepted that integrins connect the extracellular matrix (ECM, outside the cell) to the actin cytoskeleton (inside the cell), having a key role in mechanotransduction, particularly related to cell polarity and movement. Nordenfelt, P. et al (2017) tested the hypothesis of cytoskeletal force model for integrin activation with fluorescence anisotropy microscopy projected onto 4 polarization split analyzer channels [82]. The idea is that the tension exerted through integrins between actin cytoskeleton retrograde flow and the ECM on the substrate would tilt and align integrin orientation at cell surfaces during cell migration. In their work, the authors showed that centripetal actin flow pulls and align the integrin lymphocyte function-associated antigen-1 (LFA-

1,  $\alpha\beta 2$ ) particularly at the cell edges, such as in cell protrusions named lamellipodia. For polarimetric purposes, they modelled with Rosetta algorithm the GFP linked with LFA-1, and used such model to predict linker rigidity, and information of the relative orientation between the dipole and the LFA-1 structure. The LFA-1 is expected to have 3 main conformations, being the active one the extended-open and tilted form (see Figure 3.11). They concluded that force generated by actin polymerization (and not contraction with myosin) would keep the extended-open form, letting the adhesion complex active, although other indirect activation mechanisms (e.g., biochemical) could also happen in parallel for integrin regulation in migrating T cells. Moreover, the authors demonstrated that integrins closer the leading edges (lamellipodia) were more anisotropic (ordered) and aligned to the actin flow compared to integrins at regions in the center of the cell.

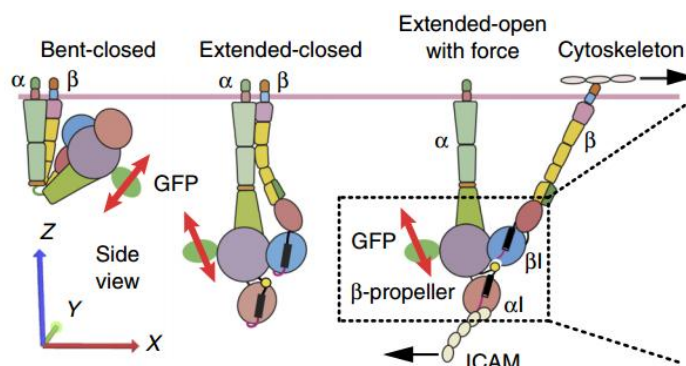


Figure 3.11 – The three main conformations of LFA-1 integrin complex: bent-closed, extended-closed, and extended-open (with force via actin filaments). ICAM, intercellular adhesion molecule. GFP, green fluorescent protein. The red double-headed arrow is the GFP transition dipole. ( $\alpha$ ,  $\beta$ ) are the domains that connect to intracellular space. The  $\beta$ -propeller contains the structurally connective head domains ( $\alpha$ ,  $\beta$ ). Figure taken from [82].

Cell membranes are a fluid-gel bilayer made of lipids enriched with proteins and carbohydrates. Membranes can be the borderline that separates life from not life (e.g., unicellular organisms, epithelial cells, etc) or between two or more neighbor cells. They are key structures that selective control what comes in and out the cell. Also, they can sense the environment and trigger important signaling processes. Due to its delicate structure (roughly 20nm thick) and diverse chemistry, to obtain organization and fluidity information of lipids in cell membranes is a challenging topic. Traditionally, *in vitro* studies with model membranes are more often used to access molecular information of lipid organization. Kress, A. et al (2013) and Wang, X. et al (2013), from our group, used two different cell membrane probes for polarimetry, the di-8-ANEPPQ (membrane intercalant) and DiI<sub>C18</sub> (tangent to membrane)[58, 73]. They used respectively a confocal and a spinning-disk linear dichroism microscopy methods to probe fixed mammalian COS-7 cells with multiple incident linear polarization angles. The linear polarization was controlled respectively with a motorized half-wave plate (HWP) and an electro-optical modulator (EOM). As comment before, linear dichroism methods are less sensitive to depolarization processes such as homo-FRET, therefore are more robust techniques and fluorescence anisotropy ensemble methods. Thanks to their approach, they could quantify the membrane perturbations made by drugs in the cytoskeleton and even membrane perturbants such as cholesterol. Thanks to cone model applied to polarized fluorescence microscopy, they

managed to compare and quantify the local order of lipids and local fold distortions in fixed cells. In untreated cells, the technique was not sensitive enough to detect small lipid domains (lipid rafts) demonstrating that if any lipid raft exist, it would affect in a very weak way the order of the lipids on the cell membranes. However, the simple addition of cholesterol to cell membranes was strong enough to induce ordering/packing changes capable to be quantified. Other actin filament drugs such as Cytochalasin D (promotes actin filament depolymerization), Latrunculin A (inhibits actin filament polymerization), and Jasplakinolide (stabilizes actin filaments) induced membrane order changes. Because the technique could be used directly in fixed cells, they could visually map the real membrane order under different conditions (see Figure 3.12).

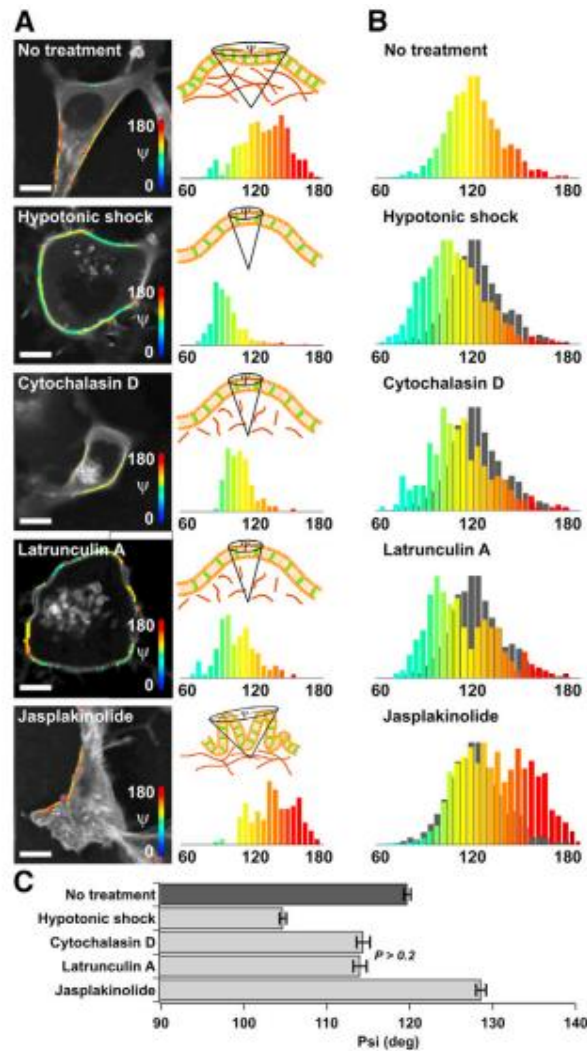


Figure 3.12 – COS-7 cell membrane local order depending on different scenarios (perturbations). (A) The polarization resolved micrographs. (B) Order  $\Psi$  histogram for each case. (C) Average histogram values. Note that, for hypotonic shock, cytochalasin D, and latrunculin A, the membrane local organization got more ordered (lower  $\Psi$  values) compared to the control (no treatment, see C). Jasplakinolide, on the other hand, induced a more disordered organization of the cell membranes. Figure taken from [58].

Finally, actin filaments have already been probed by ensemble polarization resolved microscopy methods. As previously introduced in Chapter 1, actin filaments have a role in multiple cell tasks, such as cell division, growth, shape, movement, mechanical force generation, sensing and transmission. Actin filaments can be assembled in higher order 1D structures (i.e., bundles, such as stress fibers), 2D structures (i.e., sheets or crossed network close to cell membranes), and 3D structures (3D bulk scaffolds). Due to its importance in so many cell functions, the interaction with actin filaments with other actin binding proteins (~200) has been extensively studied, but major part is still remain to be elucidated, particularly *in vivo* and in fixed cells. Mavrakis, et al (2014), from our group, have studied the interaction between septins and actin filament rings in *Drosophila melanogaster* fruit fly embryos [62]. The idea was to probe their interaction during animal cell cytokinesis (cell division). In that work, they showed that septins directly bind and crosslink actin filaments, forcing them to bend and make curved bundles. To evaluate the orientation and order of actin filament rings crosslinked with septins, they used phalloidin-AlexaFluor488 (the same probe we used in this thesis), that is ideal to investigate actin filaments in fixed cells with polarimetry. The authors used the same confocal linear dichroism microscopy setup as Kress et al (2013) with multiple linear excitation angles (30 angles, one polarization every 6°). They showed that septins are required for generating curved and tightly packed F-actin in *Drosophila* furrow canal (during cellularization process). The orientation of F-actin was tangential to the actin filament rings (azimuthal around furrow canal), and they showed that such F-actin was relatively well ordered (packed) compared to a septin mutant (*pnut*-null), see Figure 3.13 a-d. They concluded that septins contribute to the assembly, stabilization and contractility of cytokinetic rings. In their work, they also probed the order of F-actin bundles in stress fibers of COS-7 mammalian cells (see Figure 3.13 e-f).

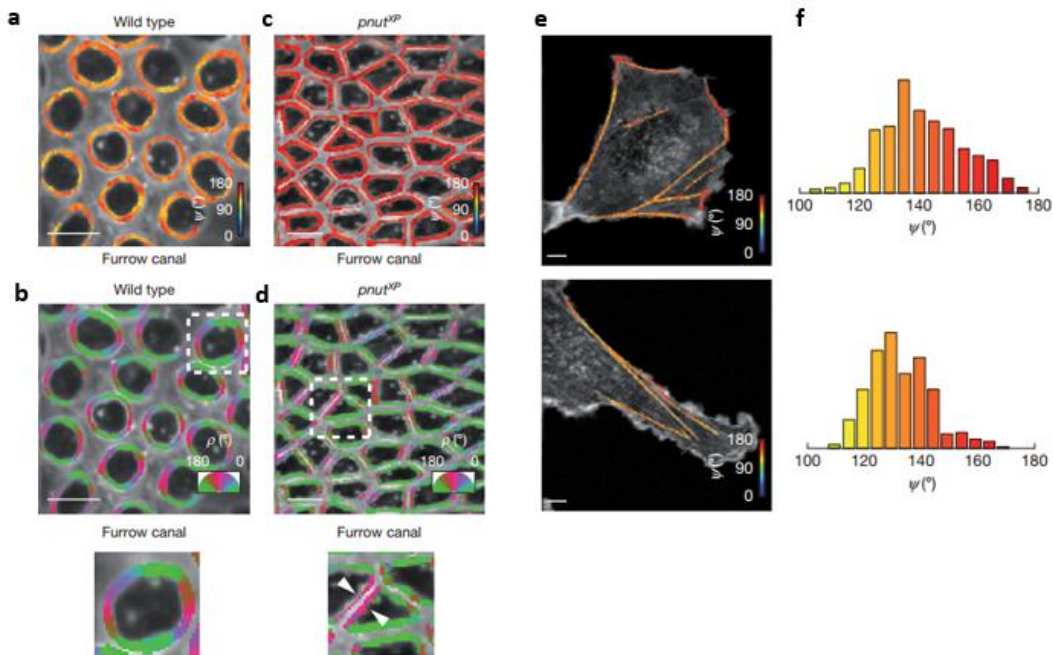


Figure 3.13 – Actin filament organization in yeast furrow canal (a-d), and on stress fibers in green monkey kidney COS-7 cells (e-f). The case (a-b) are without treatment (wild type), and (c-d) are with a septin mutant (*pnut*). The polarization resolved micrographs (a,c, and e) the colorcode stands for the order parameter ( $\Psi$ ), where the red-ish

values are more disordered regions (compare a with c). On the bottom (b and d) the colorcode stands for orientation ( $\rho$ ). The histograms in (f) are the respective to the images in (e). Figure adapted from [62].

### III.2 Ensemble vs single-molecule polarized fluorescence: why go to the single-molecule level?

Comparisons of pros and cons of ensemble versus single molecule polarization resolved methods are nicely reviewed in [50, 57, 65, 83]. To summarize, polarization measurements on a macroscopic population of fluorophores (ensemble) have the advantage of addressing the most general imaging modalities used in bio-imaging. They generally benefit from high signal to noise conditions, and because of that the experiments employed are convenient and fast. Nonetheless, they have some important disadvantages when compared to single-molecule (SM) approaches.

First, ensemble averaged signals can only be applied to biomolecular structures that have a simple, anisotropic cylindrical symmetry [57]. This method indeed cannot unravel too-complex organizations, or high order symmetry distributions, because it is intrinsically limited to a small amount of retrieved parameters (two quantities only are determined: one being averaged orientation, the other being angular aperture). A distribution of too high complexity may even lead to a retrieved isotropic distribution. Isotropic signal can indeed be generated by many different ways, which represent different sub-diffraction geometries.

Second, ensemble averaged signals might hide important microscopic organization features [59] because of the rotational mobility behavior of the fluorescent label. While this rotational mobility can be interpreted as a simple offset value for the detectable molecular order amplitude, this aspect is particularly important when trying to retrieve information with fine molecular order changes in highly disordered environment. Most importantly, the fluorophore flexibility cannot be easily quantified and constitutes a major source of artefacts for interpreting ensemble polarized measurements.

Third, a source of bias can affect ensemble polarized measurements. Since we use an incoming polarization rotation in the sample plane, the retrieved information is projected in the sample plane. Therefore any 3D orientation of a molecular angular distribution will lead to a more isotropic-like signal, and thus to an overestimation of its angular aperture (molecular order). Extra care has therefore to be brought to make sure that the observed structures are lying in the sample plane.

To get around part of the disadvantages cited above, our group has developed methods based on single molecule detection. First, polarized measurements of single molecules brings the advantage of accessing individual information on the mean orientation and angular aperture for each single molecules of a sample. This permits therefore to quantify its angular mobility extent, which is an important quantity to consider when interpreting ensemble measurements. Second, relating the mean orientation of each single molecule measured individually, reported in an image, can give access to much more complex angular distributions than those measured by ensemble measurements, as described above. In particular, main directions crossing each other might be revealed, while they appear as a close-to-isotropic distributions in an averaged-ensemble measurement. Third, single molecule orientation measurements can be combined

with their spatial localization, and therefore with super resolution imaging. This potentially gives access to a high-resolution image of bio-molecular organization, which combines alignment information (brought by polarized measurements) in addition to nanometric scale morphology (brought by localization measurements). Finally, 3D orientations are potentially accessible, since several methods have been developed that give access to off-plane tilt orientation information, thanks to single-molecule based imaging methods [84-87].

In this work, we developed a 2D (in-plane) polarized method to retrieve single molecule orientation measurements, in addition to super resolution imaging based on single molecule localization. This approach is described below.

### III.3 Single-molecule approaches

Different polarization resolved methods have already reached single-molecule (SM) level thanks to dilute labeling or to stochastic optical reconstruction approaches. Particularly, the first polarized measurements performed on single molecules have used dilute labeling to spatially isolate the fluorophores point spread function (PSF) in the FOV for orientation retrieval [65]. In most of the cases, studies have been performed *in vitro* due to the controllable level of labelling. Orientational changes have been quantified in biomolecular structures such as myosin, ATP synthase, integrins, and DNA [65, 83, 88-93]. Remarkably, dilute labelling has shown the capacity of probing large orientation changes of the lever arm myosin when walking along an actin filament, providing one of the most important evidences of hand-over-hand model (“walk”) of myosin displacement [86, 87, 94]. Recent studies have also used dilute labeling in cells to track the sparse orientation and position of actin filament dynamics in the lamella of living cells [95].

On the other hand, there are fewer polarized fluorescence microscopy (PFM) methods in the literature that rely on stochastic optical *reconstruction* imaging approaches. In such cases, ideally the biological structure is densely labelled with fluorescent labels, and the single-molecule sensitivity is retrieved thanks to the temporal separation of overlapping PSFs in the FOV, which is due to a provoked blinking process in the fluorophores. Most generally, the resulting stochastic emission process recorded for many single molecule images is followed by reconstruction methods based on the localization of the center of isolated PSFs, allowing super-resolution capabilities of conventional (saturated) labeled structures. There are many different ways one could provoke stochastic emission processes, based on the activation/deactivation of the emission of fluorophore. These methods are described in a large number of reviews, and here we recommend a few [38, 70]. The differences in the methods rely on the underlying photophysics or photochemistry that generate the fluorescence blinking. It could be photoactivatable (**off**→**on**→**bleach**), photoconvertible (**on**( $\lambda 1$ ) → **on**( $\lambda 2$ )), or photoswitchable (**off**↔**on**). In the latter, the blinking can be induced by chemicals, such as thiols [96]. Here we remind that the detection of fast (tens to hundreds of ms) fluorescence on-off dynamics was possible thanks to the fast integration time of the cameras currently on the market (in our case, the Andor Ixon 888 camera has a fastest integration time of approximately 33ms for the full chip detection).

Next, we will describe in more detail the photoswitchable approach that our lab has been using so far for direct Stochastic Optical Reconstruction Microscopy (dSTORM).



### III.3.1 Principle of dSTORM imaging

The direct STORM (dSTORM) is a photochemistry based method: the presence of chemicals such as thiols (RSH) induce redox reactions in the fluorophore. The redox reactions stochastically adds or removes electrons from the original molecule, affecting the stability of the chromophore, creating new molecular entities with different potential energy states. These reactions are in particular responsible for the long-lived dark states that are necessary for the stochastic emission of the fluorophores. Due to the creation of new energetic states, the excitation might be resting onto dark states (i.e., *long-lived* states that does not participate on the  $S_1 \rightarrow S_0$  transition, see Figure 3.14), which can stochastically be de-excited by another redox reaction (e.g., oxidation with oxygen), bringing the fluorophore back to its ground state. From these long-lived states, reactions with Reactive Oxygen Species (ROS) can also lead to a complete bleaching (see Figure 3.14).

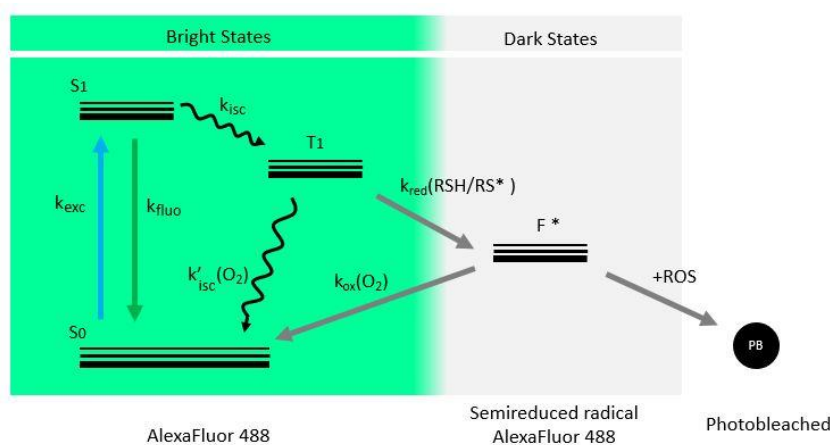


Figure 3.14 – Representative Jablonski diagram of rhodamine dyes such as Alexa Fluor 488 [97]. Blue arrow, excitation of AlexaFluor488 with 488nm laser (rate  $k_{exc}$ ). Green arrow, fluorescent emission (rate  $k_{fluo}$ ), curved arrow, non-radiative intersystem crossing transitions (rates  $k_{isc}$  and  $k'_{isc}(O_2)$ ). Grey arrows, chemical reactions. The fluorophore is excited ( $S_0 \rightarrow S_1$ ) with rate  $k_{exc}$ , and it remains in the excited state  $S_1$  over nanoseconds (ns) until it relax via radiative transition emitting fluorescence photon with rate  $k_{fluo}$  or until it enters its triplet state via intersystem crossing with rate  $k_{isc}$ . The triplet state ( $T_1$ ) has lifetime in the range of microseconds ( $\mu s$ ), that it is enough long lived to be found and collide with other molecules, such as molecular oxygen  $O_2$ . In the absence of thiols (RSH), the  $T_1$  of the fluorophore is quenched by collision with  $O_2$ , transferring the energy to  $O_2$ , repopulating the fluorophore ground state in microseconds ( $\mu s$ ) or generating Reactive Oxygen Species (ROS) which lead to bleaching. Because the camera integration times (typically in the range of milliseconds to seconds), are much slower than microseconds, they cannot distinguish when the fluorophores are dwelling in the  $T_1$  or in  $S_1$ . Hence,  $T_1$  states can be considered bright states. On the other hand, in the presence of thiols (RSH) in the buffer solution, the  $T_1$  might stochastically react with them with rate  $k_{red}$  producing new molecular entity (fluorophore semi reduced radical  $F^*$ ), that is as enough long-lived as the camera integration time. The semi reduced dye radical ( $F^*$ ) might react with  $O_2$  with a rate  $k_{ox}(O_2)$  and repopulate the fluorophore ground state ( $S_0$ ), and generating ROS that could damage organic molecules in the neighborhood, including the fluorophore itself. Figure adapted from [97].

The principle of the method is quite simple (see Figure 3.14). Thanks to the presence of redox reagents, such as thiols and other reactants, the stochastic kinetics of the chemical reactions under high power leave most of the photo-excited fluorophores dwell in the dark



states. In a few random cases, the fluorophores are recycled back to the ground state. Since the system is under constant excitation, the recovered fluorophore might be re-excited and eventually yield the fluorescence emission  $S1 \rightarrow S0$ , whose decay occur in nanoseconds.

As a result if a video is recorded over time, instead of having all labels emitting fluorescence at the same time, random and isolated bright (blinking) events occur per frame, such that the single-molecules PSFs are temporally isolated from their neighbors (see Figure 3.15). In such cases, one could perform a 2D fitting onto the diffracted spots (for example, a Gaussian fit in the simplest case), and with that extract quantitative parameters from each diffracted spot, such as its radius, peak position (e.g. localization), intensity, signal to noise (SNR) level, and background level. For conventional dSTORM or similar methods, the most important parameter to recover is the single molecules' localization, which can be estimated with a precision down to a few nanometers in high SNR conditions.

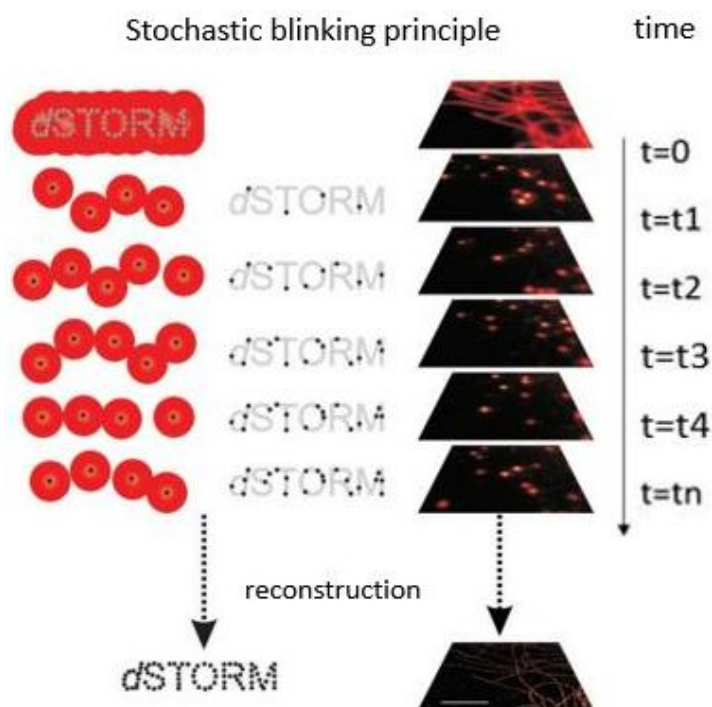


Figure 3.15 – The stochastic reconstruction from blinking events. On the top, an illustration of two diffracted limited images labeled with fluorescent labels: a dSTORM text (left) and an image of a cell (right). Below them, the figure illustrate a time trace ( $t=0, t=1, \dots, t_n$ ) simulating the stochastic blinking in time. Per time frame, only a few PSFs are detected, making it possible to fit and determine the centroid of each PSF with subdiffraction precision. After recording the whole image stack of the blinking events and fit all of them, one could reconstruct the original image in a pointillistic fashion by overlapping the frames onto a single image, with the localization precision of each spot having higher resolution than diffracted limited one. Adapted from [98]

### III.3.2 Adequate buffer for dSTORM imaging

As we brief commented before, the presence of molecular oxygen ( $O_2$ ) leads to the generation of Reactive Oxygen Species (ROS), whose can chemically react with its surrounding organic molecules, causing sample degradation and/or fluorophore bleaching. In order to avoid the  $O_2$  in the medium, it is important to use a good enzymatic oxygen scavenging system (e.g.,

Glucose Oxydase, Pyranose oxidase, and Catalase) that will protect the organic molecules from oxidative damage caused by ROS. To replace the role of oxygen in the blinking cycle of Figure 3.14 states, one could add a Reducing and Oxidizing System (ROXS system, [99]) that improves the photostability of the fluorescent label, and protects the both the sample and the labels from photo-damage (see Figure 3.16).

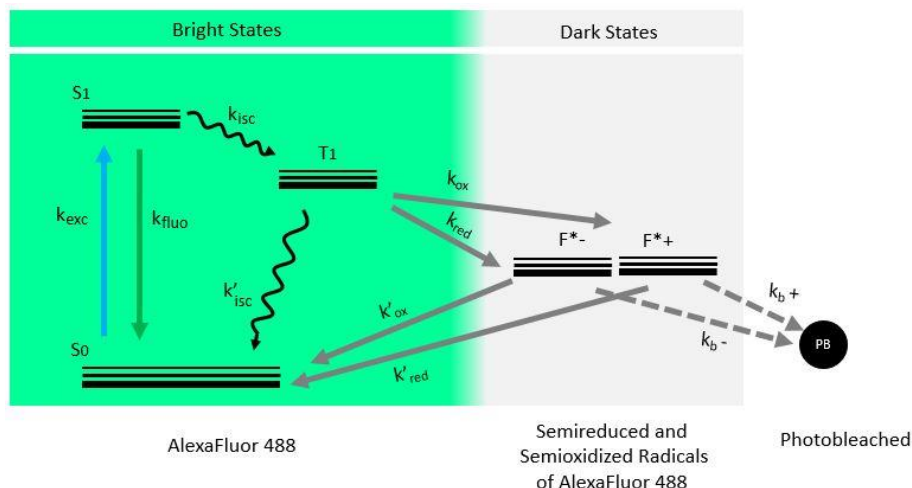


Figure 3.16 – The reducing and oxidizing system (ROXS). The formation of semireduced ( $F^{*-}$ , with rate constant of  $k_{red}$ ) and semioxidized ( $F^{*+}$ , with rate constant of  $k_{ox}$ ) radical ions are rapidly converted to singlet ground-state ( $S_0$ ) of the fluorophores after respective oxidation (rate constant of  $k'_{ox}$ ) and reduction (rate constant of  $k'_{red}$ ), avoid most of photobleaching product (PB). Typically, a radical cation it is reduced by ascorbic acid (AA), and a radical anion is oxidized by methylviologen (MV). Besides, ideally the bleaching constant rates ( $k_{b+}$  and  $k_{b-}$ ) are slower than the rates for singlet ground state recovery ( $k'_{ox}$  and  $k'_{red}$ ). Figure adapted from [99].

The ROXS system is basically a buffer that quenches the fluorophore triplet state (T1) with reducing (e.g., ascorbic acid (AA),  $\beta$ -mercaptoethylamine ( $\beta$ -MEA)), and oxidizing (e.g., methylviologen (MV)) chemical agents. The product formed are semireduced and semioxidized fluorophore radicals that are long-lived dark states (e.g., lifetimes in the range of milliseconds to seconds). Due to the presence of their complementary radical ion in the buffer, both semireduced and the semioxidized radical ions interact with each other in the medium, and are rapidly converted to the ground state ( $S_0$ ), preventing the formation of photobleaching product, thus allowing dSTORM experiments last for longer times, and protecting the sample from eventual photo-damage induced by oxygen.

### III.3.3 Retrieving quantitative parameters from dSTORM single-molecule fluorescence events

In typical dSTORM experiments, we are mainly interested in obtaining a higher precision in the localization of the centroid of the point spread functions (PSFs) spots, forming the image of single molecules. In our work, we used the Multiple-Target Tracing (MTT) algorithm [100], which searches and analyzes the blinking spots within an image made of sparse single molecule's PSF. A defined sliding window of several pixels scans the whole image searching for blinking events defined by a Gaussian shaped model (G) with local background (m) and noise (N) per pixel (i,j). Since the Gaussian model used in the fit is a continuous function, we represent the

Signal of each event as  $S_{i_p, j_p}$ , with continuous pixel coordinates defined as  $(i_p, j_p)$ , see Figure 3.17:

$$S_{i_p, j_p} = a \times G(i_p, j_p, i, j, r) + m + N_{i_p, j_p}(\sigma^2_{noise}) \quad \text{Eq. 3.7}$$

where  $\sigma^2_{noise}$  is the standard deviation of the noise level.

The Gaussian function is of radius  $r$ , is a normalized Gaussian function defined as:

$$G(i_p, j_p, i, j, r) = \frac{e^{-\frac{(i_p-i)^2+(j_p-j)^2}{2r^2}}}{\sqrt{\pi}r} \quad \text{Eq. 3.8}$$

The parameter “a” in Eq. 3.7 is used to quantify the PSF amplitude in counts of the Gaussian signal without the background (see Figure 3.17):

$$\iint (S_{i_p, j_p} - m)^2 di_p dj_p = a^2 \quad \text{Eq. 3.9}$$

This PSF amplitude will be an important parameter in the quantification of single molecule’s fluorescence intensity.

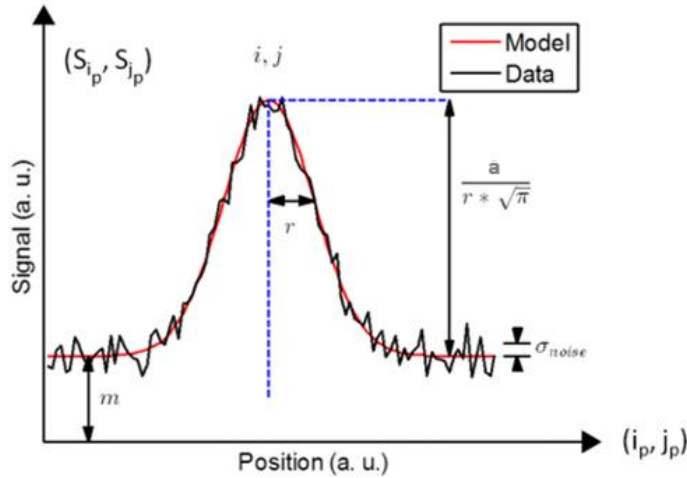


Figure 3.17 – Illustration of a transversal profile of symmetric 2D Gaussian function fit centered on an arbitrary pixel  $(i, j)$  position. Note that the values in the abscise axis are continuous pixel coordinates in  $(i_p, j_p)$ . The Gaussian fit, with the equation of the signal defined as above, can extract quantitative parameters such as, PSF radius, amplitude of the signal ( $a$ ), background ( $m$ ), and noise ( $\sigma_{noise}$ ). Figure adapted from [101].

That said, we can define the signal to noise ratio (SNR) and the intensity of the signal ( $I_{i, j}$ ) without background, centered at  $(i, j)$  by the following equations:

$$SNR = \frac{a^2}{\sigma_{noise}^2} \quad \text{Eq. 3.10}$$

And

$$I_{i, j} = \iint a \cdot G(i_p, j_p, i, j, r) di_p dj_p = 2a\sqrt{\pi}r \quad \text{Eq. 3.11}$$

### **III.4 The polar-dSTORM method**

#### **III.4.1 The current state of the art of single-molecule and super-resolution polarization resolved microscopy**

While a lot of studies have addressed the problem of single molecule orientation measurements (see above), including in 3D, there is little work on the combination of single molecule localization and orientation measurement. The main reason is that many orientation measurements are based on the modification of the single molecule's PSF, either by defocused imaging [84-85, 102-103] or by PSF engineering using phase plates in the back-focal plane of the detection path [104-105]: these methods are not always compatible with single molecule localization and stochastic reconstruction. A more direct way to retrieve orientation information is to measure the single molecule signals using various incident and possibly various emission polarized states, as developed in [87, 94, 106]. These methods however most often require the measurement of multiple sequential images of the same molecule, which is not compatible with dSTORM.

Our lab has pioneered a single molecule-based super-resolution polarization resolved microscopy method to retrieve 2D orientation information of fluorophores attached to biomolecular structures, based on a single shot measurement, called polar-dSTORM (see [59-60]). The principle of the method, which is described in detail in the next section, is based on the split of the image into several polarization states, using a circularly polarized excitation to avoid any preferential excitation photoselection. This method was inspired by a first implementation in [107], which used polarization splitting to retrieve anisotropy information in isotropic samples. With polar-dSTORM applied to anisotropic organized structures, our lab has disentangled the two parameters that characterize the orientation characteristics of single fluorophores attached to proteins: their mean orientation and wobbling angle, which quantifies the degree of angular fluctuations occurring during the integration time of the camera as defined in Chapter 2. The approach, as discussed below, is based on some hypotheses, however it has permitted to reveal parameters that are hidden in ensemble measurements, which were missing so far. Besides, this approach permitted to show that different phalloidin conjugated dyes can yield different polarization readouts in terms of wobbling, highlighting the importance of label rigidity constraints imposed by the fluorophore's linker length. Importantly, as one would expect, polarized super-resolved images were sensitive enough to detect sub-diffraction heterogeneities that were typically hidden by ensemble averaging (see Figure 3.18 A-D). The biological structures probed by the technique were cylindrically symmetric structures, such as F-actin filaments in stress fibers in cells [59], amyloids in vitro [60] and dsDNA strands deposited on a glass surface [59].

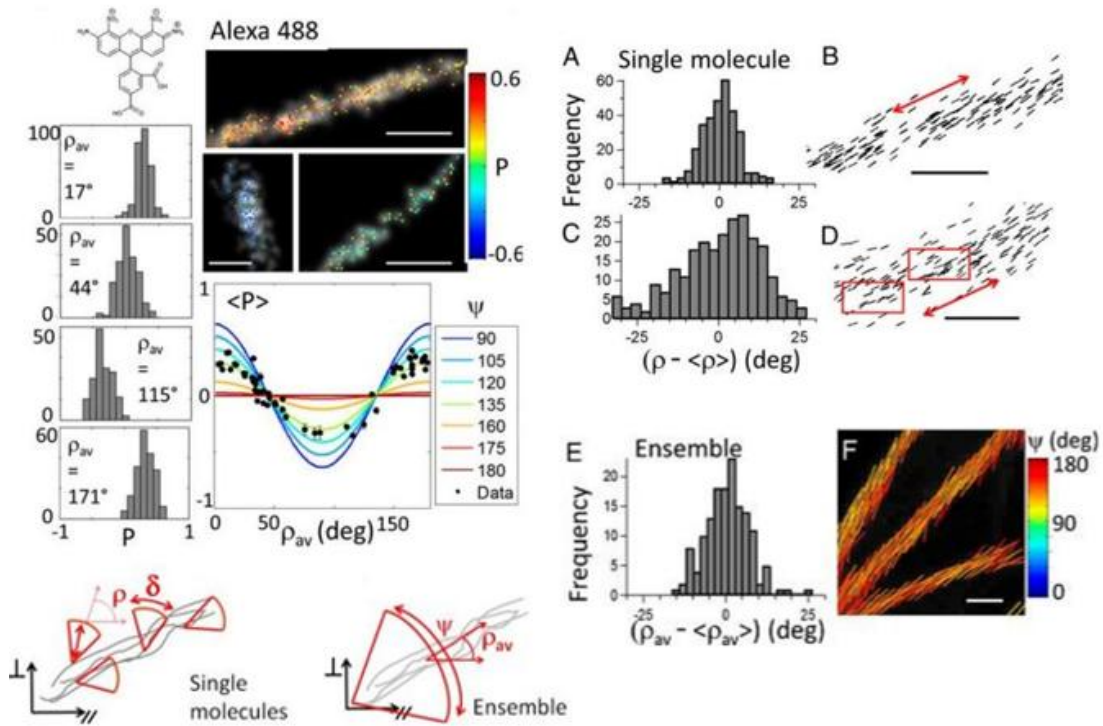


Figure 3.18 – Example of polar-dSTORM experiments in F-actin stress fibers using phalloidin-AlexaFluor488 label. On the left, the dye chemical structure (see also Figure 2.5), and four different histograms, of different ROIs retrieving their mean orientation ( $17^\circ$ ,  $44^\circ$ ,  $115^\circ$ ,  $171^\circ$ ). Also, three polarized images are shown of 3 different F-actin bundles (the polarization factor in colorcode normalized between -0.6 and 0.6). The plot on the bottom is the polarization factor plot of many bundles with different mean orientation. Note that we can also track the average ensemble (global angular aperture) value of  $\Psi \approx 120^\circ$ . On the right, comparison of single-molecule and ensemble orientation distribution angles. We can see from A-F that it is possible to detect the same (A-B) or higher (C-D) filament orientation heterogeneities in single-molecule polarization histogram compared to the ensemble case (E-F), which tends to hide small orientations deviations by ensemble averaging within the PSFs. Figure adapted from [59].

The principle behind polar-dSTORM is quite straightforward: it is a dSTORM experiment which the detection path is modified by adding a Wollaston cube to project simultaneously both vertical and horizontal orientations onto the same camera chip (Figure 3.19). By doing so, each projected channel on the chip has a dSTORM experiment whose intensity of each of the spots is proportional to their projection onto each respective analyzer orientation.

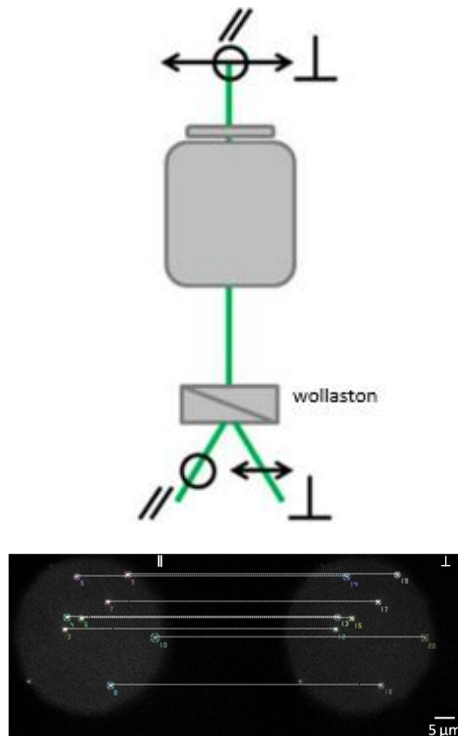


Figure 3.19 – The polar-dSTORM setup principle. A circular polarized light is used to excite the sample. The polarized emission of single fluorophores are probed by a Wollaston prism, which split the FoV in two, projecting the intensities proportionally to two orthogonal analyzer angles (parallel and perpendicular). Since each projection of the whole FoV is simultaneously detected on the same camera chip, it is possible to record a dSTORM video of the projected blinking events. After fitting, we extract quantitative parameters of each blinking event on the chip. Figure taken From [101].

Since each detected single molecule is split into two images, one can retrieve its localization (based on both images), and its intensities polarized along orthogonal directions called  $\parallel$  (intensity  $I_{\parallel}$ ) and  $\perp$  (intensity  $I_{\perp}$ ). The intensity is defined as the measured signal integrated over the PSF shape (fit as a 2D Gaussian function). The processing method that allows to measure such intensities combined with super resolution imaging is explained in more detailed in Chapter 5. With such polar-dSTORM data, one could then calculate the polarization factor as defined in the beginning of this Chapter 3 (Eq. 3.1), for each detected blinking event on each frame of the polar-dSTORM stack. Including a cone model similar to ensemble measurements in the polarization factor, it can be found that this factor is dependent on the single-fluorophore orientation ( $\rho$ ) and wobbling ( $\delta$ ), by the following equation (see also more details in Chapter 5):

$$P_0 = \frac{I_{\parallel} - I_{\perp}}{I_{\parallel} + I_{\perp}} = \cos(2\rho) \frac{\sin(\delta)}{\delta} \quad \text{Eq. 3.12}$$

In practice, the measured intensities are corrected by experimental factors to account for the polarization distortions possibly existing in the detection channels of the microscope (see Chapter 5). Note that here, as opposed to ensemble measurement, the averaged orientation  $\rho$  is the mean orientation experienced by a single molecule over the time scale of the measurement (typically 10-100ms). Reconstructing a map of many molecule's orientation  $\rho$

allows therefore to visualize the organization degree of the proteins to which the molecules are attached, since this parameter depicts their alignment independently from their angular fluctuations. In contrast, the wobbling parameter  $\delta$  is the angular extent experienced by the molecule during this same time, which is very long compared to the time scale of the lifetime and rotational motion of the fluorophore (see Chapter 2). The origin of  $\delta$  is mostly the flexibility of the linker between the fluorophore and the protein of interest.

Such approach has the advantage of minimal optical complexity. As opposed to PSF engineering methods [84, 104], it profits from preserving the single molecule's PSFs shapes as well as high signal-to-noise (SNR) ratio levels. Typically, localization precisions are in the range of 20-30nm, and angular precision reaches a few degrees to  $10^\circ$ . Both angular and localization precision are dependent of the SNR, therefore as expected, intensity thresholding is a very important step in the data analysis as it establishes the precision limits of the technique. The higher the intensity threshold performed, the higher the precision on both localization and orientation parameters. This technique has been an important benchmark for the field of polarimetry because it showed that, even though fluorophore wobbles, it is possible to estimate how the biological structures are organized at the nanoscale [59]. There are however several limitations of this technique, the most important being that orientation and wobbling cannot be determined in a completely unambiguous manner. In the next section, we will explain the limitations of polar-dSTORM.

#### III.4.2 Limitations of the polar-dSTORM method

In the Equation Eq. 3.12, we see that the quantitative values ( $\rho, \delta$  parameters) retrieved in a FoV were obtained by a single measurable value (the polarization factor  $P_0$ ). The dependence of  $P_0$  as a function of ( $\rho, \delta$ ) is depicted in Figure 3.20 where it is visible that both values affect the polarization factor. As a consequence, the orientation ( $\rho$ ) value cannot be retrieved independently from the wobbling value ( $\delta$ ). To solve this issue and access information on  $\rho$ , we need to make an assumption on  $\delta$ : all fluorophores wobble with the same angular aperture value. This is quite a reasonable assumption in first approximation, because all the labels are the same and they are labelling in principle the same structure. But, note that, this is not the general case: there might be fluorophores sensing different angular freedom in different local environments.

With the knowledge of  $\delta$ , it is therefore possible to use only one of the  $P_0(\rho, \delta)$  curves depicted in Figure 3.20 to retrieve  $\rho$  from a  $P_0$  measurement. The main issue is now to evaluate  $\delta$ . As seen in Figure 3.20,  $P_0$  takes its maximum/minimum value when the molecules are oriented on average along the parallel/perpendicular analyzer directions, which are chosen here as the horizontal and vertical directions of the sample plane respectively. This maximum/minimum value, importantly, depends on  $\delta$ , with the most extreme  $P_0 = (-1, 1)$  values reached for a small  $\delta \sim 0^\circ$ , and the smallest value  $P_0 \sim 0$  reached for a very high  $\delta \sim 180^\circ$ . A simple approach is therefore to profit from multiple orientations of the measurable molecules to evaluate the maximum/minimum values measured for  $P_0$  in the collection of detected molecules. This allows to estimate the most probable  $\delta$ , as seen in Figure 3.18. Another approach is to suppose that the studied structures are of cylindrical symmetry, which can be for

instance assumed in stress fibers made of collections of F-actin filaments. This permits to know, on a fiber portion of known orientation, what is the average  $\rho$ , and to place the collection of measured  $P_0$  values around this known average  $\rho$ . This way, the most probable  $\delta$  value can be guessed from the location of the experimental points on the  $P_0$  graphs of Figure 3.20.

This approach is valid for many important biological systems which have cylindrical symmetry: helical, tubular, circular, polygonal shaped, etc. For example, supramolecular complexes like cytoskeletal filaments (microtubules, not branched actin filament architectures, amyloid fibrils, septins, myosin filaments, etc), cytoplasmic membranes (plasma membranes, golgi, etc), double stranded nucleic acids (DNA), or any other cylindrically symmetric biological structure (protein domains, single-proteins or protein complexes with clear cylindrical symmetry).

For example, for the case of phalloidin-AlexaFluor488, it is known from the literature that the label mean orientation is aligned with the mean orientation of the actin stress fiber bundles [59]. Thus, in principle, the estimation of  $\delta$  could be performed statistically at any filament with known mean orientation. A rigorous estimation of  $\delta$  must preferentially be performed only on horizontal or vertical filaments (with mean orientational angles of  $0^\circ/180^\circ$  or  $90^\circ$ ). This is because, at these angles, we have the highest polarization factor sensitivity (see Figure 3.18 and Figure 3.20). For example, if we try to estimate the wobbling at filaments whose orientation ( $\rho$  values) lies close to  $0^\circ$ , we could distinct more easily different delta curves than at orientations close to  $45^\circ$  (see Figure 3.20). Hence, to estimate wobbling ( $\delta$ ) with high precision, it is important to have in the FoV biomolecular structures at  $0^\circ/180^\circ$  and  $90^\circ$  (aligned to the analyzer angles). If that is not the case, it is necessary to turn the sample orientation, or find another ROI that has structures with such configuration. The ambiguity at  $45^\circ$  and  $135^\circ$  orientations might be one of the main limitations of polar-dSTORM.

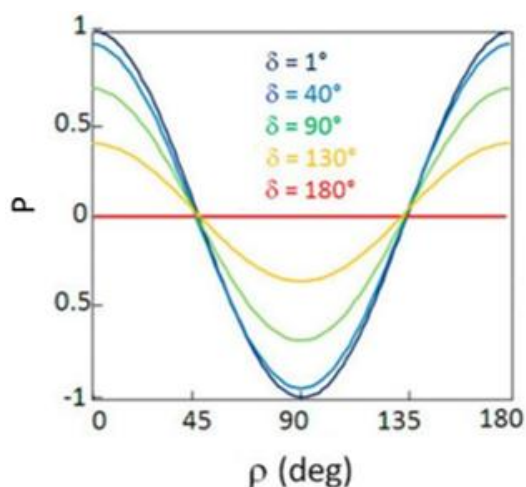


Figure 3.20 – Polarization factor (P) plot vs mean orientation of single-molecules ( $\rho$ ). Here anisotropy is defined with the polarization factor equation Eq.3.12. From the plot we see that the sharper the wobbling (cone aperture,  $\delta$ ) angle of single-molecules, the higher the amplitude range of the polarization factor (P). The latter gets maximum/minimum at  $0^\circ$  (=  $180^\circ$ ) and  $90^\circ$  orientations, which coincides with the main analyzer angles. Figure adapted from [59].



Another important limitation of this polar-dSTORM method is the ambiguity that exists between retrieved  $\rho$  values, e.g.  $\rho$  and  $(\rho - \pi)$  lead to the exact same value  $P_0$ , as seen in Figure 3.20. Here as well, some hypotheses have to be implemented. In particular, it is supposed that statistically, the  $\rho$  orientations of molecules along a structure of cylindrical symmetry are either very close or the very far in angle, from the mean orientation of a portion of the structure (typically an actin stress fiber).

The last limitation to be commented is related to the possible bias in the estimation of the wobbling angle  $\delta$ , due to a tilted 3D off-plane orientation of the measured molecules (see Figure 3.21 for three main scenarios). The reason is that the polarized signals (generated in 3D) are projected in the sample plane (2D): a tilted cone projects as a larger cone aperture when projected in the sample plane. The higher the 3D tilt ( $\eta$  angle), the higher is the bias in the wobbling values  $\delta$ , and therefore the higher is the error propagated on the  $\rho$  orientation values (Figure 3.21).

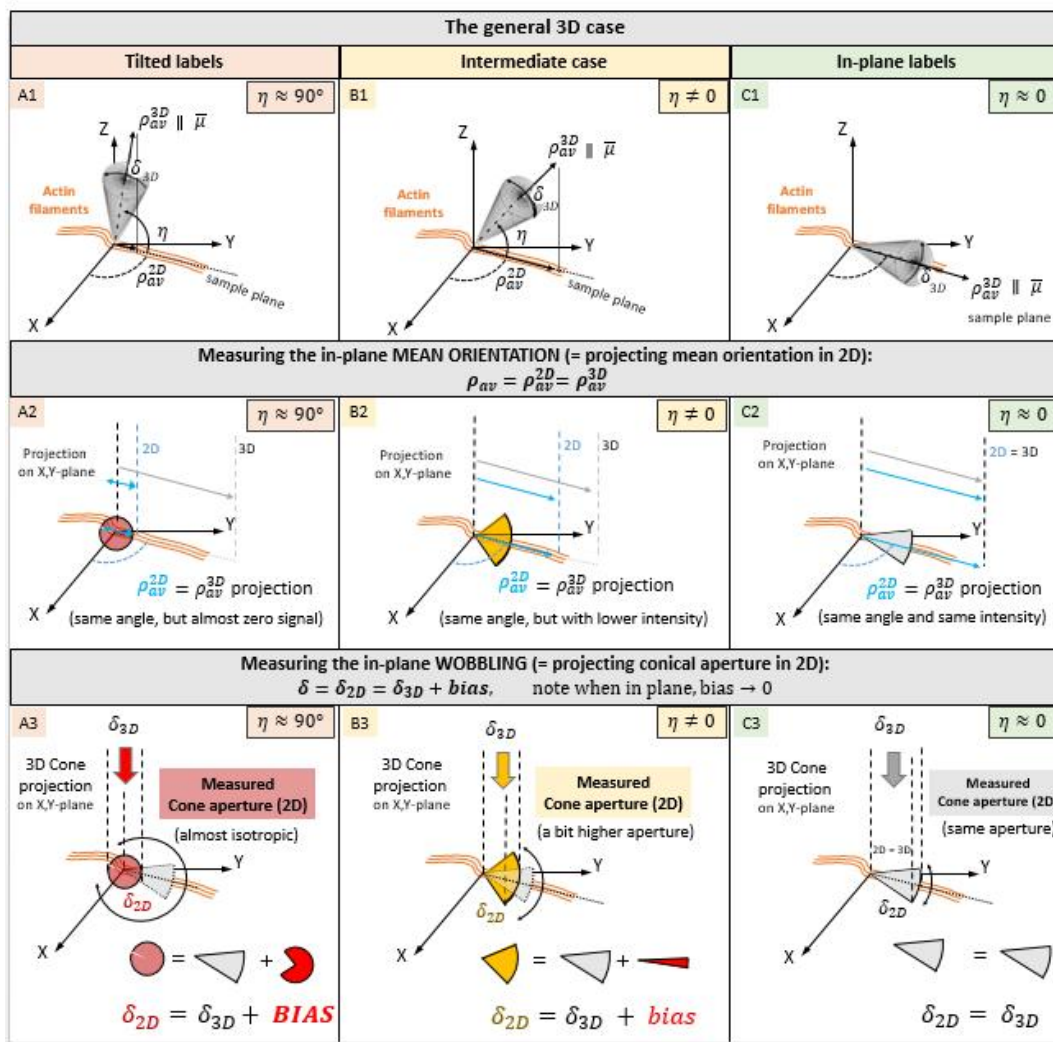
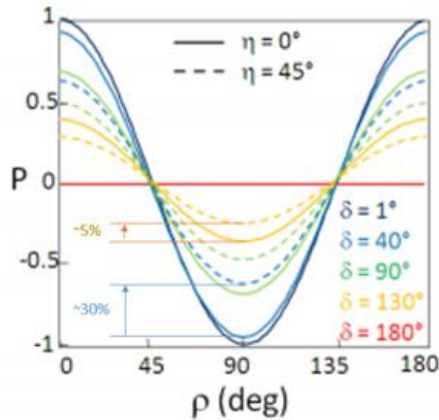


Figure 3.21 –Three main scenarios of when projecting the polarized emission in a 2D plane. First, on the right (in green boxes, C-column, with C1,C2, and C3 illustrations), we have the ideal case where the all the labels probed fit in the approximation of being lying parallel to the sample plane (ie., corresponding to the tilting angle values,  $\eta$ , being very small). In this case, the mean orientation projection (C1 to C2) and the cone aperture angle projection (C1 to C3) in

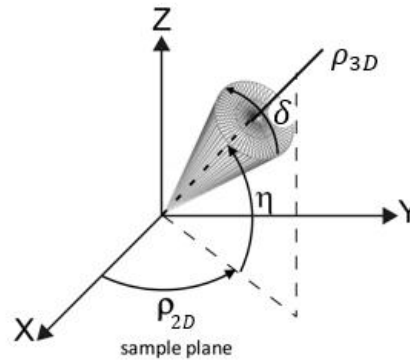
2D keeps the same vectorial mean orientation, magnitude (blue and gray arrows in C2), and cone aperture value. On the contrary case, on the left (in red boxes, A-column, with A1, A2, and A3 images), we have the scenario of very tilted angle (i.e., when the  $\eta$  is very close to  $90^\circ$ ). In such cases, the mean orientation (A1 to A2) of the cone is still the same, but the projected magnitude of the vector on the sample plane is reduced (see blue arrow compared to the gray arrow, corresponding in a very low signal projected in 2D). Importantly, when the cone aperture projection on the 2D plane (A1 to A3) suffer a significant change: the projection of the cone aperture in 2D is much wider (isotropic) than the real (3D) cone aperture. Thus, the wobbling angle value is always overestimated (biased) the more tilted is the mean orientation of the label is in relation to the sample plane (A1). In between the two previous cases, we have the intermediate situation (in yellow boxes, B-column, with B1, B2, and B3 schemes), where the mean orientation in 2D, keeps the same, but the magnitude of the signal is slightly reduced (blue and gray arrow in B2), and the measured (2D) wobbling angle is slightly increased (small bias). The quantification of the bias was simulated and therefore estimated for a variety of wobbling angles (see Figure 3.22).

The bias in the wobbling angle ( $\delta$ ) illustrated in Figure 3.21 is quantified in Figure 3.22, where the changes of the  $P_0(\rho, \delta)$  curves are visible when changing the orientation of the wobbling cone from  $\eta = 0^\circ$  (in plane cone) to  $\eta = 45^\circ$  (tilted cone). These changes are particularly dramatic for small values of  $\delta$ , as expected. Note that tilted molecules also projects in-plane with lower intensities (Figure 3.22), which makes them less detected in a dSTORM image. To some extent, this represents a natural filter to exclude such cases, since the data are generally thresholded to high intensities. Note, finally, that the bias on  $P_0$  (and consequently on  $\delta$ ), depends on the used NA for the detection channel. This is due to the fact that off-plane molecules radiate light along high propagation tilt angles (e.g. reaching large NA values), therefore affecting majorily large NA detections (see Figure 3.22 which compares NA=1.2 to NA~0 values). A rather low NA is therefore advised to minimize the effect of 3D-tilt angles biases [59]. This effect is described in more detail in Chapter 5.

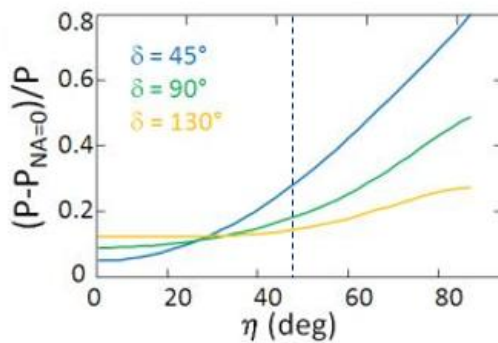
a) Wobbling bias



b) Single-molecule parameters



c) Polarization factor bias



d) Reduced intensity

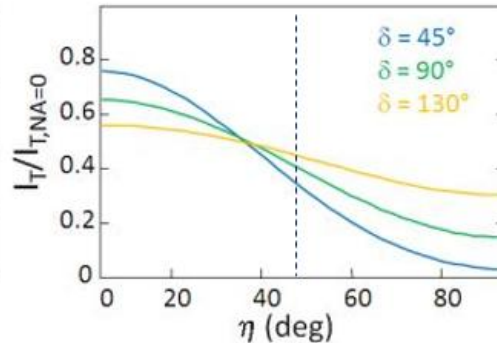


Figure 3.22 – Figure tilted bias in polar-dSTORM. (a) Quantifying the bias in the polarization factor curve when the fluorophore dipole is tilted in  $\eta = 45^\circ$ . Straight lines, when in-plane labels, dashed lines when  $\delta$  is biased. We see in (a) that, the biases due to the tilting of  $\eta = 45^\circ$  are not the same for all in-plane orientations (compare straight and dashed lines at  $\rho$  angles of  $45^\circ$  and  $90^\circ$ ), and the bias is also not the same depending on the wobbling angle (compare  $\delta=40^\circ$  and  $\delta=130^\circ$ ). We highlighted in this image that, whenever the wobbling angle is narrower, the bias is higher. Particularly for the  $\rho=90^\circ$  case, the bias when  $\delta=40^\circ$  is around 30% and when it is  $\delta=130^\circ$  the bias is only 5%. (b) Anisotropy normalized bias with different wobbling angles ( $\delta=40^\circ$ ,  $\delta=90^\circ$ ,  $\delta=130^\circ$ ). The particular **vertical and dashed line is  $\eta = 45^\circ$** . Here we see that for narrower wobbling angles ( $\delta=40^\circ$  case), the bias grow rapidly whenever increasing the tilted angle  $\eta$ . (c) Effect on the detected intensity depending on the tilting and wobbling angles of the fluorophore. We note that for narrow wobbling angles such as  $\delta=40^\circ$ , the detected intensity decreases more rapidly than for wider wobbling angles ( $\delta=130^\circ$ ) whenever tilting the angle. Here, the simulated values are calculated for a detection NA of  $NA = 1.2$ , and compared to  $NA \sim 0$  for comparison to a system not sensitive to off-plane tilt angles). Figure adapted from [59].

To summarize, in this configuration of polarization split, we cannot rigorously generalize the statement that the orientation measurements are fully independent of the fluorophores, because there is some potential wobbling bias. Nevertheless, we could probe the structural organization of structures of known 2D organization (for instance filaments lying in the sample plane, Figure 3.21 C-column), in the approximation of probing “cylindrically symmetric structures in 2D”.

The limitations stated above have led us to develop a more rigorous approach, which can measure  $(\rho, \delta)$  independently, with no ambiguity on  $\rho$ . To access this possibility, it is obvious

that one has to add extra polarization information, e.g. project the fluorescence signal on additional polarization states. Similarly as for linear dichroism described in Chapters 2 and 4, it is visible that at least 4 polarization angles are necessary for a non-ambiguous retrieval of the orientation and wobbling parameters. The development performed in this work, described below, is still done in the 2D hypothesis (e.g. it estimates in-plane projections and does not access the  $\eta$  angle), which is appropriate for a large variety of in-plane biological structures. We will nevertheless use strategies, to minimize the tilt-angle induced bias on  $\delta$ , based on quite low NA detection as described above.

### III.5 The 4polar-dSTORM method: 4 polarized analyzer channels

#### III.5.1 The state of the art in 4 polarized-split detection for polarized fluorescence imaging

There are a few examples in the literature of multiple polarization split detection for polarized fluorescence imaging, for ensemble or single molecule measurements. An important development of simultaneous detection of 4polarizing channels combined with sequential 2polarization of excitation, has allowed 3D orientation retrieval or unbiased orientation retrieval in 2D, making the technique attractive for real-time/live cell experiments [86, 87]. The 3D information, in this work, was obtained thanks to the combination of both excitation and detection polarization control, which is not appropriate to dSTORM since it requires sequential measurements. Removing the sequential excitation requires some hypotheses such as 2D-orientation (which imposes  $\eta = 0^\circ$ ), or fixed molecules (which imposes no-wobbling,  $\delta \sim 0^\circ$ ). This has been published in schemes using *4 different polarized channel detection* most often ignoring the presence of wobbling. The first published example is from Ohmachi et al. for the detection of 3D myosin orientations in vitro (supposing no wobbling) [94]. Later, Mehta et al used a similar scheme on fluorescently labeled DNA and F-actin network sparsely labelled at the leading edge of migrating human keratinocytes, septin-GFP molecules incorporated in septin bundles in growing hyphae of a filamentous fungus [95]. In this work, the authors have probed sparsely labeled actin filament flow in the lamella of living cells. Although they reached polarized and single-molecule capabilities, they did not use a super-resolution localization algorithm, so that their data is diffracted limited. Note that also in this work, a detection NA of 1.49 was used, therefore the data are potentially strongly biased by off-plane molecules detection (see Chapter 5), and wobbling information cannot be easily interpreted.

At last, two recent works have used 4-polar split detection to image membrane proteins orientational changes in 3D. These works have used a pre-knowledge of wobbling from an expected modelled structure, to infer tilt angle 3D information: [82, 93]. Both works use Rosetta modelling to provide statistically probable direction for GFP linked to the protein of interest (integrin), using a rigid labelling. The results, in these works, rely however on strong hypotheses on the molecular structure that cannot be verified in the biological sample, and do not provide super resolution imaging capabilities.

In the next section, we describe the system developed during this PhD work, which aim was to measure quantitatively orientation and wobbling parameters in 2D, together with single molecule localization, in order to retrieve structural information on actin assemblies in cells. This

method is named 4polar-dSTORM, as it uses 4 analyzed polarization directions and a dSTORM capabilities for molecular spatial localizations.

### III.5.2 The 4polar-dSTORM setup

We used the same inverted microscope (Nikon, Eclipse Ti-U) for ensemble and for single-molecule polarized microscopy in epifluorescence mode. The 488nm laser excitation beam maximum power is controlled in the same Multicolor Laser Excitation unit as the ensemble setup (Figure 3.6). However, in contrast with the polar-spinning disk setup, the single-molecule setup uses different microscope ports for the excitation and for the emission paths (see Figure 3.23).

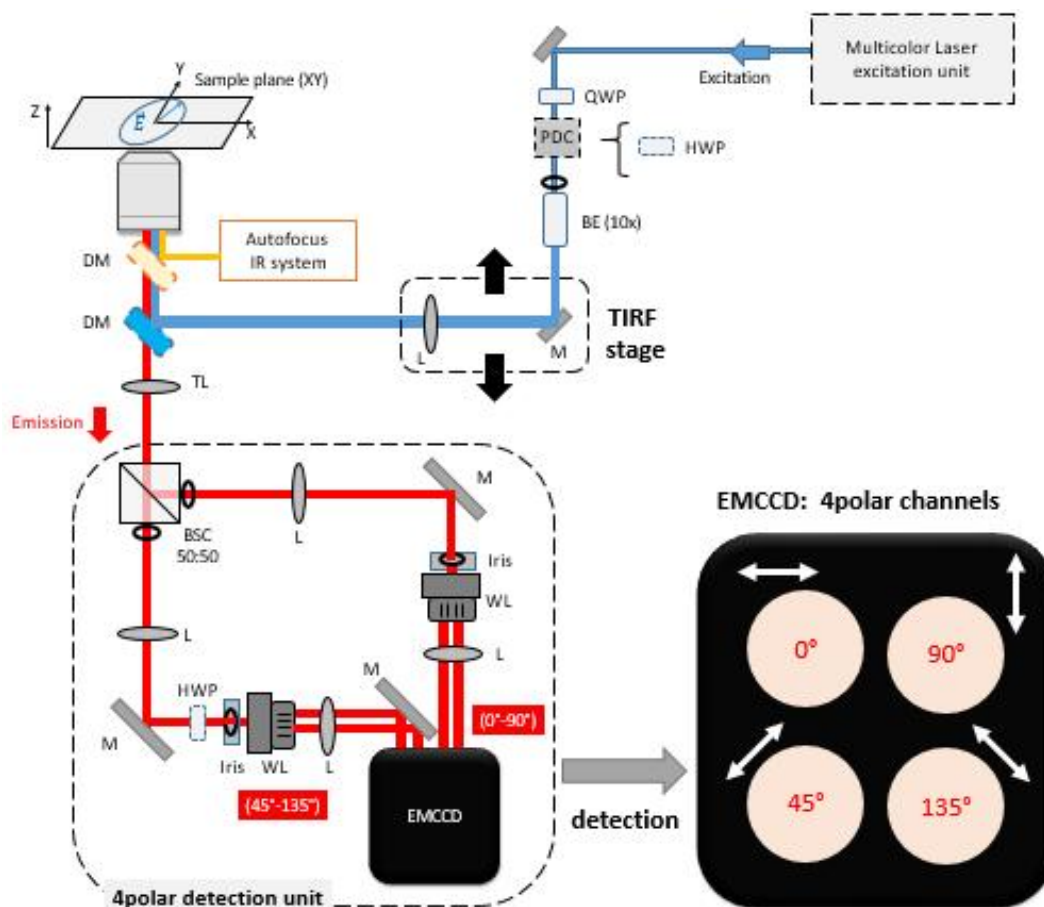


Figure 3.23 – The 4polar-dSTORM setup. Here, the 488nm laser light passes through a quarter-wave plate (QWP) and a half-wave plate (HWP) to guarantee homogeneous excitation in all direction in the field of view for any wide-field illumination scheme (see text below). The HWP acts as a polarization distortion compensator (PDC) as explained in the text below. Then, we enlarge the beam profile (beam expander, BE) and choose the wide-field illumination type by translating the TIRF stage, composed by a silver mirror (2") and a lens (2", focal distance 250mm) that focus the beam light at the back focal plane (BFP) at controlled BFP positions (see Figure 2.19 and Figure 3.24). The homogeneous excitation guarantees that all labels in the sample plane are excited, with no preferential orientation (photo-selection). The excitation beam passes through the dichroic mirror (DM), excites the sample and make the single-molecules to emit their polarized light. The polarized fluorescence passes through the same dichroic mirror (which has an emission filter mounted in the same filter wheel box), subsequently reaching the tube lens (TL, typically with 1.0x magnification). The polarized light finally reaches the 4polar detection unit, responsible for splitting the beam into 4 projected polarization resolved analyzer channels (0°, 45°, 90°, and 135°). The details of the 4polar

detection unit is described in more detail below. HWP, half-wave plate. QWP, quarter-wave plate. PDC, polarization distortion compensator. BE, beam expander. M, mirror. L, lens. DM, dichroic mirror. TL, tube lens. BSC, beam splitter cube. WL, Wollaston prism. EMCCD, electron multiplying charged coupled device camera.

For any wide-field (Epi, tilted incidence (e.g. with incidence angle below the critical angle), or Total Internal Reflection Fluorescence (TIRF, e.g. at or above the critical angle) excitation configuration chosen in the TIRF stage (see Figure 2.19 and Figure 3.24), the ideal excitation beam for the 4polar-dSTORM experiments must be homogeneous in all transverse directions at the sample plane. For example, in the simplest Epi-configuration case, a normal incidence collimated beam with circularly polarized light (or with unpolarized light) could be used to avoid privileged sampling orientation bias. Hence, in order to transform the linear polarized light into a circularly polarized beam, we added in the excitation path a quarter-wave plate, QWP (Thorlabs AQWP05M-600). The main axes of the QWP should be  $45^\circ$  oriented in relation to the incoming linear polarized beam from the laser.

For the tilted incidence and TIRF illumination cases, care must be taken because a tilted illumination scheme is used, affecting the transverse polarization state that is projected on the 2D plane of the sample, but also adding a longitudinal contribution to the excitation. Due to the tilted wave front, the relative phase between  $E_x$  and  $E_y$  projected in 2D is different than the circular polarized light. Such spatial dephasing is proportional to the tilted angle and can be pre-compensated by a polarization distortion compensator (PDC): instead of using circularly polarized light, one could use an elliptical polarized light which the projected wave on the 2D plane of the sample yields a circular polarized light.

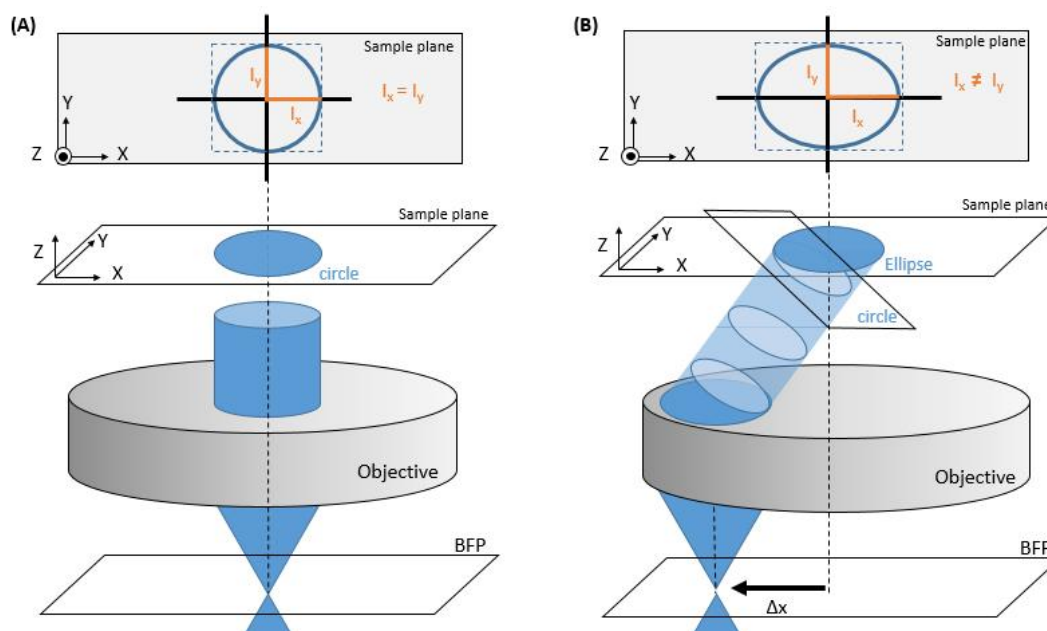


Figure 3.24 – Choice of wide-field illumination type (normal, tilted or TIRF) rely on focusing the beam at different positions in the back focal plane (BFP) of the objective. If the beam is axially aligned with the objective axis, the incidence is named normal or epi (see A). When the focus spot is translated from the main axis (by increasing  $\Delta x$ ), the excitation beam gets more tilted (see B). When the tilting angle reaches a critical angle, total internal reflection (TIR) takes place, and an evanescent wave penetrates the sample just a few hundreds of nm from the coverslip. Tilted

excitation might provide signal with lower background depending on the thickness of the sample. In particular, when in TIR, it guarantees low bulk background because the sectioning is restricted to the superficial molecules close to the coverslip. Important, inclined excitation distort the beam profile and phase relationships between the S (out of optical plane) and P (within the optical plane) polarization components of the light. The component intensity at the sample plane that is parallel to the spatial focus shift ( $\Delta x$ ) is spread over a larger area, decreasing in effective intensity. In other words, the X-component of the light has lower intensity than the Y-component (see B). This means that a perfect Gaussian circularly symmetric profile shape would be projected on the sample plane like an elliptical shape distorted along X. In order to get back a perfect Gaussian profile projected on the sample plane, a specific elliptical profile could have been used for that. Analogously, to compensate the polarization distortions of inclined illumination we must elliptically polarize the incident beam with the main axis of the ellipse aligned to the axis of the focus spot displacement (i.e., aligned to the x-axis in the figure).

Such specific elliptical polarized light can be generated by combining a slightly rotated QWP from its main axis, creating an ellipse with semi-axis power ratio of  $(I_{\max}/I_{\min}) > 1$  instead of circular polarized light  $(I_{\max}/I_{\min}) = 1.00$ . Then, by using a half-wave plate, HWP (Thorlabs AHWP05M-600) after the slightly tuned QWP we can adjust the orientation of the ellipse to be aligned to the main axes of the sample plane, so that we get homogeneous excitation on 2D plane. Here, the orientation set by the HWP acts a polarization distortion compensator (PDC) on the 2D sample plane. To know which elliptic light to send for a given tilt angle configuration, simulations have been performed on the electromagnetic fields at an interface between the sample (made of a refractive index close to that of water) and the glass substrate. This simulation permits also to quantify the amount of longitudinal contribution introduced along the Z axis, which can also affect the influence of 3D tilts angles in case of high NA detection. This aspect will be investigated in more detail in Chapter 5.

After the PDC (made of both HWP and QWP), the excitation beam passes through a 10x beam expander (Thorlabs GBE10-A), to guarantee a homogeneous and wide field of view (FoV) profile, and through a homemade TIRF translation stage. The latter is mechanical stage with manual micrometer control (Thorlabs XRN25P) which moves together a 2" silver mirror (Thorlabs PF20-03-P01) and a focusing lens (focal distance =250mm, Thorlabs AC254-250-A-ML). The mirror mount and the focusing lens mount are further connected to each other via a caged ER rod system. Such caged system is stable enough to guarantee that for any lateral translation on the stage, the 2" silver mirror will always reflect light onto the center of the focusing lens. Thus, the TIRF stage provides a manual control on where the focused spot is laterally positioned on the BFP of the objective (Nikon plan APO, 100x, NA=1.45, Oil immersion), which allows to perform Epi (normal incidence), tilted incidence or TIRF microscopy.

After passing through the TIRF unit, the beam is reflected by a dichroic mirror (Di02-R488 Semrock). Then, the beam passes through the top filter wheel, that has a mid-IR dichroic mirror (for autofocus purposes), and it finally focuses on the BFP of the objective, generating a collimated beam of around 3 mm diameter at the sample plane. The excitation beam for dSTORM purposes has around 40mW power at the BFP of the objective, yielding approximately  $0.56 \text{ W/cm}^2$  ( $5.6 \text{ kW/m}^2$ ) on the sample plane.

The fluorescence light generated by the sample is collected by the objective and is transmitted through both dichroic mirrors (DM), and is filtered by an emission filter (EM525/50 chroma, placed in the dichroic mount). The detected beam then passes through the tube lens of



the microscope (with 1.0x or 1.5x possible magnification) and it finally exits the microscope by its right side port, reaching the 4polar detection unit (Figure 3.25). The latter is responsible to simultaneously detect on the EMCCD camera chip (Andor Ixon Ultra 888, 1024x1024 pixels, 13 $\mu$ m pixel size) the 4 projected images of the whole FoV, each of these images are proportional to their respective polarization states (channels 0°, 45°, 90° and 135°). The 4polar detection unit is better described in the following section.

### III.5.3 The 4polar detection unit

The aim of the 4polar detection unit is to detect 4 analyzed directions of the fluorescence emission, along pre-defined directions, using optical path splitting and polarization beam splitters. To do so, right after the emission beam exits the microscope port, we use a non-polarizing beam splitter (BS) cube to divide the beam equally in two (Thorlabs, CM1-BS013, 400-700nm, 50:50, pol-insensitive). For each new path, we connected an iris mount to the BS mount on the caged system (Thorlabs, CP20S). Such diaphragms are positioned in the intermediate image plane (conjugated to the sample plane) and their opened diameter can limit the image FoV projected on the camera (see Figure 3.25).

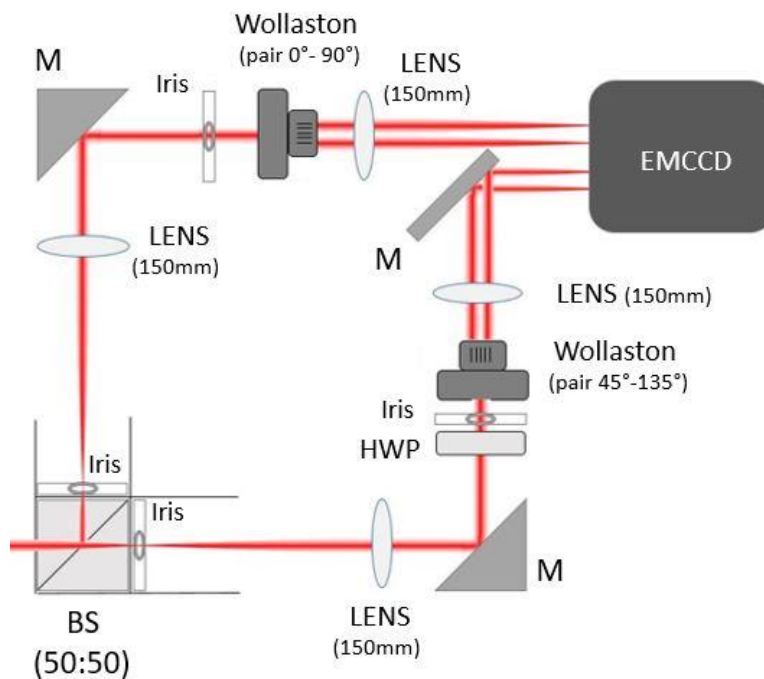


Figure 3.25 – The 4polar detection unit. After the light have passed the tube lens (TL, Figure 3.23), the light exits the microscope right port and passes through a 50:50 non-polarizing beam splitter (BS) cube dividing the polarized emission equally in two. An iris is placed on each focus spot of the two new beams and they are collimated back with 150mm lenses. The collimated light is then reflect by 2'' silver mirrors (M). Then, an iris controls the detection NA of each collimated beam, that we reduced from NA=1.45 to NA=1.20 to filter tilted components of the light. A Wollaston prism is placed on each arm to project 0° and 90° (horizontally) and 45° and 135° (diagonally). In order to projected both FoV parallel to each other on the camera chip, a HWP was placed (see Figure 3.26 and Figure 3.27). Finally all 4 polarized channels reaches simultaneously the EMCCD camera, providing instantaneous detection.



For each new path, we added a pair of 150mm focus distance achromatic lenses (Thorlabs, AC508-150-A-ML) in a 4f-system configuration (with 1x magnification). Within each pair of lenses, we added an iris in on a plane conjugated to the BFP of the objective (whose diameter controls the detection NA of each path) and a Wollaston prism (with 2° angular separation, Edmunds Scientific) whose orientation defines the orientation of the analyzer channels. At last, a square mirror is added in one of the paths to reflect the image onto the camera chip. Note that this mirror is set such as one path arrives on the top part of the camera chip, while the other arrives below. For this, small tilt angles of the mirrors have to be carefully adjusted.

The Wollaston prisms are then set to detect 4-polarization angles, the simplest being 0°, 45°, 90° and 135° polarization directions. If the Wollaston prism in one path is oriented at 0°, it will split the beam into two orthogonal beams 0° and 90° channels. Thus, to probe 4 analyzer channels such as 0°, 45°, 90° and 135° it is enough to orient the Wollaston prism of the analyzer pair 0°-90° aligned to 0° orientation, and the Wollaston prism of the pair 45°-135° should be aligned to 45° orientation in relation to the other (see Figure 3.26). By doing so, the channel pair 45°-135° would be projected in diagonal onto the EMCCD camera.

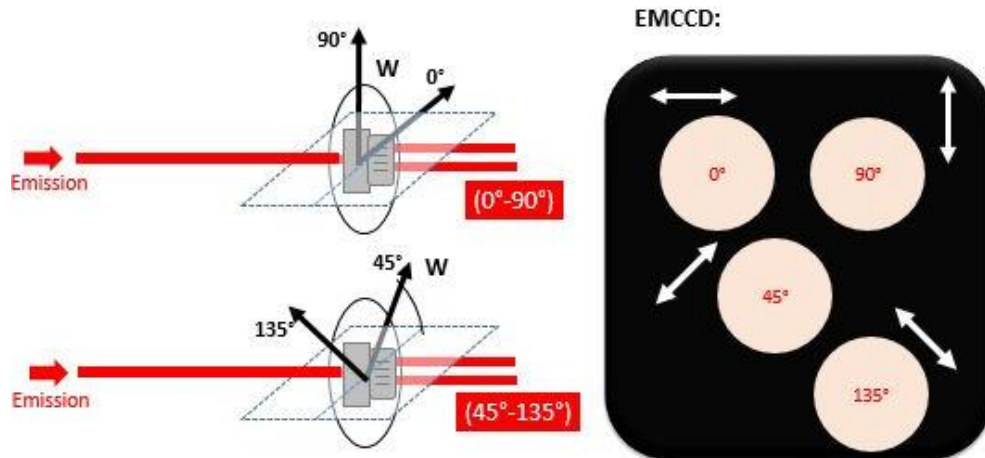


Figure 3.26 – Conventional 4 polar channels thanks to 2 polarizing Wollastons prisms (W). One Wollaston prism with axis aligned to 0° splits the beam in 0° and 90°. The other one is placed aligned to 45°, splitting the beam in a 45° and 135° in a diagonal position.

To profit more from the available space of the EMCCD camera chip, we added a HWP before the Wollaston prism of the pair 45°-135°. Instead of rotating the Wollaston, we keep it aligned at 0° (yielding another horizontal distributed pair), but we rotate the HWP placed before the Wollaston in an angle to yield 45° rotation of the polarization (i.e., HWP aligned at 22,5° in relation to the main axis of the system, see Figure 3.27). Thanks to that configuration, the available area (FoV) per polarization channel could be increased (the current FoV diameter is approximately 40µm for tube lens magnification= 1.0x).

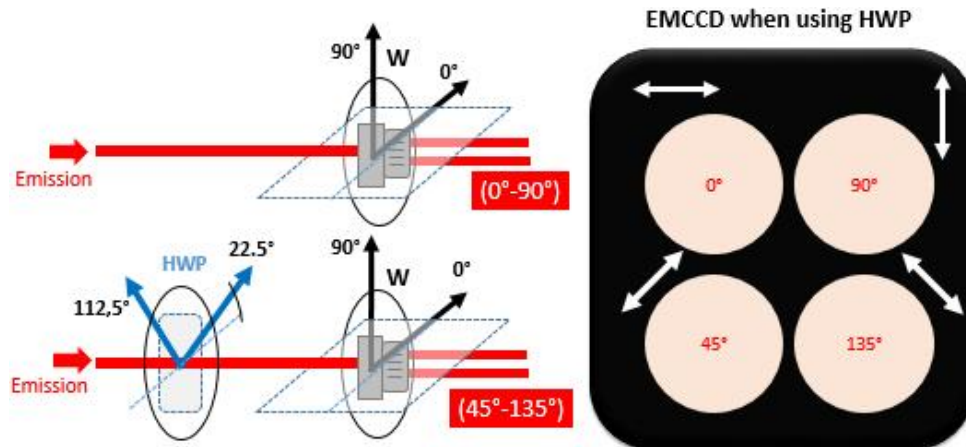


Figure 3.27 – The 4 polar channels thanks to 2 polarizing Wollastons prisms (W) and a Half-wave plate (HWP, blue). One Wollaston prism with axis aligned to  $0^\circ$  splits the beam in  $0^\circ$  and  $90^\circ$ . A HWP is placed to rotate all the polarized emission in  $45^\circ$  and the Wollaston prism is also placed aligned to  $0^\circ$ , yielding two horizontal channels of  $45^\circ$  and  $135^\circ$  projections. The advantage of this approach is that a wider FoV is achieved.

### III.5.4 The autofocus system

Axial defocusing enlarges the size of the point spread function (PSF), decreases the measured intensity, and hampers the localization precision. An autofocus system developed by Serge Monneret, from our group, can keep the focal position stable in between a few tens of nanometers (typically 50nm). Such system guarantees the focus to remain stable throughout the whole dSTORM experiment (typically takes 45min).

The idea of the autofocus system is based on the detection of the center of mass position of a reflected IR beam on the coverslip surface. If the coverslip is z-displaced, the reflected beam would be detected in a different position in a complementary metal-oxide-semiconductor (CMOS) camera (Thorlabs). By calibrating the z-drift for each center of the mass position, a linear dependence is expected. Therefore such calibration curve could be used in a feedback loop to keep the z-position stable within a range (in our case, within 50nm, with accuracy of a few nm). The user could crop the CMOS FoV to better calculate the centroid position. The program was developed in LabView platform so that the feedback loop and calibration processes with the piezo stage (National Instruments) are automated (see Figure 3.28). The laser system is an IR diode laser (980nm) coupled with an optical fiber. The laser passes through a beam splitter pellicle (BP245B3, R/T 45/55, 2" diameter, Thorlabs), that will also deflect the reflected beam (from the coverslip at the sample plane) to the CMOS camera (see Figure 3.28). Different Z-displacements at the sample plane would correspond to different centroid position at the CMOS camera.

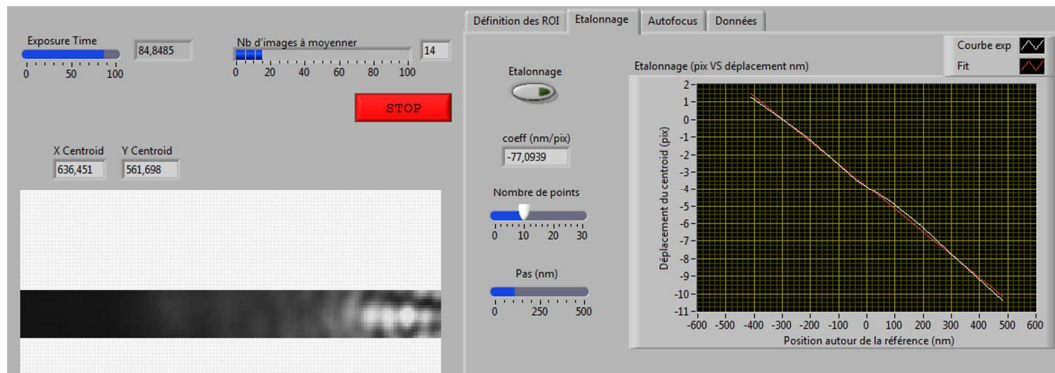
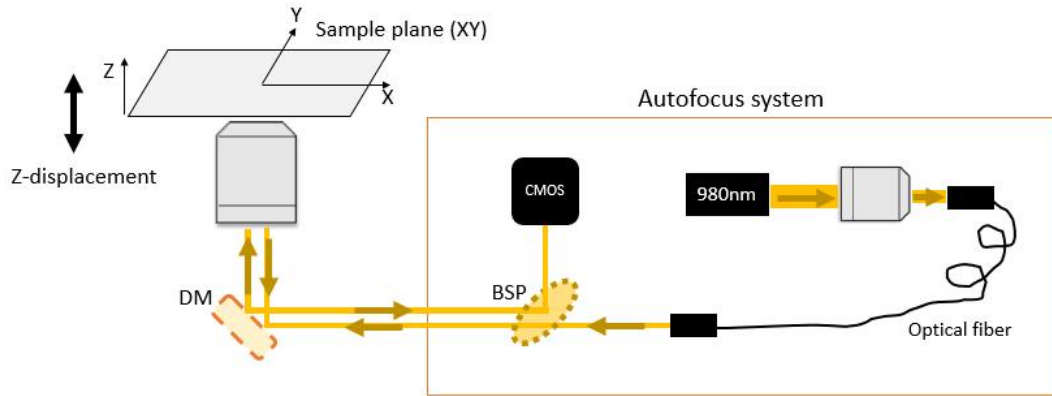


Figure 3.28 – The autofocus setup (top) and LabView platform (bottom). DM, dichroic mirror. BSP, beam splitter pellicle. In the labview (bottom). On the bottom left, a cropped region of FoV that is used for calculating the PSF centroid position displacement. When a Z-displacement in the coverslips takes place, the position of the bright drifts laterally in the CMOS camera. On the bottom right, a calibration curve (data points in white, and linear fit in red).

### III.5.5 The 4polar-dSTORM method: retrieval of orientation and wobbling parameters from a single molecule

Since we have already given the principles of polarized optical microscopy in Chapter 2, we will describe in a more direct way the equations necessary to derive the intensities measured by 4polar-dSTORM. We assume a homogeneous excitation polarization in the field of view (e.g. all polarization directions are identically excited in the sample plane), which allows us to ignore the excitation part of the equations in Eq. 2.33, and keep only what concerns the emission dipoles. We can then write the measured intensities as functions of the spherical orientation angles in the laboratory frame ( $\theta, \Phi$  of each fluorophore emission dipole  $\vec{\mu}_{em}(\theta, \Phi)$ , denoting  $(\mathbf{u}_0, \mathbf{u}_{90}, \mathbf{u}_{45}, \mathbf{u}_{135})$  the unit vectors that define the analyzer directions along the  $(0^\circ, 90^\circ, 45^\circ, 135^\circ)$  angles:

$$I_0 \propto |\vec{\mu}_{em} \cdot \vec{\mathbf{u}}_0|^2 = \cos^2(\Phi) \sin^2(\theta)$$

$$I_{90} \propto |\vec{\mu}_{em} \cdot \vec{\mathbf{u}}_{90}|^2 = \sin^2(\Phi) \sin^2(\theta)$$

$$I_{45} \propto |\vec{\mu}_{em} \cdot \vec{u}_{45}|^2 = \cos^2(\Phi - \frac{\pi}{4}) \sin^2(\Theta)$$

$$I_{135} \propto |\vec{\mu}_{em} \cdot \vec{u}_{135}|^2 = \sin^2(\Phi - \frac{\pi}{4}) \sin^2(\Theta)$$

Eq. 3.13

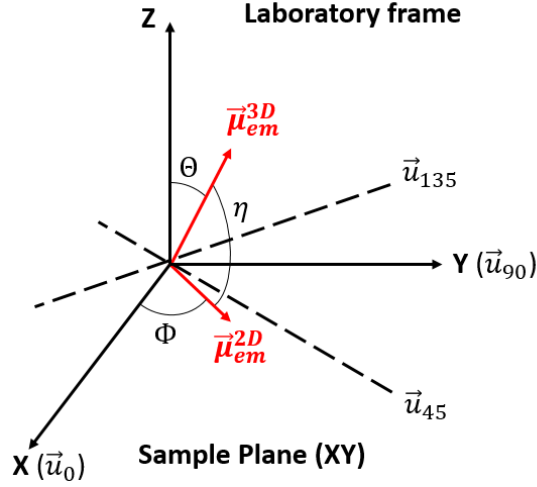


Figure 3.29 – Laboratory (macroscopic) frame. See that the analyzer channels ( $\mathbf{u}_0, \mathbf{u}_{90}, \mathbf{u}_{45}, \mathbf{u}_{135}$ ) are parallel to the sample plane (XY).

Where the equations for  $I_{45}$  and  $I_{135}$  are basically the same as  $I_0$  and  $I_{90}$  except for an angular shift of  $\frac{\pi}{4}$ . Note that here for simplification we do not account for possible polarization mixing due to high NA detection (see Eq. 2.21), but these equations could be adapted to such cases using Eq. 2.21.

To account for wobbling, one has to sum all intensities over the explored angles of the molecule during the integration time of the camera. Similarly as for linear dichroism in Chapter 2, we include the cone model  $f_{\rho, \delta, \eta}(\theta, \phi)$  into the equations (note that  $(\theta, \phi)$  are the local angles in the cone framework):

$$f_{\rho, \delta, \eta}(\theta, \phi) = \begin{cases} 1, & \text{for } 0 \leq \theta \leq \frac{\delta}{2}, \quad 0 \leq \phi \leq 2\pi \\ 0, & \text{elsewhere} \end{cases} \quad \text{Eq. 3.14}$$

Therefore the intensities are finally written:

$$I_0(\rho, \delta, \eta) \propto \int_0^{2\pi} \int_0^{\frac{\delta}{2}} |\vec{\mu}_{em}(\theta, \phi, \rho, \eta) \cdot \vec{u}_0|^2 f_{\rho, \delta, \eta}(\theta, \phi) d\theta d\phi \quad \text{Eq. 3.15}$$

And similarly for the 90°, 45°, 135° directions. Note that the proportionality sign  $\propto$  means that the factor of proportionality does not matter, since the measurements are all normalized relative to the total intensity  $I_T = (I_0 + I_{90}) = (I_{45} + I_{135})$ . Here, the dipole is expressed in the local cone frame with angles  $(\theta, \phi)$ , to simplify the integral expression :  $\vec{\mu}_{em}(\theta, \phi, \rho, \eta) = \vec{R}_{\rho, \eta} \vec{\mu}_{em}(\Theta, \Phi)$  with  $\vec{R}_{\rho, \eta}$  the rotation matrix between the cone and the macroscopic frame (similarly as explained in Chapter 2).

To simplify the writing of the expression relating the measured intensities  $(I_0, I_{90}, I_{45}, I_{135})$  and the  $(\rho, \delta)$  parameters, we derive below the equations of the intensities, supposing that the cone is lying in the plane  $(\eta = 0^\circ)$  and that all dipoles are lying in the plane (model of a 'flat' 2D cone, see Figure 3.33),  $\Theta = 90^\circ - \eta$ . We will see next that the obtained results are very close to the ones obtained from the 'real' cone. The 'flat' cone supposes that  $\vec{\mu}_{em}(\Theta = 90^\circ, \Phi)$  is only dependent on  $\Phi$  and lies in the sample plane. Therefore the intensities simplify into:

$$\begin{aligned}
 I_0 &\propto \int_{\rho-\frac{\delta}{2}}^{\rho+\frac{\delta}{2}} d\Phi. \cos^2(\Phi) = +\frac{1}{2} \cos(2\rho) \sin(\delta) + \frac{\delta}{2} \\
 I_{90} &\propto \int_{\rho-\frac{\delta}{2}}^{\rho+\frac{\delta}{2}} d\Phi. \sin^2(\Phi) = -\frac{1}{2} \cos(2\rho) \sin(\delta) + \frac{\delta}{2} \\
 I_{45} &\propto \int_{\rho-\frac{\delta}{2}}^{\rho+\frac{\delta}{2}} d\Phi. \cos^2\left(\Phi - \frac{\pi}{4}\right) = +\frac{1}{2} \sin(2\rho) \sin(\delta) + \frac{\delta}{2} \\
 I_{135} &\propto \int_{\rho-\frac{\delta}{2}}^{\rho+\frac{\delta}{2}} d\Phi. \sin^2\left(\Phi - \frac{\pi}{4}\right) = -\frac{1}{2} \sin(2\rho) \sin(\delta) + \frac{\delta}{2}
 \end{aligned} \tag{Eq. 3.16}$$

From these expressions, two polarization factor can be calculated, which we denote  $(P_0$  and  $P_{45})$ :

$$\begin{aligned}
 P_0 &= \frac{I_0 - I_{90}}{I_0 + I_{90}} = \cos(2\rho) \frac{\sin(\delta)}{\delta} \\
 P_{45} &= \frac{I_{45} - I_{135}}{I_{45} + I_{135}} = \sin(2\rho) \frac{\sin(\delta)}{\delta}
 \end{aligned} \tag{Eq. 3.17}$$

Note that in practice, the intensities are corrected by correction factors that are preliminary determined, to correct for the polarization distortions present in the detection path. This procedure is described in Chapter 5.

The quantities  $(P_0, P_{45})$  present the advantage to be independent on the total intensity of the molecules, thanks to normalization. We can then invert these two equations and obtain the two disentangled parameters independently:

$$\rho = \frac{1}{2} \arctan\left(\frac{P_{45}}{P_0}\right) \quad \text{Eq. 3.18}$$

$$\frac{\sin^2(\delta)}{\delta^2} = (P_0)^2 + (P_{45})^2 \quad \text{Eq. 3.19}$$

From the equations above we can see that the single-fluorophore orientation  $\rho$  has a relation proportional to the arctangent of ratio of  $P_0$  and  $P_{45}$ , which is a monotonic function throughout the domain. The fact that it is a monotonic function implies that there is no ambiguity in the determination of the orientation  $\rho$ , in contrast to the previously developed method based on 2 polarization measurements.

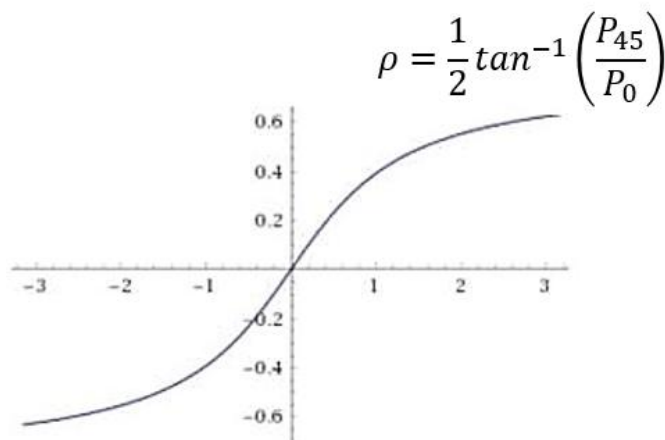


Figure 3.30 – The  $\tan^{-1}(x)$  function is monotonic. Plot done with WolframAlpha online from  $-\pi$  to  $\pi$ .

For the wobbling angle ( $\delta$ ), we see that the equation obtained is a classic parametric equation of a circle whose radius is a monotonic function in the domain of  $[0, \pi]$ , showing that there is also no ambiguity in the determination of  $\delta$ . Importantly,  $\delta$  can be determined independently on  $\rho$ , which was not possible using the 2polarization set up described above. The access to 4 polarization states gives therefore an unambiguous and unique value for both  $(\rho, \delta)$ , under the hypothesis of in-plane orientation of the wobbling cone.

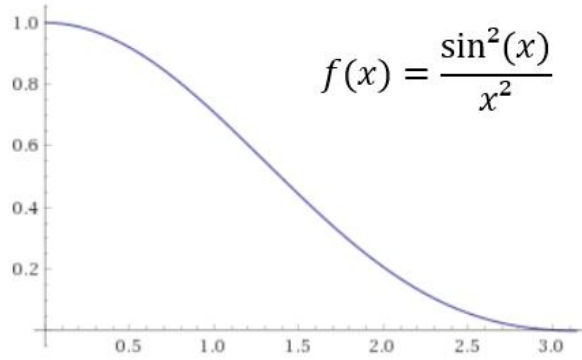


Figure 3.31 – The  $\text{sinc}^2(x)$  function plotted at Wolfram Alpha online from 0 to  $\pi$ .

Figure 3.32 plots the dependence of all accessible  $(P_0, P_{45})$  values as functions of the  $(\rho, \delta)$  parameters. These parametric circular plots highlight that it is possible to obtain orientation and wobbling independently and without ambiguity, because there is always a unique point in the plot for each  $(P_0, P_{45})$  pair. The latter confirms the unicity of the parameter pair  $(\rho, \delta)$ , because  $P_0$  and  $P_{45}$  are two independent measurables.

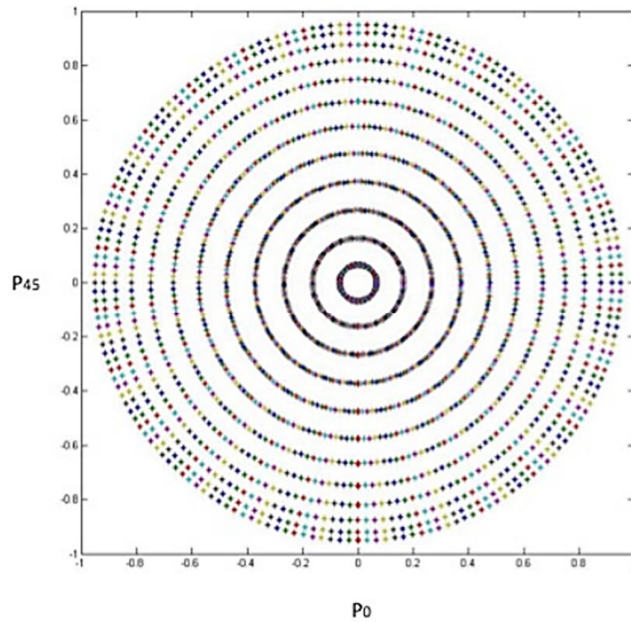


Figure 3.32 - Simulated plots demonstrating the unicity of each polarization factor pairs and parameter pair combination  $(\rho, \delta)$ . Each point corresponds to a particular  $(\rho, \delta)$  situation. The longer the radius of the shown circles, the higher the anisotropy factors, and the narrower the wobbling angle.  $\rho$  appears as the angle of rotation on the shown circles.

In Figure 3.33, we compare the obtained expressions of the ‘flat’ cone model with that of the ‘real’ cone model lying in the sample plane (called ‘full cone’). The  $(P_0)^2 + (P_{45})^2$  values, used to retrieve the  $\delta$  parameter in a flat cone model, is seen to be very close to that obtained from a full cone model. It is therefore reasonable to use such model for processing simplification, within an error of about 10%. Note that the determination of  $\rho$  is not affected by the cone model used, since this value points the mean direction of the cone projected in the sample plane, which is model independent.

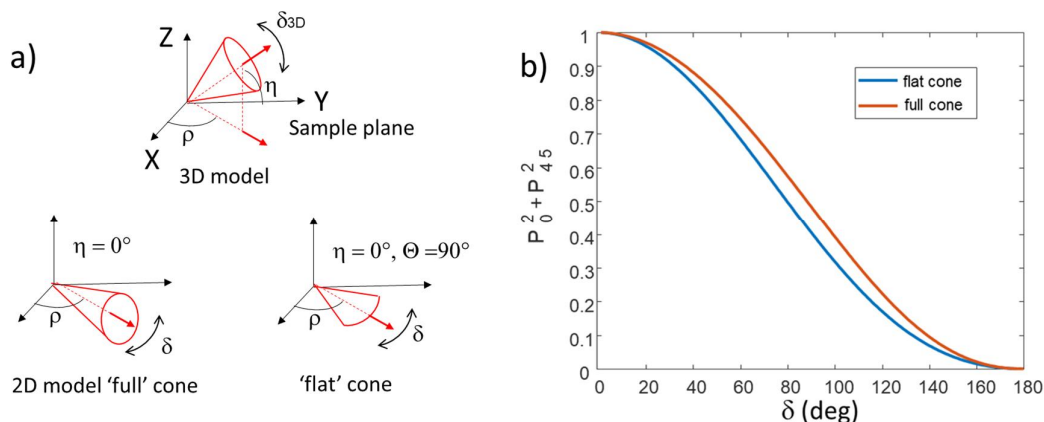


Figure 3.33 – Comparison between the ‘full cone’ model lying in the plane and the flat cone model. These cones are defined in (a). (b) shows the resulting calculation of  $(P_0)^2 + (P_{45})^2$  as functions of  $\delta$ . Simulation (b) performed by Valentina Curcio.

### III.5.6 The 4polar-dSTORM: overcoming the polar-dSTORM limitations

The major advantages of the technique are now clear: one could probe any biological structure geometry in 2D at the nanoscale, without any a priori knowledge of the sample, and the structural organization obtained is an absolute value, i.e., it is purely due to the biological structure, and does not suffer from label rotational mobility properties (wobbling). Here we use the term “absolute” to contrast all the other previous polarimetric techniques that can only be considered “relative or comparative”. Absolute here is emphasize the fact that it is the polarimetric technique capable of retrieving directly the structural organization of biomolecular structures, without any extra a priori knowledge of the sample or without the need of a referential measurement (relative or comparative study).

It is worth here to emphasize the strengths of the novel technique: the 4polar-dSTORM is a super-resolution, single-molecule, polarization resolved, fluorescent labelled optical microscopy technique which the retrieved orientations of the fluorophores are dependent only due to the biological structure of interest, and are not biased anymore by the fluorophore dynamic properties. Therefore, for us, the structural organization of our biomolecular structure of interest (SOI = actin filaments within stress fiber bundles) is a structural information at the nanoscale probed by fluorescent probes in an unbiased manner. Importantly, the wobbling is still vulnerable to bias due to tilted fluorophore angles. The wobbling sensitivity to tilted angles could be exploited or avoided.



### **III.6 Conclusions of Chapter 3**

The goal of this chapter was to give an overview of the most recent techniques that combine polarization with fluorescence microscopy, including super-resolution methods based on single molecule localization. This PhD thesis in particular profits from integrating two setups in the same epi-fluorescence microscope: an ensemble and a novel single-molecule polarization-resolved microscopy techniques. The latter, in particular is a novel polarization resolved super-resolution localization microscopy method, called 4polar-dSTORM, based on an improvement of a previously developed polar-dSTORM technique.



## Chapter 4

# Ensemble Polarized Fluorescence Microscopy applied to Actin Stress Fibers

### Introduction

Previous studies that probed the *nanoscale* organization of actin filaments in SF bundles [59, 61, 62] did not enter into the detail of comparing different SF subtypes. Oftentimes, actin stress fibers is a generic term used to describe ventral SF (contractile SFs occurring in the central part or at the peripheral boundaries of the cell, close to the substrate), however there is a large diversity of SFs, that differ in their composition (crosslinkers) and role, as described in Chapter 1. Electron microscopy (EM) studies showed that F-actin in stress fibers bundles were “well aligned” [11], when compared to other F-actin structures such as in the lamellipodia (see Chapter 1). However, to our understanding, no systematic and/or quantitative study was performed to describe how “well aligned” the actin filaments are organized in different SF bundles, if this degree of alignment depends on the SF types and their degree of contractility, and if the alignment of F-actin in SF bundles have a specific role in cells.

As we commented in Chapter 1, actin stress fibers (SF) are typically tensile bundle structures made of actin filaments in mammalian non-muscle cells that have a key role on cell adhesion, morphogenesis and motility. Particularly in human osteosarcoma U2OS cells, actin SF were categorized in different subtypes according to their localization within cells and their actin binding protein (ABP) composition [14, 16]. How such ABPs interact with actin SF could be usually monitored at cellular scale changes (microns to tens of microns) via conventional fluorescence microscopy techniques. Nevertheless, how the actin filaments are aligned or organized at the nanoscale within different SF bundles is a topic poorly studied. The latter is mainly due to the lack of suitable techniques that demands high binding specificity, imaging resolution, and wide field of view (Fov) to cover (most of) the whole bundle length. Since multiple factors dictates the stress fiber organization at the cellular scale, which affects the cell morphology, and it also reflects the cell’s response to mechanical tension with its environment (e.g., between the cell adhesions to its substrate), the stress fiber organization at the nanoscale could also be affected by the same factors. Just to mention a few important ones: cell type (e.g., naïve or mutant); cell cycle stage (e.g., not fully spread, fully spread, under division, etc); cell shape (e.g., polarized or not); cell size; stress fiber connectivity; substrate rigidity; external environment (e.g., vicinity of other cells, soluble factors, etc); presence or not of some ABP in the SF bundle (such as myosin-II,  $\alpha$ -actinin, tropomyosin, focal adhesion proteins, etc), which could be used to chemically define and distinguish stress fiber types, see Chapter1.

In this chapter, we will attempt to provide elements relating actin organization to nature and function of the SFs, by monitoring F-actin alignment by ensemble-polarized fluorescence PFM in cells. Previously, ensemble-PFM been applied on F-actin of stress fibers, comparing their F-actin organization with other F-actin structures of fruit fly *Drosophila melanogaster*, such as the F-actin of muscle sarcomeres, embryo furrow channels, and eye’s ommatium [61, 62]. In addition, SF organization was used for the purpose of proving the principle of PFM methods, and to evaluate the applicability of different labels with different linker length for polarimetry [59]. Thanks to that, we can use the knowledge of previously studied fluorescent markers on SF to calibrate our setup. We know from previous PFM studies of our group that using phalloidin-

AlexaFluor488 to label F-actin in SF yielded sub-diffraction mean orientation ( $\rho_{av}$  described in Chapter 2) that is well aligned with the bundle mean orientation [59, 61, 62]) (Figure 4.01). The parameter of sub-diffraction order (cone aperture  $\Psi$  described in Chapter 2) has been found to range between 120-130° in the very ordered sarcomere structures in drosophila pupae [61] (Figure 4.01, panels B, B') to around 130° in SFs in mammalian cells [59] (Figure 4.01, panels A, A'), and around 130°-140° in actin rings of cells contour in drosophila embryos [62].

Note that in Figure 4.01, to retrieve the  $\Psi$  histogram of fibroblast cells, the authors pooled together ROIs of different actin bundles (peripheral SF, ventral SF and filopodia) as the same category “stress fibers” (see panel A of Figure 4.01). In the present work, we would like to decipher actin alignment in specific SF types, which requires a more careful discrimination between different SFs in cells.

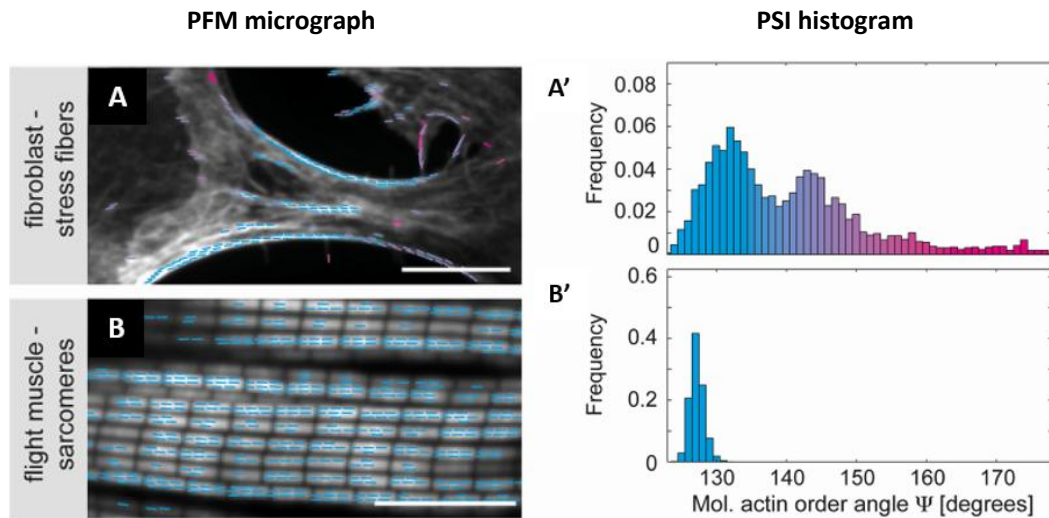


Figure 4.01 – Ensemble Polarized fluorescence microscopy (PFM) micrograph of actin stress fibers of mouse NIH-3T3 fibroblasts, and its respective PSI (order) histogram (panels A, A',  $\Psi = 130^{\circ}$ – $150^{\circ}$ ). PFM micrograph of highly ordered F-actin in mature sarcomeres of fruit fly (*Drosophila melanogaster*) muscle tissue cells, and respective PSI histogram (panel B, B',  $\Psi = 127^{\circ} \pm 1^{\circ}$ ). The white scale bars are 10 $\mu$ m. Their colorcode for PSI values is different from the one we use throughout this thesis. Figure adapted from [61].

An important conclusion of the paper mentioned here is that while it is shown that actin alignment increases in sarcomere with the age of the fly pupae, the authors demonstrate that muscle myosin motor activity was not required for high actin order build up during sarcomere maturation in fruit flies. This means that other actin binding proteins (ABP) might have a major role in F-actin sub-diffraction order build up.

The different values given in the examples cited above can be attributed to different factors, among which contractility. Based on the knowledge built up from muscle sarcomeres (the contraction machinery of muscle cells), the literature shows that mature muscles are correlated with highly aligned actin filaments, which corresponds also to the highest contractility [61]. As we saw in Chapter 1, sarcomeres are structures made of mainly F-actin, myosin filaments,  $\alpha$ -actinin, and titin molecules organized in a highly ordered fashion. SF bundles in non-muscle cells that hold myosin-II motor decoration are considered “contractile” bundles (e.g., peripheral, ventral, and transverse arcs), while the SF bundles that do not co-localize with myosin-II motors are considered “not contractile” bundles (e.g., dorsal SFs, filopodia).

Contractile SF share many of the most important biomolecular constituents of the sarcomere machinery. However, typically, the stress fibers seem to bear isometric tension, and not isotonic contraction [24].

In this chapter, we will study more carefully the influence of the SF types on the organization of F-actin filaments. We will first describe preliminary steps necessary to the calibration of the PFM method used here for the measurement of actin organization from ensemble imaging, using the spinning disk polarimetry approach described in Chapter 3. We will then describe the results obtained in naïve human osteosarcoma (U2OS) and a contractility mutant U2OS (CA-MLCK, constitutively active myosin light chain kinase gene) fixed cells labelled with phalloidin-AlexaFluor488 conjugates, focusing on the specificity of each SF fiber. For a more robust selection of SFs, we chose to study cells deposited on well identified patterned substrate of different shapes and sizes. The spinning disk PFM setup used in this chapter has been implemented by myself in the lab, with the help of Louwrens Van Dellen (engineer) for the labview interfacing part of the experiment.

## **IV.1 - Materials and methods**

### **IV.1.1 Cell preparation**

We plated between 30k to 40k U2OS cells in McCoy 5A modified complete medium on collagen coated coverslips, and let them in a CO<sub>2</sub> incubator (5-8% CO<sub>2</sub>) to spread for 10h-14h. The collagen coating on coverslips (20-mm or 18-mm of diameter) was performed with collagen solution of 25µg/ml (Rat Tail Collagen from Roche ref# 11 179 179 001), diluted in DPBS. We sterile sealed with parafilm a 12-well dish containing the coverslips immersed on collagen solution, and we put the 12-well dish into the frigo at 4°C overnight.

Experiments with a contractility mutant U2OS cell line (CA-MLCK, constitutively active myosin light chain kinase gene) could be used to further distinguish between the control (CA-MLCK U2OS cells in absence of doxycycline in the medium, “ctrl” for abbreviation) and the contractile category (CA-MLCK U2OS cells with 800ng/ml of doxycycline in the medium, abbreviated to “doxy” cell line). The category “doxy” had doxycycline in the medium during the whole process (growing, plating and spreading before fixation). We typically let CA-MLCK cells to fully spread over 6h, and made a few tests with cells still under spreading process (i.e., we fixed the cells with 4h spreading time).

Some of the experiments were performed on cells with well-defined shapes, using pre-defined fibronectin patterns (CYTOO chips) on which cells were plated before imaging. We plated 15k cells/ml of McCoy 5A modified complete medium, let them in a CO<sub>2</sub> incubator (5-8% CO<sub>2</sub>) to spread for 10h-14h on previously coated CYTOO chip with fibronectin 20mg/ml. The fibronectin coating was done per 2h @ RT, sterile, following the conventional CYTOO protocol in the manual. For more details, see Appendix-protocols.

### **IV.1.2 Imaging conditions of ensemble-PFM**

The 488nm laser power was typically 90µW at the entrance of the spinning disk unit. Typical laser power at the sample plane must be less than 180µW to avoid bleaching during the polar stack acquisition. These cells were imaged with WI Nikon 60x objective, NA=1.20, tube lens

(TL=1.5x) plus (2x) final lens magnification (see Chapter 3), yielding 72nm image pixel size. Since the camera IXON 888 ultra used for imaging has 1024x1024 pixels, each of 13 $\mu$ m size, the typical image Field of View was FoV = 73.7 $\mu$ m x 73.7 $\mu$ m. The exposure time was typically t=0.5s, and we collected a polar stack of 18 frames, with 10° linear polarization angle ( $\alpha$ ) step from  $\alpha=0^\circ$  to  $\alpha=180^\circ$ .

## IV.2 Preliminary calibrations of the setup.

The set up used in this work is based on the system described in Chapter 3, using the data analysis model described in Chapter 2. Note that in what follows, we will assume the distribution of fluorophores lying in the sample plane ( $\eta = 0^\circ$ , see Chapter 2). Since the actin SF bundles studied are mostly lying in the sample plane, and the excitation polarization also lies in the sample plane, this approximation is considered reasonable [58].

### IV.2.1 Control of the excitation polarization: polarimetry measurements

We measured the polarization state at the backfocal plane (BFP) in order to make sure that the incident polarization is properly rotating as a linear polarization with increasing angle steps. Because there is a dichroic mirror (DM) placed before the BFP (inside the spinning disk, see Chapter 3) we must investigate the possible polarization distortions of the excitation beam caused by it. We used a polarimeter made by a former PhD student, Xiao Wang, that uses the “quarter wave plate” method to obtain directly the mean orientation of the polarization ellipse ( $\theta$ ) and its ellipticity ( $\tan(\varepsilon)$ ) for each incoming angle of the polarization [52]. Briefly, the method consists in placing a polarizer after a rotating quarter wave plate, and detecting the modulation of the intensity of the light that emerges from the system, placed at the backfocal plane of the microscope objective. Thanks to a Fourier decomposition of the obtained modulation, it is possible to obtain both parameters of the polarization ellipse ( $\theta$ , the orientation angle of the ellipse, and  $\varepsilon$ , the ellipticity angle). We first used the method to evaluate the ellipticity of every input linear polarization orientation state of the light (generated by the Pockels cell system). We noticed that the polarization distortions caused by the DM of the spinning disk raised the ellipticity from  $< 0.1$  to more  $> 0.3$ . Because of that, we decided to add in the excitation path an extra QWP (QWP-488nm) in order to compensate the polarization distortions at the BFP (see options for polarization distortion compensator unit Figure 3.5). We optimized the QWP-488nm orientation in the excitation path in order to minimize the distortions of the polarized light at the backfocal plane (after the DM).

In Figure 4.02a, we see the calibration curve whose points were further interpolated for every half degree step. From that curve we could use that the approximate voltage range of -2.5V up to +2.5V applied to the Pockels cell covering all the 180° of linear polarization orientations. In such range, we may associate a single applied voltage to a specific linear orientation at the BFP. Figure 4.02a shows that a small residual diattenuation appears in the compensated distortion curve, since the voltage-angle dependence is not perfectly straight. This diattenuation is nevertheless considered negligible. On the other hand, in Figure 4.02b, we also see a residual ellipticity of  $\tan(\varepsilon) = 0.23$ , corresponding to  $\varepsilon = 12.9^\circ$ . This value is acceptable but will need to be corrected-for in the data processing step, as explained below.

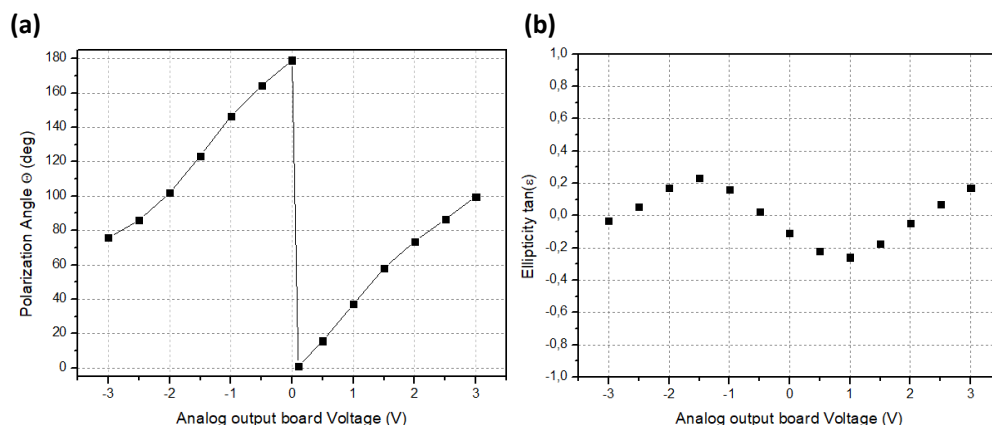


Figure 4.02 – Polarization state of the light at the backfocal plane BFP of the objective. (a) Calibration of the linear polarization orientation vs applied voltage of the Pockels cell. (b) Residual ellipticity on the excitation beam per applied voltage at the BFP.

Note that this polarization distortions' check at the BFP is also important to identify, in the interface acquisition Labview program, which input voltage to the Pockels cell corresponds to which an angle of the incident polarization in the sample plane. For this, each calibration leads to a correspondence table voltage-angle (Figures 4.02a), that is loaded in the acquisition program. This table differs depending on the wavelength used, since the Pockels cell response is wavelength dependent. On the hardware side, we need a high voltage range (hundreds of Volts) to be applied on the Pockels cell to properly modulate the polarization. Such high voltage is obtained by using a high voltage amplifier (HVA-1M, Quantum technology, whose constant offset was set to 100V) placed after the high-speed analog output board (NI-USB-6351, National Instruments, whose output range  $\pm 3V$  was used in the calibration plots Figures 4.02).

#### IV.2.2 Data representation and correction procedure of the polarization distortions for the data processing

Once the polarization distortions have been pre-characterized, it is important to account for them in the data analysis. For this, a Matlab program has been written by a previous PhD student Alla Kress [77], which simulates which polarization modulation coefficients ( $A_2, B_2$  values, Equations 3.5-6, Chapter3) corresponds to which molecular order and orientation ( $\rho_{av}, \Psi$ ) couple (we assume here that  $\eta=0^\circ$  (see Chapter 2)). Based on this lookup table, the data processing associates a ( $\rho_{av}, \Psi$ ) couple to each ( $A_2, B_2$ ) values measured at each pixel (see Chapter 3). In other words, we can assign two polarimetric ( $\rho_{av}, \Psi$ ) values per pixel after applying Fourier calculations on the polar-stack of images. Since this assignment is based on a model (Chapter 2), it can include possible polarization distortions in the incoming field such as each experimental setup can be related to a specific lookup table.

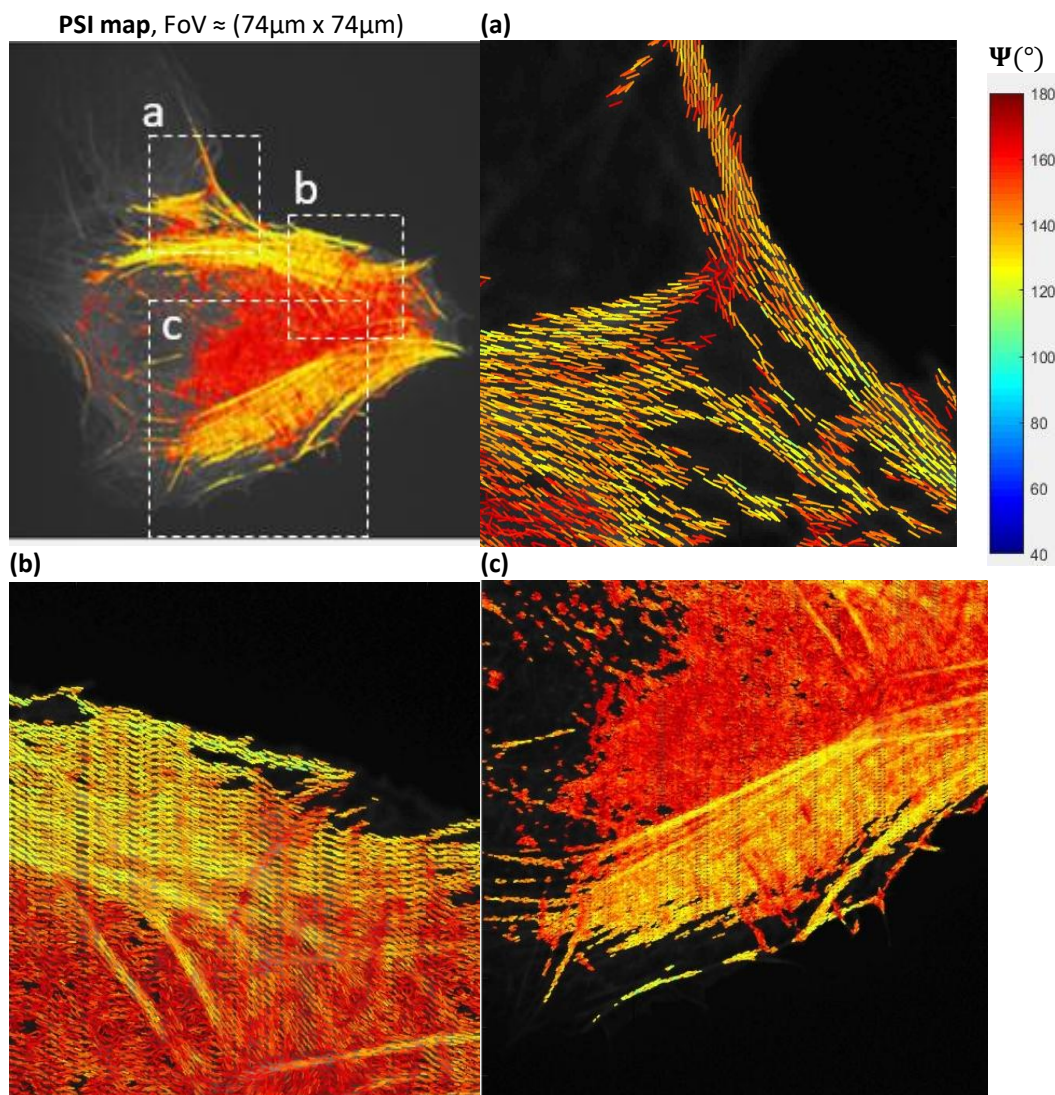


Figure 4.03 – Example of ensemble-polarimetric micrograph. Here, the stick representation is overlaid over the grayscale image of the fluorescence intensity map of the cell (see also Figure 4.04). The color of the stick stands for the cone aperture angle (molecular order,  $\Psi$ ), and the stick orientation is the mean orientation of the labels in that region ( $\rho_{av}$ ). (a-c) zoomed ROIs showing the regions that are more ordered (yellow) than others (red).

The ( $\rho_{av}$ ,  $\Psi$ ) data are depicted using a stick representation overlaying the intensity image represented as a grey-scale background (Figure 4.03). The sticks orientation in the (X,Y) plane corresponds to the  $\rho_{av}$  angle, while the stick color is given by the  $\Psi$  value (Figure 4.04). This permits to visualize at once both mean orientation ( $\rho_{av}$ ) and molecular order ( $\Psi$ ) properties. Obviously in this image, a SF bundle appears as much more ordered (yellow) than its surrounding (red), showing that actin F-filaments are well aligned in this region, in contrast with a more isotropic meshwork of actin in its surroundings. The interpretation of the measured  $\Psi$  values in SF bundles is made in the next section.



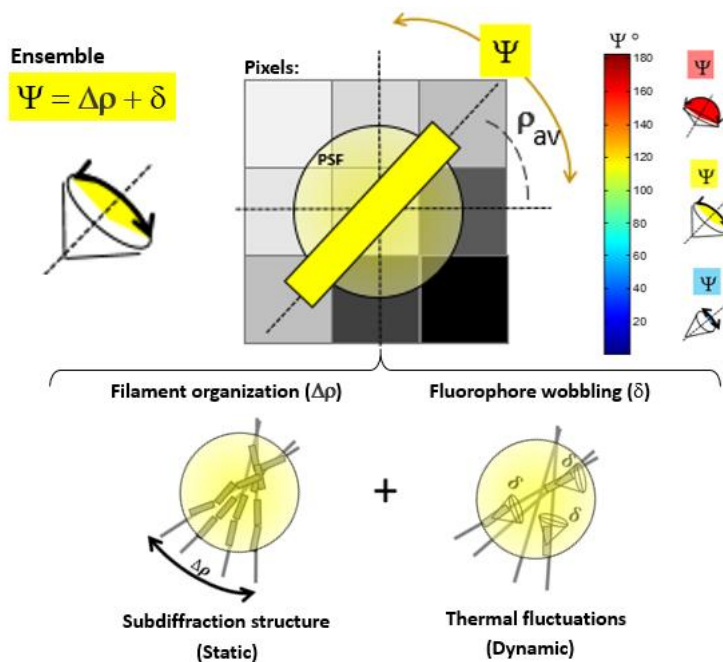
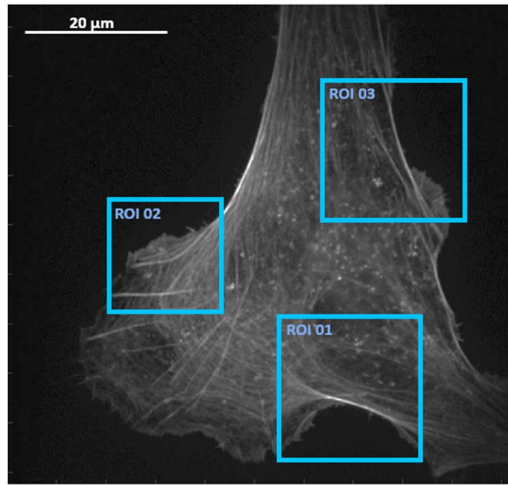


Figure 4.04 – The stick representation of the polarimetric data. A stick can be added on top of the gray pixels of the image to represent the two quantitative ensemble parameters: the average orientation ( $\rho_{av}$ ) and the cone angular aperture of the integrated orientations ( $\Psi$ , order). The orientation of the stick represents the mean orientation of the labels probed within the point spread function (PSF). On the other hand, the cone aperture angle information can be encoded as a color of the stick. The wider the cone aperture, the red-ish the stick; the narrower the cone aperture, the blue-ish the stick. The  $\Psi$  is the cone aperture angle is that encompasses the range of all probed orientations of an ensemble of labels within the PSF. The cone can be affected by static orientations of the labels bound to the probed nanoscale structure ( $\Delta\rho$ ), by the offset angle that the label makes with the orientation of the structure (not shown for simplicity), and by the intrinsic fast thermal fluctuations that the labels have ( $\delta$ , fluorophore wobbling).

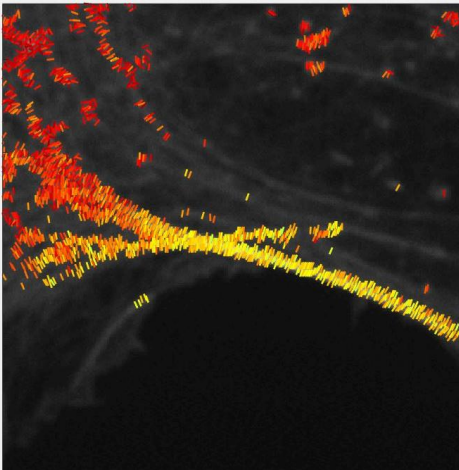
Note that the example given in Figure 4.03 was corrected from polarization distortions. Before correction, this stick representation permits to quickly identify deviations from a perfect correction. Figure 4.05 shows that a lack of distortion correction can lead to sticks deviating from their expected directions, and  $\Psi$  values that depend on the SF orientation (while  $\Psi$  is expected to be independent on the fiber orientation). These two effects are due to a diattenuation factor in the incident path of the excitation polarization and to dichroism (presence of ellipticity in the incident polarization). We could evaluate if such distortions are present and are affecting our data by evaluating the sticks behavior at regions where isolated SF makes 3 main angles. For example, isolated vertical, diagonal and horizontal bundles should have the same stick color and stick alignment to the main bundle orientation. At last, if such stick distortions are not present, we may adjust the offset angle of the incident alpha angle in relation to the main axis of the system, which needs to be properly set.

To introduce polarization distortion corrections in the processing algorithm, we built up a new lookup table that associate each expected ( $\rho_{av}, \Psi$ ) value sets to simulated (A2, B2) values including offset, ellipticity ( $\varepsilon$ ) and diattenuation (if any) parameters as measured in the calibration step. The correction procedure can be refined by a visual check of the mean orientation ( $\rho_{av}$ ) and order ( $\Psi$ ) values of isolated SF bundles with different orientations in the field of view FoV.

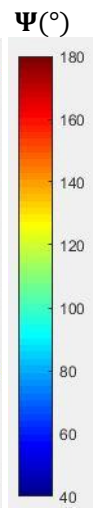
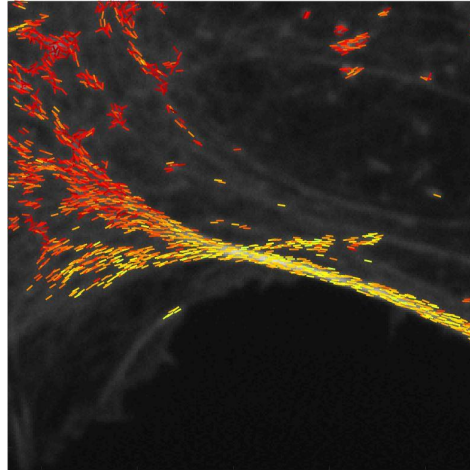


**Not calibrated**                      **Calibrated**  
**(corrected distortions + offset tuning)**

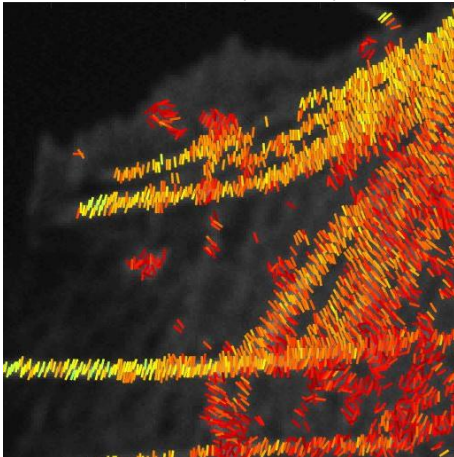
ROI 01 FoV(20 $\mu\text{m}$  x 20 $\mu\text{m}$ )



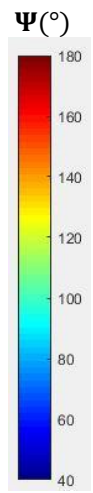
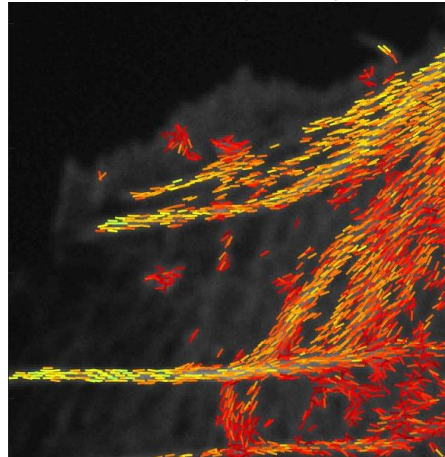
ROI 01 FoV(20 $\mu\text{m}$  x 20 $\mu\text{m}$ )



ROI 02 FoV(15 $\mu\text{m}$  x 15 $\mu\text{m}$ )



ROI 02 FoV(15 $\mu\text{m}$  x 15 $\mu\text{m}$ )



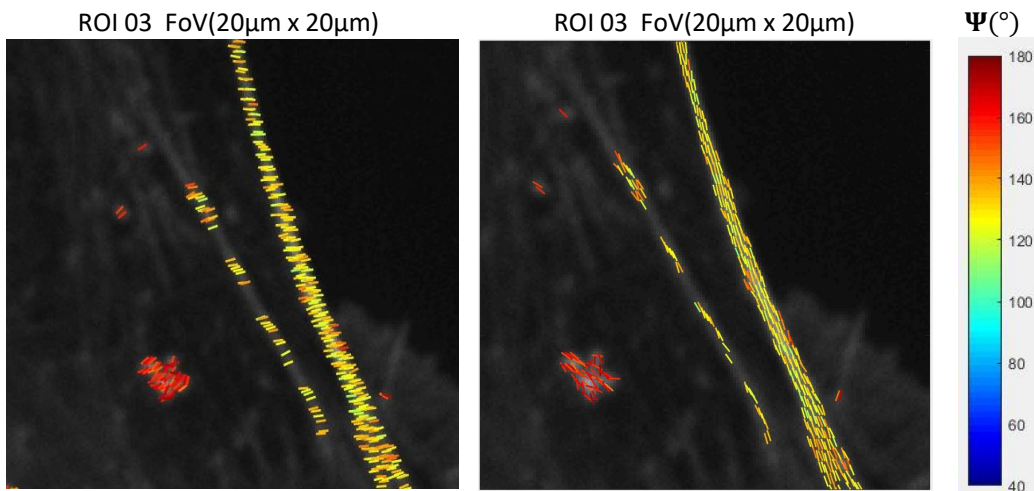
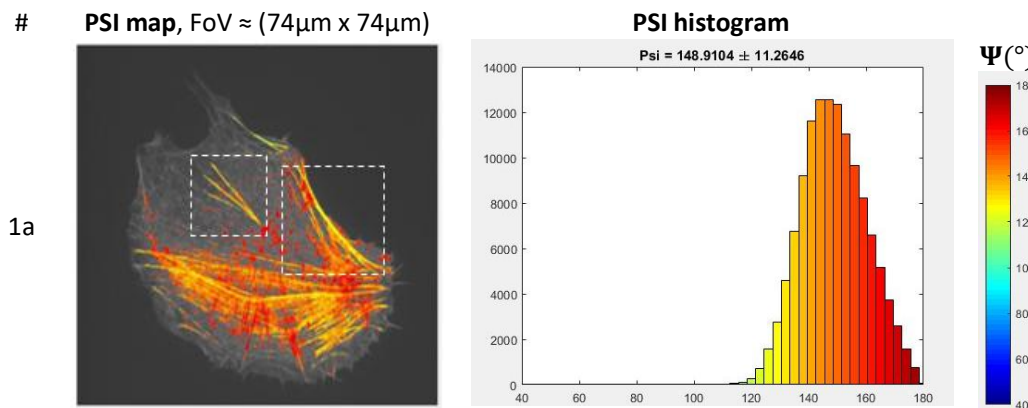
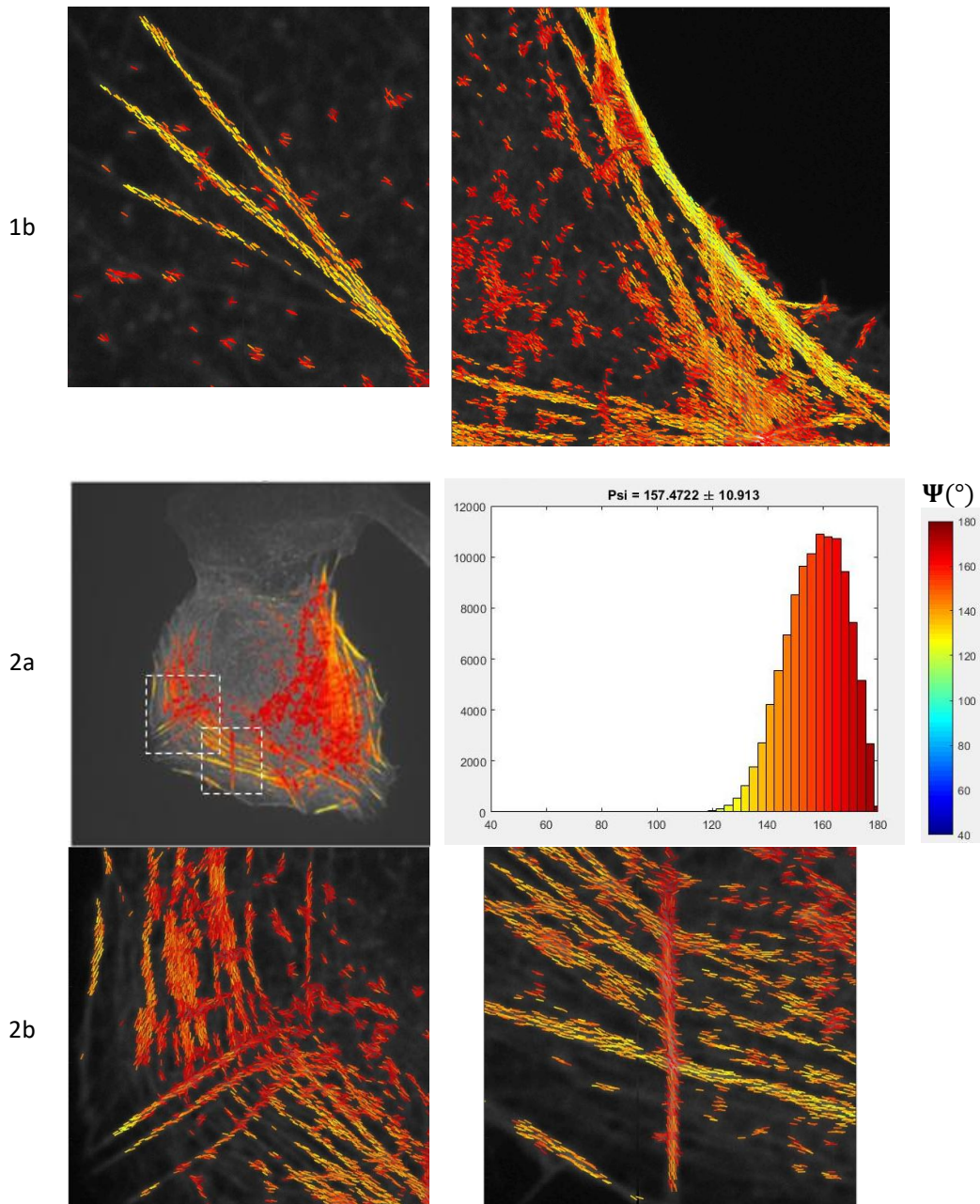


Figure 4.05 – Typical U2OS cell stained with phalloidin-AlexaFluor488 displaying many stress fibers at different orientations. These ROIs were used to find the best sticks alignment. Images on the left are not calibrated, and on the right are calibrated. The stick orientation is the ensemble averaged sub-diffraction mean orientation ( $\rho_{av}$ ), and the color is the ensemble averaged sub-diffraction order ( $\Psi$ ). Threshold used: 15k counts, polarization corrections are :  $\tan(\varepsilon) \approx 0.25$  ( $\varepsilon = 14.04^\circ$ ), diattenuation of  $\gamma = 0$ , and polarimetric offset  $\alpha_0 = 100^\circ$ . The colorcode used is the matlab jet scale normalized color-code from  $40^\circ$  to  $180^\circ$ .

### IV.3 Interpretation of the measured $\Psi$ value in SFs.

Figure 4.06 shows two examples of SFs taken from a few U2OS fixed cells labelled with phalloidin-AlexaFluor488. In all cells (36 cells in total), the cone aperture values ( $\Psi$  angle in degrees) obtained lie in the range  $120^\circ < \Psi < 180^\circ$ . Psi values around  $120^\circ$ - $130^\circ$  corresponds to pixels located on the SFs while  $\Psi > 160^\circ$  is seen in regions with no well-defined fiber morphology.





Figures 4.06 – Typical U2OS cells probed with ensemble-PFM without SF segmentation. On the left (#1a, #2a), the intensity map (greyscale) overlaid with PSI maps (colorcode =  $\Psi(^{\circ})$ ) = cone aperture angle in degrees). On the right (#1a, #2a), the PSI histograms (same colorcode) respective to the PSI map, with the mean value  $\pm$  std. Zoomed ROIs are shown (#1b, #2b). Typical z-plane is  $z=0.0\mu\text{m}$  (closest one to the substrate). Note that, oftentimes isolated SF bundles are more ordered (more anisotropic, with pixels with color typically in between  $120^{\circ} \leq \Psi \leq 140^{\circ}$ ) than SF bundles of the inner part of the cell (more disordered or isotropic). Intensity threshold used: 15k counts,  $\text{max}(\text{ellipticity})=0.25$ ,  $\text{offset}=100^{\circ}$ . Field of view (FoV) =  $73.9\mu\text{m} \times 73.9\mu\text{m}$ .

To interpret the  $\Psi$  angle values obtained in SFs, it is important to consider the contribution of both the actin filaments' structural disorder and the orientational flexibility of the label itself (Figure 4.04). Previous studies have shown that the  $\Psi$  value measured in SFs in fixed cells is largely dependent on the fluorescent label used, even in phalloidin conjugates [59]



(Figure 4.07). In particular, fluorophores with a longer linker length would exhibit a larger  $\Psi$  value, which is expected from a larger mobility from the fluorophore-phalloidin linkage.

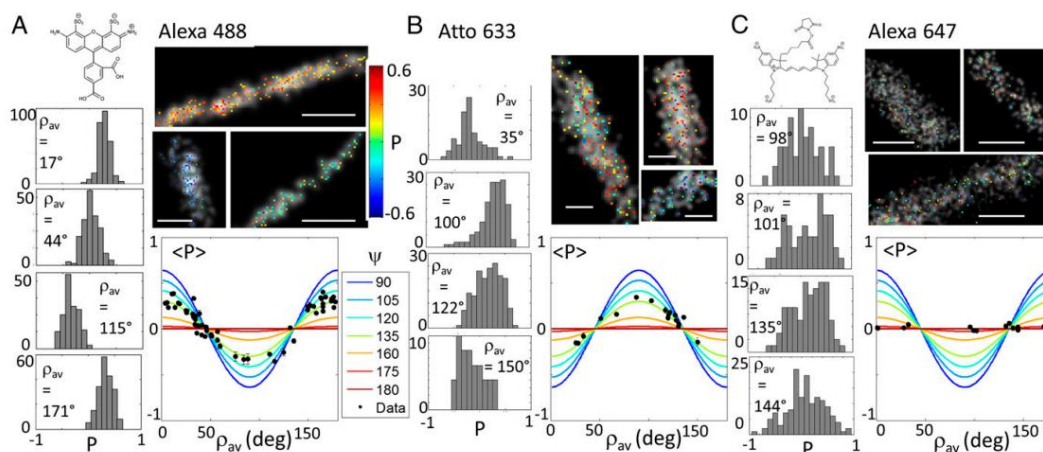


Figure 4.07 - The comparisons of fluorophore mobility among phalloidin conjugates. Here, phalloidin-AlexaFluor488 displayed the narrowest  $\Psi$  value ( $\Psi \approx 120^\circ$ , 'A' panel), meanwhile the phalloidin-AlexaFluor647 displayed the widest  $\Psi$  value ( $\Psi \approx 180^\circ$ , 'C' panel). The 'B' panel displays an intermediate case for Phalloidin-Atto633 label for F-actin. The polarization factor plot (P) displays the data points overlaid with simulated cone aperture angles, the narrower the cone aperture, the more anisotropic (blue-ish color, with stronger modulation) is the curve, and vice-versa. The histograms on each panel shows the single-molecule orientations probed on different SFs. Figure taken from [59].

Figure 4.07, based on single-molecule measurements, shows that the wobbling angle of phalloidin-conjugate labels on F-actin in SFs can reach up to  $90^\circ$ - $100^\circ$  [59]. Note that this wobbling angle can only be measured by a single molecule estimation, as will be described in Chapter 5. Since the  $\Psi$  values are affected by the intrinsic wobbling angle (thermal fluctuations) of the fluorophores, we typically chose the fluorophore with lowest estimated wobbling angle for the ensemble-PFM we knew [59]. The wobbling angle is generally the reason why the lower bound limit of the  $\Psi$  parameter in ensemble-PFM is a relatively wide cone aperture angle (here  $\approx 120^\circ$ ): with a wobbling value of  $90^\circ$ - $100^\circ$ , a perfect F-actin filaments organization would lead to a psi value of alignment of  $90^\circ$ - $100^\circ$ . Similarly, large disorders of F-actin filaments will be difficult to assess since a  $\Psi$  angle close to  $180^\circ$  will be reached even for a non-complete isotropy. This effect constitutes a limitation of the ensemble-PFM method that we will try to circumvent by single molecule data (see Chapter 5). Nevertheless, the ensemble method allows for comparison between different alignment types, which can be done in comparative studies.

Figure 4.06 depicts another possible limitation of ensemble-PFM : in crowded structures (e.g. SF bundles over a dense actin-meshwork) or structures crossing each other's, the measured  $\Psi$  and  $\rho_{av}$  values are likely to be biased. Indeed what is then measured is the SF organization superimposed with another organization (isotropic, or of different orientation), leading to a different ensemble angular distribution. This emphasizes the complexity that the cell morphologies might impose in the SF analysis when using polarization resolved method: in particular to compare  $\Psi$  values from different types of SFs, branched or crossing regions should be ideally avoided and values should be measured in well isolated SFs. This is also a motivation

for using well defined cell shapes (by the use of CYTOO patterns, as described later), where fibers morphologies are comparable.

#### IV.4 Comparing molecular order in different SFs: data processing.

##### IV.4.1 Choice of cell shapes

In order to compare molecular order values in different types of SFs, a rigorous segmentation (ideally unsupervised) of stress fiber ROIs is needed, which avoids as much as possible surrounding disordered regions in the cell's cytoplasm or in underlying actin meshworks (represented by red pixels in Figure 4.03.b-c). Moreover, the statistics made on different SFs has to be independent on the user ROI selection variabilities, therefore SFs of similar sizes and shapes have to be selected.

Ensemble-PFM was applied to retrieve SF organization information in cells. The advantage of using PFM is clear: the method affords a wide FoV (tens to hundreds of microns), which is enough to visualize the whole cell, localizing different SFs. Nonetheless, as we saw in Figures 4.03-4.06, cells can be of very different shapes and sizes, which can represent an experimental obstacle to get reproducible SF conditions to be rigorously compared. One way to circumvent complexity of cell morphology is to plate the cells onto a substrate with adhesive micro-patterns (see Figure 4.08 below, [28, 29]). The latter induces the cells to spread onto it with specific geometry, and therefore obtain a more reproducible SF organization at the cellular scale.

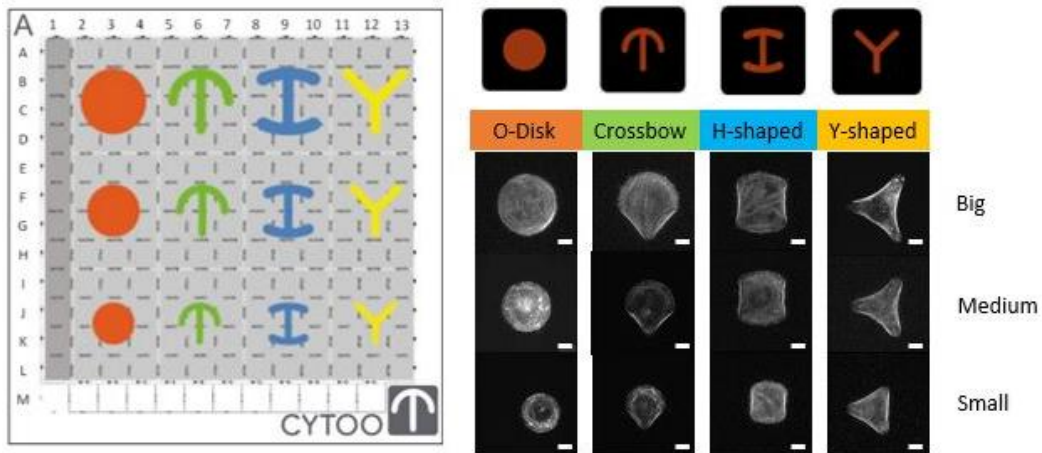


Figure 4.08 – Cells plated onto CYTOO chip (standard), whose adhesive area has a specific shape and size. The CYTOO substrate has 19.5 x 19.5 mm, 170 $\mu$ m glass thickness, and it includes many adhesive patterns with different shapes (O-disk, crossbow, H-shaped, Y-shaped) and sizes (big, medium, and small). Typical adhesive areas are: small=700 $\mu$ m<sup>2</sup>, medium=1100 $\mu$ m<sup>2</sup>, and big=1600 $\mu$ m<sup>2</sup>. Scale bar = 10 $\mu$ m, default coating with Fibronectin 20 $\mu$ g/ml, sterile at RT. See appendix and materials and methods section for detailed protocol.

The experimental difference between unpatterned and patterned cells is how the substrate is coated with adhesive polymeric matrix. On the usual unpatterned cells, the whole substrate (coverslip) is homogeneously coated with adhesive matrix (e.g., Fibronectin or Collagen), so that the cells are free to spread with any shape. On the other hand, cells plated on CYTOO chips adhere and spread only onto the adhesive area with specific geometrical pattern

(e.g., O-disk, Crossbow, H-shaped or Y-shaped, see Figure 4.08). Since there is anti-adhesive coating surrounding the adhesive patterns, cells are restricted to spread only onto the area of the pattern.

Using such CYTOO standard substrate to plate our U2OS cells, we focused our studies on the patterns of Crossbow, H-shaped and Y-shaped with big and medium sizes, because they were showing the highest diversity of well-defined SF-subtypes (i.e., easily distinguishable). Cells that adhered onto Crossbow and H-shaped patterns displayed clear peripheral SF, ventral SF, dorsal SF and transverse arcs (Figure 4.09). In contrast, the Y-shaped patterned mainly displayed peripheral SF and ventral SF. The O-disks pattern displayed also many SFs, but the SF network was often too crowded (highly interconnected), which made it delicate to find an equivalent in default conditions (not patterned) to be compared.

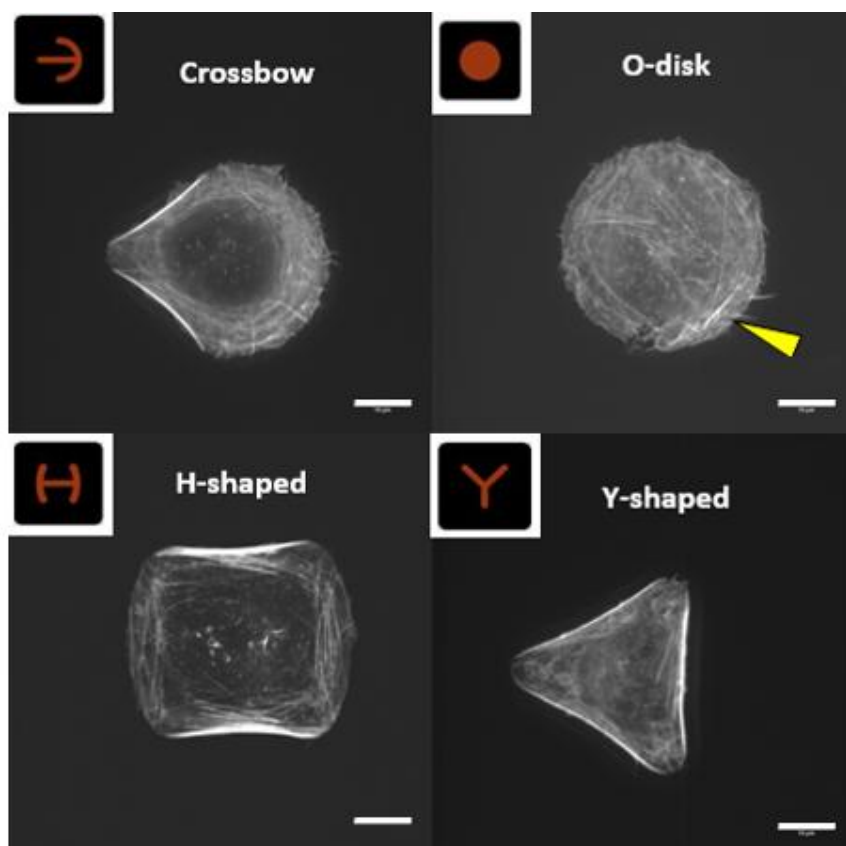


Figure 4.09– Example of cells plated onto CYTOO chip (standard), whose adhesive area has a specific shape and size. Adhesive areas for medium size is  $1100\mu\text{m}^2$  for all shapes. Default coating (recommended CYTOO protocol) with Fibronectin  $20\mu\text{g}/\text{ml}$ , sterile at RT. See appendix for detailed protocol. Yellow arrow highlights actin filaments that have a not well defined organization (yellow arrow head) which is difficult to classify what they are. Scale bar =  $10\mu\text{m}$ .

#### IV.4.2 Stress fiber segmentation

In the sarcomere paper mentioned above [61], the size and shape of sarcomeres structure in a single FoV were highly reproducible, so that the sarcomere segmentation (i.e., ROI selection) was a straightforward task. On the other hand, stress fibers in non-muscle cells have different lengths, thickness, curvature, and biochemical composition on each micrograph (Figure 4.06, and panel A, A' of Figure 4.01). The usage of CYTOO patterned substrate indeed helps in

retrieving similar cell morphology, and therefore similar SF structures to be compared. However, since there are different SFs types on the same FoV, the decision of how to segment the actin SF bundles can vary from person to person, which could lead to less reproducible results.

In this sense, to perform the SF segmentation *per se* is a challenge to be overcome. The SF segmentation should be as little user-dependent as possible. As we will see below, with the help of a semi-automated freeware software named FilamentSensor (FS), we develop a code in Matlab® that provides a more rigorous SF segmentation for a semi-automatic SF classification, that will be used to calculate different SFs statistics in a more reproducible fashion.

The FilamentSensor (FS) is an open access code (Java and Python scripts available) that detects and records the geometrical properties of the straight filaments of an image [108]. The inputs of the program are the fluorescence intensity map in “.png” format, and a sequence of preprocessing image parameters (image filters) that a user can set to optimize the detection of the filaments of an image. Because the user needs to choose the optimal set of parameters for different cells, the FS is considered “semi-automated”. However, once the chosen parameters were defined, any other user could repeat the image processing with the same set of values to get reproducible filament binarization, and therefore segmentation results.

The FS program is mainly divided in two steps. The first one, the image enhancement and binarization filters; and the second one, the extraction of filament geometrical properties from the binarized image (see Figure 4.10). The second step extracts the geometrical properties from the binary image, including location, orientation, length, and width for each local filament found in the image. The segment sensor output is a binarized mask with the total size of the input “intensity.png”. The binarized mask of each cell has a value “1” on the pixels that were detected by the segment sensor, and “0” on the rest of the image. We can choose the color of the binarized segments that can be overlaid with the “intensity.png” image, and afterwards use this color information to further localize the pixels related to the SF in our polarized imaging processing. In particular, we chose the color *orange* in RGB(255, 200, 0) for the binarized segments in the output (see Figure 4.10).



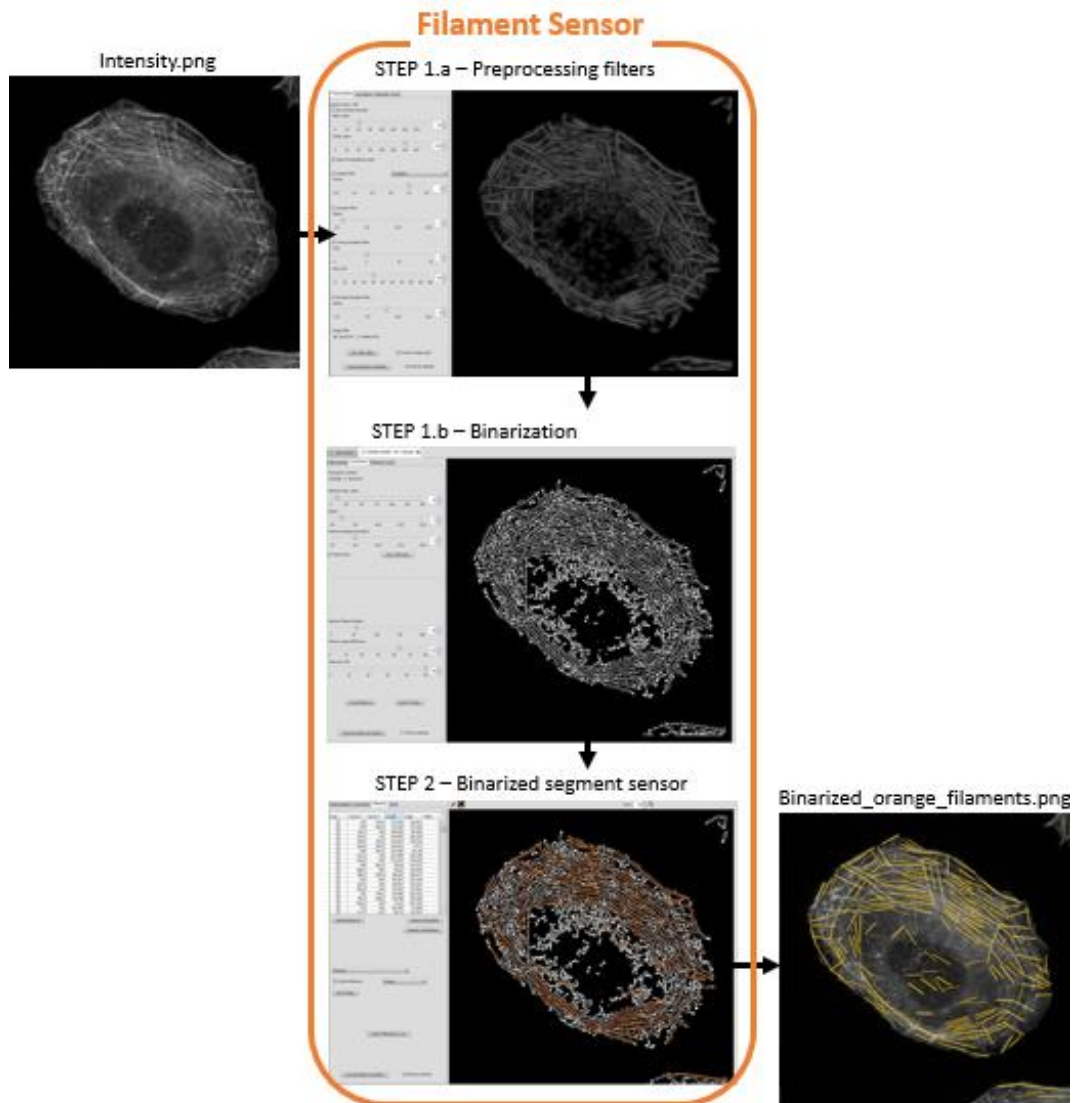


Figure 4.10 – Filament Sensor (FS) workflow. From the raw data we need the intensity image to be used in the FilamentSensor program. The FS is able to detect straight filaments of each cell image (intensity.png), generating binarized mask of the detected filaments. The first FS step is basically a set of intensity filters to highlight the SF of interest (for example: to avoid very short filaments, or crossings). Subsequently, a binarization filter is applied on the previous enhanced image. The last step is the detection of binarized straight segments of the binarized image. A set of segment sensor parameters can be chosen to restrict the types of detected binarized filaments on the binarized data. The detection algorithm extracts the geometrical properties (length, width ...) from the binarized image.

#### IV.4.3 Stress fibers selection and classification

To produce the SFs selection described above, we first need a simple “.png” file of the intensity image of each cell stained with phalloidin-AlexaFluor488. Our raw polarized data has a “.tiff” format, consisting in an image stack of 18 alpha angles (sometimes up to 36 if the signal is too low), i.e., a sequence of 18 frames related to 18 different linear polarized excitation angles (P18). Thus, the “intensity.png” image can be constructed based on the sum of the intensity counts per pixel along all polar frames. For that we created a matlab code “AutoPNG.m” that

automatically creates the “cell-ID\_Intensity.png” files from a list of raw data in the format “cell-ID\_polarstack\_P18.tiff” files present in the same folder address. Such “cell-ID\_intensity.png” file is used as an input in the Filament Sensor graphical use interface (GUI) (see above), and, in parallel, the intensity.png file can also be used to overlay with a co-staining image (typically with focal adhesion marker) that will be further used to help to distinguish and classify each SF-subtype (peripheral, ventral, transverse arcs and dorsal SF), see workflow Figure 4.11.

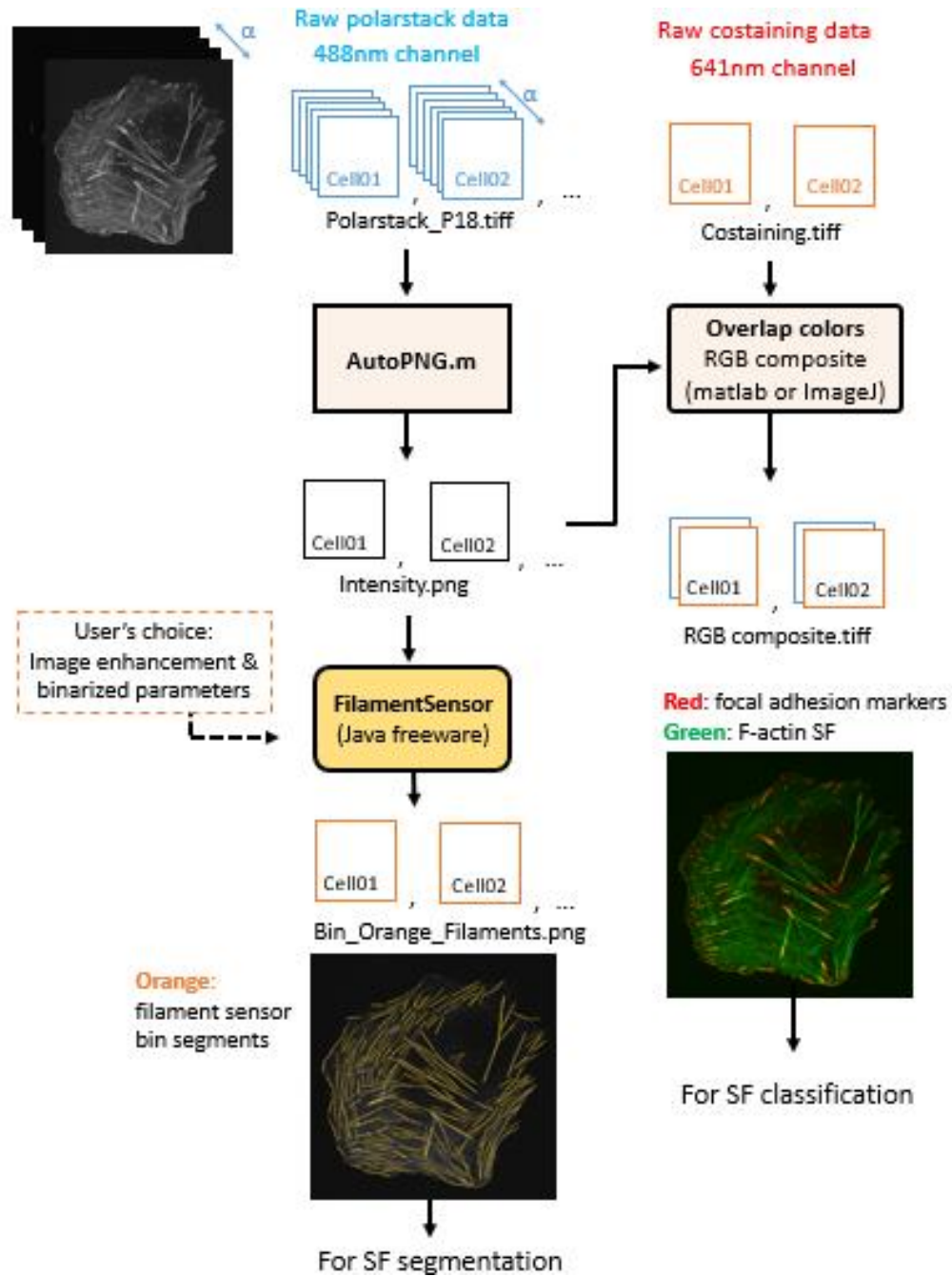


Figure 4.11 – Data processing workflow part 1. From the raw data we need the intensity images to be used in the FilamentSensor program, which detect the filaments of each cell, generating binarized mask.

Once the binarized mask with segments of selected SFs is constructed (see above), we need to classify each identified SF segment into its SF type. There are many ways we can distinguish SFs. To classify SF with only F-actin staining, we could take into account how far from the substrate the SFs are, or how close to the cell borderline, or if the bundle is tilted or not (if we make a Z-stack for example). In addition, if we use focal adhesion (FA) markers, the RGB composite image (from co-stained actin and FA) can assist the SF classification. We can in particular analyze how many focal adhesions a SF is bound to: one (dorsal), two (ventral, peripheral) or none (transverse arcs). Here are the main characteristics that allowed us to classify the different detected SFs into SF-types (Chapter 1, Figure 1.12 and Figure 1.18):

- **Peripheral SF:** found at the ventral part of the cell (closest to the substrate) and at the cell border. Its shape can be a straight or a concave (bent inward) bundle on the borderline of the cell. It is bundle decorated with non-muscle myosin II (NMII) and is made of F-actin filaments that are antiparallel aligned in between two focal adhesion markers.
- **Ventral SF:** found at the ventral part of the cell (closest to the substrate) it is a straight bundle that can interconnect laterally with other bundles in the central or peripheral part of the cell (i.e., with other ventral or peripheral SF). Typically is a bundle that is decorated with NMII, and the F-actin filaments should be antiparallel aligned in between two focal adhesion markers; sometimes, one focal adhesion edge overlaps with a focal adhesion of a peripheral SF (when a ventral bundle connects with a peripheral bundle laterally).
- **Transverse arcs:** found mainly in the front part of the cell, in the lamella region. These are bundles that migrate from the ventral part of the cell to the dorsal part of the cell thanks to the connection with dorsal SF bundles. Thus, a z-stack can easily detect them. Transverse arcs typically are convex bundles whose shape follows the curvature of the front of the cell. Besides, in general, the edges of transverse arcs are not connected with focal adhesions, except when transverse arcs are on the process to be converted to ventral SF. Transverse arcs are considered contractile bundles.
- **Dorsal SF:** found from the ventral part, but mainly localized in the dorsal part of the cell. Dorsal SF can be tilted bundles following the shape of dorsal part of the cell. Of note, dorsal SF are considered “not contractile” by the literature because they are not decorated with non-muscle myosin II (NMII). Typically, dorsal SF are radially distributed, and are bound to one focal adhesion on the ventral part of the cell. The other edge is connected with a transverse arc on the dorsal part of the cell. Thus, its signature is to be a bundle with a single focal adhesion marker.
- **Other SF:** any stress fiber in the field of view that is not easily categorized has been pooled as “other SF”.
- **All SF:** includes all of the previous SF types (it also includes other SF).

We developed a matlab script (called “Colormask\_creator.m”) that allows us to classify the selected (orange-encoded) segments into different SF sub-types (for example, by giving

them a specific RGB color for each SF type). Such decision should be done ideally according to the co-staining FA localization information. The user has to select a set of orange segments using *roipoly* matlab function, and choose their SF-classification. By doing so, the program will automatically convert the selected orange segments into their new SF-color classification on the image (for each cell in a list). Thus, the “Colormask\_creator.m” program basically reads a list of “cell-ID\_bin\_orange\_filaments.png”, overlay with the intensity image of each cell (given by the raw data), and display multiple user-interactive loops (for each SF type, on each Cell-ID of the list), asking which color (i.e., SF type) the selected segments should be. For each cell, only the remaining segments to be classified are displayed for the user. The use of FilamentSensor binarized masks allows a minimal user-dependent choice of the analyzed regions on the SFs. One possible mistake a user could make is to perform a wrong classification of the selected SFs. For such sparse cases, we developed another program, “Colormask\_editor.m” that can change the SF color of any given colormask (See workflow below, Figure 4.12).

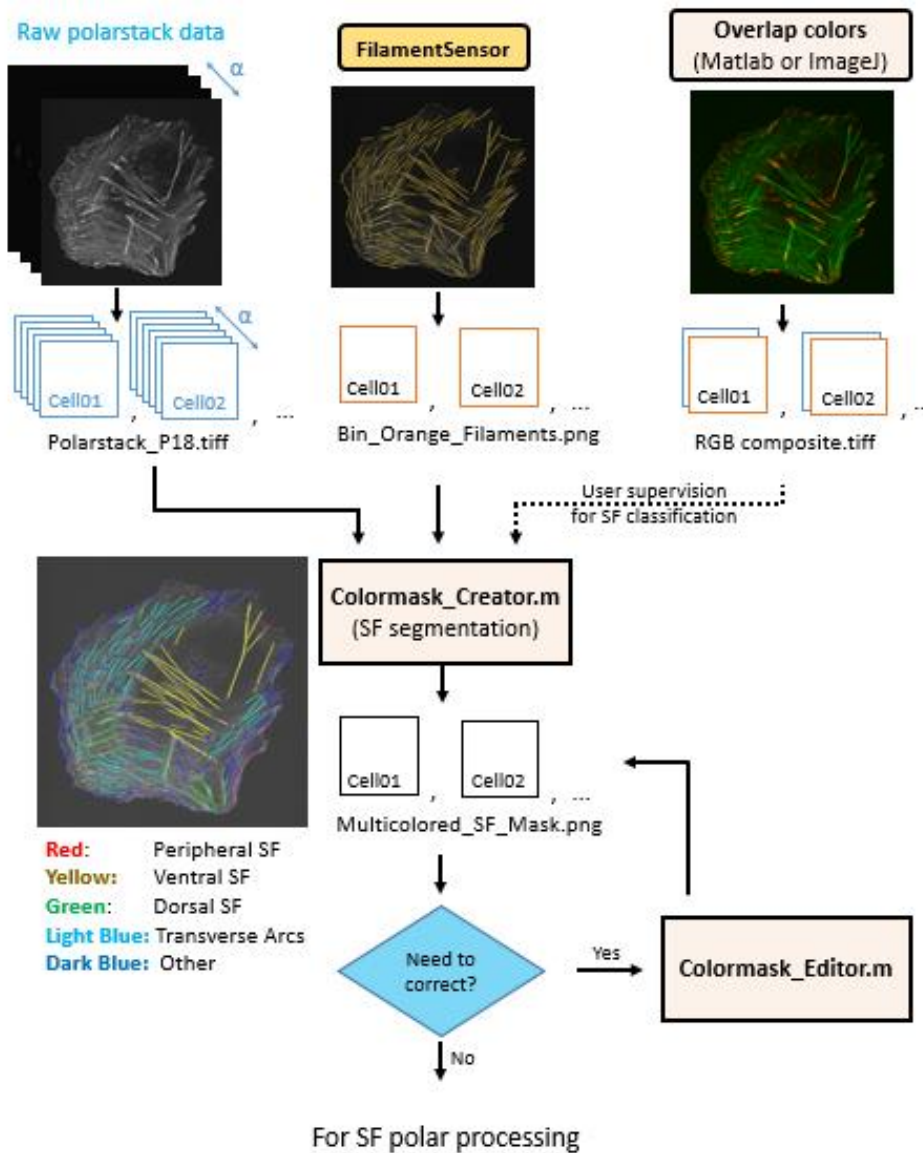


Figure 4.12 – Data processing workflow part 2.

#### IV.4.4 Polarized image processing and molecular order parameters retrieval

Once the SFs segmentation and classification is done, the selected pixels are used for the polarized imaging analysis. Having the colormask file for each cell, the polarization calculations will be performed separately for each SF type, for each cell-ID. To automatize this analysis, we need a list of raw data cells, their respectively colormask, the polarization distortion information, and define a low intensity threshold. The intensity threshold is an important parameter because low intensity pixels naturally lead to lower precision and accuracy issues (i.e. bias) in the parameters determination. The “Colormask\_reader.m” program created for this purpose, automatically calculates for each SF of each cell on the list the polarization-dependent Fourier decomposition onto each SF pixels, as described in Chapter 3. With the latter we can get per SF per cell (see the workflow below, Figure 4.13):

- The PSI histogram (histogram of the order values,  $\Psi$  )
- The PSI map image (order parameter color,  $\Psi$  in degrees, overlaid with the intensity of the cell)
- The  $\rho_{av}$  and  $\Psi$  images assembled in a stick image where the sub-diffraction mean orientation ( $\rho_{av}$ ) information is encoded on the linear stick orientation and order information ( $\Psi$ ) is encoded on the stick color
- A general Results.mat file, which gathers all the quantitative values obtained in the analysis

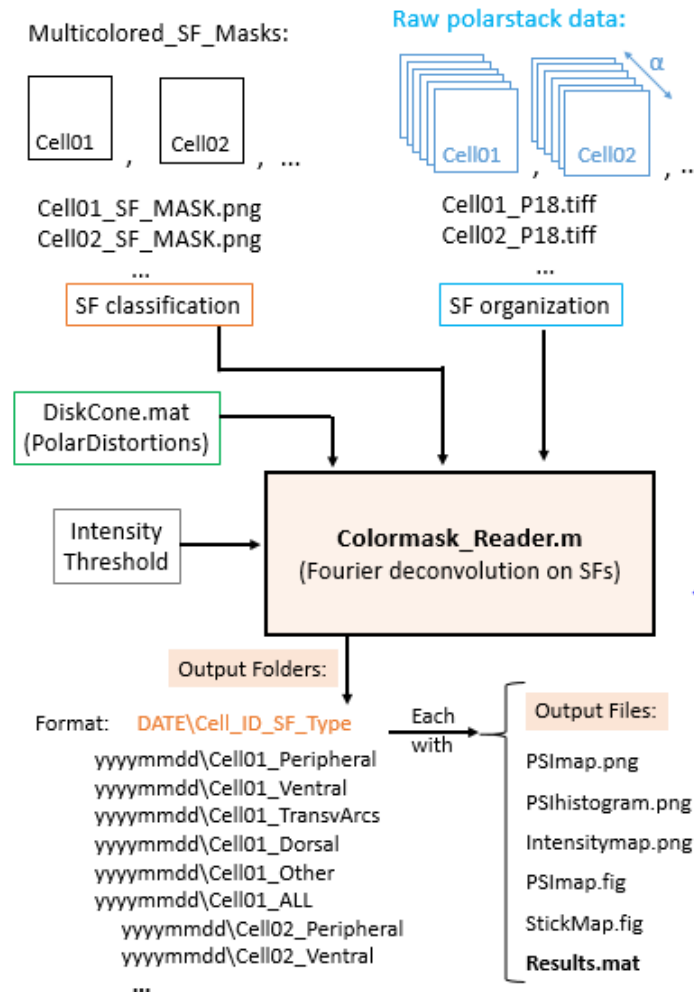
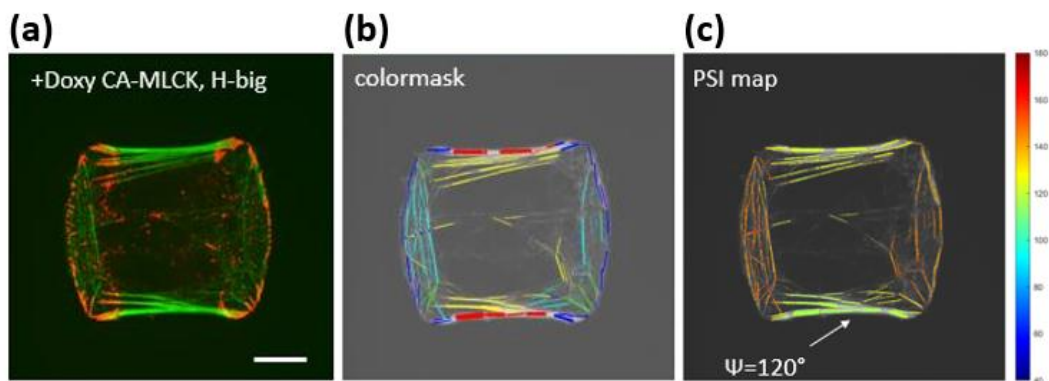
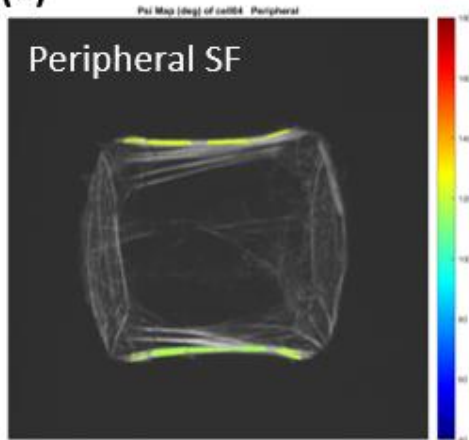


Figure 4.13 - Data processing workflow part 3. The colormask\_reader.m performs the Fourier decomposition of the polarization-modulated image only over the pixels previously segmented and classified (cell-ID\_colormask.png). The result files are the different images and files indicated in the outcome of the workflow, which permit to quantify and represent all molecular order parameters per image pixel.

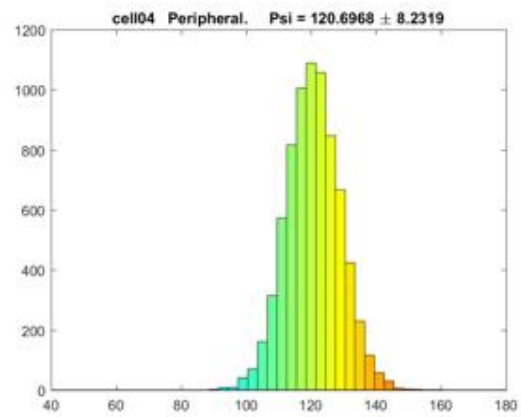
A typical result of data analysis is shown in Figure 4.14 below.



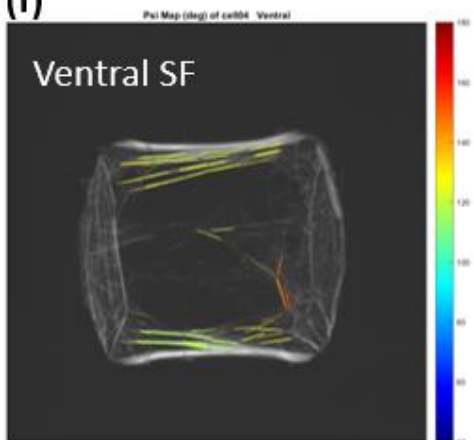
(d)



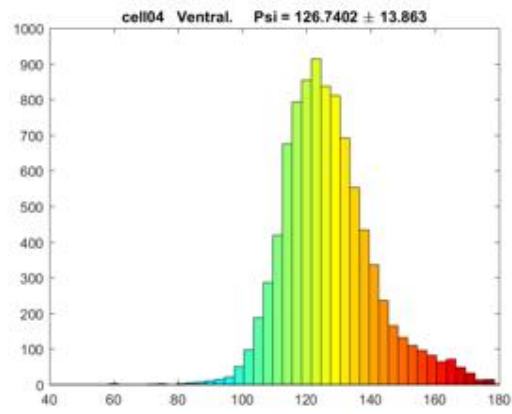
(e)



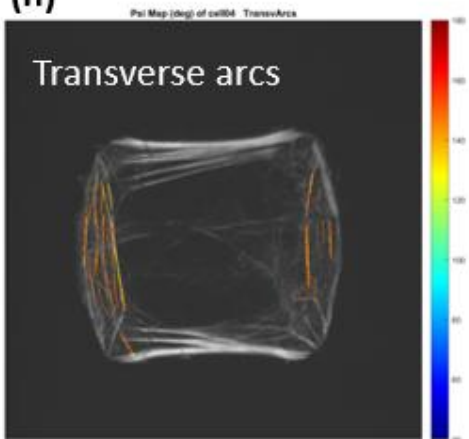
(f)



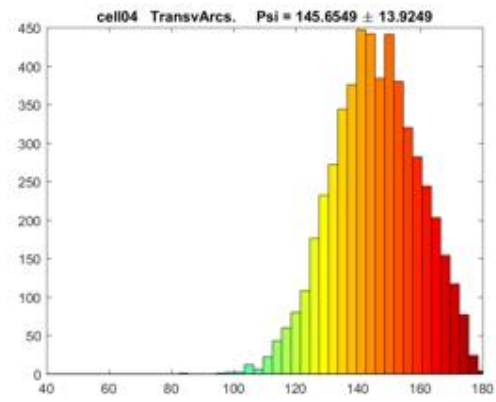
(g)



(h)



(i)





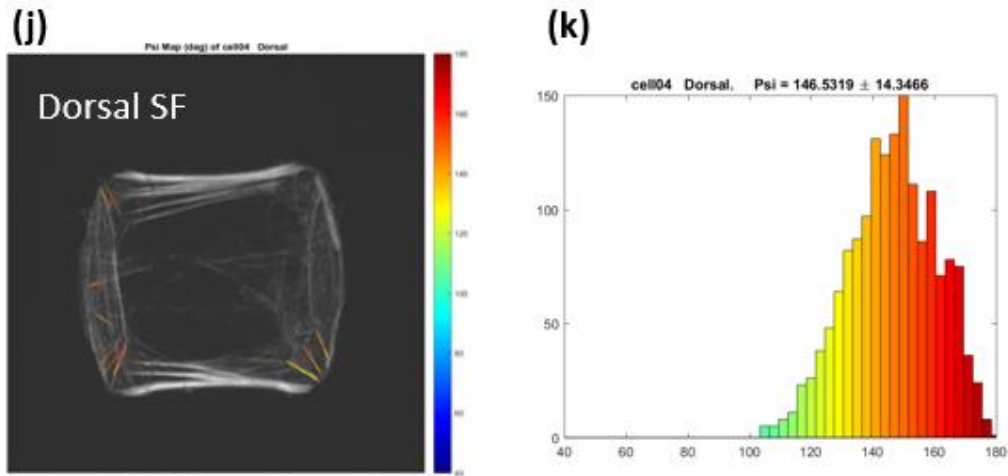


Figure 4.14 – Typical result obtained after segmentation and SFs classification. The segmentation is performed on a CYTOO patterned cell (CA-MLCK + doxy) H-shaped big size. (a) Fluorescence image of the costaining of F-actin (green, phalloidin-AF488) and focal adhesion (red, phospho-FAK). Such costaining helps in the selection of the SF category for each bundle. (b) The colormaks displaying all the segmented categories (like in Figure 4.12). (c) The Psimap: it has  $\Psi$  values (pixels with RGB color) overlaid with the grayscale intensity pixels of F-actin. (d,f,h,j) Psimap of the segmented peripheral, ventral, transverse arcs and dorsal SF and their respective (e,g,i,k)  $\Psi$  histograms . Note that, on the contrary to naïve cells, mutant CA-MLCK cells+doxy reached  $\Psi$  values as low as the lowest bound limit for Alexa-Fluor 488 (around  $\Psi \sim 120^\circ$ ) in peripheral SF bundles discussed below.

#### IV.5 Comparing molecular order in different SFs and conditions: results

The analysis described in the previous section has been performed on a collection of U2OS cell shapes on CYTOO chip patterns, resulting in the following statistics:

- 9 naïve U2OS cells – crossbow big
- 9 naïve U2OS cells – crossbow medium
- 5 naïve U2OS cells – H-shaped big
- 6 naïve U2OS cells – H-shaped medium
- 5 naïve U2OS cells – Y-shaped big
- 5 naïve U2OS cells – Y-shaped medium

Note that O-disks of all sizes were ignored for the sake of simplicity. For each CYTOO pattern above mentioned, we will analyze the stress fibers with the following confidence level (i.e. possibly occurring for some reasons explained below):

STRESS FIBER TYPE	CONFIDENCE LEVEL	WHY
▪ Peripheral SF	very high	(well defined, high contrast, easiest interpretation of the results)
▪ Ventral SF	high	(well defined, however sometimes overlapped with isotropic background)
▪ Transverse arcs	medium	(can be embedded in a dense meshwork and/or often crossings with Dorsal SF)



- Dorsal SF                    medium                    (often crossings with TransvArcs SF)
  
- Other SF                    low                    (not well defined)

#### IV.5.1 Comparison among SF types in naïve U2OS cells

We first investigated the order parameter order ( $\Psi$ ) obtained in different SF types for a given cell type (shape and size) in naïve U2OS cells. The lowest obtained  $\Psi$  values in naïve U2OS cells are seen in the **peripheral SFs**, for which  $\Psi$  values can reach down to  $136^\circ \pm 8^\circ$  (Table 4.01, see crossbow-big and Y-shaped medium cells). An average of  $\Psi = 138 \pm 10^\circ$  is obtained in peripheral SFs over all naïve cells measured. This value is close to other reported values in non-patterned fixed cells (see Figure 4.06.1b) and higher than the  $\Psi$  obtained in sarcomere actin organization (see Figure 4.01), as expected. From the known estimations of AlexaFluor488 mobility (single molecule based estimation, see [59]), it is expected that out of this total measured order value, about  $90^\circ$ - $100^\circ$  is attributed to the angular fluctuations undergone by the dye, which is connected to phalloidin via a not completely rigid linker. The remaining  $26^\circ$ - $36^\circ$  may be attributed to disorder obtained between the single filaments within the bundle formed in the peripheral SF. Another parameter which could come into account in this value however is the tilt angle that the AF488 molecules make, on average, relative to the F-actin filaments: this disorder range is therefore an upper limit value. Note that recent estimation made in our lab on single F-actin filaments show that  $\Psi$  values in single filaments labeled with AF488-phalloidin conjugates reach about  $123^\circ$ - $126^\circ$  [109], which is close to the sarcomere value. It is therefore likely that an offset tilt angle of about  $20^\circ$  exists between the AF488 dye axis and F-actin filaments (Figure 4.15).

By pure comparison to single filaments or values obtained in sarcomere structures, our measurement in peripheral SFs shows therefore that the F-actin filaments disorder in such structure can reach up to roughly  $136^\circ$ - $126^\circ \sim 10^\circ$ . This confirms the highly aligned character of F-actin filaments in contractile peripheral structures. This value is supported by further investigations we made in this PhD on single molecule analyzes, see Chapter 5. Note in addition, that the error bar obtained ( $10^\circ$ ) is slightly higher than the precision value expected from the level of intensities measured (which we expect to be about a few degrees, following estimations similarly as in [58, 77]). This higher error margin reflects the possible heterogeneity among SFs organization, even though not reaching a very large extent.

**Ventral SFs** display, on average, higher  $\Psi$  values ( $\Psi = 149 \pm 10^\circ$ ), despite the fact that the SFs composition is not expected to be very different from peripheral SFs. This higher disorder value could however be attributed to the fact that ventral SFs are often not completely isolated from the underlying actin meshwork, which can add some isotropic contribution in the measurement of angular order (see zooms in Figure 4.03 and Figure 4.06). Since the  $\Psi$  value scales almost linearly with the  $\sqrt{A_2^2 + B_2^2}$  (Equation 3.6) in the estimation from the Fourier decomposition of the polarization-dependent intensity, it is expected that a mixture of the ordered structure of  $\Psi = \Psi_0$  with a portion of  $X\%$  of an isotropic contribution, would increase the measured  $\Psi$  value to about  $\Psi = \left(1 - \frac{X}{100}\right)\Psi_0 + \left(\frac{X}{100}\right)180^\circ$ . For example, an initial  $\Psi_0$  value of  $130^\circ$  mixed with 20% proportion of isotropic distribution would therefore raise the measured

psi value to 140°. More investigation made in single molecule measurements will confirm that ventral SFs are indeed of similar molecular order than peripheral (see Chapter 5).

**Transverse arcs** exhibit  $\Psi$  values that are quite close to ventral SFs ( $\psi = 152 \pm 10^\circ$ ). Such structures are however often measured over a background of actin meshwork that can be complex in morphology (see zooms in Figure 4.06), therefore the measured psi value is expected to be, here as well, slightly overestimated by the average nature of the measurement.

At last, **dorsal SFs** are seen to exhibit the highest degree of disorder ( $\psi = 156 \pm 10^\circ$ ), even when well isolated from isotropic backgrounds. We attribute this property to either a true disorder (due to their specific nature that is non-contractile, therefore composed of other types of crosslinkers), to possible crossings with arcs (see zooms in Figure 4.06), or to a pure geometrical effect. Indeed dorsal SFs are seen to display a 3D oriented nature, being present in different planes of the Z-stacks performed. Such fibers are therefore not completely in plane, which presents another source of possible bias in the measurement (see Chapter 3, Figure 3.21).

Overall this study shows a general trend that the peripheral SFs are the most organized structures in fixed cells, however with a confidence level which is not high enough to be able to compare it to other SFs structures: this is mostly due to the influence of the local environment of the measured SFs that can strongly influence average polarization dependent measurements, but also to geometrical factors (3D tilts). To circumvent the drawback of the first effect, single molecule measurements will be required (see Chapter 5). Nevertheless, we will consider ensemble measurements as robust enough to permit comparison between different cell types (shapes and sizes), since sources of bias are very similar in those samples. This effect however excludes the comparison of non-patterned cells, which exhibit a very heterogeneous range of SF morphologies.




Naive U2OS	# cells	Mean PSI VALUES (°)	Peripheral	Ventral	Transverse Arcs	Dorsal	All SF
	9	Crossbow – big	136 ± 10	149 ± 10	152 ± 10	156 ± 11	147 ± 12
	9	Crossbow – med	139 ± 9	154 ± 9	153 ± 10	157 ± 9	147 ± 12
	5	H-shaped – big	142 ± 7	153 ± 9	149 ± 11	155 ± 11	148 ± 10
	6	H-shaped – med	139 ± 7	151 ± 8	145 ± 9	155 ± 9	146 ± 10
	5	Y-shaped – big	137 ± 7	147 ± 10	-	-	140 ± 10
	5	Y-shaped – med	136 ± 8	146 ± 10	-	-	139 ± 9
		<b>mean ± max(std)</b>	<b>138 ± 10</b>	<b>150 ± 10</b>	<b>150 ± 11</b>	<b>156 ± 11</b>	<b>145 ± 12</b>

Table 4.01 – Table of the mean ± std of the order  $\Psi$  values of each SF type from naive U2OS cells (fully spread) on CYTOO patterned substrate. On the left part of the table we have both the CYTOO morphology (crossbow, H, Y) and the number (#) of cells pooled together to accumulate pixels of SFs. The mean value is calculated over the segmented pixels of each SF category (see example in Figure 4.14).

**Legend table of the colors:**

Mean PSI range	Relative table color
$135^\circ \leq \Psi < 145^\circ$	$\Psi$
$145^\circ \leq \Psi < 155^\circ$	$\Psi$
$155^\circ \leq \Psi < 165^\circ$	$\Psi$

ordered

↑

↓

disordered

The legend table for ensemble-PFM cone aperture ( $\Psi$ ) values. The colors divides the order values in 5 ranges of 10° centered at 140°, 150°, and 160°.

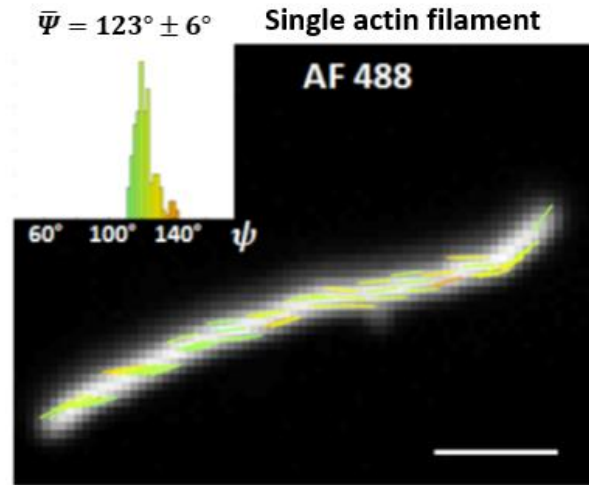


Figure 4.15 - Ensemble-PFM measurement of a single actin filament (not a SF bundle). We see that the value of filament order  $\Psi$  is around  $\Psi=123^\circ$ , meaning that the angular aperture made by the fluorescent labels orientation is wide, corresponding to a dynamic motions (thermal fluctuations, ~wobbling) plus a static slightly tilted angle between the filament orientation and the label dipole orientation (binding offset angle). Figure taken from [109].

#### IV.5.2 Comparison among cell shapes and sizes in naïve U2OS cells

The analysis performed above was performed for all cell shapes and sizes, the results are summarized in Table 4.01 which gives the mean  $\Psi \pm \text{std}$  (rounded values of the order parameter for each category) for each cells and SFs types. The qualitative trend previously noted on unpatterned cells (Figures 4.06) that peripheral SF are more ordered than any other SF bundles is confirmed in all CYTOO patterned cells, whatever the cell shape. Peripheral SF are at least  $10^\circ$  more ordered (i.e., with narrower cone aperture angle  $\Psi$ ) than any other SF types in all selected CYTOO morphology types (Crossbow, H-shaped, and Y-shaped). This trend is also *independent* of the cell size (see the Peripheral SF column at Table 4.01). Note that the origin of this more ordered value can be either a true higher alignment or an overestimation of the disorder in other structures, due to the possible bias sources mentioned in the section above. On the other hand, the Dorsal SF (not contractile bundles) are always more disordered (with wider cone aperture  $\Psi$ ) compared to any other contractile bundle (Peripheral SF, Ventral SF, Transverse Arcs), the reason for this apparent higher disorder being discussed above as well.

Apart from shape, size did not cause drastic changes on the  $\Psi$  values, but only a small shift (less than  $5^\circ$  in the  $\Psi$  value). Note that for the measured intensity levels, differences of more than  $2^\circ$  are considered significant since higher than noise-limited values. Since  $\Psi$  mean values were averaged over all pixels (more than 5000 pixels per SF category), differences of  $< \Psi >$  higher than  $2^\circ$  led also to statistically significant results (ANOVA test done by “*multcompare*” function in Matlab). For example, big crossbow had peripheral SF that were more ordered (around  $4^\circ$  difference in  $\Psi$ ) than medium size crossbow (table 4.01). On the other hand, big H-shaped cells had the opposite trend for peripheral bundles (medium size were more ordered than the big). The small differences obtained show that the size of the cells does not drastically

influence the actin order in peripheral SFs. One reason can be that these SFs are not undergoing drastic physical differences in their tension, resulting in poor modification in their organization.

### IV.5.3 Comparison among different contractile conditions

At last, we wanted to study how cell contractility (tension) affects F-actin nanoscale alignment in SF bundles. One way we could tackle such question is by comparing dorsal SF with all the other contractile SF types. The previous result of Dorsal SF compared to all the other SF types suggests that SF bundles might have a more aligned F-actin organization thanks to their contractile nature (by the presence of NMMII). However, due to the confidence level issues we met to compare different SFs, this behavior in Dorsal SF is not entirely trustable since it might be just a misinterpretation of ensemble-PFM data when probing unavoidable crossed regions. There are other ways one could try to tackle the contractility issue, for example:

- 1) Pharmacologically (adding drugs that affect contractility);
- 2) Genetically (probing a mutant U2OS cell line);
- 3) Computationally simulating SF overlap (quantifying  $\Psi$  bias due to crossed regions);
- 4) Probing SFs with a single-molecule polarization-resolved technique that naturally overcomes ensemble averaging problem.
- 5) Using different spreading time

One way we decided to tackle the problem was genetically, by using a constitutively active (CA) mutant of myosin light chain kinase (CA-MLCK) of U2OS cell line, which was kindly donated by Prof. Kumar, S. (Berkeley, USA). Such cell line has the advantage of having incorporated in their genes an inducible promoter for the expression of MLCK. Such promoter is induced to express the gene in the presence of doxycycline (tetracycline derivative). Depending on the concentration of doxycycline, we could modulate (with graded control) the activation of the MLCK gene, thus the contraction machinery of the cells via MLCK biochemical pathway [22].

The activation of MLCK induces phosphorylation of the non-muscle myosin II (NMMII) regulatory light chain (RLC), typically localized on Peripheral SF bundles [22]. Thanks to that, according to a detailed study by Kassianidou, E. et al., the induced expression of CA-MLCK cells had a major effect in activating contraction of Peripheral SF bundles, but Ventral SF were also partially affected by MLCK expression [22]. From their work, we decided to select the doxycycline concentration for which they reported the highest expression of CA-MLCK, e.g. 800ng/mL doxycycline in cell culture medium [22]. Hence, we could compare CA-MLCK U2OS mutant cells without doxycycline (what we call “ctrl”), and with 800ng/mL of doxycycline (what we call it “doxy”). The latter condition is expected to induce significant contractility in the cells, particularly of Peripheral SFs. The U2OS cell lines that were not mutants are here called “naïve” U2OS cells:

The new categories to be analyzed is a new cell line, under or not inducible contraction, are therefore:

- CA-MLCK U2OS cells without doxy → Ctrl cells
- CA-MLCK U2OS cells with doxy → Doxy cells
- Not mutant U2OS cells → naïve U2OS cells

Our hypothesis is that contractility induces higher actin alignment in Peripheral SFs: we would therefore a narrower ( $\Psi$  blue-shifted) in the ‘doxy cells’ condition (Figure 4.16). Importantly, naïve cells represent a control of the “Ctrl” condition, since Constitutively Active (CA) gene might have a basal expression activity even in absence of doxycycline (i.e., a leaked expression). Hence, the expected order outcome would be  $\Psi$  (Naïve)  $\leq$   $\Psi$  (Ctrl)  $\leq$   $\Psi$  (Doxy).

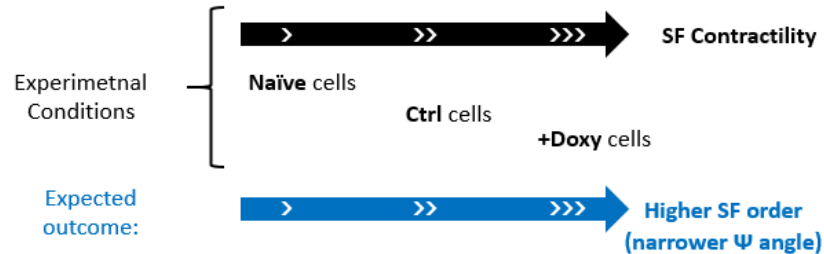


Figure 4.16 – The contractility hypothesis: the more tensioned (“contractile”) is the SF, the more aligned would be their F-actin filaments at the sub-diffraction scale.

In addition, we decided to test different contractility levels depending on the spreading time of the cell after plating them onto the coverslip. We expect to obtain a higher contraction levels (thus, ordered structures) in fully spread cells (matured) compared to cells under spreading process.

Here, we will list the all possible categories to be analyzed:

- Cell shape:
  - Crossbow, H-shaped, Y-shaped, O-shaped, and NP (not patterned)
- CYTOO size:
  - Big, Medium, and Small
- Cell line:
  - Naïve, Ctrl, and Doxy
- Stress Fiber type:
  - Peripheral, Ventral, TransvArcs, Dorsal, Other, ALL SF
- Spreading time:
  - Fully spread (6h or more), under initial spreading time (first 4h)


Since now we have extra conditions to be compared, we extended our categories develop a Matlab code that is sensitive to other filenames “flags”. Before, we were just comparing SF types according to cell shape, size, and SF type. Now we want take to account also the mutant cell lines CA-MLCK U2OS without doxy (filename flag: “ctrl”), CA-MLCK U2OS cells with 800ng/ml of doxy (filename flag: “doxy”), and the wild type of U2OS (filename naïve). With the categorical flag directly in the results file name, they are now written as “Category-A-cell-ID-Results.mat”.

Based on that, we created a matlab toolbox for managing the filenames. A long list of files that have in common the same experimental conditions could be automatically renamed with the corresponding “flag”. Furthermore, such files could be pooled together later for a more automated statistical analysis.

Since Dorsal SF are tough to be interpreted via ensemble-PFM due to amount of crossed regions along the bundle, it would be desirable to tackle the contractility hypothesis by selecting

the “cleanest” SF bundles (i.e., with less unavoidable crossings along the bundle). The latter could be done by giving a major priority on our statistical analyzes to Peripheral and Ventral SF (the ones with higher confidence level). Besides, since we know now that the CYTOO cell shape and size have not affected much our ensemble-PFM data, we do not need to analyze all combinatorial categorical possibilities, but just a few representative ones. For this reason, if we analyzed only “H-med”, “H-big”, and “Crossbow-med” conditions. Below, we present tables grouping all results (Tables 4.02-4.05). We used a new  $\Psi$  color-range code that can cover all recorded values:

Mean PSI range	Relative table color
$115^\circ \leq \Psi < 125^\circ$	$\Psi$
$125^\circ \leq \Psi < 135^\circ$	$\Psi$
$135^\circ \leq \Psi < 145^\circ$	$\Psi$
$145^\circ \leq \Psi < 155^\circ$	$\Psi$
$155^\circ \leq \Psi < 165^\circ$	$\Psi$

ordered  
  
disordered

- Control CA-MLCK U2OS cells (fully spread)



CA-MLCK ctrl	# cells	Mean PSI VALUES (°)	Peripheral	Ventral	Transverse Arcs	Dorsal	All SF
	4	Crossbow – med	130 ± 10	135 ± 15	142 ± 17	148 ± 15	137 ± 15
	4	H-shaped – med	120 ± 7	126 ± 13	142 ± 12	147 ± 12	132 ± 15

Table 4.02 – Table of the mean ± std of the order  $\Psi$  values of each SF type from the category Control CA-MLCK U2OS cells (fully spread and without doxy) on CYTOO patterned substrate.

- Doxy CA-MLCK U2OS cells (fully spread)



CA-MLCK +doxy	# cells	Mean PSI VALUES (°)	Peripheral	Ventral	Transverse Arcs	Dorsal	All SF
	4	Crossbow – big	128 ± 11	130 ± 19	139 ± 18	143 ± 17	135 ± 17
	4	Crossbow – med	129 ± 13	128 ± 16	143 ± 18	143 ± 18	133 ± 16
	4	H-shaped – big	120 ± 7	130 ± 13	145 ± 14	148 ± 13	132 ± 14
	8	H-shaped – med	121 ± 11	130 ± 18	133 ± 17	143 ± 17	130 ± 17

Table 4.03 – Table of the mean ± std of the order  $\Psi$  values of each SF type of the category +Doxy CA-MLCK U2OS cells (fully spread and with doxy) on CYTOO patterned substrate.

- Control CA-MLCK U2OS cells (under spreading, fixed after 4h plating)


CA-MLCK ctrl	# cells	Mean PSI VALUES (°)	Peripheral	Ventral	Transverse Arcs	Dorsal	All SF
	4	H-shaped – med	123 ± 7	129 ± 12	142 ± 15	142 ± 17	135 ± 16

Table 4.04 – Table of the mean ± std of the order  $\Psi$  values of each SF type of the category Control CA-MLCK U2OS cells (under spreading, fixed after 4h plating on CYTOO patterned substrate).

- **Doxy CA-MLCK U2OS cells (under spreading, fixed after 4h plating)**



CA-MLCK +doxy	# cells	Mean PSI VALUES (°)	Peripheral	Ventral	Transverse Arcs	Dorsal	All SF
	4	H-shaped – med	126 ± 11	134 ± 14	144 ± 16	145 ± 16	137 ± 16




Table 4.05 – Table of the mean ± std of the order  $\Psi$  values of each SF type of the category Doxy CA-MLCK U2OS cells (under spreading, fixed after 4h plating on CYTOO patterned substrate).

We present below the main conclusions of these results.

- **All SFs types in CA-MLCK mutant cells are more ordered than in naïve U2OS cells**

The obtained results show that first, the CA-MLCK mutant cells (with or without doxy) exhibit a F-actin organization more ordered than naïve U2OS cells, for all cells and SF types (see table 4.01 with the tables 4.02 - 4.05). The clearest examples are the peripheral and ventral SF of H-shaped cells (fully spread). We summarize the results (only fully spread) of peripheral and ventral SF in the following table 4.06 (Peripheral) and table 4.07 (Ventral), that also display their relationship with their expected contractility behavior.

**Peripheral SF Contractility** 

	Naïve U2OS	CA-MLCK ctrl	CA-MLCK +doxy	
	Mean PSI VALUES (°)	Peripheral	Peripheral	Peripheral
	Crossbow – big	136 ± 10	-	128 ± 11
	Crossbow – med	139 ± 9	130 ± 10	129 ± 13
	H-shaped – big	142 ± 7	-	120 ± 7
	H-shaped – med	139 ± 7	120 ± 7	121 ± 11
	Y-shaped – big	137 ± 7	-	-
	Y-shaped – med	136 ± 8	-	-

Peripheral SF  
Crossbow → 10° more ordered!

Peripheral SF  
H-shaped → 20° more ordered!

Table 4.06 – Comparison of Peripheral SF in different cell line conditions (naïve, ctrl and +doxy), fully spread cases



**Ventral SF Contractility**

	Naive U2OS	CA-MLCK ctrl	CA-MLCK +doxy	
Mean PSI VALUES (°)	Ventral	Ventral	Ventral	
Crossbow – big	149 ± 10		130 ± 19	Ventral SF Crossbow → 20°-25° more ordered!
Crossbow – med	154 ± 9	135 ± 15	128 ± 16	
H-shaped – big	153 ± 9		130 ± 13	Ventral SF H-shaped → 20°-25° more ordered!
H-shaped – med	151 ± 8	126 ± 13	130 ± 18	
Y-shaped – big	147 ± 10	-	-	
Y-shaped – med	146 ± 10	-	-	

Table 4.07 – Comparison of Ventral SFs in different cell line conditions (naïve, ctrl and +doxy), fully spread cases.

In naïve U2OS cells, peripheral SF had around  $\Psi \approx 140^\circ$ , meanwhile in CA-MLCK cells H-big and H-med cells have peripheral SF 20° more ordered, with  $\Psi \approx 120^\circ$ . We also obtained a similar trend when analyzing only ventral SFs (from  $\Psi \approx 150^\circ$  in naïve cells to  $\Psi \approx 130^\circ$  in CA-MLCK cells). In ventral SFs, a  $\Psi$  blue-shift was even higher, of 20° to 25° in order. Both results are in agreement with our hypothesis that the higher the contractility, the more aligned would be the F-actin within SFs (Figure 11). However, the fact that CA-MLCK cells (ctrl and +doxy) resemble more each other than with naïve U2OS suggests that the basal expression of the “Ctrl” CA-MLCK mutant are similar to the case “Doxy”. Interestingly, the standard deviation obtained on the “Doxy” case was always larger than the “Ctrl” case, suggesting a wider population. Such result is in agreement with the fluorescence and viscoelastic results of Kassianidou, E. et al. [22]: the differences between the Ctrl and Doxy cases were subtle (although statistically significant), having a clearer effect in the spreading of their data.

This trend is summarized in Table 4.08, where we grouped conditions by a count of the number of SFs types with a mean  $\Psi$  fitting within the 5 main  $\Psi$  ranges of 10° wide. We can observe a contractility-order trend in different cell lines (naïve, CA-MLCK ctrl, CA-MLCK +doxy): the more contractile, the higher the number of SF in the ordered range. We pooled together crossbow and H-shaped medium SFs, each with 5 SF categories: peripheral, ventral, transverse arcs, dorsal and all SF (Table 4.08).

Mean PSI range	Relative table color	naïve U2OS	CA-MLCK (ctrl)	CA-MLCK (+doxy)	
$115^\circ \leq \Psi < 125^\circ$	$\Psi$	0	1	1	order  disorder
$125^\circ \leq \Psi < 135^\circ$	$\Psi$	0	3	6	
$135^\circ \leq \Psi < 145^\circ$	$\Psi$	2	4	3	
$145^\circ \leq \Psi < 155^\circ$	$\Psi$	6	2	0	
$155^\circ \leq \Psi < 165^\circ$	$\Psi$	2	0	0	

Table 4.08 – Comparison of the obtained order in SF population in different cell line conditions (naïve, ctrl and +doxy), fully spread cases. The number given in the table is the count of the number of SF types obtained in a given  $\Psi$  range.

As we can see from Table 4.08, the SF order increases following the trend Naïve < CA-MLCK ctrl < CA-MLCK +doxy. In order to quantify this effect per cell, we also made a category



plot of the case where the differences were the cleanest: H-shaped cells of medium size (Figure 4.17).

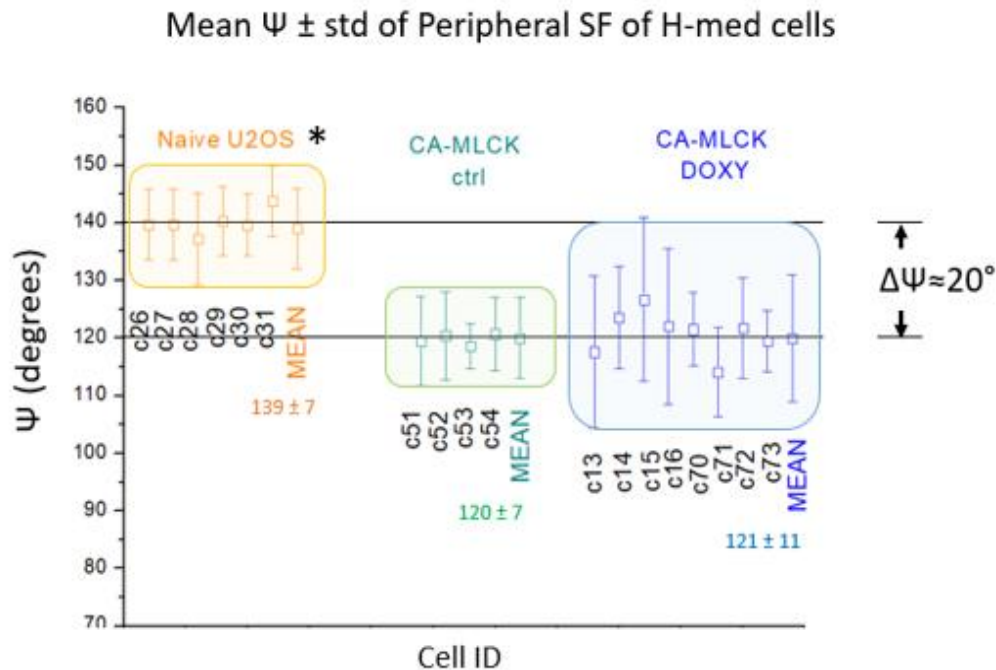


Figure 4.17 – Categorical plot of mean order value of Peripheral SF in H-med cells, comparing Naïve U2OS cells with CA-MLCK cells (doxy and ctrl). The \* represents significant different population ( $p$ -value of  $5.10^{-9}$  in ANOVA test in *multcompare* Matlab function). Populations with mean value differences higher than  $3^\circ$  were considered statistically different.

Finally, a few typical results on individual cells are presented in Figure 4.18, Figure 4.19, and Figure 4.20, where we display the Psimaps and the histograms of the peripheral SFs used to build up the plot of Figure 4.17.

In principle, we were expecting that naïve and “Ctrl” CA-MLCK would behave similarly, because we did not expect any gene expression in absence of doxy from the mutant gene. However, it seems Ctrl CA-MLCK condition has a leakage in the gene expression, and behaves like an intermediate condition between naïve U2OS and CA-MLCK +doxy. In agreement to that, the SFs and cell morphology of the population of CA-MLCK ctrl and CA-MLCK +doxy cells spread onto conventional coverslip (non-patterned) substrate were more similar to each other compared to naïve cells (not shown). Oftentimes, peripheral SF bundles were thicker in both mutant cells compared to naïve cells, and were also more straight (Figures 4.18-4.20). This more important curvature observed in naïve cells is consistent with a lower tension (see Chapter 1). Besides, a larger number of ventral SF were seen in mutant cells compared to naïve cells. Taken together these data suggests that CA-MLCK ctrl and CA-MLCK +doxy should experience a more contractile condition than naïve cells, and the difference between ctrl and +doxy condition might be subtle.

Histogram per cell of peripheral SFs  
Naïve U2OS cells – H-shaped medium size

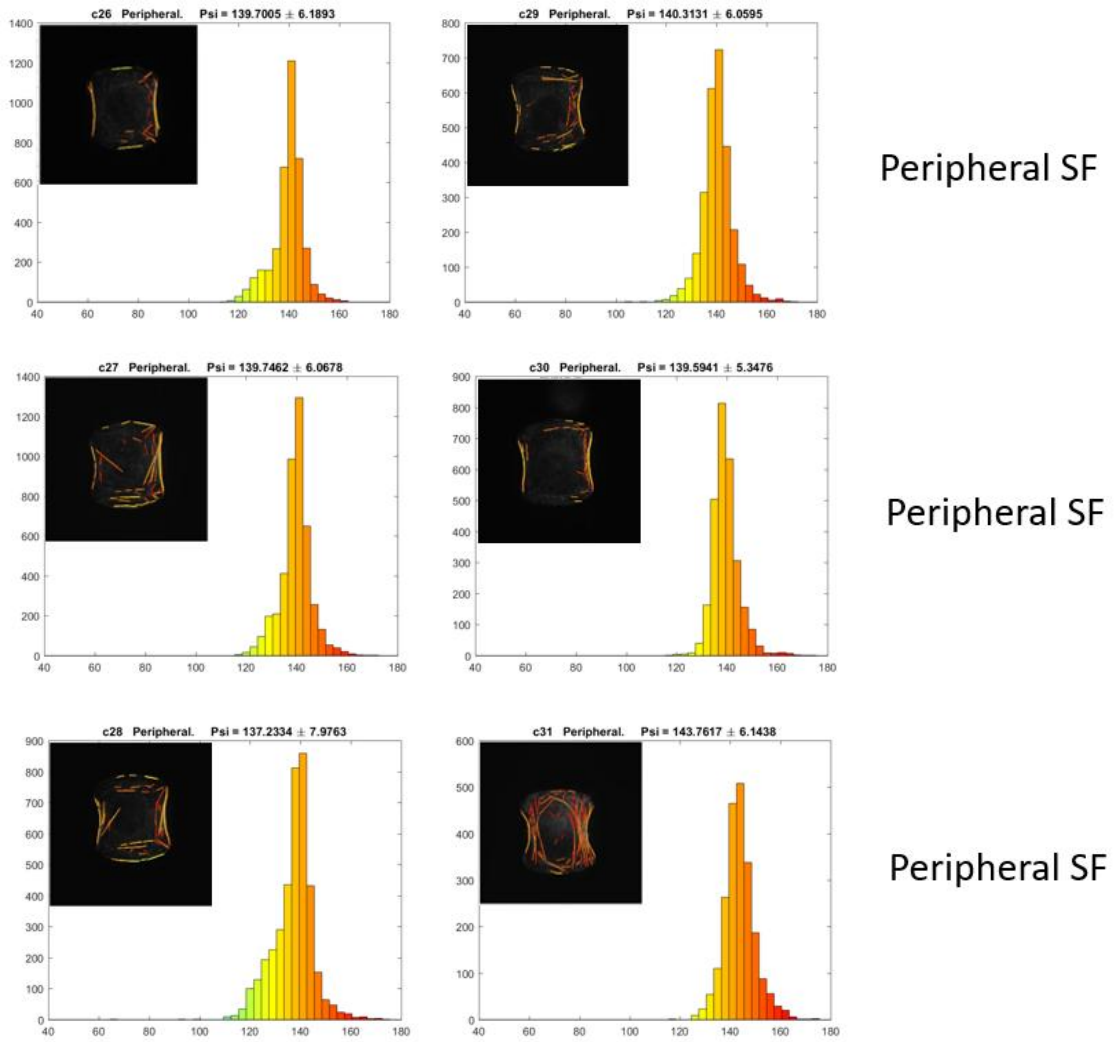


Figure 4.18 – Histograms of Peripheral SF per cell of naïve H-med U2OS cells. Note that the peak is around  $\Psi=140^\circ$ , and sometimes there is a shoulder in between  $120^\circ$ - $140^\circ$ .

### Histogram per cell of peripheral SFs

#### Ctrl CA-MLCK U2OS cells – H-shaped medium size

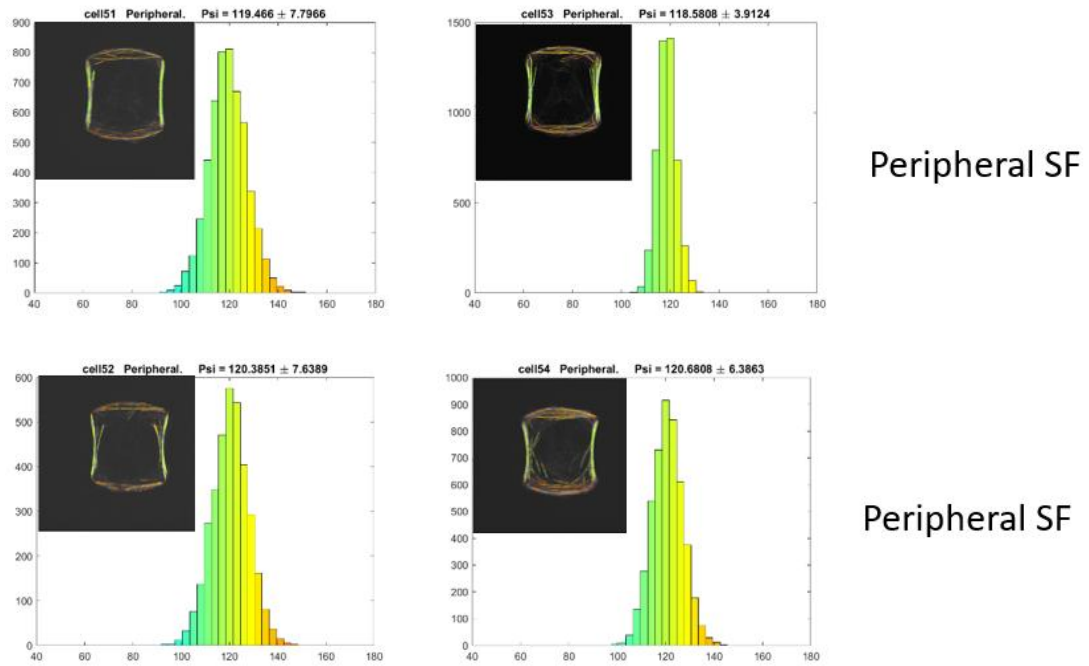
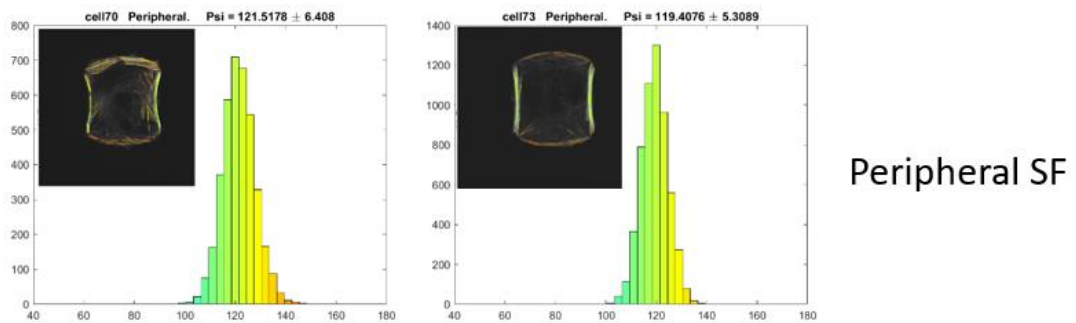


Figure 4.19– Histograms of Peripheral SF per cell of Ctrl (without doxy) CA-MLCK H-med U2OS cells. Note that we only see a single peak around  $\Psi=120^\circ$ , and the std is quite narrow (around  $7^\circ$ ).

### Histogram per cell of peripheral SFs

#### Doxy CA-MLCK U2OS cells – H-shaped medium size



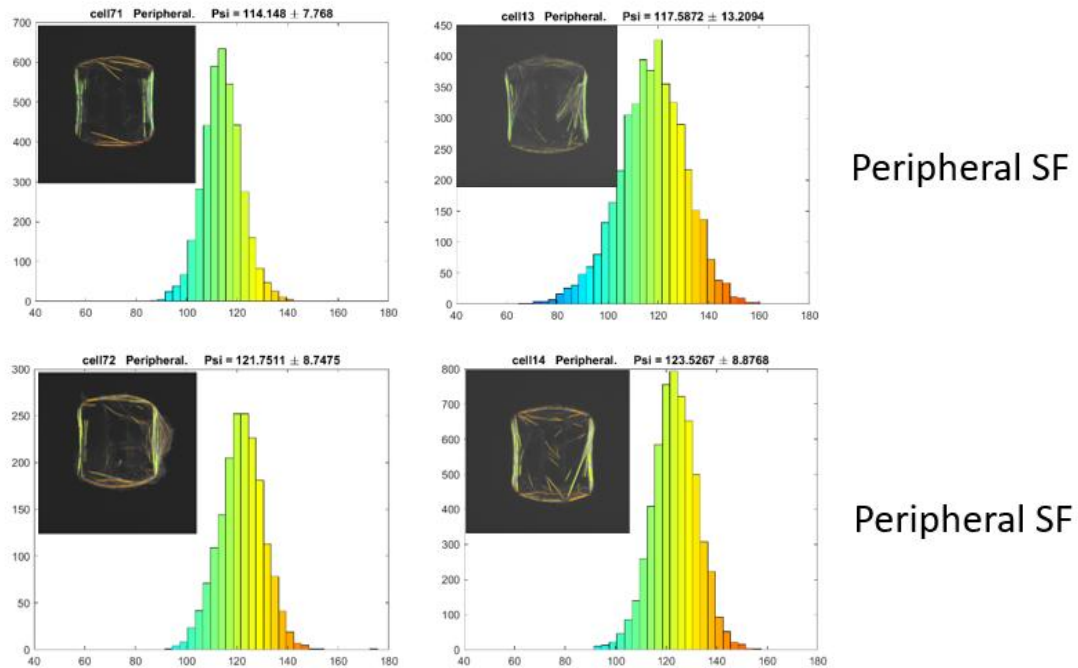


Figure 4.20 – Histograms of Peripheral SF per cell of Doxy CA-MLCK H-med U2OS cells. Note that we only see a single peak around  $\Psi=120^\circ$ .

#### IV.5.4 Comparison among different cell morphologies in CA-MLCK U2OS cells

- **The CYTOO cell morphology has an effect in CA-MLCK cells, but not in naïve U2OS**

We can readily see from table 4.06 see that different CA-MLCK cell morphologies lead to differently F-actin organizations. Peripheral SF of crossbow cells has a mean order value around  $\langle\Psi\rangle=130^\circ$ , and on H-shaped cells the mean value were even narrower: of  $\langle\Psi\rangle=120^\circ$ . Examples of Ctrl and Doxy H-med and Crossbow-med are given in (Figures 4.21-4.23). Both values are smaller than what we obtained with naïve cells, whose mean were close to  $\langle\Psi\rangle\approx 140^\circ$  (see table 4.01 and Figures 4.18). Interestingly, cell size did not seem to have an effect in any case (Naïve or Doxy, see also peripheral SF of the table 4.03 and Figures 4.21-4.23). Note that in general, we observed that the highest orders were observed in very thick and straight SFs (which are more predominantly found in CA-MLCK H-med cells): this aspect seems to be the most predominant reason for a tight organization of the filaments.

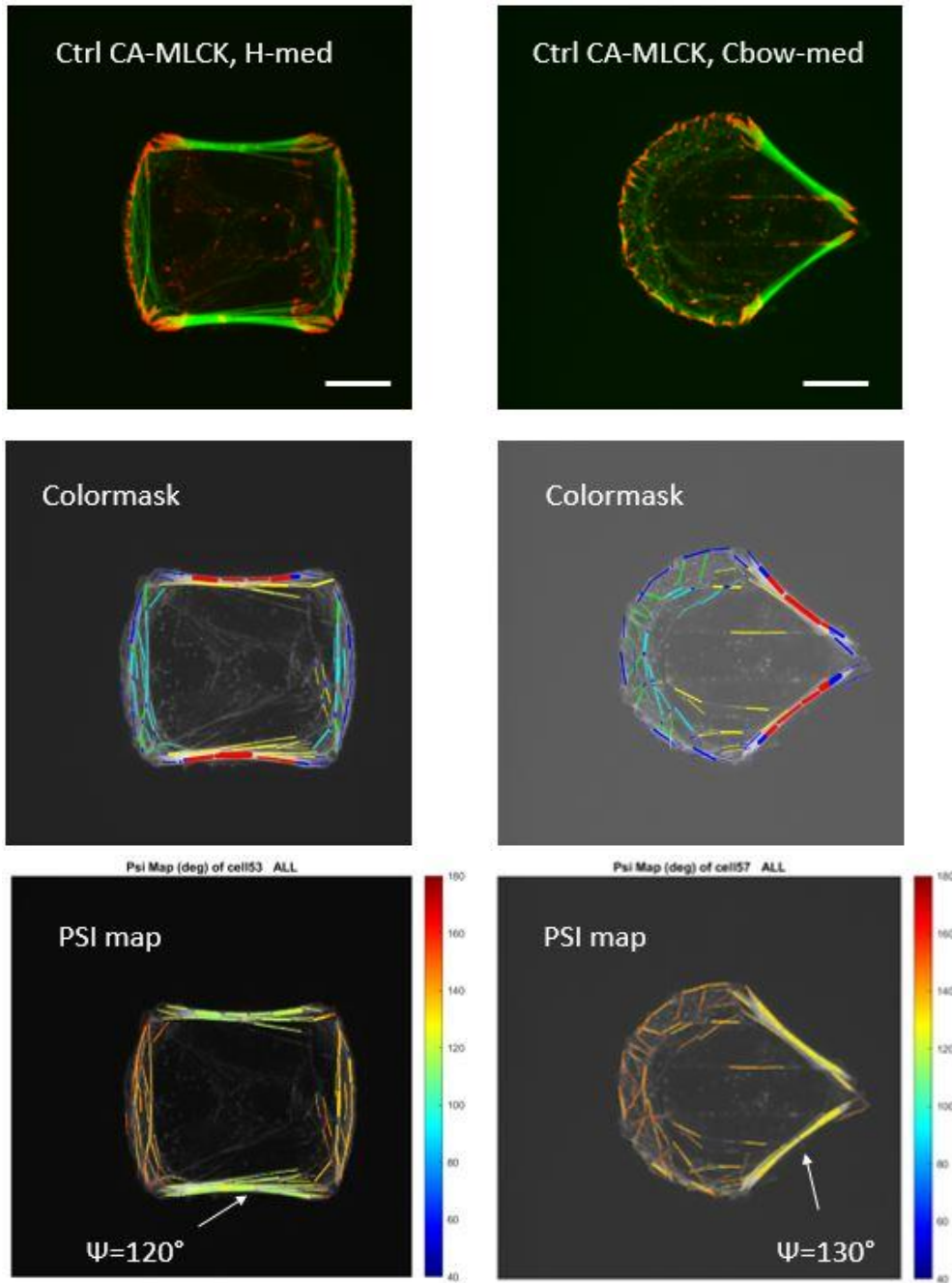


Figure 4.21 – Ctrl CA-MLCK H-shaped-medium size and Crossbow-medium size patterns. Costaining in RGB (top), colormask (center) and Psimap (bottom). White scale bar is 10 $\mu$ m. In the costaining (top), F-actin (green) and Phospho-FAK (focal adhesion, in red). Colormask legend: red(Peripheral), yellow(Ventral), light blue(Transverse arcs), green(Dorsal SF), darkblue(other SF). In the Psimap (bottom).

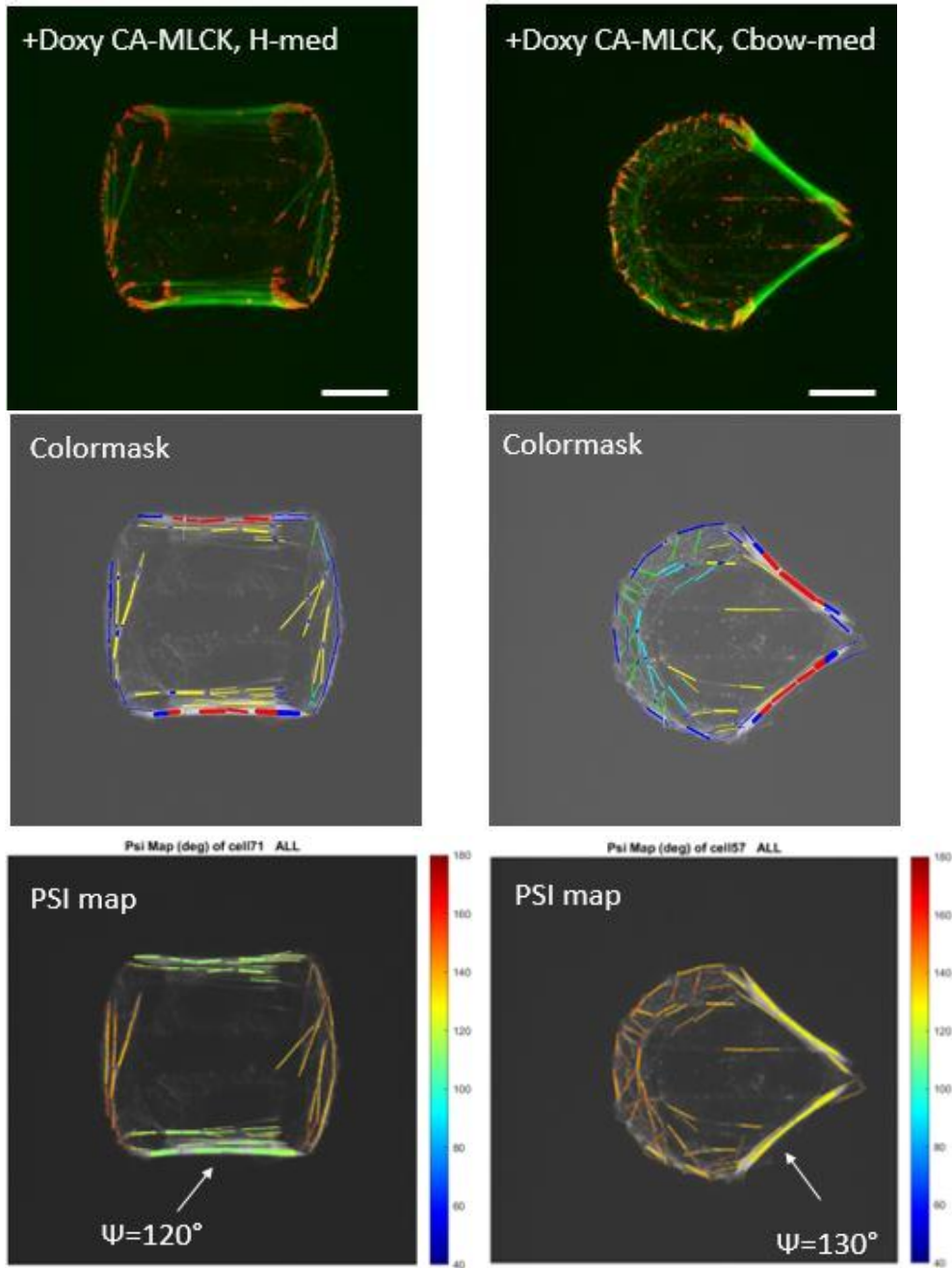


Figure 4.22 – Doxy CA-MLCK H-shaped-medium size and Crossbow-medium size patterns. Costaining in RGB (top), colormask (center) and Psimap (bottom). White scale bar is  $10\mu\text{m}$ . In the costaining (top), F-actin (green) and Phospho-FAK (focal adhesion, in red). Colormask legend: red(Peripheral), yellow(Ventral), light blue(Transverse arcs), green(Dorsal SF), darkblue(other SF). In the Psimap (bottom).

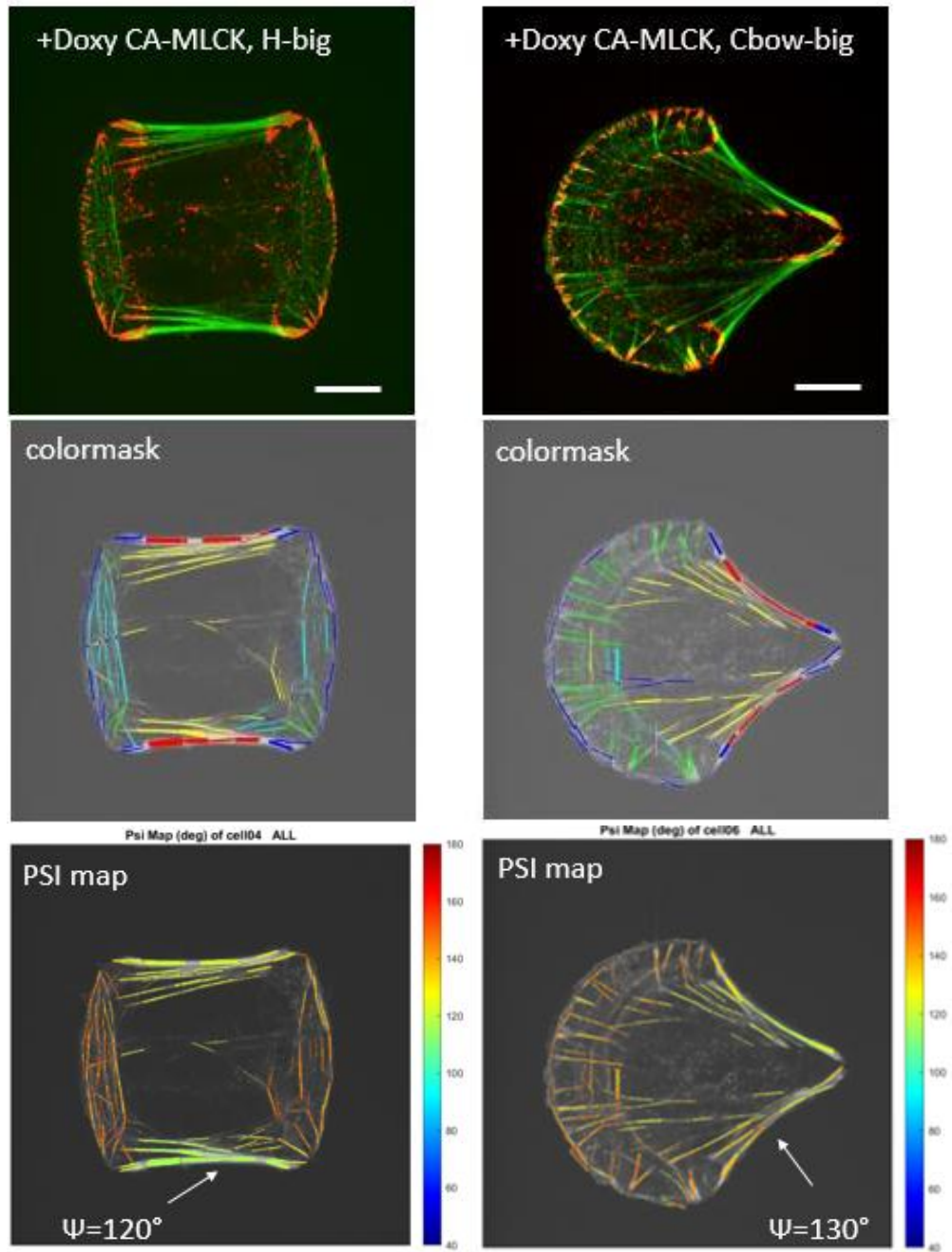


Figure 4.23 – Doxy CA-MLCK H-shaped-big size and Crossbow-big size patterns. Costaining in RGB (top), colormask (center) and Psimap (bottom). White scale bar is 10 $\mu$ m. In the costaining (top), F-actin (green) and Phospho-FAK (focal adhesion, in red). Colormask legend: red(Peripheral), yellow(Ventral), light blue(Transverse arcs), green(Dorsal SF), darkblue(other SF). In the Psimap (bottom).



#### IV.5.5 Comparison between different spreading times in CA-MLCK U2OS cells

- **Spreading time had a subtle effect in CA-MLCK cells**

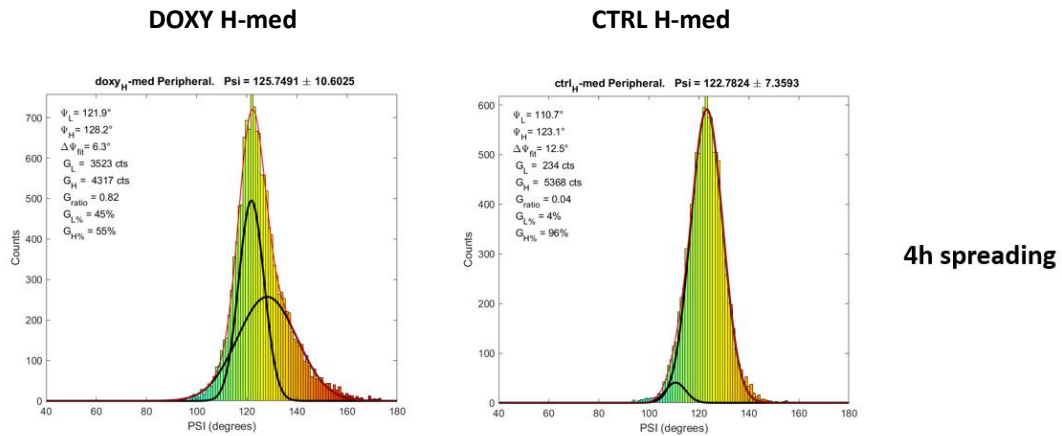
Comparing the table 4.03, with tables 4.04, and 4.05, we could see that H-med cells under an intermediate spreading process (fixed after 4h plating the cells onto CYTOO substrate) had peripheral and ventral SFs slightly more disordered (around 5° difference) than the fully spread case (table 4.03). This is agreement with our hypothesis that the more spread the cells, the higher the tension/contractility level in SF bundles (see Chapter1) and therefore the higher the order (F-actin alignment in SF).

- **Double Gaussian fit of histograms might show the main components of each SF type**

We have seen above in the CA-MLCK cells that the main effect of doxy was an increase in the standard deviation of psi values. A large standard deviation might however hide a more complex population information. In other words, we might have to consider the shape of the recorded populations, and possibly investigate the presence of more than one  $\Psi$  populations in the recorded histograms.

In Figure 4.24, we see that the peak in Doxy Peripheral SFs histograms could be derived from 2 populations: first, a fully ordered population called below  $\Psi_{low}$  component (mean  $\Psi$  around 120°, common in peripheral SFs), and a second and partially less ordered population called  $\Psi_{high}$  component (around 130°, more commonly found in ventral SF). By applying the 2-Gaussian peak approach in doxy cells, we could detect in more detail the changes in the histogram profile during the ordering process from 4h spreading to fully spread cells. The most ordered peak ( $\Psi_{low}$ ) had just a small  $\Psi$  blue-shift of 3° difference from 4h spreading to fully spread and got enriched in counts. On the other hand, the most disordered peak red-shifted (from  $\Psi_{high}=128^\circ$  to  $\Psi_{high}=140^\circ$ ) and decreased in counts. That behavior is responsible for shifting the histogram mean value from  $\sim 126^\circ$  to  $121^\circ$ . On the other hand, Ctrl CA-MLCK cells were best described by a single peak on both situations: 4h spreading and on the fully spread case.

#### PERIPHERAL SF





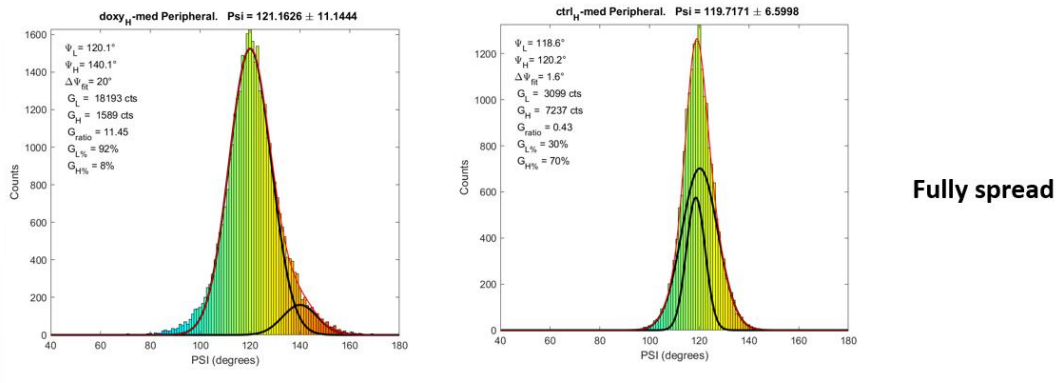


Figure 4.24 – Histograms with double Gaussian fit of **peripheral SF** of DOXY and CTRL cells, under spreading (4h) and fully spread (6h). In red line, the double Gaussian fit profile, and in black lines the profile of each fitted peak (the peak with the lowest mean, named  $\Psi_{low}$ , and the Gaussian peak with highest mean,  $\Psi_{high}$ ).  $\Delta\Psi_{fit}$  is the difference between both peaks  $\Delta\Psi_{fit} = \Psi_{high} - \Psi_{low}$ . The number of counts of each peak  $G_L$  (low) and  $G_H$  (high), and the relative percentage  $G_{L\%}$  and  $G_{H\%}$ . The ratio between the low peak and the high peak is  $G_{ratio} = G_{low}/G_{high}$ . The colorcode is the jet(40-180), and the histogram bars are of 1 degree.

When analyzing the ventral SFs, we could also detect subtle shifts (Figure 4.25). Subtle here means a difference in the mean value of equal or less than  $5^\circ$ . For example, Ctrl CA-MLCK cells shifted from  $129^\circ$  (table 4.04, under 4h spreading) to  $126^\circ$  (table 4.02, fully spread). However, when we analyze the histogram profiles we see that, when the CTRL cells were fully spread, their histogram displayed a clear new peak that did not exist on 4h spreading cells. The new peak in the ventral SF of fully spread Ctrl cells ( $\Psi_{low}$ ) was around  $120^\circ$  (common in peripheral SF of CA-MLCK cells), and the second peak ( $\Psi_{high}$ ) was kept around  $130^\circ$  (common in ventral SF of CA-MLCK cells). On the other hand, when cells were treated with doxycycline, the mean shifted from  $133^\circ$  (under 4h spreading) to  $130^\circ$  (fully spread). However, the histogram profile of both cases were quite similar: a wide single peak close to  $130^\circ$ . In order to investigate with more details the reasons of the small  $\Psi$ -shift, we tried to analyze if the histogram had lower and higher peak components with the 2 Gaussian fit procedure. The gain in order of  $3^\circ$  psi blue-shift could be explained by an increase in counts of the low psi component: before the  $\Psi_{low}$  component had 40% of the counts, and when DOXY cells were fully spread, the  $\Psi_{low}$  component increased to 88% of the histogram counts.

## VENTRAL SF

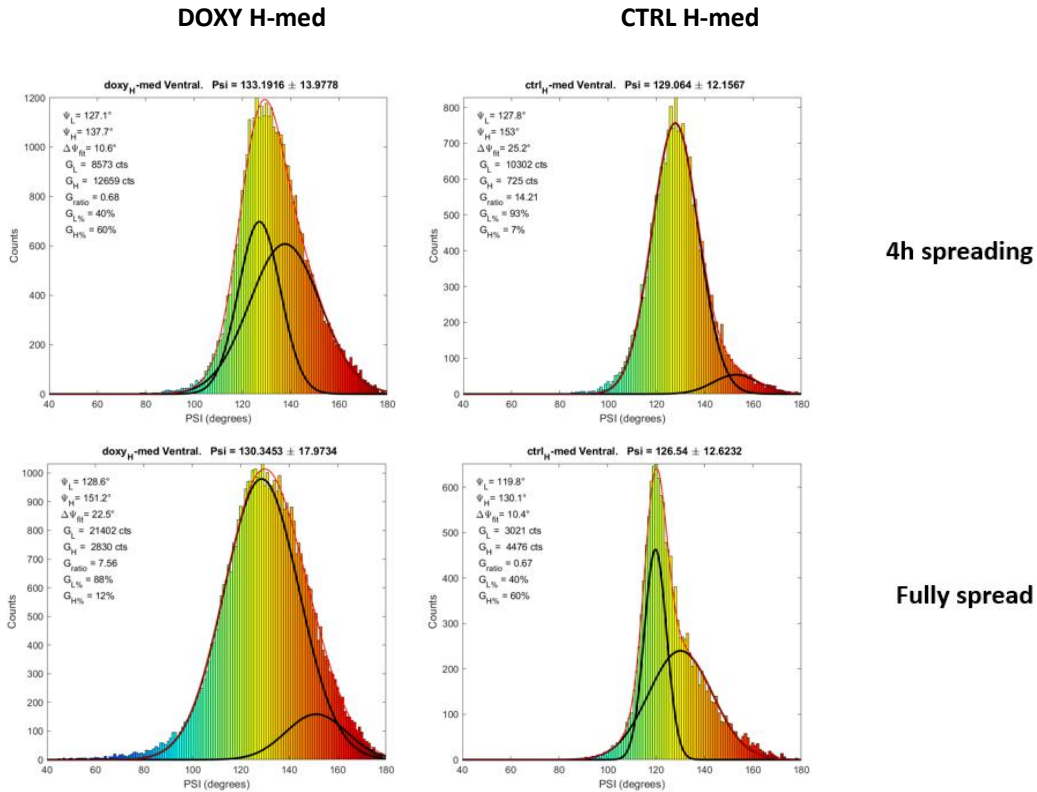


Figure 4.25 – Histograms with double Gaussian fit of **ventral SF** of DOXY and CTRL cells, under spreading and fully spread. In red line, the double Gaussian fit profile, and in black lines the profile of each fitted peak (the peak with the lowest mean, named  $\Psi_{low}$ , and the Gaussian peak with highest mean,  $\Psi_{high}$ ).  $\Delta\Psi_{fit}$  is the difference between both peaks  $\Delta\Psi_{fit} = \Psi_{high} - \Psi_{low}$ . The number of counts of each peak  $G_L$  (low) and  $G_H$  (high), and the relative percentage  $G_{L\%}$  and  $G_{H\%}$ . The ratio between the low peak and the high peak is  $G_{ratio} = G_{low}/G_{high}$ . The colorcode is the jet(40-180), and the histogram bars are of 1 degree.

Comparing Peripheral and Ventral SFs in Ctrl CA-MLCK cells showed that ventral SFs had a narrower width  $\Psi$  histogram distribution compared to the ventral SF of +Doxy. In Ctrl case, we could directly conclude (without any 2-Gaussian fit) that there were in the histogram profile two population peaks, but not in the Doxy case. In Doxy cells, we typically detect a single-peak with a wider width, which is in agreement with the large width per cell case Figure 4.17. In the Figure 4.26, we tried to fit 2-Gaussian peaks on the  $\Psi$  histogram of peripheral and ventral SF of Ctrl and Doxy CA-MLCK H-med cells. We see that Ventral SFs from Ctrl CA-MLCK cells cannot be considered constituted from a single population, but it has components of high and low  $\Psi$  values.

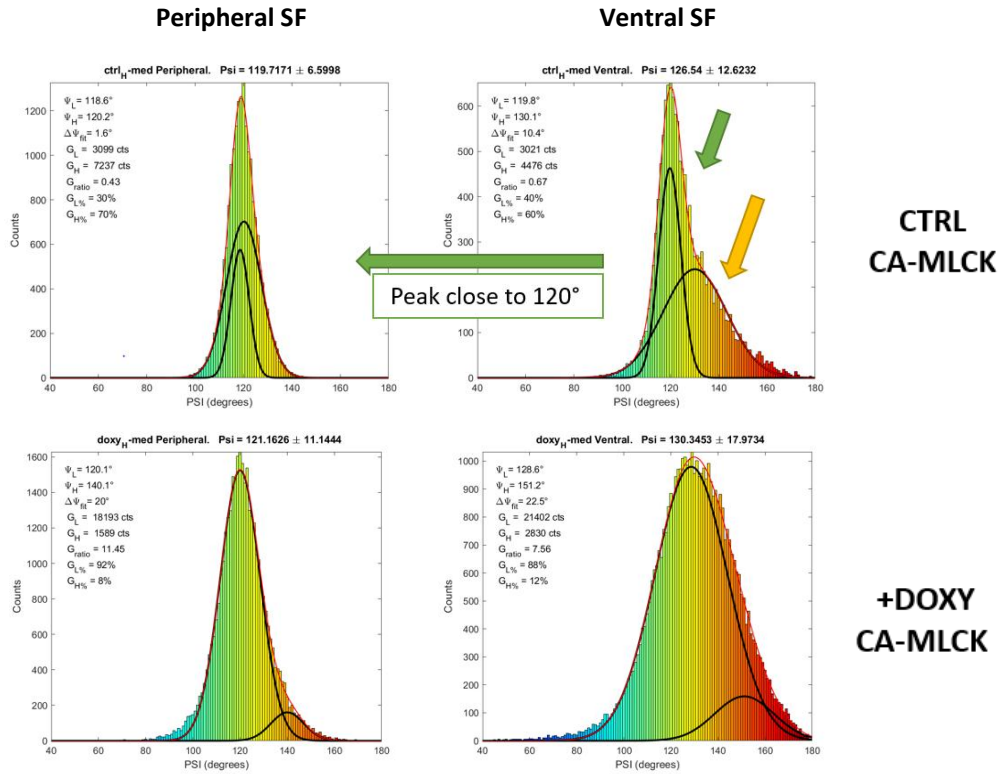


Figure 4.26 –  $\Psi$  histograms of peripheral and ventral SF of Ctrl and Doxy CA-MLCK H-med patterned cells (only fully spread). The red line, the double Gaussian fit profile, and in black lines the profile of each fitted peak (the peak with the lowest mean, named  $\Psi_{low}$ , and the Gaussian peak with highest mean,  $\Psi_{high}$ ).  $\Delta\Psi_{fit}$  is the difference between both peaks  $\Delta\Psi_{fit} = \Psi_{high} - \Psi_{low}$ . The number of counts of each peak  $G_L$  (low) and  $G_H$  (high), and the relative percentage  $G_{L\%}$  and  $G_{H\%}$ . The ratio between the low peak and the high peak is  $G_{ratio} = G_{low}/G_{high}$ . The colorcode is the jet(40-180), and the histogram bars are of 1 degree.

When we used double Gaussian fits on the SF histograms of CA-MLCK cells, we can see that are Gaussian peak components that are often seen on each category. Here we will show the trends for H-shaped and Crossbow. We recall that size did not make a clear difference. We summarize below the results obtained from this analysis.

-  $\Psi$  components in H-shaped medium CA-MLCK cells (H-med):

- Peripheral SF →  $\langle\Psi\rangle \sim 120^\circ \pm 3^\circ$
- Ventral SF →  $\langle\Psi\rangle \sim 130^\circ \pm 3^\circ$
- Transverse Arc →  $\langle\Psi\rangle \sim 130^\circ \pm 3^\circ$ , and  $\langle\Psi\rangle \sim 138^\circ \pm 3^\circ$
- Dorsal SF →  $\langle\Psi\rangle \sim 140^\circ \pm 3^\circ$ , and  $\langle\Psi\rangle \sim 148^\circ \pm 3^\circ$

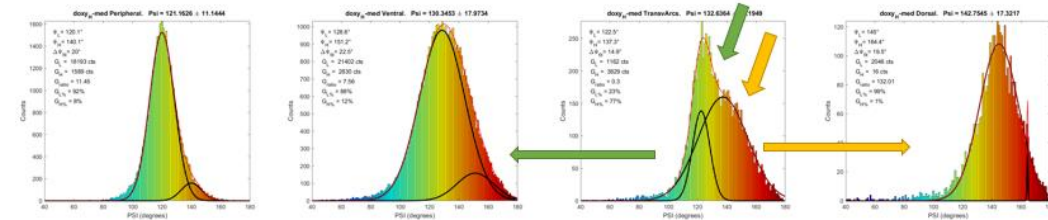
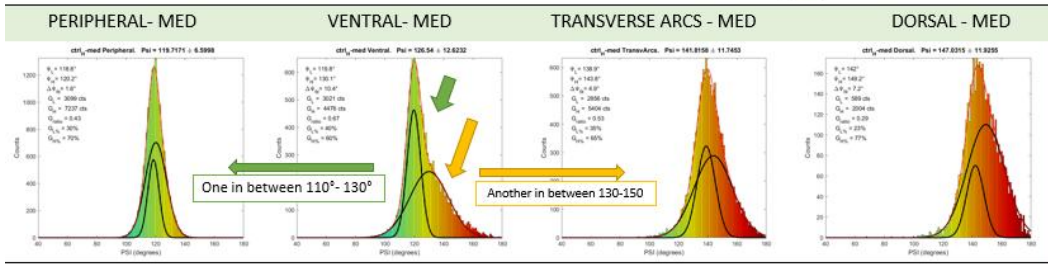


Figure 4.27 –  $\Psi$  histograms of peripheral, ventral, transverse arcs, and dorsal SF of Ctrl and Doxy CA-MLCK H-med patterned cells (only fully spread). The green and yellow arrow points for the peaks shared in common the psi components (peak center in psi). The red line, the double Gaussian fit profile, and in black lines the profile of each fitted peak (the peak with the lowest mean, named  $\Psi_{low}$ , and the Gaussian peak with highest mean,  $\Psi_{high}$ ).  $\Delta\Psi_{fit}$  is the difference between both peaks  $\Delta\Psi_{fit} = \Psi_{high} - \Psi_{low}$ . The number of counts of each peak  $G_L$  (low) and  $G_H$  (high), and the relative percentage  $G_L\%$  and  $G_H\%$ . The ratio between the low peak and the high peak is  $G_{ratio} = G_{low}/G_{high}$ . The colorcode is the jet(40-180), and the histogram bars are of 1 degree.

-  $\Psi$  components in Crossbow medium CA-MLCK cells (Crossbow-med):

- Peripheral SF →  $\langle\Psi\rangle \sim 130^\circ \pm 3^\circ$
- Ventral SF →  $\langle\Psi\rangle \sim 130^\circ \pm 3^\circ$ , and  $\langle\Psi\rangle \sim 138^\circ \pm 3^\circ$
- Transverse Arc →  $\langle\Psi\rangle \sim 138^\circ \pm 3^\circ$ , and  $\langle\Psi\rangle \sim 153^\circ \pm 3^\circ$
- Dorsal SF →  $\langle\Psi\rangle \sim 138^\circ \pm 3^\circ$ , and  $\langle\Psi\rangle \sim 153^\circ \pm 3^\circ$

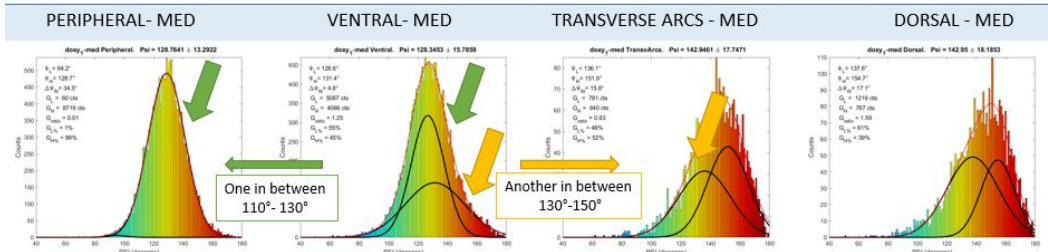
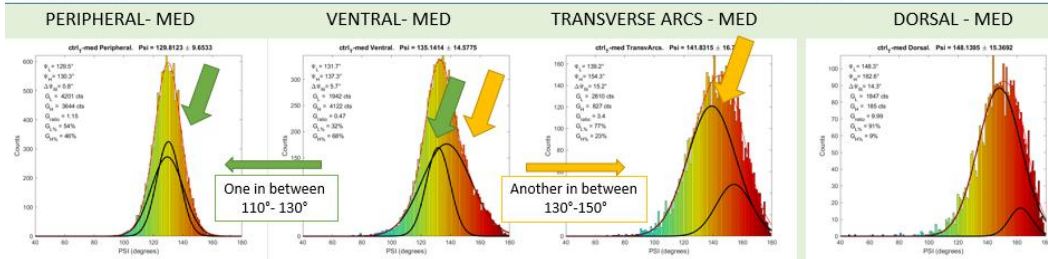


Figure 4.28 –  $\Psi$  histograms of peripheral, ventral, transverse arcs, and dorsal SF of Ctrl and Doxy CA-MLCK crossbow-mediated patterned cells (only fully spread). The green and yellow arrow points for the peaks shared in common the psi components (peak center in psi). The red line, the double Gaussian fit profile, and in black lines the profile of each fitted peak (the peak with the lowest mean, named  $\Psi_{low}$ , and the Gaussian peak with highest mean,  $\Psi_{high}$ ).  $\Delta\Psi_{fit}$  is the difference between both peaks  $\Delta\Psi_{fit} = \Psi_{high} - \Psi_{low}$ . The number of counts of each peak  $G_L$  (low) and  $G_H$  (high), and the relative percentage  $G_L\%$  and  $G_H\%$ . The ratio between the low peak and the high peak is  $G_{ratio} = G_{low}/G_{high}$ . The colorcode is the jet(40-180), and the histogram bars are of 1 degree.

Thus with 2-Gaussian fit that we could get deeper insights on the behavior of the  $\Psi$  histogram peaks that could be particularly useful to evaluate subtle differences in  $\Psi$  histogram profiles. The population of higher  $\Psi$  values is most probably representative of a more isotropic environment around the measured SFs, which could be excluded thanks to this 2-Gaussian fit. Moreover, we could detect with our ensemble-PFM hidden populations F-actin organization in the histograms that could have biological interpretation. However, when considering the contractility-order hypothesis, the most relevant  $\Psi$  histogram differences were significantly large ( $\sim 20^\circ$  in Peripheral and Ventral SF), and the main message of 2-Gaussian fit is still the same as the simple Gaussian statistics approach: the higher the contractility the higher the order parameter (narrower  $\Psi$  values).

#### IV.6 Conclusions of Chapter 4

In this chapter, we demonstrated the use of ensemble polarized fluorescence microscopy (PFM) technique on different stress fiber (SF) categories using a fast rotating incident polarization (modulated by a Pockels cell) and a fast parallel confocal scanning imaging tool (Yokogawa spinning disk). Such experimental concept had been already built by a former student (Xiao Wang) but at that time, only one excitation laser was used and automated analysis was not performed. Importantly, since dichroic mirrors are used to deflect the beam before the objective, a careful calibration of the polarization distortions at the back focal plane (BFP) need to be performed to guarantee proper incident polarization condition on the excitation field. In particular, our image acquisition speed is mainly limited by the integration time (typically 0.5s per frame). Thus, a polar stack of 18 frames (a frame every  $10^\circ$  of linear polarization orientation) can be done in a few seconds. Although not emphasized in this chapter, we typically imaged 4 z-planes spaced by 500nm in Z to help us in SF segmentation, once we could interpret 3D behavior of SF in our cells (typically  $60\mu\text{m}$  wide, and  $4\mu\text{m}$  thick). For example, dorsal SF are 3D tilted bundles that shows up in all z-planes, while other SF bundles not. Therefore, in around 40s we could finish 4 polar-stack of 18 frames each, giving enough information of SF in 3D. Besides, an immunolabelled focal adhesion costaining (p-FAK) was done to support us in the SF segmentation, and SF could easily be categorized by the number of focal adhesions it binds (see Chapter 1).

An important step in the analysis was that we tried to make the segmentation of SF the least prone to user bias possible. For that, we used a freeware software (filament sensor) available in the literature that tracks straight segments of cell filaments in a fluorescence micrograph. We used the output information of filament sensor as a binarized mask in Matlab. In the latter, we developed a code that the user could manually select the binarized filaments and categorize it as peripheral, ventral, dorsal, transverse arc, or other SF. During the processing

steps, when saving the files, the filename of the treated data had the distinct “flag” relating to the experimental category that the cell was. An automatic statistical analysis and plot could be performed by just pooling together data with similar filenames afterwards (e.g., histograms, Gaussian fit, double Gaussian fit). Although not emphasized in the text, support Matlab toolboxes to edit filenames and filament colors was also done. As commented in the previous works, the expected angular precision in the orientation ( $\rho_{av}$ ) and order ( $\Psi$ ) parameters is about  $1^\circ$ .

On the analysis side, we had to deal with the challenging task of interpreting SF data with different confidence level. As we commented, peripheral SF are the SF category with higher confidence level and that is the reason why we focused the interpretation of the data on such structure in this chapter. Besides, because non patterned cells displayed complex F-actin network (bundles with different geometrical properties), we opted to plate cells on standard patterned substrate (CYTOO®) to obtain reproducible cell shape, and thus reproducible SF organization. In all cell morphologies and sizes we tested, the SF categories (peripheral, ventral, transverse arcs, and dorsal SF) followed the same  $\Psi$  trend of order: Peripheral (most ordered) < Ventral  $\leq$  Transverse Arcs < Dorsal (most disordered). In particular, the average order value of peripheral SF was  $\Psi=138^\circ$ , and for dorsal SF it was  $\Psi=156^\circ$ , suggesting that F-actin alignment in peripheral SF bundles was around  $\sim 20^\circ$  more organized. However, due to a presence of more complex F-actin network in the background of dorsal SF (likewise in ventral SF, and transverse arcs), such differences in order might be just a misinterpretation of the order in the bundle. Single-molecule polarization resolved measurements will address this question (see chapter 5). On the other hand, if the hypothesis that peripheral SF were indeed more ordered than dorsal SF, contractility level could explain the difference in F-actin alignment.

In order to test if contractility plays a role in F-actin alignment in SF, there were a few ways we could tackle such question. The way we mainly opted was to use mutant U2OS cell lines whose expression of myosin light chain kinase (MLCK) could be activated by the presence of doxycycline. In constitutively active (CA) MLCK cells, we obtained F-actin organization more ordered in all SF types. A shift to narrower  $\Psi$  values was observed in all SF categories. This in agreement to our hypothesis that a higher degree of contractility might align more the F-actin in the SF bundles. The reason why all SF became more ordered and not only peripheral SF could also indicate a possible tension crosstalk among the SF categories, as already observed in the literature [22]. Interestingly, the  $\Psi$  shift was particularly clear in peripheral and ventral SF (bundles with the highest confidence level) in H-shaped cells. Peripheral SF in H-shaped CA-MLCK cells became around  $20^\circ$  more ordered compared to naïve cells, and reached the bottom limit  $\Psi=120^\circ$  (the same obtained in single-filaments due to purely thermal fluctuations and tilted binding). The latter indicates maximum possible alignment of F-actin filaments in SF bundles. This low value was seen mostly in thick SF bundles, indicating that bundle thickness could also be a factor in the higher organization of F-actin filaments. On the other hand, ventral SF became  $20^\circ$ - $25^\circ$  more ordered in H-shaped medium size CA-MLCK cells (ctrl and doxy categories) compared to naïve cells. Similar results obtained for CA-MLCK cells (ctrl and doxy) suggests that even in absence of doxycycline the CA-MLCK cell line has already a significant basal (“leaked”) expression of the contractility gene. Although similar, the overall result pooling together the range of  $\Psi$  values (Table 4.08) suggests that SF in Ctrl cells were slightly less ordered than SF in Doxy cells. Overall, ensemble-PFM results applied on mutant cell lines were in agreement with our hypothesis that the contractility might play a role aligning actin filaments in SF bundles, and followed the trend: Naïve (more disordered) < Ctrl (intermediate case) < Doxy (more ordered). Besides, we performed a quick test to evaluate if spreading time (tension maturation) could also

affect the F-actin alignment in H-shaped medium size cells. Spreading time had a very subtle effect ( $\leq 5^\circ$  in average) in  $\Psi$  histograms. Since ANOVA test in a large  $\Psi$  distribution ( $> 5000$ ) of pixels led to statistically significant events any difference of average  $\Psi$  higher than  $2^\circ$ , such subtle differences in due to spreading time might be considered statistically significant. However, the differences in  $\Psi$  histograms became only clearer when trying to use double peak Gaussian fit (to evaluate subpopulations within the histogram). Such approach could be eventually used to explore subpopulations of F-actin order in any histograms and we showed that based on data we got, the subpopulations (Gaussian peaks) of tend to have the same position in  $\Psi$  histograms in different SF types. However, a more robust (higher number of cells) systematic study of the use of 2-Gaussian fit and its biological interpretation is still lacking.

Finally, our ensemble-PFM technique demonstrated to be very useful for screening SF organization in many experimental conditions. However, the presence of an underlying complex actin network in the bulk, particular with crossed filaments and/or tilted structures still could bias the polarimetric readout. The two main ways we could tackle such limitations is by computational simulation and by experimental single-molecule methods. Since the main source of the bias in the ensemble-PFM depends on averaging over an ensemble of fluorophores within each PSF, going to single-molecule level would in principle overcome such limitations. Based on that, we decided to implement a new polarized single-molecule super-resolution fluorescence microscopy method, that is described in Chapter 3 and in Chapter 5.





## Chapter 5

# Polarized Single-molecule Super-resolution Fluorescence Microscopy applied to Actin Stress Fibers

### Introduction

The results of Chapter 4 show that it is possible to use ensemble polarized resolved measurements in order to compare different actin organization, providing that the measurements conditions allow to avoid any strong overlap with isotropic background organizations or crossed directions. In addition, this measurement cannot be used to measure quantitatively the order (angular aperture) of actin filaments, since we do not know how much angle disorder is attributed to the fluorophore wobbling. Recent works [59] have shown that it is possible to estimate this wobbling value from single molecule measurements, projecting single molecule's images on 2 polarization states. As described in Chapter 3, the approach has still some limitations since 2 polarization states allows to determine only either the averaged orientation of the molecules, or their wobbling, providing that the other parameter is known. In this Chapter, we present a method, inspired from [94], that uses 4 projected polarization states. This method has been used in other works during the time course of this PhD [82, 93, 95].

We will first describe the technical aspects of the implementation of this method, in particular with respect to its calibration and image processing and analysis. We will then evaluate its performance on model samples (polarized beads) and apply it to actin imaging in cells.

### V.1. 4polar-dSTORM setup: calibration and correction of spatial distortions

#### V.1.1. Calibration factors

As we described in Chapter 3, the 4polar-dSTORM is a method that consists in obtaining each single-emitter orientation and wobbling by detecting their fluorescence anisotropic signal simultaneously projected onto 4 analyzer channels along the directions  $0^\circ$  (i.e. horizontal in the sample plane),  $45^\circ$ ,  $90^\circ$  and  $135^\circ$ . The corresponding measured intensities are named  $I_0$ ,  $I_{45}$ ,  $I_{90}$ , and  $I_{145}$ . Since these intensities are measured using a setup that requires beam splitting and use of polarizing beamsplitters, imperfections of the optical splitters will necessarily induce some imbalances and polarization leakages of the polarized intensities into unwanted channels. We therefore need to guarantee that each analyzer channel is properly calibrated. Another factor to take into account is the spatial distortion which occurs over the field of view of the image, i.e. the fact that each polarized image does not necessarily undergo the same distortions as the other ones.

We first describe below the calibration procedure that corrects for intensities imbalances and polarization leakages. Ideally, if we probe an isotropic sample such as fluorescent beads or a white paper, each analyzer channel must detects the same intensity as the other each channels: this situation permits to quantify intensity imbalances (e.g. occurring from 50/50 prism imperfections or diattenuation in Wollaston beamplitters). On the other hand, the use of a perfectly known polarized sample will allow quantifying the polarization leakages existing in polarizing beamplitters, occurring from their non-ideal nature.

To perform the intensity imbalance calibration, we first use a white lamp shining a white paper placed at the sample position, followed by the emission filter used for experiments (see Fig. 5.1). With the latter, we will estimate the factors that need to be used to weight the measured intensities  $I_0$ ,  $I_{45}$ ,  $I_{90}$ , and  $I_{145}$ , called G-factors [43, 59]. The G-factors are intensity constants that multiply the polarization factor ratios to guarantee equal detection efficiency.



Figure 5.1 – All 4 channels from white paper. On the left, an example of raw data, on the right an illustration of the ideal 4 polarized detection channels. We can get the mean intensity value of each channel (i.e., measuring  $I_0$ ,  $I_{45}$ ,  $I_{90}$ , and  $I_{145}$ ) to use in the G-factors. When working with tube lens TL=1.0x, we obtain a FoV diameter of  $40\mu\text{m}$ .

To first calibrate the intensity imbalance each polarized channel independently, we define the compensation factors  $G_0$  and  $G_{45}$  such as:

$$G_0 = \frac{I_0}{I_{90}}, \quad \text{on a white paper} \quad \text{Eq. 5.1}$$

$$G_{45} = \frac{I_{45}}{I_{135}}, \quad \text{on a white paper} \quad \text{Eq. 5.2}$$

If the Wollaston prisms would not introduce any diattenuation,  $G_0$  and  $G_{45}$  would be equal to 1. So whenever making measurements on anisotropic (ordered) sample, the polarization ratio equations ( $P_0$  and  $P_{45}$ ) (see Chapter 3) of the pair 0-90 and of the pair 45-135 should be:

$$P_0 = \frac{I_0 - G_0 \cdot I_{90}}{I_0 + G_0 \cdot I_{90}}, \quad \text{on an anisotropic sample} \quad \text{Eq. 5.3}$$

$$P_{45} = \frac{I_{45} - G_{45} \cdot I_{135}}{I_{45} + G_{45} \cdot I_{135}}, \quad \text{on an anisotropic sample} \quad \text{Eq. 5.4}$$

Besides, we also need to compensate the residual imbalance of the 50:50 non-polarizing beam splitter cube using the factor called  $G_{BS}$ :

$$G_{BS} = \frac{I_{45} + I_{135}}{I_0 + I_{90}}, \quad \text{on a white paper} \quad \text{Eq. 5.5}$$

That is applied whenever there is a ratio or comparison between the two non-polarizing beam splitter cube *pair* arms ( $P_0$  and  $P_{45}$ ). This factor comes into play in the equations 3.18 and 3.19 (see Chapter 3) that retrieve the mean single molecule's orientation and wobbling:

$$\rho = \frac{1}{2} \arctan\left(\frac{1}{G_{BS}} \frac{P_{45}}{P_0}\right), \quad \text{on an anisotropic sample} \quad \text{Eq. 5.6}$$

$$\frac{\sin^2(\delta)}{\delta^2} = (P_0)^2 + \left(\frac{P_{45}}{G_{BS}}\right)^2, \quad \text{on an anisotropic sample} \quad \text{Eq. 5.7}$$

In addition to these three G-factors ( $G_0$ ,  $G_{45}$ , and  $G_{BS}$ ), we noticed that the 45°/135° split channels exhibit some leakage of polarization from one channel to the other. This requires two other G-factors (named  $G_1$  and  $G_2$ ) to include, which compensate for this effect (see Figure 5.2 for an illustration).

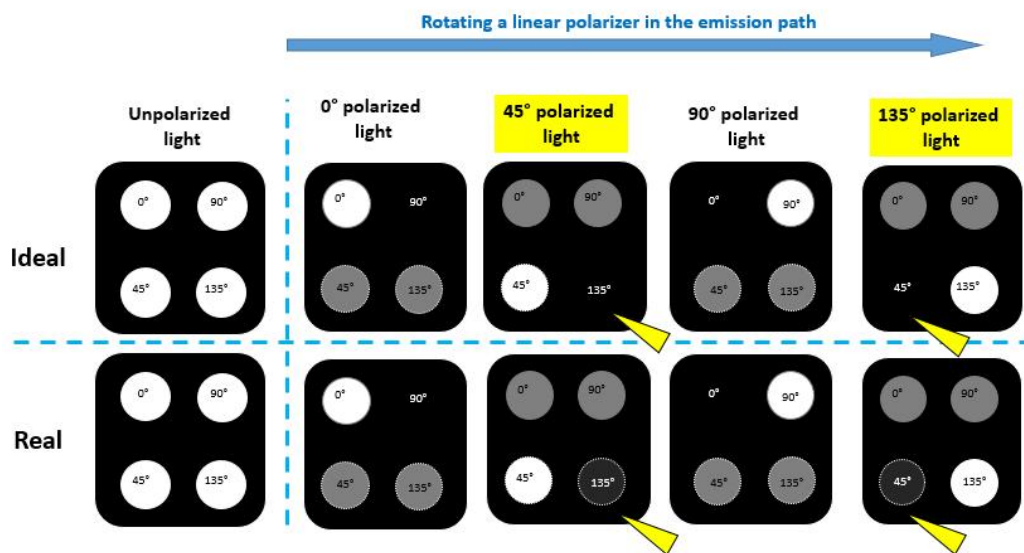


Figure 5.2 – Illustration of the leakage of 45° and 135° channels using an isotropic sample (e.g., white paper). Here the circles represent the FoVs projections of 4 polar channels on the same camera chip. When channels are white, the FoVs are very bright; channels in grey are intermediate bright; channels in dark grey with white border represent channels with dim light (“leakage”); and channels fully black are fully dark. The 4 polarized channels together represent a single state of the light polarization. On the top, we have the idealistic situation, and on the bottom we illustrate what we get experimentally (real). On the left, the detection of unpolarized light (the 4 channels have the same very bright intensity). On the right side, we illustrate the case when we add in the emission path a linear polarizer before splitting the emission beam in 4. Note that when we want to experimentally detect a pure 45° and 135° linear

polarized light, a leakage of light is still projected on the orthogonal channel (but it should be zero in the ideal situation, see the yellow arrowheads). To compensate such behavior, we must use two extra G-factors (**G1** and **G2**): one when 45° is leaked into 135°, and the second when the 135° is leaked into the 45°.

The correction factors need to be introduced in the measured  $I_{45}$  and  $I_{135}$  values. We denote  $I_{45,corrected}$  and  $I_{135,corrected}$  the corrected values of the intensities, which we need to express as a function of the detected ones ( $I_{45}$  and  $I_{135}$ ). Denoting G1 the amount of light leaked from the 45° to the 135° channel, and the G2 is the amount of light leaked from 135° to 45° channel, one gets:

$$I_{45} = (1 - G_1) \cdot I_{45,corrected} + G_2 \cdot I_{135,corrected} \quad \text{Eq. 5.8}$$

$$I_{135} = (1 - G_2) \cdot I_{135,corrected} + G_1 \cdot I_{45,corrected} \quad \text{Eq. 5.9}$$

Where G1 and G2 can be directly obtained when detecting respectively 45° and a 135° linear polarized light. We will start disregarding the influence of  $G_{45}$  for simplicity, and later we will put it back into the equations. This said, when working with 45° linear polarized light, we obtain G1:

$$I_{45,corrected} = I_{45} + I_{135}^{leak} \quad , \quad \text{using } 45^\circ \text{ linear polarized light} \quad \text{Eq. 5.10}$$

$$G_1 = \frac{I_{135}^{leak}}{I_{45,corrected}} \xrightarrow{45^\circ \text{ pol}} G_1 = \frac{I_{135}^{leak}}{I_{45} + I_{135}^{leak}} \quad , \quad \text{using } 45^\circ \text{ linear polarized light} \quad \text{Eq. 5.11}$$

And, when working with 135° linear polarized light, we obtain G2:

$$I_{135,corrected} = I_{135} + I_{45}^{leak} \quad , \quad \text{with } 135^\circ \text{ linear polarized light} \quad \text{Eq. 5.12}$$

$$G_2 = \frac{I_{45}^{leak}}{I_{135,corrected}} \xrightarrow{135^\circ \text{ pol}} G_2 = \frac{I_{45}^{leak}}{I_{135} + I_{45}^{leak}} \quad , \quad \text{with } 135^\circ \text{ linear polarized light} \quad \text{Eq. 5.13}$$

Finally the corrected intensities ( $I_{45,corrected}$  and  $I_{135,corrected}$ ) can be rewritten from the equations 5.8 and 5.9 as following:

$$I_{45,corrected} = \frac{(1 - G_2) \cdot I_{45} - G_2 \cdot I_{135}}{(1 - G_1 - G_2)} \quad \text{Eq. 5.15}$$

$$I_{135,corrected} = \frac{(1 - G_1) \cdot I_{135} - G_1 \cdot I_{45}}{(1 - G_1 - G_2)} \quad \text{Eq. 5.16}$$

Adding such equations in the pure form of  $P_{45}$  (still without  $G_{45}$ ):

$$P_{45}^c = \frac{I_{45,corrected} - I_{135,corrected}}{I_{45,corrected} + I_{135,corrected}} \quad \text{Eq. 5.17}$$

We obtain:

$$P_{45}^c = \frac{(1 + G_1 - G_2) \cdot I_{45} - (1 - G_1 + G_2) \cdot I_{135}}{(1 - G_1 - G_2) \cdot (I_{45} + I_{135})} \quad \text{Eq. 5.18}$$

Since we know (when using unpolarized light) that there is a small constant imbalance between the channels  $45^\circ$  and  $135^\circ$ , we can add *ad-hoc* the G-factor  $G_{45}$  to compensate  $I_{135}$  from  $I_{45}$  like we did in equation 5.4:

$$P_{45}^{corrected} = \frac{(1 + G_1 - G_2) \cdot I_{45} - (1 - G_1 + G_2) \cdot G_{45} \cdot I_{135}}{(1 - G_1 - G_2) \cdot (I_{45} + G_{45} \cdot I_{135})}, \quad \text{Eq. 5.19}$$

The two fully corrected equations of the pairs P0 and P45 that we will effectively use from measured intensities are the equations 5.3 and 5.19. With them, we will retrieve the single-molecule polarization parameters ( $\rho, \delta$ ) via the equations 5.6 and 5.7. Thus, by using a white paper as an isotropic sample, and by adding when needed a polarizer in the emission path, we can calculate all the five G-factors of our setup ( $G_{BS}$ ,  $G_0$ ,  $G_{45}$ ,  $G_1$ , and  $G_2$ ). Typical values are written on the table 5.1 below.

G-factor	Value	Equation	Illumination
<b>G0</b>	0.92727	Equation 5.1	Unpolarized
<b>G45</b>	1.12191	Equation 5.2	Unpolarized
<b>GBS</b>	1.273738	Equation 5.5	Unpolarized
<b>G1</b>	0.130038	Equation 5.11	polarized $45^\circ$
<b>G2</b>	0.153068	Equation 5.13	polarized $135^\circ$

Table 5.1 – G-factors of our setup, equations used, and illumination used.

### V.1.2. Spatial distortions can be corrected with Fluorescent beads

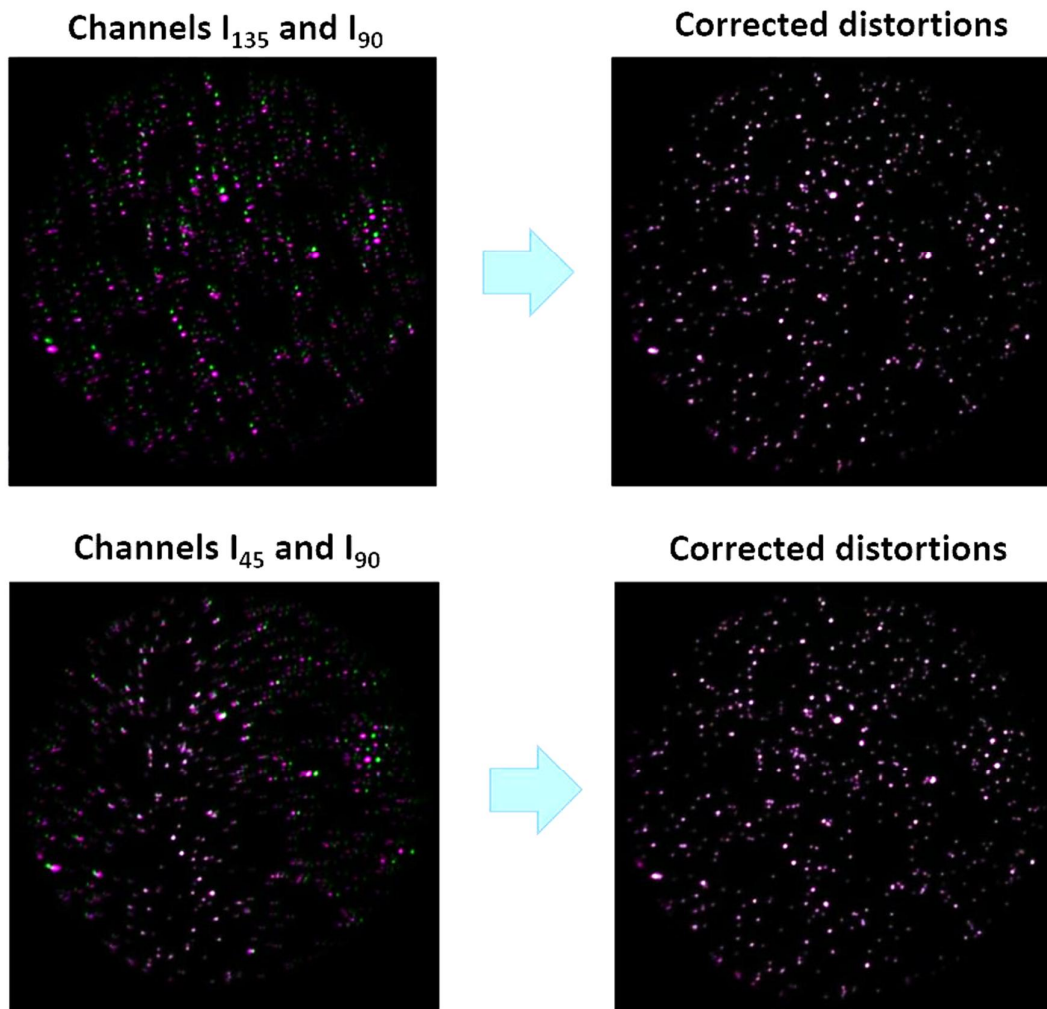
In addition to intensity misbalances, the image split by the Wollaston prisms introduces visible distortions of the field of view, which are known to increase with the angle of deviation of the prisms. Since the detected image on each of the 4 channels should be a perfect replica, their position and shape in relation with the center of the whole FoV should be the same, and any deviation from that must be corrected for. By considering one arbitrary channel as the reference one (named 'fixed'), we relate the spatial transformation matrix (named '*tform*') that

transforms the channel to be compensated (named 'moving') into the reference channel ('fixed'). In this sense, we would have one fixed (static) channel, and need to correct the 3 remaining ones (with 3 different transformation matrices). This estimation is done through a calibration step that uses 100nm fluorescent beads (emission ~520nm) distributed as point emitters over the FoV. The code to determine the transformation and its correction was developed by a former PhD student, César A. Valadés-Cruz (Mosaic team, Institut Fresnel).

In order to obtain the transformation matrix ('tform') for each channel to be corrected, we use the Matlab command '*imregform*'. The geometrical transformations to be used are defined as '*affine*'. The latter takes into account the following geometrical transformations: translation, rotation, scale, and shear:

*tform = imregform (moving, fixed, 'affine', optimizer, metric)*

By applying the specific *tform* onto its respective channel, we in principle would retrieve back the image of the fixed reference (i.e., we correct the distortion). In order to apply such geometric transformations on each channel, we used the command '*imwarp*'. We show an example of 3 corrected channels in Figure 5.3. Note that it is visible that the transform matrix is not homogeneous over the whole FoV, with generally larger distortions at the border of the FoV.



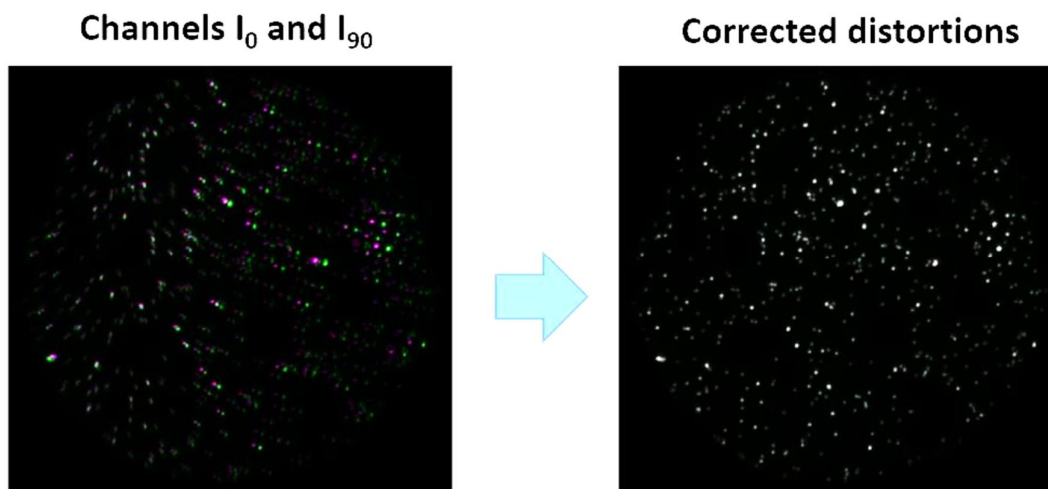


Figure 5.3 – On the left, images of two channels (green and pink) of the same bead sample (100nm) before correcting the spatial distortions. In green, is the channel to be corrected (‘moving’), and in pink the reference channel (‘fixed’). On the right, the overlap of both channels (in white-ish) after we correct the distortions using ‘*imwarp*’ command of its respective transformation matrix ‘*tform*’. In principle, all channels become equal to the reference channel (here the  $I_{90}$  channel). The parameters of ‘*imregconfig*’ are the following: [*optimizer, metric*] = *imregconfig* (‘*multimodal*’); *Optimizer.InitialRadius*=0.001; *Optimizer.Epsilon*=1.5e-6; *Optimizer.GrowthFactor*=1.001; *Optimizer.MaximumIterations* = 500;

Such bead correction can be understood as a pre-processing step, once it is applied to all the frames before the main steps of the polar-dSTORM algorithm. To perform the spatial correction in all frames, we first convert raw data “.tiff” files in “.mat” files, then we apply the matrix transformations in all frames of the 4polar-dSTORM stack.

## V.2. 4polar-dSTORM processing and analysis software: principle

The data processing software of 4polar-dSTORM are Matlab codes developed by the former PhD student César Augusto Valadés-Cruz (Mosaic team, Institut Fresnel). César adapted for nanoscale fluorescence anisotropy another script on single-particle detection and analysis algorithm (named multiple-target tracing, MTT), firstly implemented by Nicolas Bertaux (Phyty team, Institut Fresnel) [59, 100, 110]. The MTT algorithm has the capacity of detecting single-molecules’ positions in a noisy image, and accurately estimate their intensity, i.e. the integrated signal over their PSF, from the molecule’s PSF size and amplitude. From MTT, César has used such intensity estimation of single-molecules (among other important quantitative parameters) to perform single-molecule fluorescence anisotropy analysis in the previous polar-dSTORM setup which used two polarized projections along  $0^\circ$  and  $90^\circ$ . The 4polar-dSTORM data analysis software developed here is an extended version of the previously developed polar-dSTORM code [59, 60], introducing extra features since two other channels ( $45^\circ$ ,  $135^\circ$ ) need to be coupled. In the following sections, we will describe the main principle as well as the processing steps of the parameters retrieval of the polar-dSTORM setup (which detects the  $0^\circ$  and  $90^\circ$  polarized directions) prior to explaining the 4polar-dSTORM code (which detects the  $0^\circ$ ,  $45^\circ$ ,  $90^\circ$ , and  $135^\circ$  polarized directions).

## V.2.1 Principle of the polar-dSTORM data processing software

### V.2.1.1 Polar-dSTORM data processing overview

The key idea behind the code is based on the fact that each analyzer channel is spatially displaced from its orthogonal channel by a translation vector. Therefore, when blinking events occur on the sample image, the fluorescence of such events are split (by the Wollaston prism(s)) by the same displacement vector. This unique vector, defined once the spatial distortions of the image have been corrected for, relates the projections of all blinking events on each channel's field of view, as illustrated in Figure 5.4. In what follows, we call // and  $\perp$  the images produced by the  $0^\circ$  and  $90^\circ$  channels (this notation can be applied to the  $45^\circ$  and  $135^\circ$  channels later in the 4polar-dSTORM setup). By estimating the vector that relates the // and  $\perp$  images of single molecules, one can accurately relate the projected intensities of all blinking spot pairs of the whole dSTORM data stack, and therefore retrieve the necessary single molecule's orientation parameters based on equation 3.17 in Chapter 3.

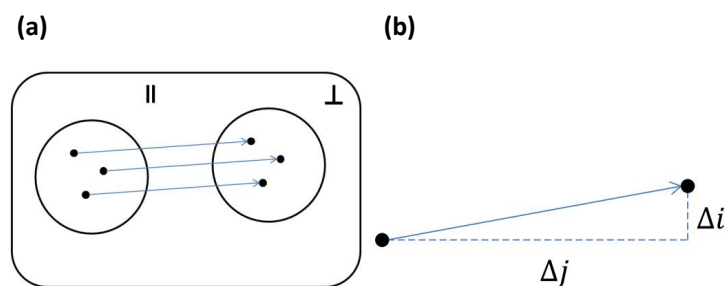


Figure 5.4 – Scheme showing the representative vector of a single channel pair  $I_0$  (parallel) and  $I_{90}$  (perpendicular). (a) Illustration of a single frame simultaneously detecting 3 blinking events on both channels (para and perp) on the same EMCCD chip. The large circles represent both parallel and perpendicular FoV channels, and the points inside of the channels represent each blinking event projection (in general with different intensities). (b) The blue arrow (with exaggerated tilt) is the representative vector  $(\Delta i, \Delta j)$  that is the same for all blinking particles on such frame (and also in the whole image stack). Figure adapted from [110].

After correcting the spatial distortions of all frames of a sample (using a bead calibration sample, see Section V.1.2) the polar-dSTORM code is divided in four parts (see Figure 5.5): (1) single molecules' detection and localization, (2) pairing of single molecules from the  $0^\circ$  and  $90^\circ$  polarization channels, (3) calculation of the polarization factor  $P_0$  per molecule (see eq. 3.17), (4) "anisotropy analysis" i.e., for each detected single molecule, retrieval of the orientation parameters  $\rho$  and  $\delta$  from  $P_0$  (see Chapter 3).



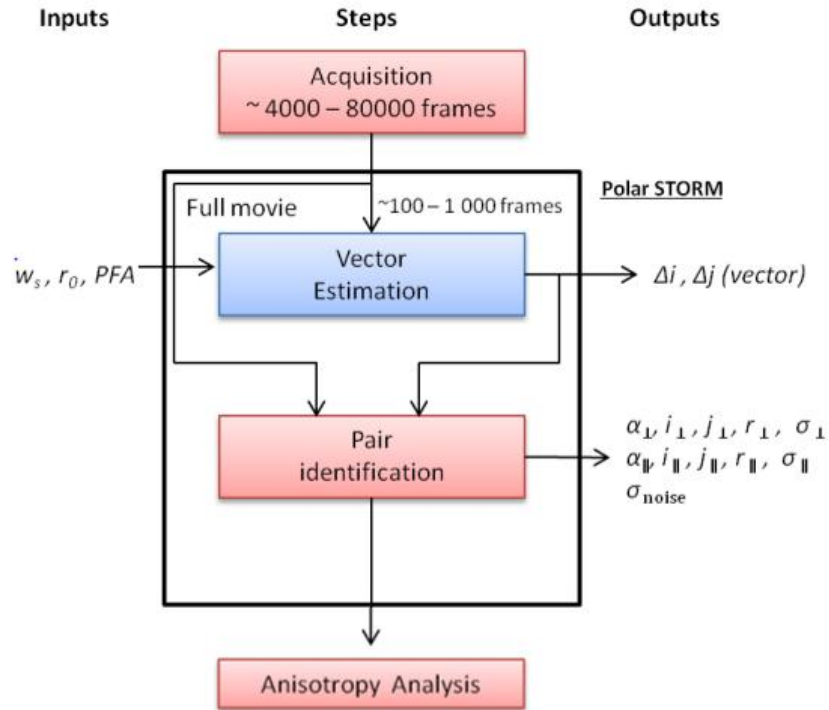


Figure 5.5 – Simplified polar-dSTORM flowchart with inputs and outputs. (1) single molecule detection inputs: spatial sliding window width used for particle detection ( $w_s$ ), initial radius ( $r_0$ ), probability of false alarm (PFA) for detection quality test. (2) vector parameters ( $\Delta i, \Delta j$ ). (3) Outputs: amplitude of the PSF ( $\alpha$ ), localization coordinates ( $i, j$ ), final radius estimation (fitted  $r$ ), localization precision ( $\sigma$ ), standard deviation of the noise ( $\sigma_{noise}$ ). (4) the anisotropy analysis retrieves the orientation parameters from the calculation of the polarization factor per molecule. The details of the inputs and outputs is described in the text. Figure taken from [110].

### Single molecule detection: spatial 2D localization

In order to measure the main displacement vector between the projections of the blinking events, first the polar-dSTORM program needs to detect the candidate molecules present on each frame. This detection is based on the multiple-target tracing (MTT) algorithm [100]. With MTT, each blinking event is modelled as Gaussian peak, with background and noise included. A pre-set sliding window with width size ( $w_s$ ) and initial Gaussian radius ( $r_0$ ) are used to scan the FoV searching for Point Spread Function (PSF) events. It has been shown that their Gaussian model can be successfully used to model Airy function of the PSFs in noisy data [100]. The acceptable noise here is controlled by a parameter called Probability of False Alarm (PFA), which establishes a threshold limit to test the presence or not of a Gaussian particle in a noisy background, see Figure 5.6.

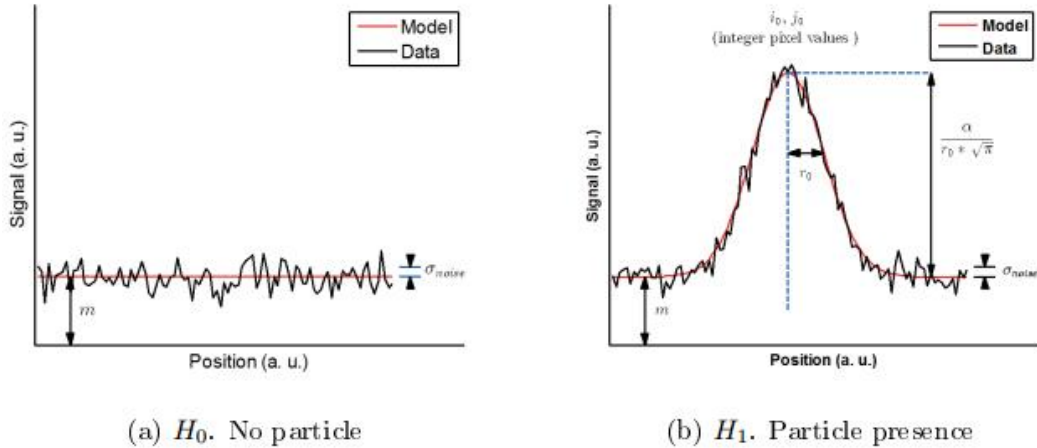


Figure 5.6 – Example of the two hypothesis (a) and (b): the presence (case  $H_1$ ) or not (case  $H_0$ ) of a Gaussian particle inside the sliding window (typical size 13x13 pixels), with initial fitting parameter Gaussian radius  $r_0$  (typical  $r_0=1.3$  pixels in our experiments). A particle on the position  $(i_0, j_0)$ , amplitude  $\alpha$ , and radius  $r_0=1.3$  pixels, might be detected or not depending on the  $H_1/H_0$  ratio, and on a threshold limit dictated by the probability of false alarm (PFA) of an event. Figure taken from [110].

A generalized likelihood ratio test (GLRT) is performed on each sliding window and frame to confirm or not the presence of Gaussian PSFs on the whole image stack. For each centered position of the sliding window  $(i, j)$ , single molecules might be detected or not depending on the estimated hypothesis  $H_1/H_0$  ratio, and the probability of false alarm (PFA), which is a threshold limit. The  $H_1/H_0$  ratio is a number that suggests the presence or not of a particle. The hypothesis  $H_1$  means that the window contains a PSF peak centered in  $(i_0, j_0)$ , with a fixed constant radius  $r_0$  and amplitude  $\alpha$ . On the other hand,  $H_0$  is the null hypothesis, i.e., the sliding window detects only Gaussian noise with a standard deviation ' $\sigma_{noise}$ ' and background offset ' $m$ '. Such GLRT decision test has the advantage of not depending purely on the signal counts (that fluctuates from experiment to experiment), but on the resemblance of a PSF peak on a noisy data. The accuracy of this detection is set by the PFA threshold [100]. For example, to obtain a probability of false alarm (PFA) of less than 1 pixel per image of 512x512 pixels, it is necessary to set this threshold to  $PFA \leq 10^{-6}$  [110]. Besides, when validating the MTT algorithm, A. Sergé et al showed that with such a PFA value, the detection of particles was very close to 100% as soon as the molecules' signal to noise (SNR) ratio is higher than  $\sim 20$  dB (see Figure 5.7) (SNR is equal to  $\alpha^2 / \sigma_{noise}$ ). Typical STORM SNR values lie in the range of 20-35dB [110].

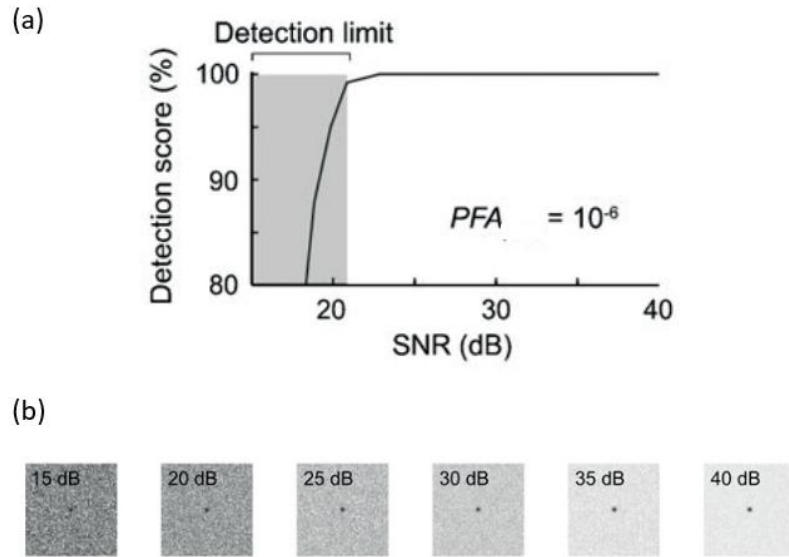


Figure 5.7 – (a) Detection efficiency of GLRT in percentage, and (b) representative SNR levels in dB in 100x100 pixel images. Note that, for SNR better than ~20 dB ( $PFA \leq 10^{-6}$ ), the MTT algorithm is capable of detecting all the particles (for sure more than 95%) in a Monte Carlo simulated data. We used PFA related to 24dB in our analysis. Figure taken from [110].

The performance of the GLRT approach to find candidates to be further fitted by Gauss-Newton multi-parametric regression was already evaluated in the literature by Monte Carlo simulation, and it has been shown to be optimal (i.e. able to reach the highest possible precision, see Figure 5.8) [100]. In this thesis work, we used a SNR threshold limit of 24dB, therefore we expect to reach a localization precision of around 0.1 pixel (corresponding to 13nm in our data) (see Figure 5.8).

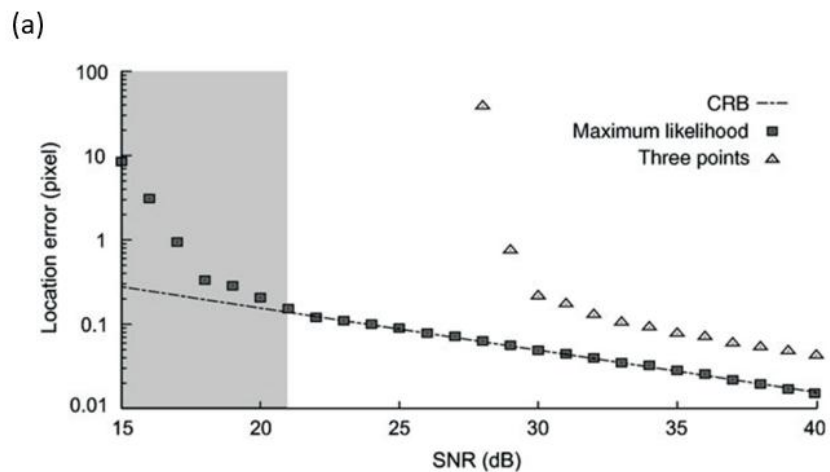


Figure 5.8 – Gauss-Newton regression fit performance on the localization error (in pixels), with different noise levels. (a) We see that the localization precision of the Maximum likelihood approach reaches the theoretical minimum error for noise levels above 20dB (Cramer-Rao lower bound limit, CRB, expressed as pointed-dashed line). In triangles are the results of another approach in the literature (not used here). Figure taken from [110].

### V.2.1.2 Vector estimation and pair identification

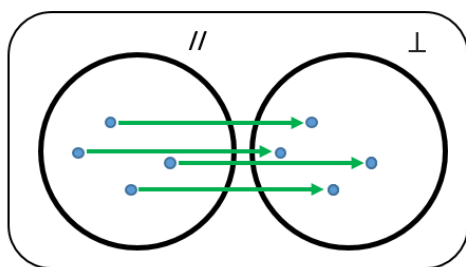
- **Vector estimation, Part I: detection of single molecules for a stack sub-set of images**

A subset of 100-1000 frames from the whole data is used to estimate the vector (see Figure 5.5). Once we detect the position  $(i,j)$  at the pixel level of each blinking event on this subset, we refine their position accuracy to sub-pixel level by a Gauss-Newton multi-parametric regression fit (see previous section). Here the former GRLT parameters such as radius  $(r_0)$  and window center position  $(i_0, j_0)$  are used as initial parameters on the multi-parametric fit. The main output parameters obtained on each detected peak on both  $//$  and  $\perp$  images are (see Figures 5.5 and 5.6): Gaussian amplitudes  $(\alpha_{//}$  and  $\alpha_{\perp})$ , radii  $(r_{//}$  and  $r_{\perp})$ , sub-pixel localization  $(i_{//}, j_{//}$ , and  $i_{\perp}, j_{\perp})$ , with each localization precision  $(\sigma_{//}$  and  $\sigma_{\perp})$ , and noise  $(\sigma_{\text{noise}})$ . The localization precision is defined as the standard deviation of the fitted sub-pixel position, assuming symmetric PSFs. At this point, only the fitted localization will be used to estimate the representative displacement vector.

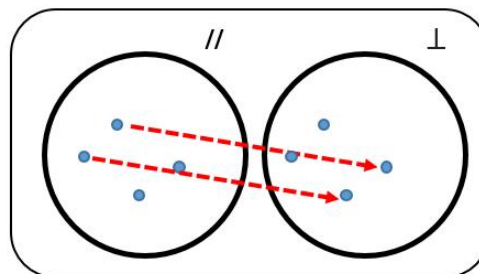
- **Vector estimation, Part II: finding the best vector**

Once having detected all the positions of the blinking events, we need to estimate the main vector that will be used to pair the  $//$  and  $\perp$  PSFs. For this, we statistically obtain the norms of the possible vectors that connects events from the left ( $//$ ) and right ( $\perp$ ) channels. We obtain the candidate norms by accumulating the 2D position differences  $(\Delta i, \Delta j)$  between the detected molecules on the 2 channels. The distribution of the obtained vectors norms has a standard deviation called  $\sigma_{\text{norm}}$ . Statistically, vectors that connect two effectively split molecules' PSFs are more present than 'incorrect vectors' that connect wrong pairs of molecules (see Figure 5.9). The more frames we use to estimate the vector, the more correct vectors we accumulate, and the more precise we get to define the main vector norm and orientation. The main vector can be statistically chosen by the median norm value accumulated over 100-1000 of data frames. Besides, the standard deviation  $(\sigma_{\text{norm}})$  of the distribution of the accumulated norms will be further used in the next step to identify pairs of the particles.

a) Correct vector



b) Incorrect vector



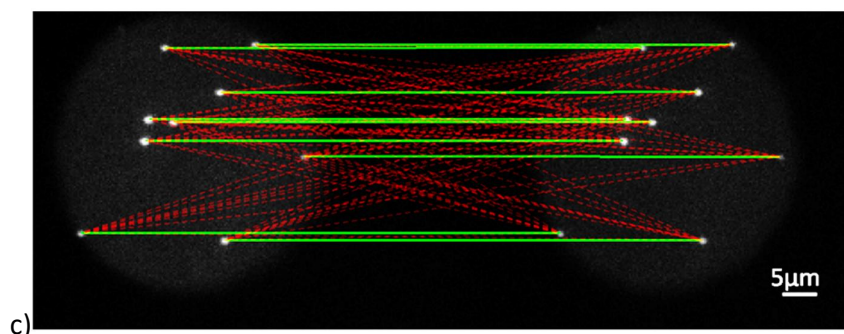


Figure 5.9 – Possible vector norms and orientations. (a) Correct vector, (b) Wrong vector. (c) A single frame of polar-dSTORM vector estimation. Red dashed lines are wrong coupled particles, and green lines are the correct vector that represents the beam displacement due to the Wollaston prism. Figure adapted from [59].

Once having estimated the main vector  $(\Delta i, \Delta j)$  (see above), we consider as correct paired PSFs the PSFs which distance deviates from the main vector value by less than  $4.2 \cdot \sigma_{norm}$  (Figure 5.10). Such searching range should guarantee with 95% confidence that we associate proper pairs of molecules [59]. With such criterion at hand, we can then search and couple all candidates of blinking pairs in the whole polar-dSTORM image stack (tens of thousands of frames).

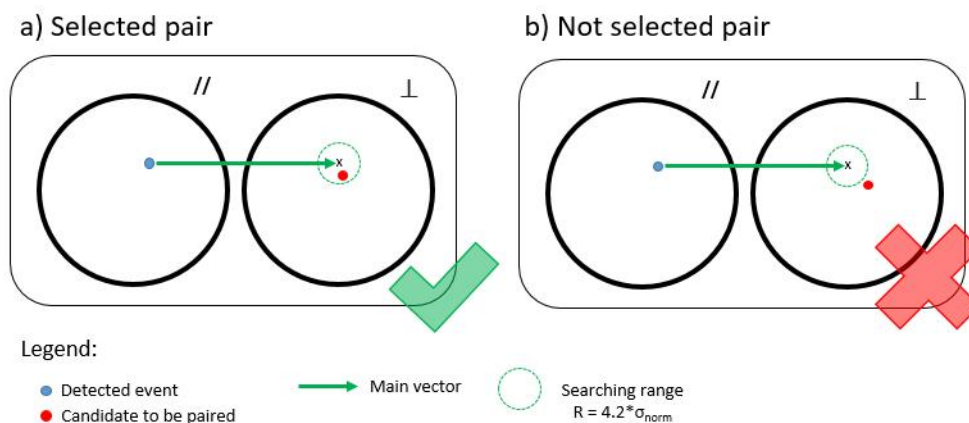


Figure 5.10 – Identifying pairs of blinking events with the main estimated vector. The dashed circumference encloses the searching region of the nearest neighbor candidate, which radius is exaggerated in the image for illustrative purposes. Thanks to the main vector, we can exclude incorrect couplings between both channels. Figure adapted from [110].

### V.2.1.3 Single molecules' pairs parameters retrieval

With the knowledge of the main vector, we can finally perform the multi-parametric Gauss-Newton regression fit on the whole data stack (not only on a sub-set), to extract all the quantitative information we need (see Figure 5.11).

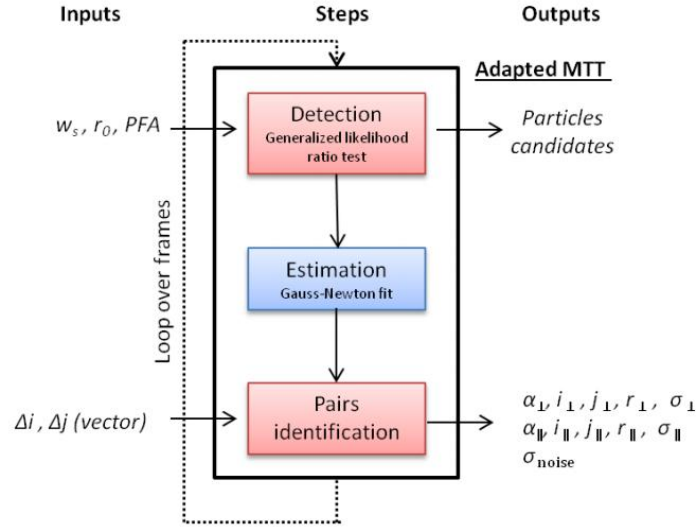


Figure 5.11 – Flowchart of the process of “Pairs identification” and parameter retrieval for all blinking events with the main estimated vector as an input. Process is performed on all frames of the dataset. Figure taken from [110].

The outcome of these parameters determination is 2D localization ( $i_{//}$ ,  $j_{//}$ , and  $i_{\perp}$ ,  $j_{\perp}$ ), localization precisions ( $\sigma_{//}$  and  $\sigma_{\perp}$ ), radius ( $r_{//}$  and  $r_{\perp}$ ) and amplitudes ( $\alpha_{//}$  and  $\alpha_{\perp}$ ) of all Gaussian fitted PSFs in the whole polar-dSTORM images stack. From these parameters, the intensities of each single molecule can be determined by the operations:  $I_{//} = \alpha_{//} * r_{//}$  and  $I_{\perp} = \alpha_{\perp} * r_{\perp}$ . These intensities will be then used to estimate the polarization factors from each single molecules. We recall the Equation 3.12, without the correction factors from Chapter 3:

$$P_0 = \frac{I_{//} - I_{\perp}}{I_{//} + I_{\perp}} = \cos(2\rho) \frac{\sin(\delta)}{\delta} \quad \text{Eq. 5.20}$$

The orientation properties ( $\rho, \delta$ ) of each single molecules is then deduced from the polarization factors as detailed in Chapter 3 (see also Eq.5.6 and Eq.5.7).

## V.2.2 The 4polar-dSTORM data processing principle

In order to obtain single molecules' complete orientation parameters from 4 analyzer channels, we need to couple (identify pairs) of the first Wollaston prism arm (that yields  $I_0$  and  $I_{90}$  images), of the second Wollaston prism arm (that yields  $I_{45}$  and  $I_{135}$  images). This permits to obtain first two different polarization factors images similarly as above :  $P_0$  on the one side, and  $P_{45}$  on the other side (here expressed without correction factors) (see Chapter 3):

$$P_0 = \frac{I_0 - I_{90}}{I_0 + I_{90}} = \cos(2\rho) \frac{\sin(\delta)}{\delta} \quad \text{Eq. 5.20}$$

$$P_{45} = \frac{I_{45} - I_{135}}{I_{45} + I_{135}} = \sin(2\rho) \frac{\sin(\delta)}{\delta} \quad \text{Eq. 5.21}$$

The two different polarization factors are then connected together for the final orientation parameters retrieval. This is done by coupling of the  $P_0$  and  $P_{45}$  images (see Figure 5.12). The way each pair is identified and coupled follows the same strategy of polar-dSTORM described above: GLRT followed by Gauss-Newton multi-parametric fit, and then use of main vectors to connect single molecule's pairs (see Figure 5.11 and Figure 5.12).

We show below a general outlook of the 4polar-dSTORM data treatment (Figure 5.12).

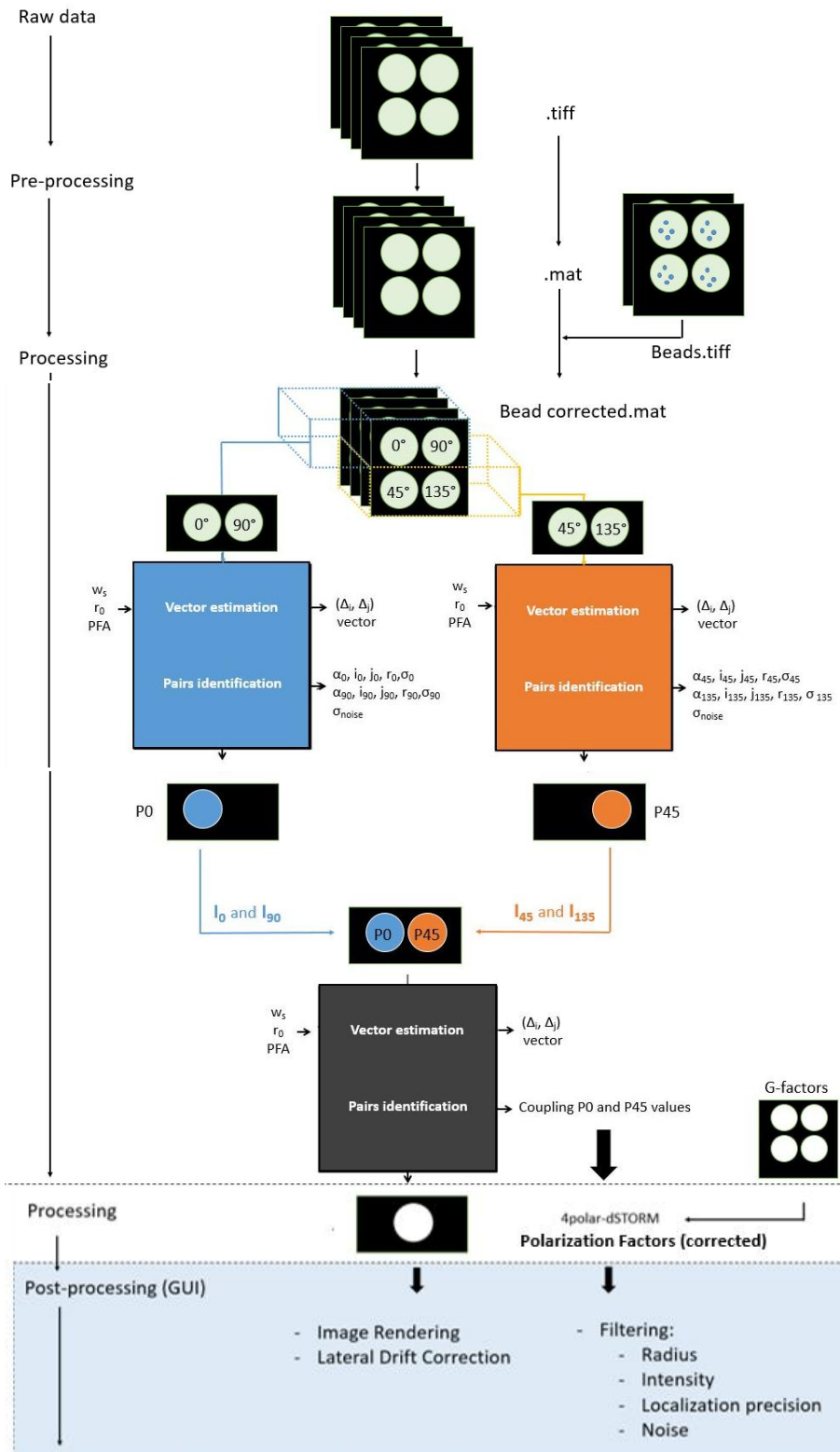


Figure 5.12 – The 4polar-dSTORM complete flowchart. In the pre-processing step, the raw data (.tiff image stack files) is transformed into “.mat” files to be further spatially corrected by the bead calibration in matlab. The bead-corrected.mat files are processed by polar-dSTORM matlab software (i.e., MTT adapted) for each Wollaston polarized arm (in blue, the pair 0-90, and in orange, the pair 45-135). On each arm, the polar-dSTORM routine is applied: GLRT is done to find the best vector, which is further used to identify (couple) blinking pair events. A multi-parametric



Gaussian-Newton fit is done to retrieve quantitative parameters of the blinking particles, such as position ( $i,j$ ), localization precision ( $\sigma_{ij}$ ), the amplitude ( $\alpha$ ), radius ( $r$ ), and noise ( $\sigma_{\text{noise}}$ ). Since we know the position of all detected particles on each arm (0-90) and (45-135), we can put both on the same image frame displaced by another representative vector whose norm between the centers guarantee total separation of the coupled pair P0 and P45 channels. A final vector estimation and pair identification (coupling) is done to connect the information retrieved from P0 and P45. The last step of the data treatment is to calculate the orientation parameters for each blinking particle in the reconstructed image. For that, we need the G-factors (i.e., the intensity calibration). The most common post-processing steps are (1) lateral drift correction (based on cross-correlation with the localization themselves), (2) choice of image rendering, (3) blinking event filtering for robust orientation parameters interpretation, and (4) choice of the stick representation.

### V.2.2.1 Orientation parameters retrieval and expected precision

Finally, each molecules' polarization factors P0 and P45 is used to estimate, non ambiguously, its 2D orientation parameters ( $\rho, \delta$ ) from the parameters retrieval operations (see Chapter 3). We recall that putting together Eq.5.20-Eq.5.2, and using the corrected polarization factors (P0, P45) equations, we would obtain the following corrected orientation parameters ( $\rho, \delta$ ):

$$\mathbf{P}_0 = \frac{I_0 - G_0 \cdot I_{90}}{I_0 + G_0 \cdot I_{90}}, \quad \text{Eq. 5.22}$$

$$\mathbf{P}_{45} = \frac{(1 + G_1 - G_2) \cdot I_{45} - (1 - G_1 + G_2) \cdot G_{45} \cdot I_{135}}{(1 - G_1 - G_2) \cdot (I_{45} + G_{45} \cdot I_{135})} \quad \text{Eq. 5.23}$$

$$\rho = \frac{1}{2} \arctan \left( \frac{1}{G_{BS}} \frac{\mathbf{P}_{45}}{\mathbf{P}_0} \right) \quad \text{Eq. 5.24}$$

$$\frac{\sin^2(\delta)}{\delta^2} = (\mathbf{P}_0)^2 + \left( \frac{\mathbf{P}_{45}}{G_{BS}} \right)^2 \quad \text{Eq. 5.25}$$

While  $\rho$  is directly estimated,  $\delta$  is retrieved from an interpolation of the *sinc* function. The data are represented using a stick representation similarly as the ensemble data (see Chapter 4) but here using one stick per molecule. We use in particular different colormaps for the  $\rho$  and  $\delta$  parameters, which can be both important to visualize. The sticks images are overlaid with the pure non-polarized STORM image, obtained from the sum of the four (0°-45°-90°-135°) intensities and averaged localization of all four polarized images. Some examples of these representations are shown in the sections below.

Note that the other obtained parameters (localization precision, radius, intensity, background level) will be used as important information to estimate the quality of the estimation. In particular, it is known that the estimation precision of both  $\rho$  and  $\delta$  angles depend on the level of signal and signal to background ratios. To estimate the precision level reachable in our experiment, Monte Carlo calculations were performed by Valentina Curcio (PhD student in the team) starting from different ( $\rho, \delta$ ) situations and intensity levels. The noise was

introduced by using a distribution function resembling Poisson noise but accounting for the measured camera noise, by a preliminary estimation of its noise-to-intensity relation (see Figure 5.13a,b). The results show that for the typical level of intensity observed from a single molecule per STORM image (2000-5000 photons, corresponding in our setup to an intensity level of  $10^4$ - $10^5$  camera counts), the expected precision is about 4 deg for  $\rho$  and 8-10 deg for  $\delta$  ( Figure 5.13a,b). This precision will globally scale as the squared of the obtained intensity. It will be important, in the data analysis, to keep the information of molecules intensity levels : in particular setting a proper PFA value (see above) already a security that events with too low SNR levels are not detected.

It is also expected that the precision will slightly decrease in the presence of background, which is generally the case in cell samples. From the previous works on polar-dSTORM [59, 60], it is expected that the addition of background noise observed in our data will typically decrease the angles' precisions by a few degrees. Overall, the expected precision is very close to the angle precisions obtained from other approaches that measure single molecules' orientation: these approaches however rarely determine both mean orientation and wobbling at the same time. In works that measure orientations from fixed molecules, precisions have shown to reach a few degrees [111]. In works that estimate wobbling, precisions are about 5-10 deg [112, 113], however these approaches need a fit of the PSF shape and apply only to molecules close to the surface.

At last we verified that the method used here to estimate orientation parameters introduces very little loss of accuracy. Figure 5.13c,d shows the bias expected in the presence of noise, this bias is important only in very specific situations where we indeed expect bias : either on  $\delta$  in very low wobbling conditions, or on  $\rho$  in very high wobbling conditions. This simulation show noise-induced bias only: experimental bias introduced for instance by out-of-plane orientations will be addressed in the sections below.

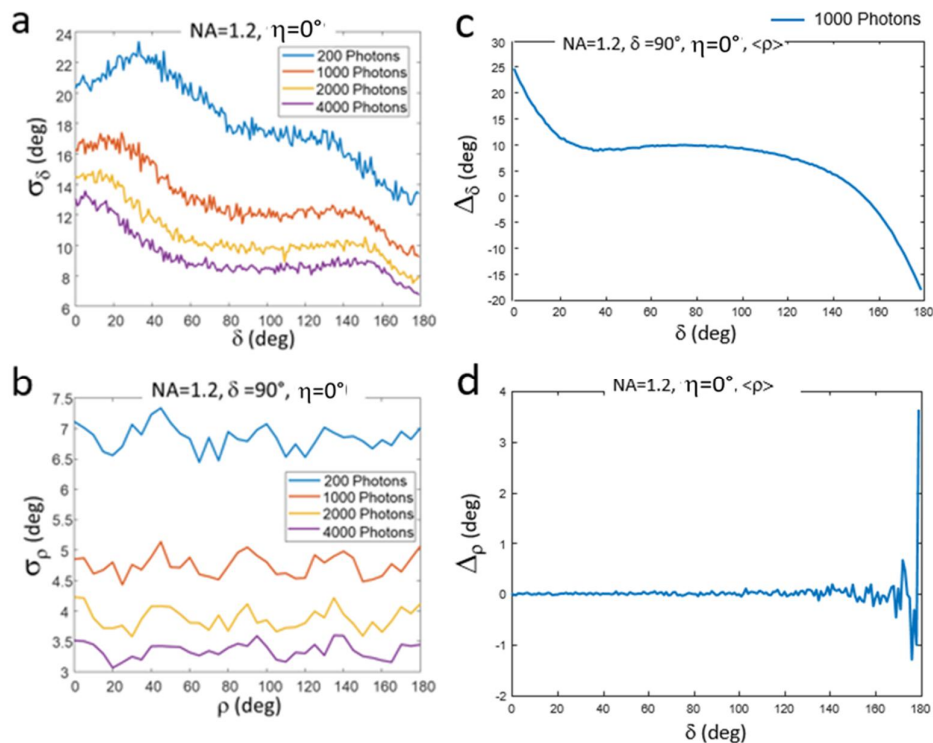


Figure 5.13 – Localization precision (a,b) simulations in the presence of noise. Wobbling (c) and orientation (d) accuracy simulations in the presence of noise, for a wobbling molecule lying in the sample plane. Figure taken from [109].

### V.3 4polar-dSTORM setup: validation

One way to estimate the orientation accuracy and precision of our setup is to use fluorescent nanobeads and a linear polarizer in the emission path before splitting the emission beam. When we use such combination, we could control (with the polarizer) and detect (with the 4-polarization detection) single-molecule-like linear polarizations. The nanobeads are 100nm beads containing fluorescent dyes (FluoSpheres Carboxylate-Modified Microspheres, Molecular Probes, F8803) sufficiently dispersed to behave like isolated, single-molecule like PSFs (slightly blurred due to their size). In such configuration, we expect to obtain a similar behavior of Figure 5.2, but with beads isolated emitters instead of a white paper. Thus, all the nanobeads present in a FoV would change in intensity according to their projection on the channels. The fluorescent beads would have different 4polar projection intensities, according to the chosen input linear polarizer angle. On Figure 5.14 we plot the expected polarization angle vs detected polarization for variable expected polarizations rotating in the sample plane every 15 degree step. The orientation accuracy (max deviation from the expected value) was  $8^{\circ}$ , but for most of the time it was better than  $5^{\circ}$ . The max standard deviation (precision) for each detected orientation (measured on 50-100 nanobeads) was lower than  $3^{\circ}$ , and in most of the times it was lower than  $2^{\circ}$ . These values are close to the expected precision modelled from Monte Carlo simulations (see above). At polarizer angles corresponding to the directions of the analyzer channels, we are unable to detect the pairs 0-90 or 45-135 because in one channel we do not detect any visible emitter. This situation is very specific to perfectly polarized emitters. In

practice, depending on fluorophore wobbling, SNR, and robustness of PFA detection, we are able to detect all angles in the FoV (see Section V.5).

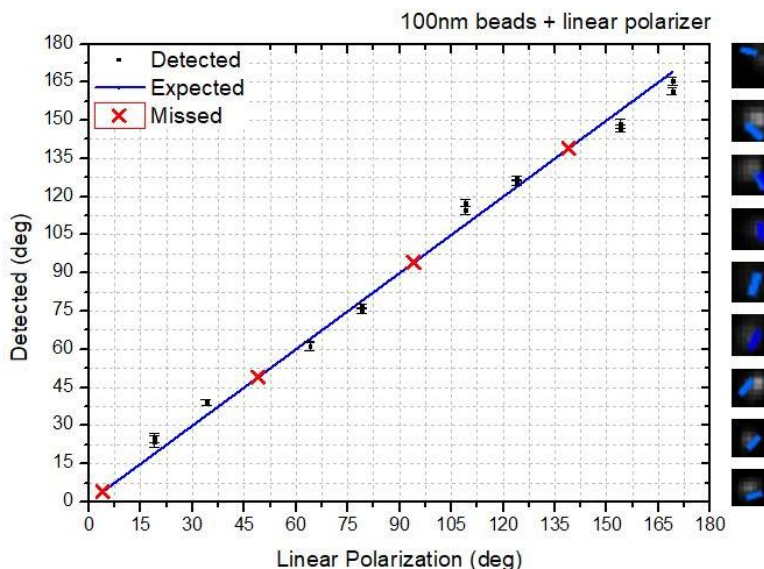


Figure 5.14 – Experimental evaluation of the orientation accuracy and precision of the 4polar-dSTORM setup. The orientation accuracy can be defined as spatial deviation of the square symbols from the blue line in the plot, and the orientation precision is the standard deviation of the square symbols. Here, fluorescent bead emission passes through a linear polarizer (before splitting the emission beam in 4) to simulate single-molecule orientation in a controlled manner. On the right side of the plot, some representative cases of single nanobead orientations: the narrow wobbling angle (represented by the blue color of the stick) is a consequence of the narrow angular filter of our linear polarizer (obtained delta values were in the range of  $(0^\circ < \delta_{\text{polarizer}} < 60^\circ)$ ).

## V.4 Effect of the illumination and detection aperture conditions

### V.4.1 The illumination condition (normal incidence versus total internal reflection) affects the detection efficiency

The way we illuminate the sample is expected to modify the way molecules are photo-excited, since the excitation polarization state in the sample depends on the incidence angle. Previous work has used normal incidence conditions using circular polarization, in order to introduce the least preferential photoexcitation in the sample plane [59, 60]. In such conditions, it is also expected that the polarization component along the axial z direction is negligible, which permits to decrease possible bias due to off-plane tilt angles, in the orientation parameters retrieval. We first used the 4polar-dSTORM in epi (normal incidence) excitation, and after treating the data we promptly observed a sparse reconstruction of the actin filaments of the cells, even for long acquisitions (40k frames). An example of low number of localizations is displayed in Figure 5.15a, where we measured around 80k coupled molecules in 40k frames. Thus, on average 2 molecules per frame were localized and paired, which is a low mean number of molecules per frame. Another example of the sparse detection in normal illumination conditions is shown in Figure 5.16c. In principle, such sparse reconstruction could be consequence of many factors, experiment-wise (e.g.: sample labeling, switching buffer, excitation type, tube lens, detection NA, etc.) and processing-wise (e.g.: data analysis input

parameters, such as window size, initial radius, and PFA). After many tests, we ascertained that our sample and buffer preparation were satisfactory, since the cells looked qualitatively nice and the blinking process induced by the buffer seemed satisfactory. We rather attribute the low number of detected molecules to the presence of a high background due to the normal incidence illumination, since other parts of the cell are excited along the propagation direction: this background is known to decrease the single molecule detection probability. As a comparison, we decreased this background by using Total Internal Reflection Fluorescence (TIRF) excitation, which confines the excitation to the evanescent wave at a  $\sim 100\text{-}200\text{ nm}$  depth close to the sample surface. A typical 4polar-dSTORM stack (30k frames) under TIRF excitation leads to more than one million of localizations in naïve unpatterned U2OS cells (Figure 5.15b).

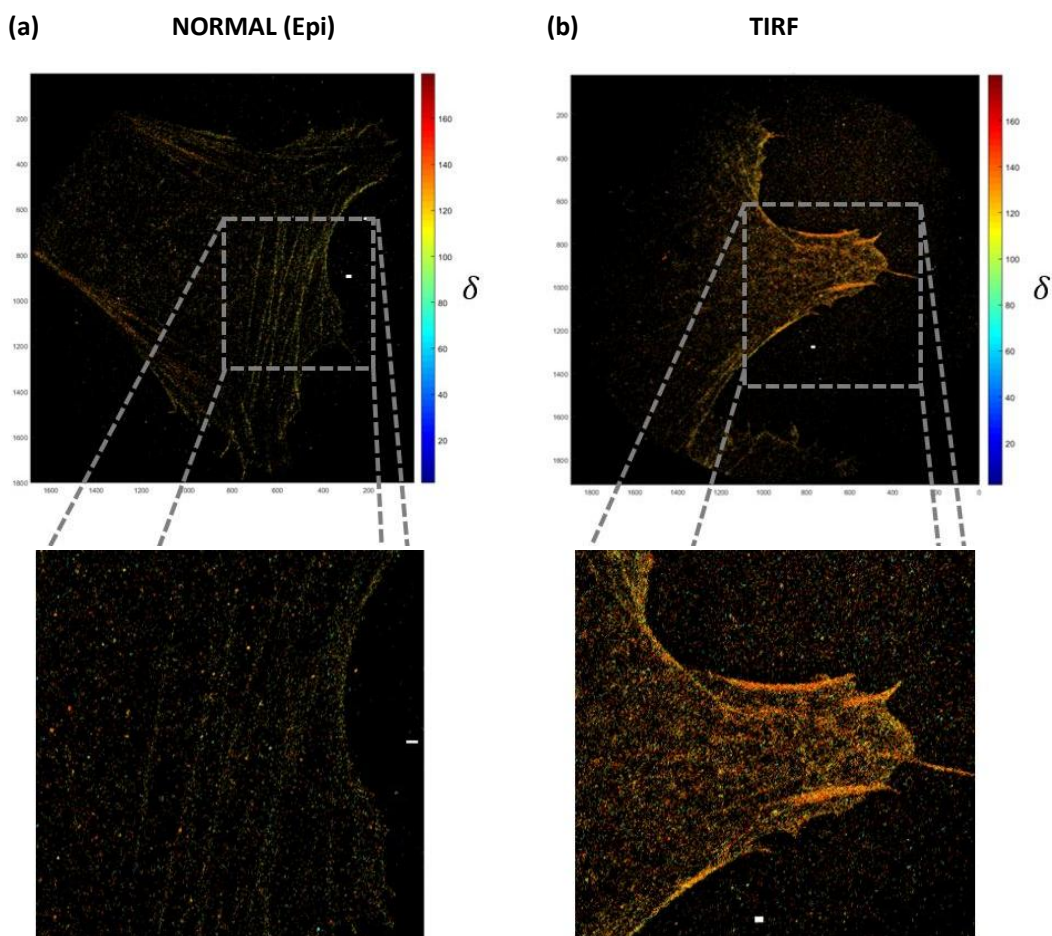


Figure 5.15 – Differences in number of localized particles can be visually seen for (a) normal vs (b) TIRF excitation cases. (a) 40k frames in normal incidence yielded around 80k number of coupled particles. (b) 20k frames of TIRF incidence yielded around 120k coupled particles. In general, TIRF excitation improves the number of detected particles of a factor between 2 to 5 times. Both excitation and detection NA were 1.45, white scale bar is 500nm, no post filtering. Note that the color code used here encodes each single molecule by its retrieved value  $\delta$ . The label employed was phalloidin-AlexaFluor488.

This is qualitatively observed in Figure 5.15 and Figure 5.16, where the use of TIRF excitation yields obviously a higher number of localized molecules in the same type of cells. The data on the left (normal incidence, Figure 5.15a, Figure 5.16c) had filaments very poorly defined



(low sampling), compared to the data on the right (where we clearly see the stress fiber bundles, Figure 5.15b, Figure 5.16d). To quantitatively evaluate the number of localized molecules, cells of similar shape or even the same cell were used. The regions of interest were always SFs at the ventral part of the cell (closest to the substrate). TIRF illumination led, on average, to between 1.5x and 2.0x times more coupled molecules than normal illumination.

Another important aspect when choosing TIRF excitation, is that labelled structures close to the substrate (a few hundreds of nm from it) will be more excited with the evanescent wave than structures far from the substrate. In Figure 5.16b we see a peripheral SF (on the left side) that is close to the substrate plane, and another peripheral SF (on the right) that is slightly bent off-plane along the Z direction (Figure 5.16b). In the normal excitation mode (Figure 5.16c), we see the low sampling behavior of the whole cell, and particularly, for out of plane regions of the bent peripheral (the central part), it probably gets a fewer localized particles due to high local background). On the other hand, when we choose the TIRF excitation mode (Figure 5.16d), the number of localized molecules is overall higher, but the central part of the peripheral bundle gets less localized particles than regions of the same bundle that are close to the substrate (e.g., close to the focal adhesions, see Figure 5.16a for comparison). It is therefore important to be aware that the TIRF illumination data can be affected by the 3D morphology of the cell.

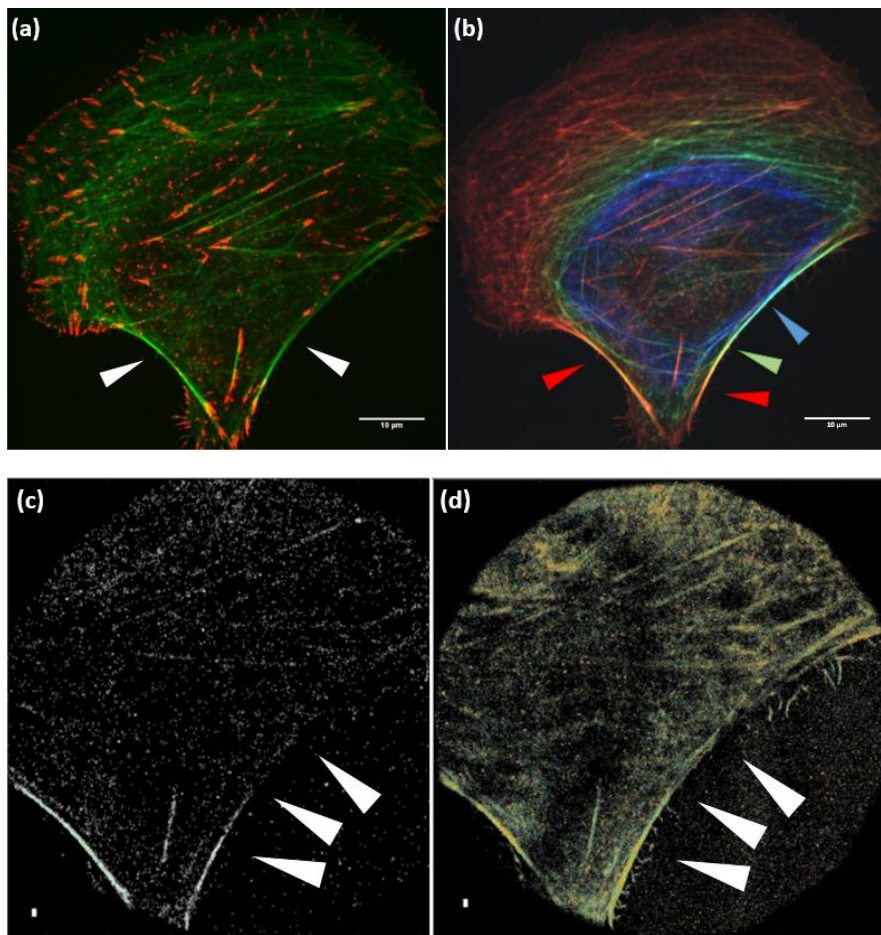


Figure 5.16 – The effect of TIRF excitation mode in 4polar-dSTORM experiments. (a) spinning disk image of U2OS cell stained for F-actin (phalloidin-AF488, in green) and p-FAK (in red, a focal adhesion marker). The focal plane is the one closest to the substrate ( $z_0=0\text{nm}$ ). This polarized cell has two clear peripheral SF bundle localized at the border of the

cell (white arrow heads). Note that the peripheral SFs are in between two focal adhesions. Scale bar = 10 $\mu$ m. (b) spinning disk z-stack composite of 3 z-planes spaced by 500nm each. In red,  $z_0=0$ nm; in green,  $z_1=500$ nm; in blue, the  $z_2=1000$ nm from the substrate. Note that the peripheral SF on the left is fully at the  $z_0=0$ nm (red), while the peripheral SF on the right is bent along Z (red, green and blue colors). (c) 4polar-dSTORM micrograph obtained with normal excitation mode. The label used was also phalloidin-AF488. (d) 4polar-dSTORM micrograph obtained with TIRF mode. Note that at the central part of the right side of the peripheral we detected less particles, but in TIRF mode (d) the number of localized particles is still better. 4polar-dSTORM FoV diameter = 40 $\mu$ m. On both (c) and (d) the detection NA was  $\text{detNA}=1.20$ . Note that the color code used here encodes each single molecule by its retrieved value  $\delta$ .

#### V.4.2 Other parameter potentially affecting the detection efficiency

In order to optimize the number of localized and coupled molecules, we decided to evaluate the effect of processing parameters on the detection efficiency in the first 5k frames. We found that the sliding window size was optimal for 13x13 pixels (in between 1.1x to 1.5x better detection efficiency than other options), the probability of false alarm  $\text{PFA}=24$  was a very good compromise (below 24 it was noisier, and above 24 the sampling was in between 1.1x to 1.5x sparser).

At last, experimental parameters can also play a role in the detection efficiency. The setup tube lens  $\text{TL}=1.0x$  yielded more localizations (in between 1.5x to 2.0x more) than  $\text{TL}=1.5x$ , which is due to the larger PSFs (hence lower signal per pixel) obtained under larger tube lens focal length. Besides, we set the experimental detection NA to be  $\text{detNA}=1.20$ , although the excitation NA was  $\text{excNA}=1.45$  (Nikon 100x objective, oil). The reduction of the detection NA was performed to filter out the possible out of the plane molecular orientations (which is explained below). Surprisingly, there was no striking difference in number of coupled molecules between  $\text{detNA}=1.20$  and  $\text{detNA}=1.45$ , which is probably due to the fact that  $\text{detNA}=1.20$  is a sufficient condition for high detection efficiency.

#### V.4.3 The illumination condition affects the retrieved wobbling parameter ( $\delta$ )

Although we obtain a higher number of localized and coupled particles in the TIRF mode, one should keep in mind that TIR excitation tilts the incidence of the excitation beam (Figure 2.19 and Figure 3.24). This means that, tilted fluorophore dipoles in the sample that were previously poorly excited in normal incidence excitation, can now be visible under TIR excitation. Because such fluorophores have a tilted angle with respect to the sample plane (high  $\eta$  value, see Figure 3.21, column A), we expect these spots to have lower intensity (reduced projected vector magnitude on the sample plane, which is parallel to the detection plane, see Figure 3.21, A2). However if they pass the detection limit, these molecules will also exhibit an apparent wider cone aperture angle projection (Figure 3.21, A3), which will tend to overestimate their wobbling angle value: this bias obtained in the retrieved biased values is quantified in Figure 5.17 for both normal and TIRF illumination conditions. Visibly, the TIRF excitation does not imply an increase of  $\delta$  bias for a given  $(\delta, \eta)$  situation (it actually even decreases this bias for in-plane wobbling molecules). However since higher- $\eta$  (tilted) molecules are now more accessible from the TIRF excitation, TIRF might induce, over a large population of molecules, a higher population of high- $\eta$  detected molecules, and therefore a higher global  $\delta$  bias.

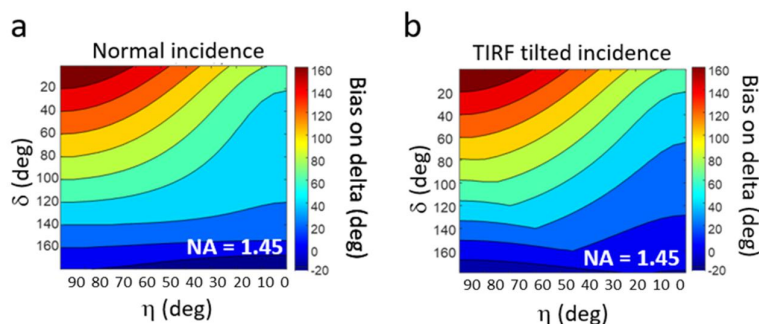


Figure 5.17 – Monte Carlo simulations of the bias induced on the measured wobbling  $\delta$ , vs illumination conditions, at NA 1.45. The bias is obtained from the difference between the retrieved wobbling cone aperture  $\delta$  and the true  $\delta$  value, for varying  $\delta$  from very small to isotropic and for  $\eta$  values varying from in-plane wobbling cones ( $\eta = 0^\circ$ ) to cones along the longitudinal direction  $z$  ( $\eta = 90^\circ$ ). Figure adapted from [109].

#### V.4.4 Minimizing the bias on fluorophore's wobbling ( $\delta$ ) under TIRF conditions

It is possible to minimize the detection of highly tilted molecules (which induce a higher bias on  $\delta$ ) experimentally in our setup. It is known indeed that the more the fluorophore dipole is oriented towards the  $z$  longitudinal direction, the more the radiated light out of this dipole will fill up the highly inclined emission angles, due to the donut-like radiation pattern of the radiating dipole. A way to decrease the effect of longitudinal dipoles projections is to select rather low inclinations of emission angles of the fluorescence light. This can be done technically by decreasing the detection NA in our 4polar detection unit (Figure 3.25). The expected decrease of the bias on delta is illustrated in Figure 5.18, which uses the same model as in Figure 5.17. Visibly, when comparing Figure 5.18 and Figure 5.17, there is a clear improvement of the bias obtained on  $\delta$  in both normal-incidence and TIRF illumination conditions, especially for off-plane tilt angles  $\eta$  below  $45^\circ$ . Above this value, cones are so much out-of-plane that the  $\delta$  values are still biased. We believe however that in such conditions, the intensity from these molecules is also strongly decreased which makes their detection more challenging.

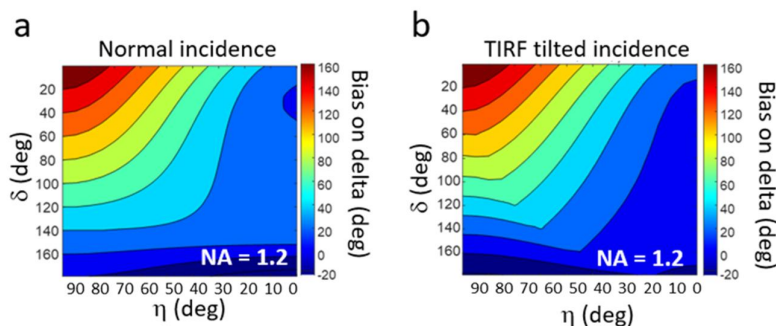


Figure 5.18 – Monte Carlo bias simulations of the bias induced on the measured wobbling  $\delta$ , vs illumination conditions, at NA 1.2 (similar calculations as in the Figure above), for varying  $\delta$  from very small to isotropic and for  $\eta$  values varying from in-plane wobbling cones ( $\eta = 0^\circ$ ) to cones along the longitudinal direction  $z$  ( $\eta = 90^\circ$ ). Figure adapted from [109].



Based on the simulations (Figure 5.18), we aimed at achieving a detection NA of  $\text{detNA}=1.20$ , which was also used in previous work to minimize out-of-plane induced biases [59]. In practice, the diameter of the collimated beam at the BFP image plane of the objective in the detection path is  $d=4.35\text{mm}$ , corresponding to an  $\text{detNA}=1.45$ . To decrease this NA to  $\text{detNA}=1.2$ , we had to reduce the diameter of a diaphragm placed in both arms in the 4polar detection unit, at the intermediate image plane of the backfocal plane of the objective. To get  $\text{detNA}=1.20$ , the diameter of both diaphragms were set to be  $d'=3.60\text{mm}$ , corresponding to the TL lens magnification of 1.0x used in all of our experiments.

We quantified experimentally the average of wobbling values obtained in F-actin stress fibers (SFs) in fixed cells labelled with phalloidin-AF488 conjugates. Average delta values were obtained by selecting several SFs in a whole U2OS cell under different illumination and detection NA conditions. When using the TIRF mode and  $\text{detNA}=1.45$ , the obtained average delta is around  $125^\circ$ , which corresponds to the expected most biased case. In the intermediate situation (TIRF mode and  $\text{detNA}=1.20$ ), the obtained average wobbling value was  $115^\circ$ . In the ideal “unbiased” situation (normal incidence, and  $\text{detNA}=1.20$ ), the average wobbling value was  $105^\circ$ . These results suggest that TIRF illumination and  $\text{detNA}=1.45$  induce a bias on  $\delta$  of at least about  $20^\circ$ . This is close to the expected value (Figure 5.18) if we consider that the highest reachable tilt angle in the F-actin phalloidin-AF488 staining is about  $20^\circ$ - $30^\circ$ : this aspect will be further discussed in the next section. Note that in the “ideal unbiased” situation, we obtained a  $\delta$  value that is close to the published wobbling angle found from our group in COS-7 cells, where an average lower bound limit wobbling of around  $90^\circ$  was found using the same SFs staining [59].

A better statistical analysis on the experimental bias obtained was performed using cells of similar shapes, in order to select well-defined SFs. After setting the detection NA to  $\text{detNA}=1.20$ , we performed 4polar-dSTORM experiments with TIRF excitation on micro patterned cells (e.g., CYTOO coverslips). We used CYTOO patterns of “H-medium” morphology and mainly aimed at peripheral and arc SF types (which were the most visible), to evaluate the wobbling values under normal and TIRF excitation, as well as under a slightly higher incidence angle than TIRF, called ‘xTIRF’ (Figure 5.19). After SF segmentation via Matlab into many small rectangular regions, we quantified the wobbling values of each region on the stress fibers. We see that, for normal incidence (Figure 5.19.a,c), the fluorophore wobbling aperture ( $\delta$ ) is relatively narrow for peripheral SF (values in between  $80^\circ$ - $90^\circ$ , in agreement with the value obtained by the previous polar-dSTORM setup), whereas for TIRF mode (Figure 5.19.b,c) the  $\delta$  values got more spread around  $\delta=110^\circ$ . Such behavior shows that there is still a shift of  $\delta$  to higher values (bias) in TIRF with  $\text{detNA}=1.20$ . However, because the  $\delta$  distribution has also a wider width in TIRF, this also means that a wider fluorophore population is actually being probed (i.e., in-plane and tilted fluorophores). Thus, for peripheral SFs when using TIRF, both in-plane and out-of-plane labels are being simultaneously probed and this should be taken into account when interpreting our data. In contrast to peripheral SFs, transverse arcs exhibited less differences between the normal incidence and TIRF conditions. We believe that because they are thinner, transverse arcs contain a less-prominent population of off-plane tilted filaments in their bundles. This aspect will also be discussed below when comparing different SF types.

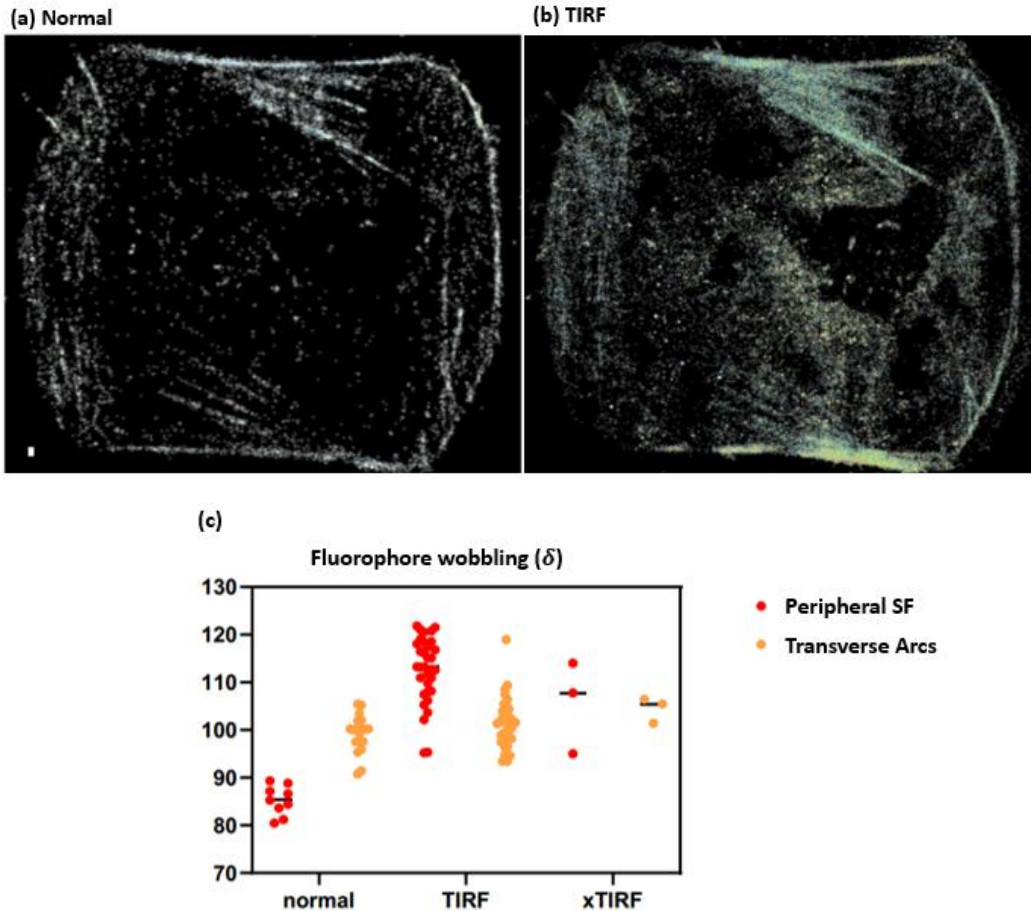


Figure 5.19 – Comparison of the wobbling ( $\delta$ ) values in normal and in TIRF excitation mode in stress fibers (detNA=1.20). (a) H-med cell probed with 4polar-dSTORM under normal excitation. (b) The same H-med cell, probed by 4polar-dSTORM TIRF mode. (c) Quantification of the wobbling ( $\delta$ ) values among normal, TIRF, and extreme TIRF (xTIRF) modes (explained in the text). Note that in peripheral SF (red points) there is a  $\delta$  shift (bias) mainly due to out-of-plane actin filament population present in the bundle, whereas for transverse arcs (orange points), probably contains only in-plane population of actin filaments due to no change in the  $\delta$  values distribution under normal and TIRF.

At last, we also checked our TIR excitation angle dependence with TIRF and extreme-TIRF (xTIRF). In TIRF mode, the excitation incidence angle for TIR is the closest one after the critical angle, whereas for xTIRF it is a more inclined one, thus far from the critical angle. The advantage to check xTIRF excitation is that it guarantees that we have a correct TIR angle for TIRF, and the disadvantage of using xTIRF in the routine is that its evanescent wave delivers less intensity to the sample compared to TIRF. Hence, xTIRF is in principle it is not ideal for us, since we already split the detection in four channels. Figure 5.16 shows that both TIRF and xTIRF showed the same overall trend for wobbling ( $\delta$ ), confirming that our excitation angle in TIRF (with TIR incidence angle closest to the critical angle, with more intense evanescent wave) was enough correct after the critical angle.

## V.5 Quantitative estimation of orientation and wobbling in SF regions in a fixed cell

### V.5.1 Retrieved detection and orientation quantities

We then proceeded to the quantification of F-actin filaments organization in fixed cells in different types of SFs, under conditions TIRF and  $\text{detNA}=1.2$ . For this, it is important to quantify, within each SF's ROI, the distribution of in-plane orientations ( $\rho$ ) that is representative of the way F-actin filaments are organized within SFs actin bundles. To make sure that this determination was unbiased by signal or physical sources, we investigated the statistical behaviors of the retrieved parameters over a large collection of SFs' data.

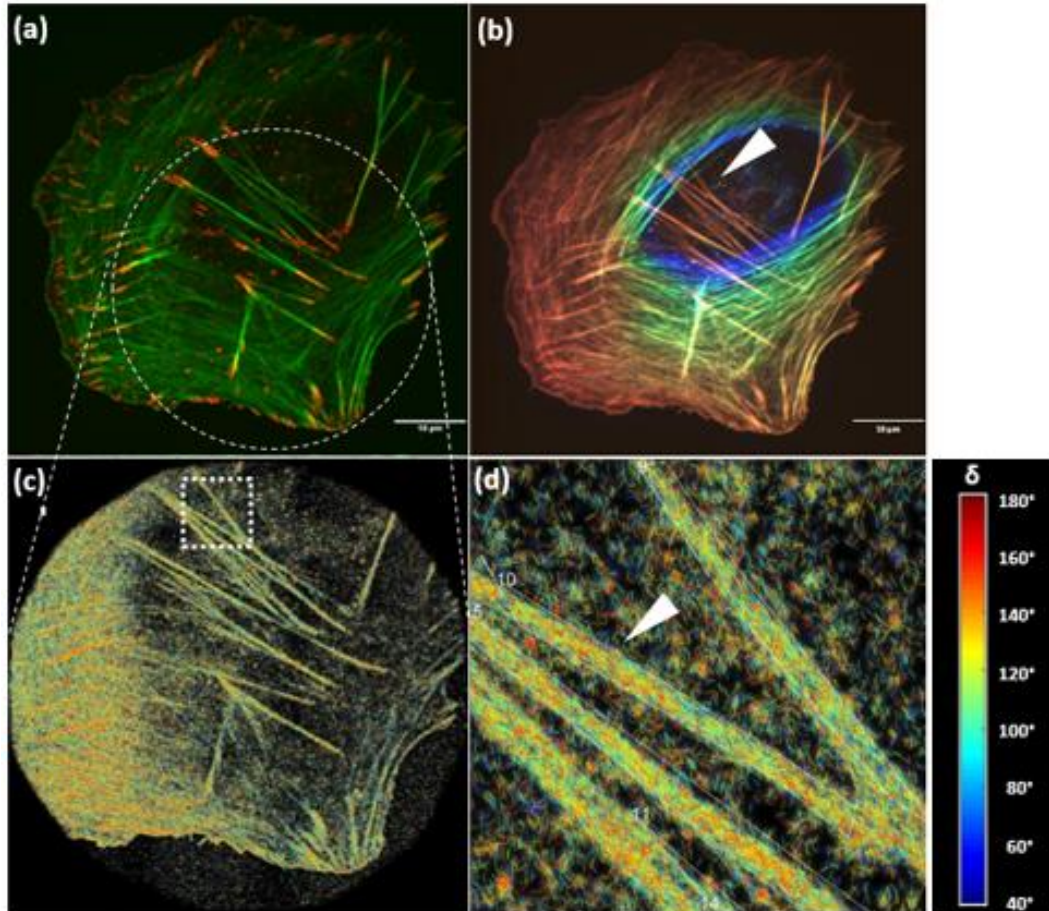


Figure 5.20 – Stress fibers used in the post-processing filtering procedure. (a) Spinning disk image of U2OS cell stained for F-actin (phalloidin-AF488, in green) and p-FAK (in red, a focal adhesion marker). The focal plane is the one closest to the substrate ( $z_0=0\text{nm}$ ). Scale bar =  $10\mu\text{m}$ . (b) Spinning disk z-stack composite of 3 z-planes spaced by  $500\text{nm}$  each. In red,  $z_0=0\text{nm}$ ; in green,  $z_1=500\text{nm}$ ; in blue, the  $z_2=1000\text{nm}$  from the substrate. The ventral SF used have a white arrow head pointing to red bundles (flat at  $z_0=0\text{nm}$ ). (c) 4polar-dSTORM micrograph obtained with TIRF excitation mode. The white dashed square (approximately  $8\mu\text{m}\times 8\mu\text{m}$ ) is the zoomed region in d. (d) zoomed 4polar-dSTORM, with the ventral SF #10 pointed with white arrow head. The detection NA was  $\text{detNA}=1.20$ . The colors of the sticks in (c,d) correspond to the different wobbling values (jet colormap normalized in between  $40^\circ$ - $180^\circ$ , blue are narrow aperture, red are wide ones).

A typical collection of data is shown in Figure 5.20: a cell is measured both at the spinning disk side of the microscope (Figure 5.20a,b) and the 4-polar STORM side (Figure 5.20c,d). This allows first to visualize the nature of the visible SFs by their attachment, or not, to focal adhesions (visualized in red in the co-staining image of Figure 5.20a), and to evaluate the possible tilted nature of the imaged SFs (visualized in the z-stack data of Figure 5.20b). 4-polar STORM data cover a smaller FoV due to the 4-polar split of the image, however the SFs are generally easily recognized on both ensemble and STORM images. Note that in all measurements reported here in STORM, the sample is stabilized in z by a home-made autofocus system (see Chapter 3) while it is not corrected for drifts in the X,Y directions. While there is a way to correct for potential drifts using correlations between successive piles of images [59. 110], we noticed that such correction had, in general, very little effect on the obtained images and we therefore ignored this addition of postprocessing steps in what follows.

After the 4-polar STORM analysis is performed (see Figure 5.20c), ROIs are identified on sub-regions of SFs that are sufficiently straight to estimate the width of the  $\rho$  distribution around their average value, which generally lies along the main direction of the visible SF (Figure 5.20d). In each identified ROI, a large collection of molecules (from a few hundreds to ten thousands) is obtained. The typical information retrieved from these populations are histograms of radius ( $r$ ), localization precision ( $\sigma$ ), total intensity ( $I$ , summed over all 4 polar channels), mean orientation per molecule ( $\rho$ ) and wobbling ( $\delta$ ). We recall that all these quantities are obtained after fitting the detected and coupled particles in the FoV (see Sections above). Both radius and localization precision are given in pixel units (where pixel size=1 is equivalent to 130nm), and the intensity is given in counts (e.g. camera counts).

Figure 5.21 depicts typical histograms obtained on these quantities, for an ROI such as displayed in Figure 5.20d, corresponding to the ventral SF region named ROI #10 (pointed by the white arrowhead). These histograms are very similar to those obtained for other SFs in similar cells. The localization precision  $\sigma$  ranges between 0.05 pixel to 0.3 pixel, which in nm scale corresponds to a range between 6,5nm to 39nm, with average value of 13nm. This obtained value puts the present 4-polar STORM method at a quite reasonable position when it comes to localization precision, as compared to other optical super-resolution microscopy techniques. The range of radii is in general in between 1.0 to 1.5 pixels (130nm to 195nm), with average value of 1.1 pixel (143nm): this is what is roughly expected from the used excitation NA in the sample (note that aberrations in the optical setup induce a PSF of slightly larger size than the theoretical diffraction limit). The range of total intensity is in between  $0.25 \times 10^5$  to approximately  $2.5 \times 10^5$  camera counts, with average value of  $0.7 \times 10^5$  counts. The range of values obtained for the wobbling aperture ( $\delta$ ) was large, with average value of  $106.7^\circ$ . Finally, the range of measured orientations ( $\rho$ ) was also quite large, with an average value  $\langle \rho \rangle$  of  $134.3^\circ$  lying along the SF direction, and a standard deviation of  $\Delta \rho = 27.3^\circ$ .

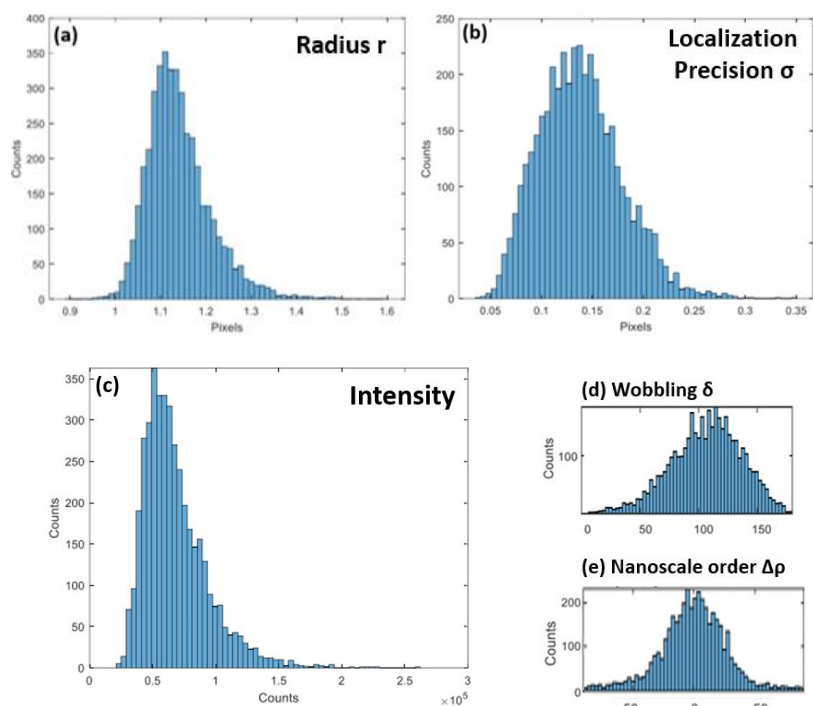


Figure 5.21 – Histograms obtained from a 4-polar STORM analysis on a typical SF ROI in a U2OS fixed cell stained with phalloidin-AF488 conjugates, displaying: fitted radius  $r$  (a), localization precision  $\sigma$  (b), intensity (c), wobbling  $\delta$  (d), orientations around the mean  $\rho - \langle \rho \rangle$ , which histogram width  $\Delta\rho$  represents the nanoscale order, or degree of alignment of the fluorophores (e). Pixel size is 130nm. Wobbling and orientation values are given in degrees.

An important observation in the region pointed in Figure 5.21d and its corresponding histograms, is the large expansion of the obtained  $\delta$  and  $\rho$  values. Since this ventral SF (#10 in Figure 5.20d) is seen to be lying in-plane, one can suppose that all F-actin filaments belonging to this bundle lie in-plane, which would lead to narrower histograms. Histogram widths expected for high SNR conditions are indeed around  $10^\circ$  (see noise simulations in Figure 5.13). Note that the width  $\Delta\rho$  of the histogram of  $\rho$  values is an important experimental readout, since it gives information about the nanoscale organization of F-actin single filaments within the SF bundle, or in other words, their degree of alignment. In these figures,  $\Delta\rho$  is a measure of the standard deviation of  $\rho$  around its mean, represented in an histogram plotting the difference between the single molecule's  $\rho$  values and their average  $\langle \rho \rangle$  within the ROI. Ultimately,  $\Delta\rho$  permits to compare different actin organization in different types of assemblies. It is therefore important that this quantity is measured with minimized sources of bias. To find out the reason for the obtained broad histograms, we investigated (1) possible correlations between the retrieved quantities (radius, intensity, sigma,  $\rho$ ,  $\delta$ ) and (2) if filtering detection parameters such as (radius, intensity, sigma) has an effect on the obtained distributions for ( $\rho$ ,  $\delta$ ).

### V.5.2 Correlations between retrieved quantities

The first striking observation is that the largest expansion of the observed  $\rho$  values is seen to be correlated with large  $\delta$  values (Figure 5.22). It therefore appears that the molecule's which  $\rho$  value is the most along the SF, are those for which the  $\delta$  measured value is the closest

to the range 80°-110°. Interestingly, the molecules exhibiting large expansion of  $\rho$  values are also those which radius  $r$  is the largest (Figure 5.23) and which total intensity is the smaller (Figure 5.24). The fact that this “largest  $r$  + lower intensity” population also corresponds to the largest obtained  $\delta$  values is confirmed in (Figure 5.25).

These observations tend to show that the molecules which are slightly off focus (corresponding to large  $r$  values) and/or of lower total intensity (e.g. potentially more tilted off plane) are also measured with the highest bias in  $\delta$ . Note that the low detNA chosen here does not completely suppress possible bias on  $\delta$  due to off-plane orientations (it only minimizes it), as discussed in the previous section. Under such scenario, a high  $\delta$  value can be attributed to an off-plane cone projected in the sample plane, which would correspond to F-actin single filaments in the SF bundle that undergo off-plane orientations with larger  $\eta$  values. Based on these considerations, the  $\delta$  values within the range [70-110°] are attributed to in-plane filaments, while values above would correspond to off-plane filaments. Considering an in-plane delta average value of 100°, a 130° measured value would correspond to a tilt  $\eta$  angle of 40° (see simulations in Figure 5.18).

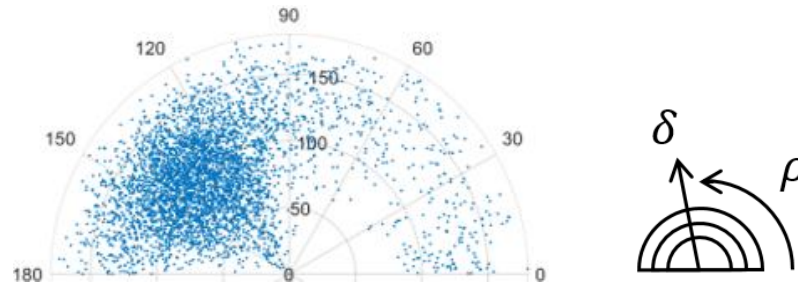


Figure 5.22 – Ventral SF (#10) polar plot of the probed orientations ( $\rho$ , angular coordinate) vs wobbling aperture ( $\delta$ , radial coordinate). Most of the orientations are closely distributed around the mean  $\langle\rho\rangle = 134.3^\circ$ . At wide wobbling values ( $\delta \rightarrow 180^\circ$  in the plot radius) the probed orientations get more scattered (i.e.,  $\Delta\rho \rightarrow 180^\circ$ ).

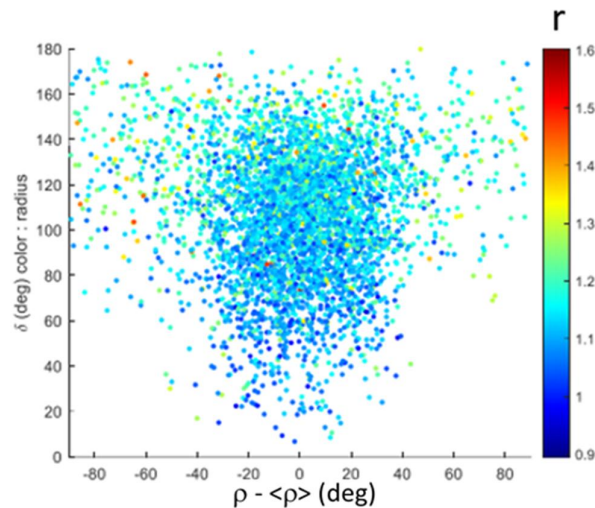


Figure 5.23 – Ventral SF (#10) plot of wobbling ( $\delta$ ) vs the nanoscale order (extent of  $\rho - \langle\rho\rangle$ ) vs fitted radius (represented as the color of the markers, the colorbar is given in pixel units). We see that for large radii and wobbling values, the plot tend to be more scattered in  $\rho$ .



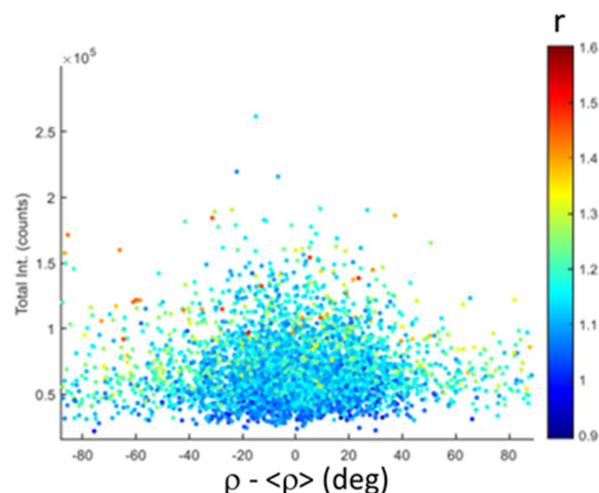


Figure 5.24 – Ventral SF (#10) plot of intensity (counts) vs the nanoscale order (extent of  $\rho - \langle \rho \rangle$ ) vs fitted radius (represented as the color of the markers, the color bar is given in pixel units). We see that for large radii and low intensity values, the plot tends to be more scattered in  $\rho$ .

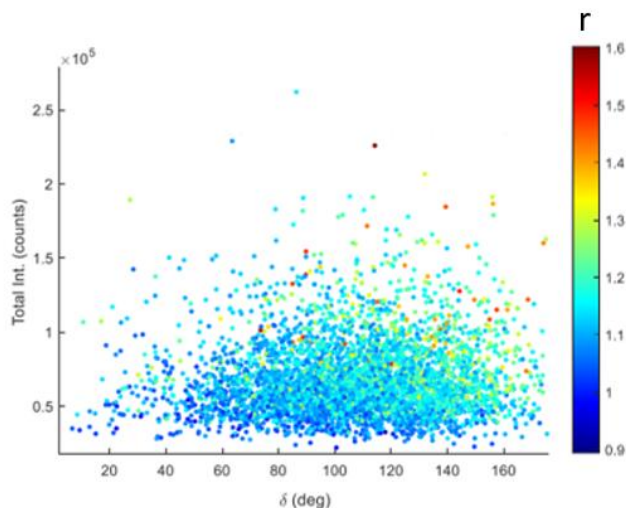


Figure 5.25 – Ventral SF (#10) plot of intensity (counts) vs the wobbling aperture ( $\delta$ ) vs fitted radius (color, in pixel units). We see that both low and high intensity values are correlated with large wobbling angles and large radius values, however larger  $\delta$  correlates with larger  $r$  values.

### V.5.3 Results after filtering detection parameters

When evaluating the intensity dependence plotted in Figure 5.24, it appears clearly that the low intensity values tend to spread largely the obtained  $\rho$  values. We therefore decided to establish a low intensity threshold of  $0.6 \times 10^5$  counts as a good compromise between avoiding bias and avoiding to lose too many molecules. However, when looking at the intensity vs wobbling vs radius plot of Figure 5.25, we realized that an upper bound limit of intensity would also be needed, since high intensity values were correlating slightly with large wobbling values, and therefore bias (we do not have a clear explanation for these high intensity events, which could possibly be attributed to the presence of several molecules measured at the same time). Similarly, we opted for a narrowing of radius and localization precision parameters, in order to

minimize the biasing effects of data falling off the range of averaged measured values. At last, a possible way to select only in-plane orientations for the un-biased evaluation of the in-plane organization of F-actin filaments is to select only  $\delta$  values close to the range [70-110°].

Based on these considerations and the plots given above, we decided to test the following lower and upper bound limits to filter all the regions of interest (ROI) (Table 5.2).

	<b>Lower bound</b>	<b>Upper bound</b>
<b>Radius (r)</b>	1.05 pixels (136.5nm)	1.15 pixels (149.5nm)
<b>Intensity</b>	0.6x10 <sup>5</sup> counts	1.0x10 <sup>5</sup> counts
<b>Wobbling (<math>\delta</math>)</b>	70°	110°
<b>Localization precision (<math>\sigma</math>)</b>	0.05 pixel (6.5nm)	0.13 pixels (16.9nm)

Table 5.2 – Lower and upper bound limits to filter the data.

The results of the filtering procedures on the ( $\rho, \delta$ ) histograms of Figure 5.21 is shown in Figure 5.26. Surprisingly, when performing only intensity filtering there was no clear differences in  $\Delta\rho$  (e.g. width of  $\rho$  histograms) and in  $\delta$  (Figure 5.26b). This shows that the measured intensity range is not a major source of increase of precision in the measured values. However, when performing radius filtering, a reduction in  $\Delta\rho$  and in the average of  $\delta$  was observed of a few degrees ( $\Delta\rho$  shifted by -3.3°;  $\langle\delta\rangle$  shifted by -4.7°) (Figure 5.26c). This shows that the factors enlarging our histograms are rather physical factors, such as the off-plane tilt angle that we mentioned above. On the other hand, filtering only by wobbling values (e.g. keeping  $\delta$  in the range [70°-110°]) yielded the largest reduction of the  $\Delta\rho$  histograms width (shifted by -4.1°) (Figure 5.26d). This important change observed upon filtering of  $\delta$  confirmed our initial hypothesis: the observed biases and enlargements of  $\rho$  histograms are largely attributed to off-plane orientations that would explore a more random range of directions. Indeed when keeping  $\delta$  in the range [70°-110°], we essentially select only wobbling molecules that lie in the sample plane. Finally, localization precision ( $\sigma$ ) could also be used as a parameter to be filtered, although radius (r) filtering showed to be equivalent or more effective than  $\sigma$  to reduce the histograms widths. Sigma filtering induced a shift of -3.6° for  $\Delta\rho$ , and of -2.4° for  $\langle\delta\rangle$  (Figure 5.26e).



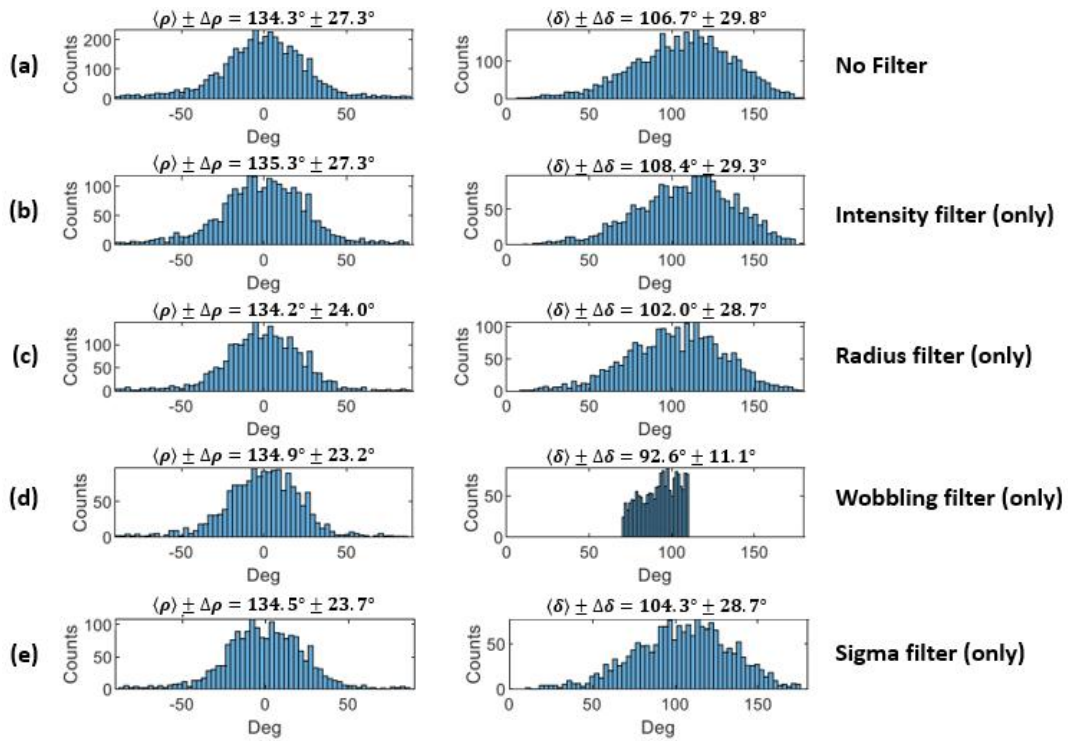


Figure 5.26 – Single SF (ventral region #10) bias removal due to post processing filtering. (a) The default condition, with no filtering. The nanoscale organization given by the extent  $\Delta\rho$ , and the wobbling angle ( $\delta$ ) are the key parameters to be evaluated when analyzing the removal of the bias on the data. (b) Intensity filtering histograms of  $\rho$  and  $\delta$ . (c) Radius filtering histograms of  $\rho$  and  $\delta$ . (d) wobbling filtering histograms of  $\rho$  and  $\delta$ . (e) Localization precision filtering histograms of  $\rho$  and  $\delta$ .

We evaluated at last the combination of intensity filtering with other parameters to filter together. The intensity with radius filter reduced slightly more the bias: shift in  $\langle \Delta\rho \rangle = -4.4^\circ$ ; shift in  $\langle \delta \rangle = -5.7^\circ$  (Figure 5.27c). On the other hand, when applying wobbling and intensity filter, it reduced the bias in  $\delta$  dramatically: shift in  $\langle \Delta\rho \rangle = -4.4^\circ$ ; shift in  $\langle \delta \rangle = -14.0^\circ$  (Figure 5.27d). Finally, when we applied sigma and intensity filtering together we got: shift in  $\langle \Delta\rho \rangle = -3.9^\circ$ ; shift in  $\langle \delta \rangle = -0.8^\circ$  (Figure 5.27e). Again, the localization precision ( $\sigma$ ) seems to be an alternative way to filter the data towards lower  $\Delta\rho$  and  $\langle \delta \rangle$ , but the radius and wobbling filtering are more effective in bias removal. With the condition of radius/wobbling and intensity filtering (Figure 5.27c-d), the final unbiased 2D nanoscale alignment ( $\Delta\rho$ ) got around 16% more ordered thanks to the removal of off-plane tilted population.

Finally, based on such approach, we expect that our observed ventral SF region exhibits an in-plane filaments' organization angular spread of  $\Delta\rho \sim 23^\circ$ , with a fluorophore mean wobbling value of about  $100^\circ$ . This molecular order value corresponds to a quite tight alignment of filaments around the mean direction of the SF, since the obtained value is close to what was obtained in single in vitro F-actin filaments [109]. However it is clear from our study that in addition to this in-plane population, additional off-plane filaments are present which explore a larger range of  $\rho$  values.

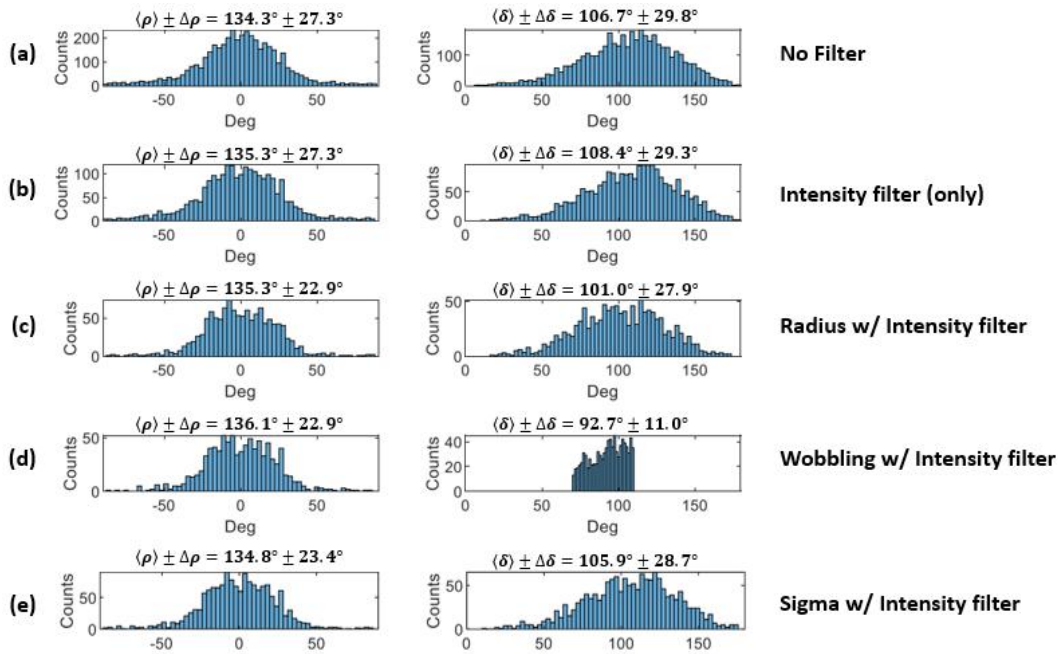


Figure 5.27 – Single SF (ventral region #10) bias removal due to post processing filtering. (a) The default condition, with no filtering. The nanoscale organization  $\Delta\rho$ , and the wobbling angle ( $\delta$ ) are the key parameters to be evaluated when analyzing the removal of the bias on the data. (b) Intensity filtering histograms of  $\rho$  and  $\delta$ . (c) Radius with intensity filtering histograms of  $\rho$  and  $\delta$ . (d) wobbling with intensity filtering histograms of  $\rho$  and  $\delta$ . (e) Localization precision with intensity filtering histograms of  $\rho$  and  $\delta$ .

These results provide an important conclusion for our 4-polar STORM analysis: we can now quantify the nanoscale organization information of F-actin filaments in various structures, and in particular compare different organizations without the drawbacks present in ensemble measurements (see Chapter 4). Note that a major finding of the present study is the confirmation of the significant wobbling angle of the AF488 label in the phalloidin conjugate linkage. Out of the molecular order value measured in ensemble spinning disk data (roughly  $130^\circ$ ), it is now confirmed that about  $100^\circ$  is purely due to the wobbling of the label. This wobbling is attributed to the non-negligible length connecting the dye part to the phalloidin molecule, which is expected to be itself tightly attached to actin.

#### V.5.4 Effect of post-processing filtering on the 4polar-dSTORM polarimetry images

Performing the post processing filtering implies removing detected and coupled molecules in the field of view (FoV). By applying it, the quality of the images (e.g., sampling) could be affected. In Figure 5.28 we show 4polar-dSTORM wobbling maps (where the colorcode is for wobbling,  $\delta$ ) before (a,c) and after (b,d) filtering with intensity, radius and sigma together. Here we demonstrate that significant amount of the molecules remain in the FoV for quantitative analysis. Moreover, the filtering procedure seemed to reject a lot of background molecules (for instance the dorsal SF in Figure 5.28b were more visible than without filtering in Figure 5.28a). Besides, it is possible to visually see the wobbling values shifted to narrower values (more blue-ish colors) after filtering (Figures 5.28b,d). Interestingly, however, for very

thick bundles, like in peripheral SF of micro-patterned H-med cells (Figures 5.28c,d) it is more difficult to remove molecules that correspond to large wobbling values (red-ish/yellow-ish) from the dataset. This means that off-planes tilt angles reached by single filaments in such structures are probably larger than in thin SFs. To evaluate the actin filament organization of very thick bundles, it will be strictly necessary to perform a wobbling filter (e.g. limit delta to the [70-110°] range) to guarantee un-biased quantification of the in-plane organization of F-actin filaments.

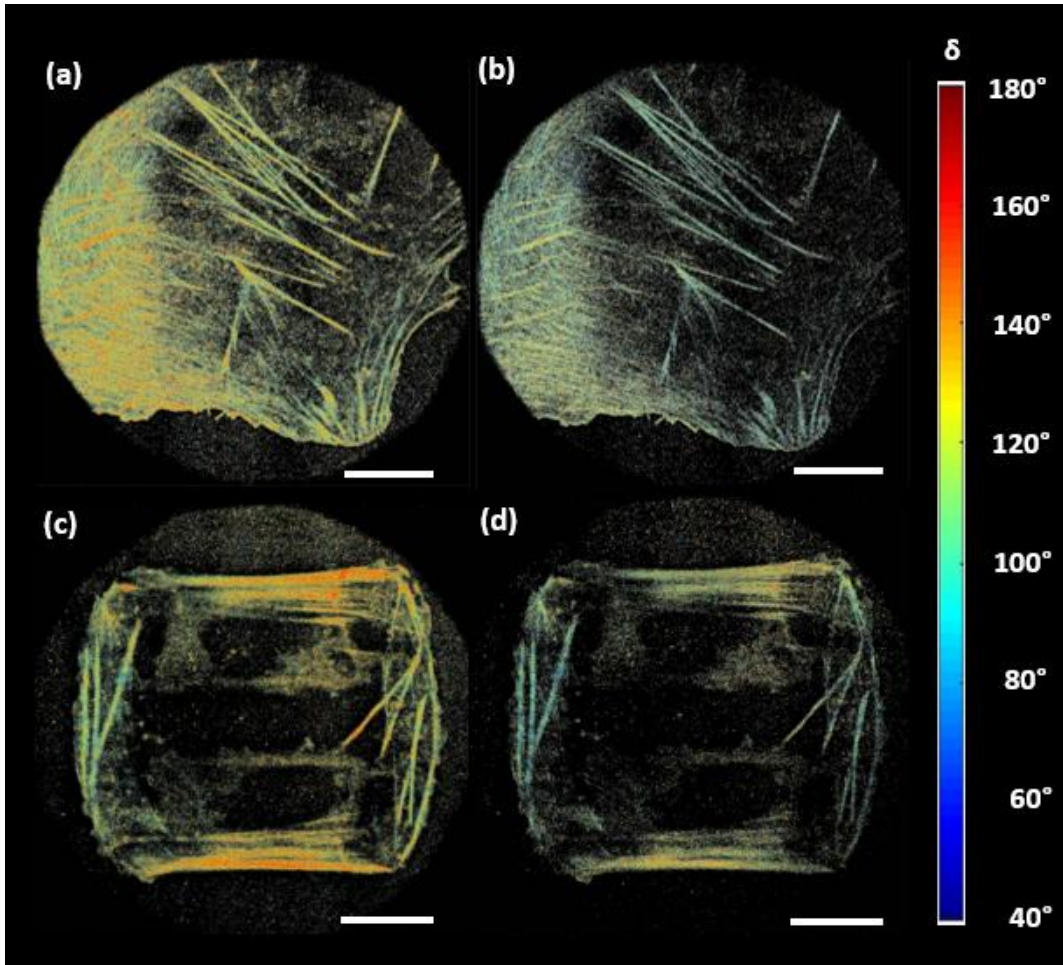


Figure 5.28 – Effect of post-processing filtering in 4polar-dSTORM – wobbling images. (a,c) Before filtering with intensity, radius and sigma together. (b,d) After applying the combined filter. The color code is jet normalized between 40-180 (degrees), being red-ish colors for wider cone aperture and blue-ish colors for narrower wobbling aperture values. On the top (a,b), non-patterned cell. On the bottom (c,d), H-med CYTOO patterned cell. White scale bar is 10 $\mu$ m.

As expected, on the orientation side, very subtle differences are observed in 4polar-dSTORM orientational maps before and after the filtering process (see Figure 5.29). The effect of post processing filtering will most likely be more visible in histograms, as detailed above and in the next section. Maybe the most prominent feature in  $p$  images, is the mean orientation of dorsal SF which is better highlighted when crossing with transverse arcs after filtering (Figure 5.29b) thanks to a reduction in background molecules.

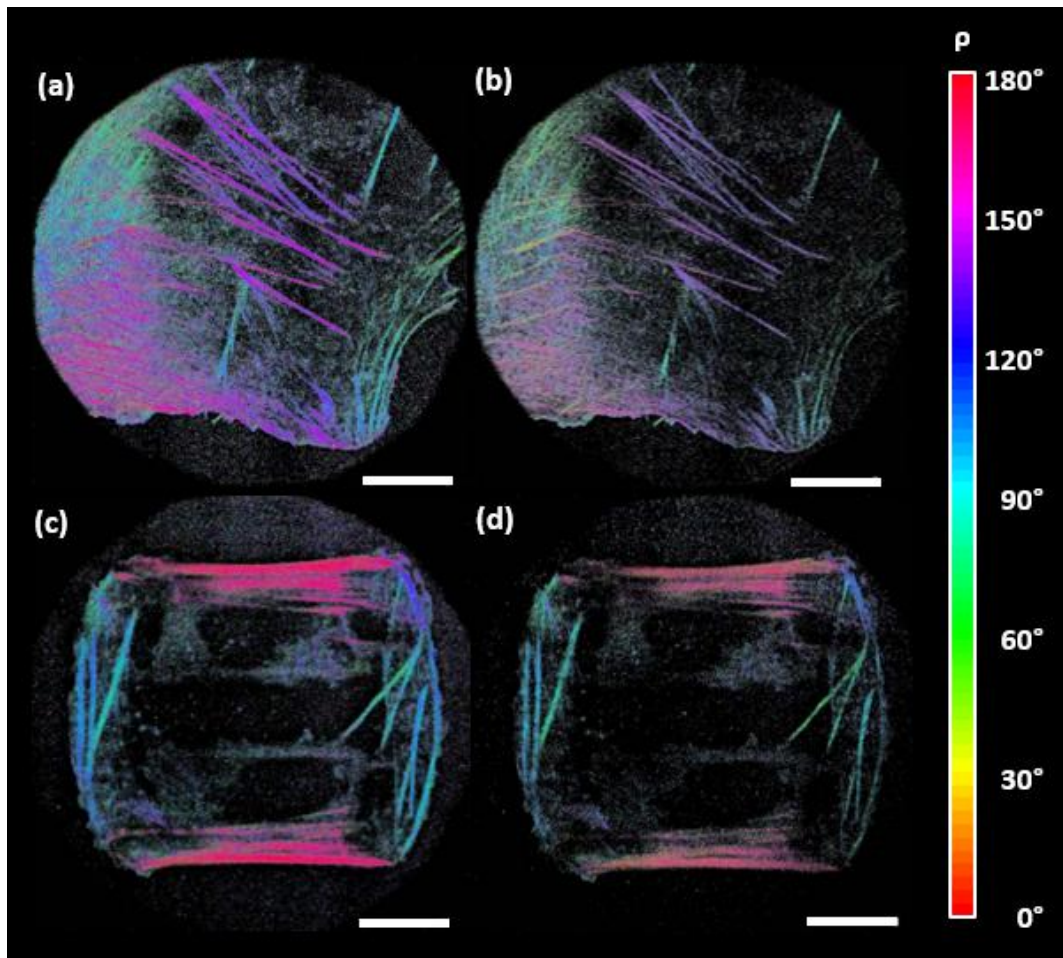


Figure 5.29 – Effect of post-processing filtering in 4polar-dSTORM – orientation images. (a,c) Before filtering with intensity, radius and sigma together. (b,d) After applying the combined filter. The color code is hsv, a cyclic colorbar between 0-180 degrees. On the top (a,b) non-patterned cell. On the bottom (c,d), H-med CYTOO patterned cell. White scale bar is 10 $\mu$ m.

## V.6 Qualitative comparison of actin organization in different SFs regions of a fixed cell

This section is dedicated to the illustration of the previous processing, in different regions of the observed SFs. We will display only a few representative filtering procedures.

### V.6.1 Focal adhesions regions

In addition to the central part of ventral SFs, we decided to evaluate regions of ventral SF close to focal adhesions (FA) (see Figure 5.30). These regions are interesting for their supposed differences in SF stiffness (which also correlates with tension) and actin binding protein (ABP) distribution (see Chapter1). Thus, it would be interesting to evaluate if actin filament alignment is different in such regions, which is an open question. Interestingly, in our data we observed quite often that thick focal adhesion sites exhibited large wobbling  $\delta$  values (ROI #41 in Figure 5.30b, white arrowhead). Similarly as above, we display the corresponding correlation plots relating intensity, wobbling ( $\delta$ ), nanoscale organization ( $\Delta\rho$ ), and radii, in



Figures 5.31 and Figure 5.32. The results show very similar behaviors as in the previous analysis, performed within the center of the ventral SF.

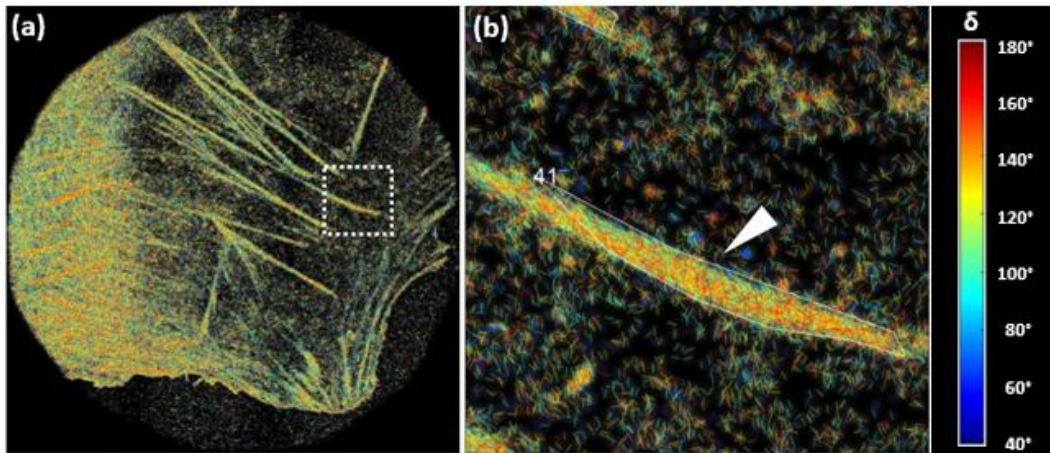


Figure 5.30 – Ventral SF region close to focal adhesion (terminus #41) used in the post-processing filtering procedure. (a) 4polar-dSTORM micrograph obtained with TIRF excitation mode. The white dashed square (approximately  $8\mu\text{m} \times 8\mu\text{m}$ ) is the zoomed region in b. (b) zoomed 4polar-dSTORM, with the ventral SF #41 pointed with white arrow head. The detection NA was  $\text{detNA}=1.20$ . The colors of the sticks in (a,b) correspond to the different wobbling values (jet colormap normalized in between 40 -180, blue are narrow aperture, red are wide ones).

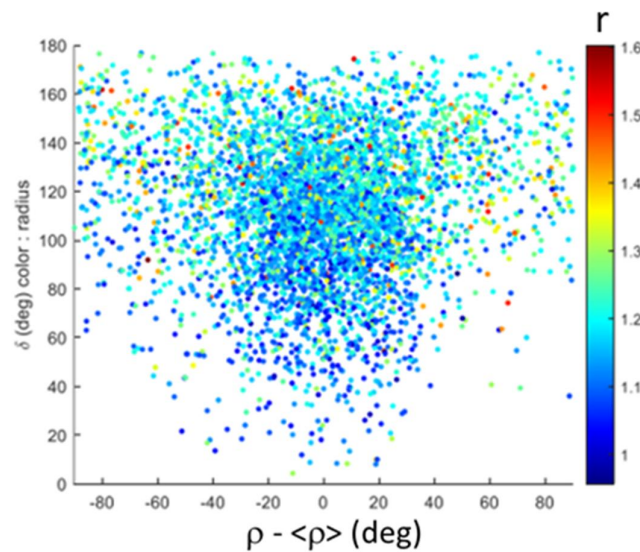


Figure 5.31 – Ventral SF close to focal adhesion (terminus #41) plot of wobbling ( $\delta$ ) vs the nanoscale order (extent of  $\rho - \langle \rho \rangle$ ) vs fitted radius (color, in pixel units). We see that for large radii and wobbling values, the plot tend to be more scattered in  $\rho$ .

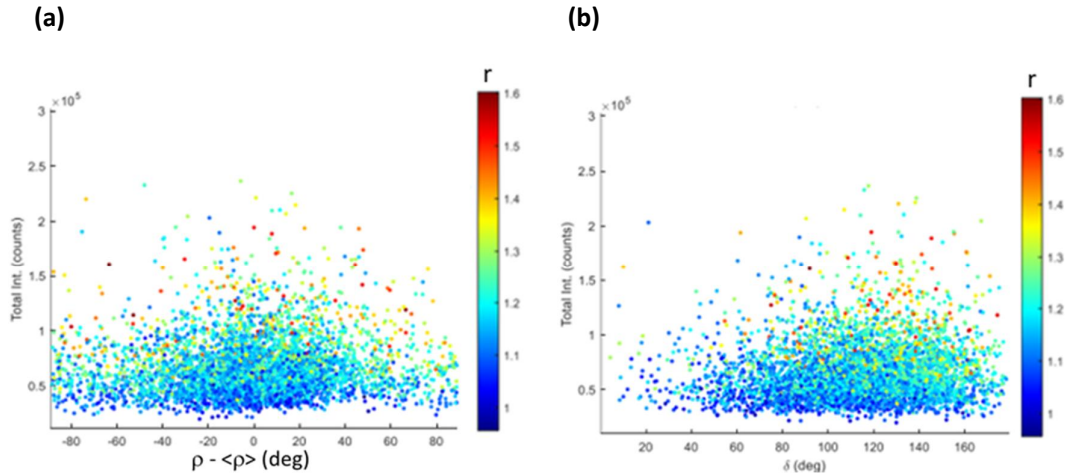


Figure 5.32 – Ventral SF close to focal adhesion (terminus #41) Intensity plots. (a) Intensity (counts) vs the nanoscale order (extent of  $\rho - \langle \rho \rangle$ ) vs radius (color, in pixel units). (b) Intensity (counts) vs wobbling angle ( $\delta$ , degrees) vs radius (color, in pixel units). We see that for large radii, the plot tend to be more scattered in  $\rho$  and  $\delta$ .

We filtered the data from ROI #41 (using bounds given in table 5.2), and we obtained the results shown below (Figure 5.33). We observe that, the mean wobbling values observed in this region are slightly higher than the center of the ventral SF, with  $\langle \delta \rangle \pm \Delta \delta = 113.4^\circ \pm 29.8^\circ$ , Figure 5.33a) compared to the central part of the ventral SF  $\langle \delta \rangle \pm \Delta \delta = 106.7^\circ \pm 29.8^\circ$ , Figure 5.26a). This could be the sign of a higher population of tilted filaments in the FA region. When we used radius (r) or wobbling ( $\delta$ ) filter, the results confirm that this difference corresponds to more tilted molecules/F-actin filaments, since a more prominent reduction in the wobbling values was observed. For example, for radius filtering we observed a reduction in bias of: shift in  $\langle \Delta \rho \rangle = -3.1^\circ$ ; shift in  $\langle \delta \rangle = -7.5^\circ$ . On the other hand, with wobbling filtering we obtained: shift in  $\langle \Delta \rho \rangle = -5.2^\circ$ .

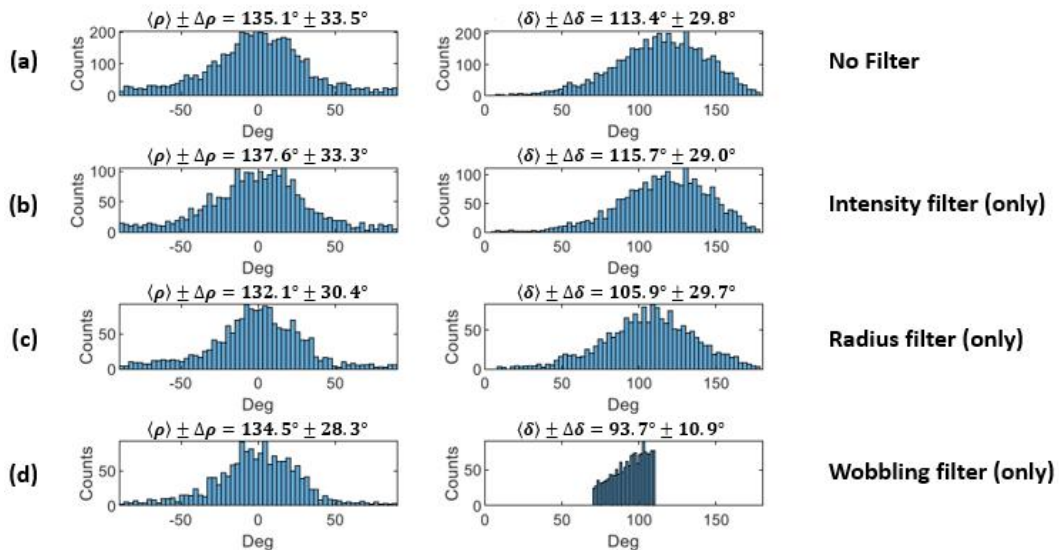


Figure 5.33 – Single SF (ventral terminus region #41) bias removal due to post processing filtering. (a) The default condition, with no filtering. The nanoscale organization  $\Delta\rho$ , and the wobbling angle ( $\delta$ ) are the key parameters to be evaluated when analyzing the removal of the bias on the data. (b) Intensity filtering histograms of  $\rho$  and  $\delta$ . (c) Radius filtering histograms of  $\rho$  and  $\delta$ . (d) wobbling filtering histograms of  $\rho$  and  $\delta$ .

Note also that the nanoscale alignment ( $\Delta\rho$ ) after filtering is slightly more disordered for this focal adhesion region (ROI#41,  $\Delta\rho=28.3^\circ$ ) compared to the previous ventral SF (ROI#10, width ( $\Delta\rho$ )= $22.9^\circ$ ), suggesting that both regions might have subtle differences on actin filament alignment in 2D.

Note that different focal adhesions regions do not necessarily give similar results. For example, at the ROI#38 (see Figure 5.34b and Figure 5.35, white arrowhead), the F-actin organization behaved closer to the central part of the ventral SF (ROI#10). This observation also confirms the possible large diversity of organization in FAs, which can depend on their maturity stage for instance.

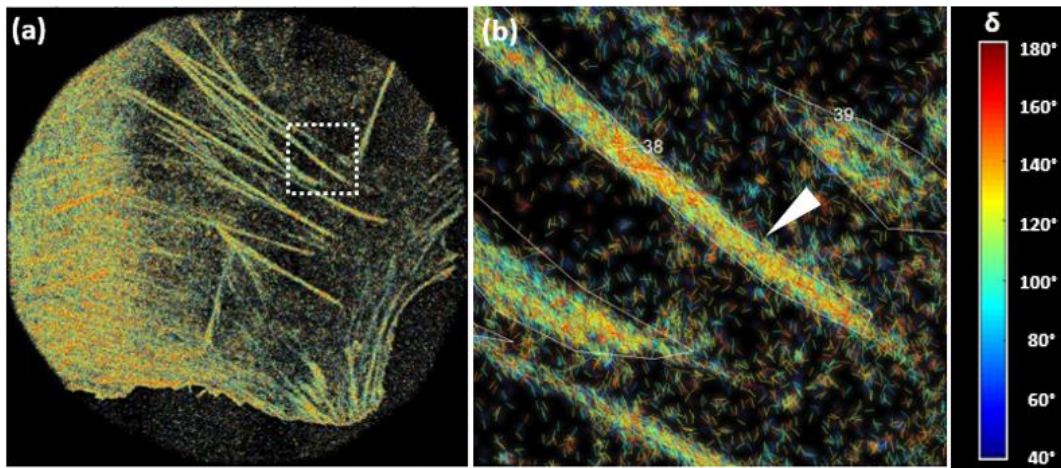


Figure 5.34 – Ventral SF region close to focal adhesion (terminus #38) used in the post-processing filtering procedure. (a) 4polar-dSTORM micrograph obtained with TIRF excitation mode. The white dashed square (approximately  $8\mu\text{m}\times 8\mu\text{m}$ ) is the zoomed region in b. (b) zoomed 4polar-dSTORM, with the ventral SF #38 pointed with white arrow head. The detection NA was  $\text{detNA}=1.20$ . The colors of the sticks in (a,b) correspond to the different wobbling values (jet colormap normalized in between 40 -180, blue are narrow aperture, red are wide ones).



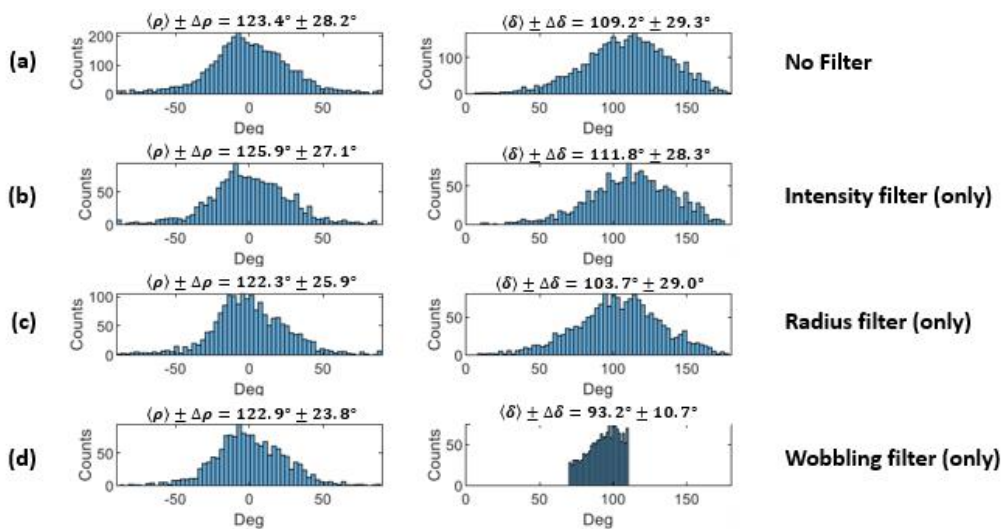


Figure 5.35 – Single SF (ventral terminus region #38) bias removal due to post processing filtering. (a) The default condition, with no filtering. (b) Intensity filtering histograms of  $\rho$  and  $\delta$ . (c) Radius filtering histograms of  $\rho$  and  $\delta$  (d) wobbling filtering histograms of  $\rho$  and  $\delta$ .

### V.6.2 Dorsal SF regions

Finally, we could also analyze the effect of post processing filtering in more complex regions such as in dorsal stress fibers crossing with transverse arcs, (see Figure 5.36). The analysis of ROI#31 (Figure 5.36b, white arrowhead) is given in Figure 5.37 and Figure 5.38 (scatter plots) and in Figure 5.39 (post processed histograms).

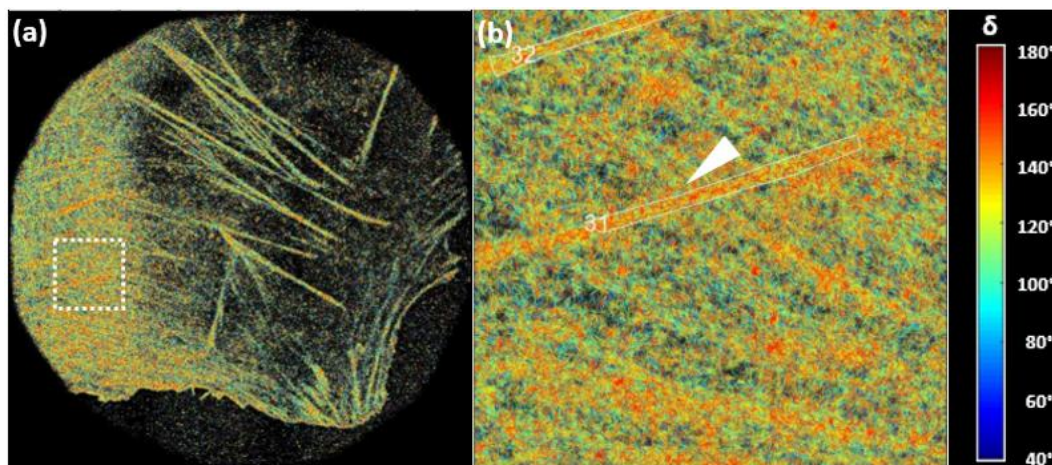


Figure 5.36 – Dorsal SF region crossing with transverse arcs (ROI #31) used in the post-processing filtering procedure. (a) 4polar-dSTORM micrograph obtained with TIRF excitation mode. The white dashed square (approximately  $8\mu\text{m} \times 8\mu\text{m}$ ) is the zoomed region in b. (b) zoomed 4polar-dSTORM, with the region #31 pointed with white arrowhead. The detection NA was  $\text{detNA}=1.20$ . The colors of the sticks in (a,b) correspond to the different wobbling values (jet colormap normalized in between 40 -180, blue are narrow aperture, red are wide ones).



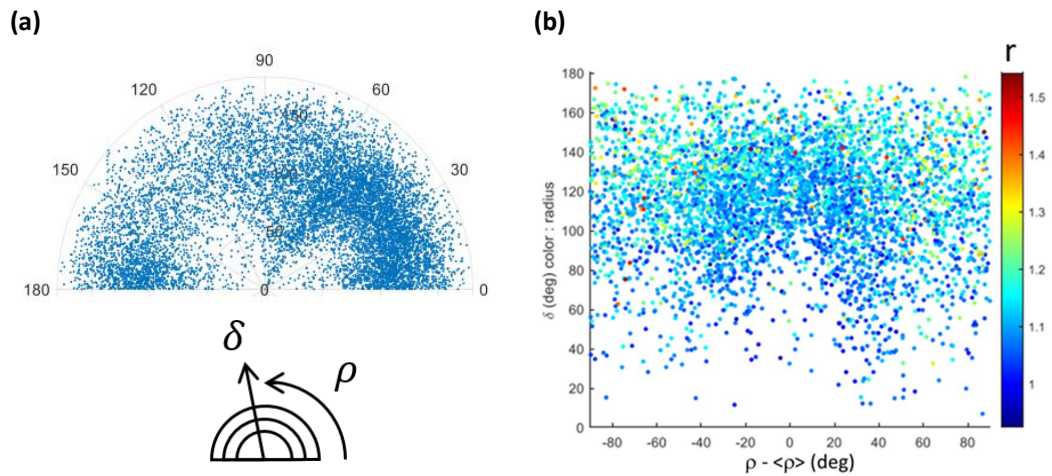


Figure 5.37 – Dorsal SF (ROI #31) polar plots. (a) The probed orientations ( $\rho$ , angular) vs wobbling aperture ( $\delta$ , radially). Many different orientations yields a wider distribution of orientations due to the nature of dorsal SF, and the crossings with transverse arcs. (b) The plot of wobbling ( $\delta$ ) vs the nanoscale order (extent of  $\rho - \langle \rho \rangle$ ) vs fitted radius (color, in pixel units). We can qualitatively see at least two mean clusters in the plots.

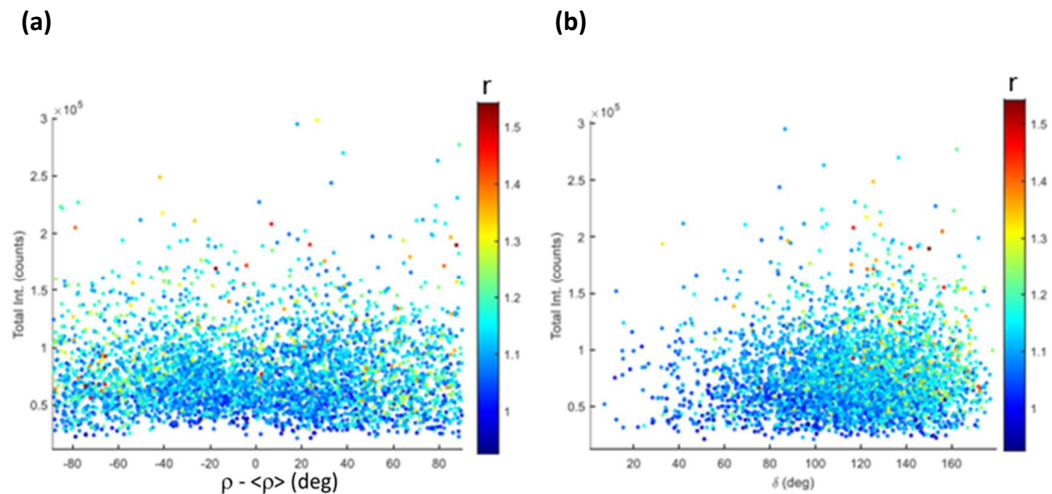


Figure 5.38 – Dorsal SF crossed with transverse arcs (ROI #31) Intensity plots. (a) Intensity (counts) vs the nanoscale order (extent of  $\rho - \langle \rho \rangle$ ) vs radius (color, in pixel units). (b) Intensity (counts) vs wobbling angle ( $\delta$ , degrees) vs radius (color, in pixel units). We see that there is no clear trend in (a), but in (b) for large radii we keep observing the trend to be more scattered in and  $\delta$ .

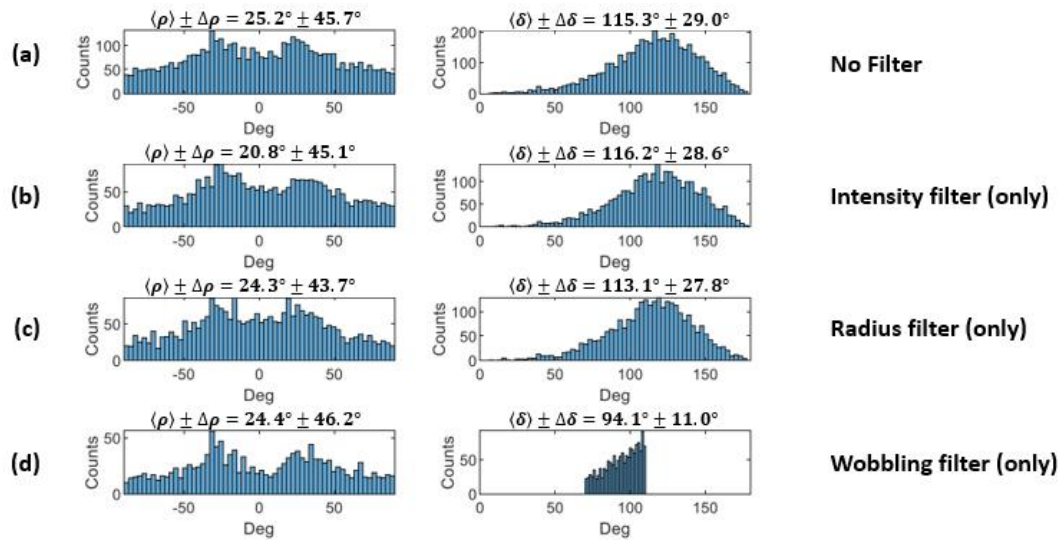


Figure 5.39 – Dorsal SF (ROI #31) bias removal due to post processing filtering. (a) The default condition, with no filtering. (b) Intensity filtering histograms of  $\rho$  and  $\delta$ . (c) Radius filtering histograms of  $\rho$  and  $\delta$  (d) wobbling filtering histograms of  $\rho$  and  $\delta$ . We see from the  $\rho$  plots that at least two clusters of orientations are seen (two peaks) at crossed regions.

As we can see from Figure 5.37 and Figure 5.38a, the orientation distribution is far more scattered in dorsal regions than other more isolated SFs. In Figure 5.38b we still see some correlation among radius, wobbling and intensity, meaning that in such regions, filtering parameters still has an effect on the data. In Figure 5.39 we observe a different orientation ( $\rho$ ) distribution profile compared to the previous SF regions: instead of having a peak at  $0^\circ$ , we observe at least two peaks around the mean. These two peaks are visibly due to a collection of transverse arcs crossing with the main orientation of the measured dorsal stress fiber. The obtained nanoscale alignment ( $\Delta\rho$ ) is therefore wider than for an isolated bundle (with values higher than width  $\Delta\rho=40^\circ$ ), but we must bear in mind that it is due to a mix between the pure organization of the dorsal SF, and the arcs that cross the dorsal SF. The interpretation of the plots get more complex as a consequence. Interestingly, the wobbling values at dorsal regions were clearly wider compared to the transverse arcs (more red-ish, see Figure 5.36b), suggesting that actin filaments in dorsal might be more tilted compared to transverse arcs. This is expected from the more tilted behavior of the dorsal SFs themselves, which are known to be less flat than ventral SFs (see Figure 5.20b). However, a not very pronounced bias reduction after radius filtering was observed: typically a shift of  $\langle\delta\rangle=-3.1^\circ$ . Again, this is most likely due to a possible population of highly tilted molecules.

### V.6.3 Summary of the qualitative SF regions analysis

The analysis of molecular wobbling values obtained in the different SFs shows, even after radius-filtering conditions, different values for  $\langle\delta\rangle$ . We know, from the sections above that this is most likely related to off-planes orientations of F-actin filaments in the investigated populations. Interestingly, we can infer from the measured  $\langle\delta\rangle$  value, the mean tilt angle ( $\eta$ ) that the filaments undergo in the SFs. For this, the bias graph of Figure 5.18 can be used.

Assuming an in-plane value of  $\delta = 100^\circ$ , a bias of  $\langle\delta\rangle$  of about  $3^\circ$  (typically seen in peripheral, ventral and FAs) corresponds to a tilt angle  $\eta$  in the range  $[0^\circ-20^\circ]$ , e.g. slightly out of plane. In dorsal SFs however,  $\langle\delta\rangle$  is shifted by about  $15^\circ$  which corresponds to  $\eta$  approaching  $30-40^\circ$ , which corresponds to a higher off-plane tilt, as expected from dorsal SFs.

We conclude from this section that post-processing filtering can be used to remove the residual bias in  $\delta$  values that correspond to a population of labels that have a non-negligible tilted orientation in relation to the sample plane. The nanoscale orientation and organization ( $\rho$  and  $\Delta\rho$ ) were clearly more robust parameters after the post-processing filtering than fluorophore wobbling aperture ( $\delta$ ), demonstrating that the technique even without post filtering was relatively unbiased in the orientation determination ( $\rho$  values). For example, the average mean orientation ( $\rho$ ) kept almost constant in all cases. This was particularly clear when comparing “no filter” condition with “wobbling filter” (fully removal of tilted labels) case. Such behavior was expected, because, in theory, we do not get experimental bias in the in-plane mean orientation of the labels ( $\rho$ ), only in the cone aperture parameter ( $\delta$ ). Probing extra population in TIRF that is mainly tilted could explain the subtle changes in the nanoscale alignment ( $\Delta\rho$ ) after post filtering procedures. On the other hand, the bias removal tracked by the changes in the  $\delta$  values demonstrated that all the labels detected in TIRF excitation condition must not be assumed to be in-plane population in principle. A positive consequence of such behavior is that, thanks to post-processing filtering, we may qualitatively infer how much tilted labels (actin filaments) are distributed in loci. Therefore, although the technique does not aim at 3D orientation estimation retrieval of biological structures, we may reach a qualitative estimation of the 3D features in the data.

## **V.7 Quantitative comparison of different stress fibers and their sensitivity to contractility perturbations**

### **V.7.1 Comparison of F-actin degree of alignment in different SFs**

It is of our interest to compare the actin filament alignment on different SF types in a quantitative manner in 2D (which is the least biased situation). In what follows, we will therefore concentrate on the  $\Delta\rho$  values measured, after post filtering procedures performed on radius and intensities similarly as above. Stress fibers of at least 3 cells were pooled together to perform the statistics, leading to about 10 to 20 SFs per conditions. We selected peripheral SFs, transverse arcs, ventral SFs, terminal regions (identified as FAs in the spinning image) of ventral SFs, dorsal SFs, and terminal regions of dorsal SFs. The results are summarized in Figure 5.40. Overall, the nanoscale alignment ( $\Delta\rho$ ) in 2D of different stress fibers were very similar, within the range of  $20^\circ$  to  $40^\circ$ . Dorsal SF were slightly more disorganized than the other regions, but this subtle trend might be due to crossings with transverse arcs and their more prominent 3D tilt angles. Focal adhesion regions (SF termini) were seen to be more ordered than dorsal SFs, most probably because of the reasons mentioned above. FAs measured at the termini of ventral SFs on the other hand, exhibit very similar organization as in ventral SFs, with only a slight shift of higher disorder. Peripheral SFs were seen to be less ordered than ventral SFs, which we attribute to their larger thickness, seen to correlate with larger 3D tilted organizations. The order measured in transverse arcs is similar to peripheral SFs.

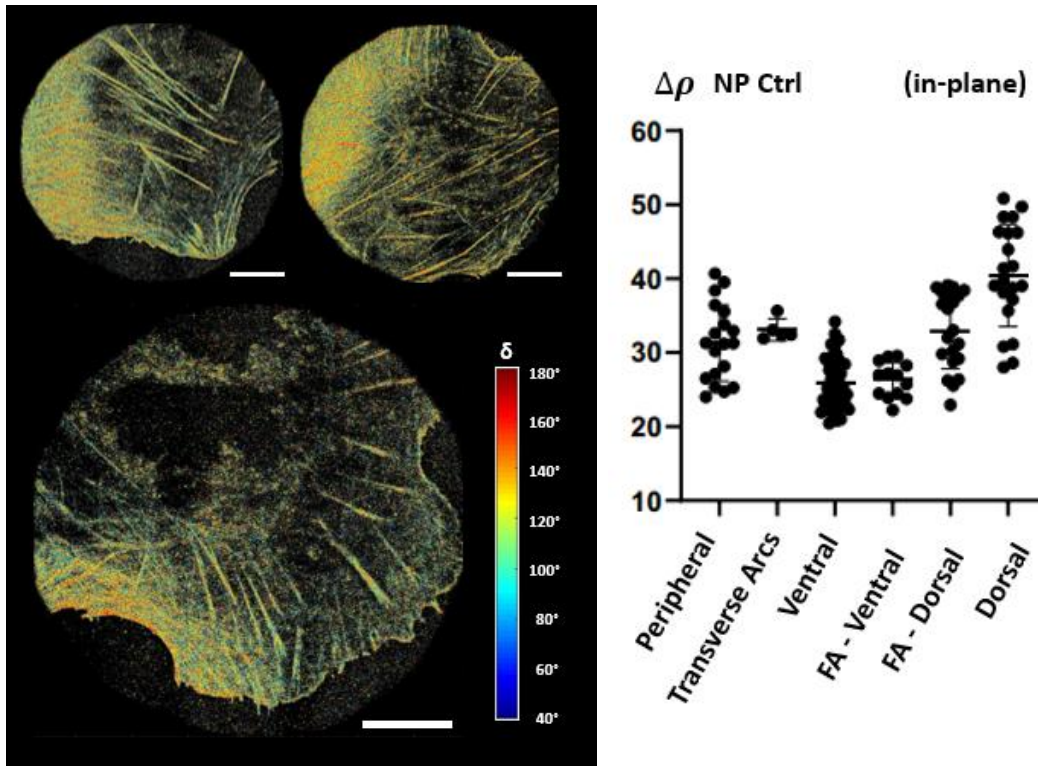


Figure 5.40 – In-plane nanoscale degree of alignment ( $\Delta\rho$ ) of different stress fibers. The cells used were non-patterned (NP) cells of CA-MLCK U2OS Ctrl cells, i.e., mutant cells without doxycycline stimulus for contractility. Naïve cells behaved similarly to CA-MLCK Ctrl cells (data shown below). On the left, 4polar-dSTORM micrographs (color for  $\delta$  values). White scale bar: 10 $\mu$ m.

### V.7.2 F-actin alignment at the nanoscale is robust to perturbations

There are a few ways we could try to perturb F-actin alignment in U2OS cells. To better evaluate the perturbation of F-actin alignment, we investigated micropatterned cells plated on H-shaped (CYTOO patterns), that display similar stress fibers. We could try to perturb F-actin alignment in cells by stimulating or inhibiting contractility. In order to stimulate contractility, for example, the literature provides that wider cells tend to form stress fibers with higher tension. Under higher tension (contractility), we expect to see more aligned (ordered) actin filament in stress fibers, because a higher order correlates with higher contraction efficiency in muscle sarcomeres (the main molecular contractility model). Importantly, the effect of contractility in F-actin alignment in stress fibers is still an open question. Another way to study contractility is by using mutant cell lines. In this context, it is also possible to use a stable cell line of U2OS with a constitutively active (CA) mutant gene for myosin light chain kinase (MLCK) that is activated upon presence of doxycycline (doxy). In principle, such mutant cells could have their contractility behavior switched on when we add doxy in the system in a dose dependent manner (Figure 5.41). Thus, we measured different SF alignment under a few conditions: medium and big mutant cells with doxycycline (doxy), medium size mutant cells without doxy (ctrl), and medium size naïve U2OS cells. We expect that big mutant cells in the presence of doxy to be under highest tension, and the medium size naïve cell with the lowest tension. In Figure 5.41 we see very similar results were obtained in all conditions, but in general peripheral SF seemed to be

*slightly* more disordered (higher  $\Delta\rho$  values) when contractility is stimulated (bigger size and/or MLCK activity). However, the cells with the highest contractile behavior (Figure 5.41c, H-big +doxy), together with the intermediate case (Figure 5.41b, H-med +doxy) had almost the same behavior than H-med control, whose had slightly more disorganized F-actin than naïve U2OS cells. In general, all mutant CA-MLCK cells always displayed a slightly more disorganized fashion of actin filaments compared to the naïve U2OS conditions. This observation is in contradiction to ensemble measurements (Chapter 3), and shows that different read-outs of the organization are measured in the two measurements. Here in particular, an important factor seems to play a role in F-actin organization: in very thick SFs such as observed in CA-MLCK cells, a large portion of high delta (high tilt angles) molecules were visible, signature of a higher disorganization not induced by contractility, but rather by the morphology of the SF itself. This 3D organization is likely to not affect 2D-ensemble measurements. Overall in the super-resolution measurements shown here, there was very little modification of the actin organization under high contractility stimulus, which shows that the actin organization is very robust to contractility. The lack of a clear differences between naïve cells and mutant cells+doxy on actin fibers makes, at this stage, difficult to conclude on any subtle correlation between contractility and actin organization.

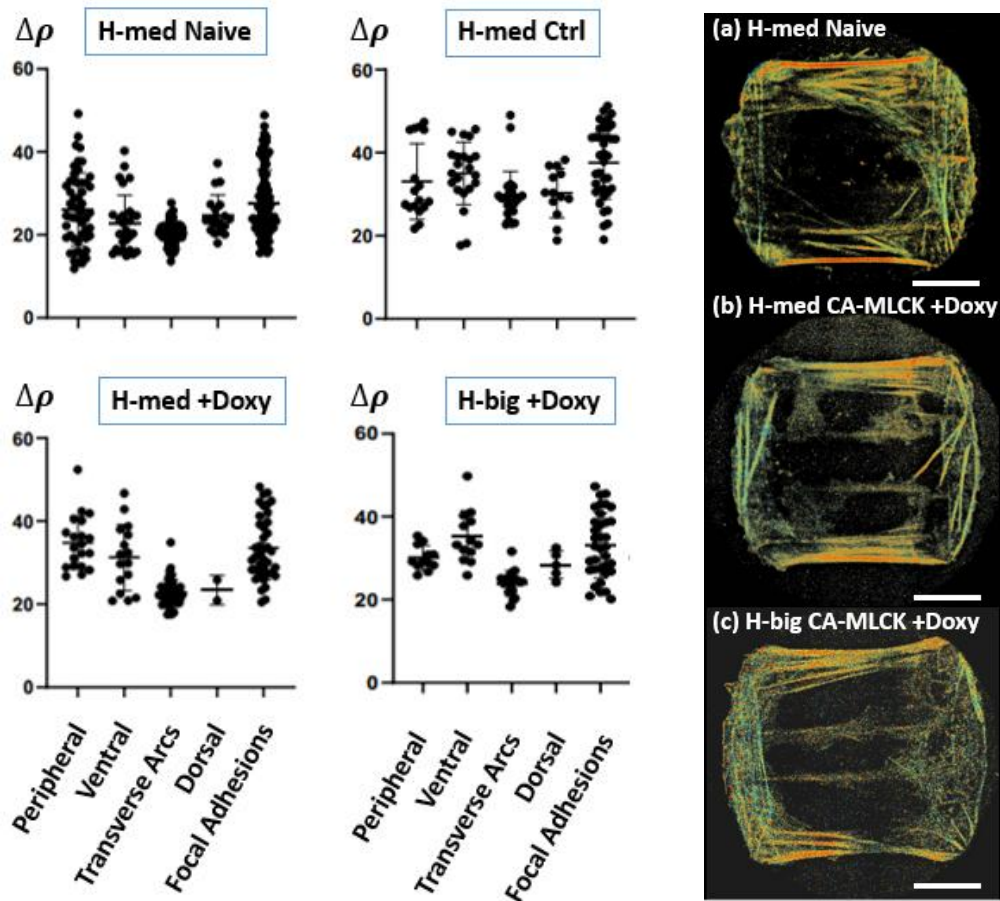


Figure 5.41 – In-plane nanoscale degree of alignment ( $\Delta\rho$ ) of different stress fibers in CYTOO patterned cells upon contractility stimulus. The non-mutant cells (naïve) and the mutant cells used were plated on H-shaped pattern of medium and big size (H-med, H-big) cells. Mutant cells were constitutively active (CA) myosin light chain kinase (MLCK) U2OS cells. On the right side, three main examples of 4polar-dSTORM micrographs from (a) Naïve, (b) H-med +doxy, and (c) H-big +doxy conditions. The colors in (a-c) were for wobbling values. White scale bar: 10 $\mu$ m.



On the other hand, we could perturb the contractility of stress fibers by inhibiting myosin with a drug named Blebbistatin (Figure 5.42). Blebbistatin is a myosin II inhibitor, thus it perturbs acto-myosin contractility behavior. The effect of the drug changes slightly the cell morphology (increase of the curvature of peripheral SFs) and seems to cause a subtle decrease in the nanoscale F-actin order of the still visible bundles (slightly higher  $\Delta\rho$  values in the presence of Blebbistatin).

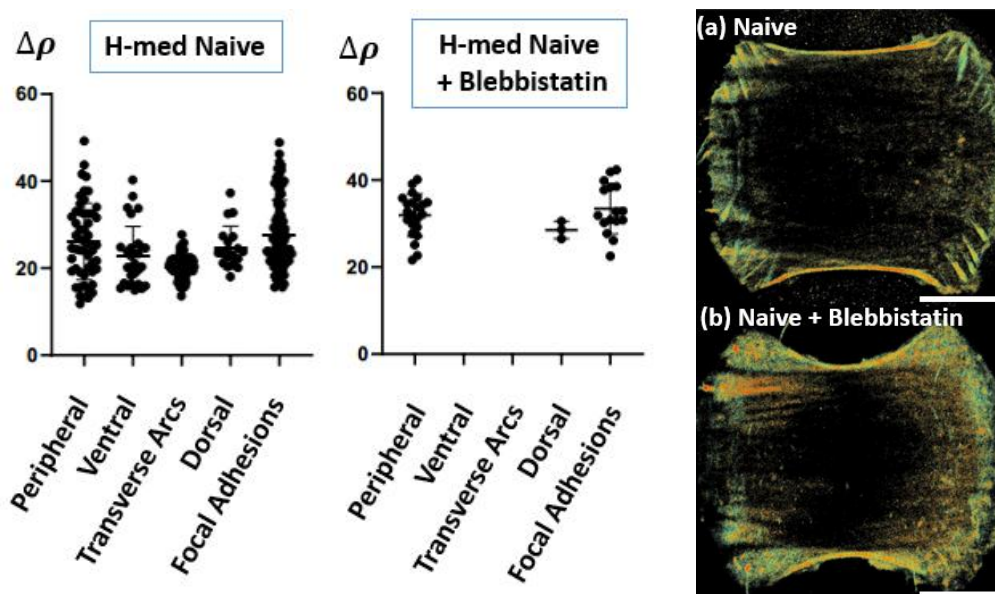


Figure 5.42 – In-plane nanoscale degree of alignment ( $\Delta\rho$ ) of different stress fibers in H-med CYTOO patterned cells upon contractility inhibition. The non-mutant cells (naïve) were tested with (b) and without (a) a drug that inhibits myosin contractility behavior (Blebbistatin).

In order to visualize what perturbation experiments (blebbistatin) does to F-actin at the nanoscale, we selected the same straight SF region before and after the perturbation (see Figure 5.43). In Figure 5.43a,b we display the orientation map, and in Figures 5.43c,d we display the wobbling map after post-processing filtering ( $\delta < 110^\circ$ ). We can see that before the blebbistatin treatment (a,c) the actin filaments are more organized (aligned) along the mean orientation, whereas in the presence of blebbistatin (b,d) they become slightly more disorganized (less aligned). It seems therefore easier to perturb F-actin organization by a loss of contractility than by a gain of contractility, as exposed above.

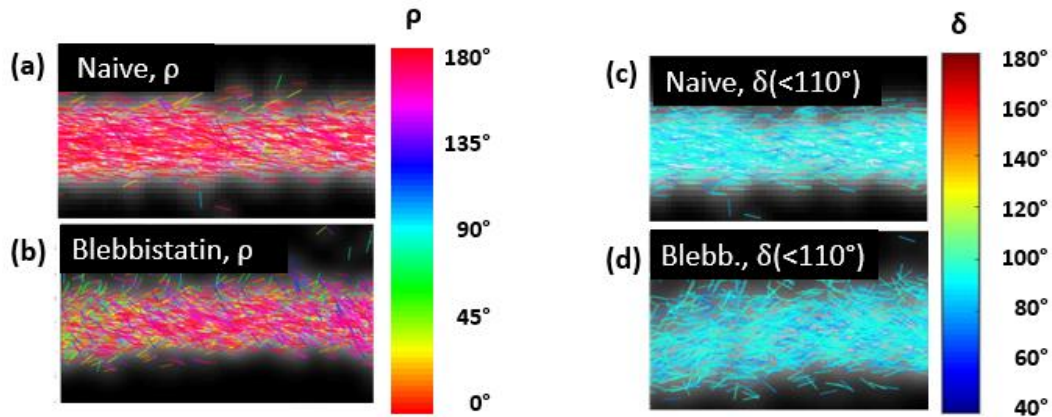


Figure 5.43 – In-plane nanoscale degree of alignment ( $\Delta\rho$ ) of peripheral stress fibers in H-med CYTOO patterned cells before (a,c) and after (b,d) blebbistatin treatment, a drug that inhibits myosin contractility. The wobbling map is blueish because we selected to display only ( $\delta < 110^\circ$ ).

Finally, the values obtained for actin organization, grouped by SFs types, cells types and treatments, are summarized in Figure 5.44.

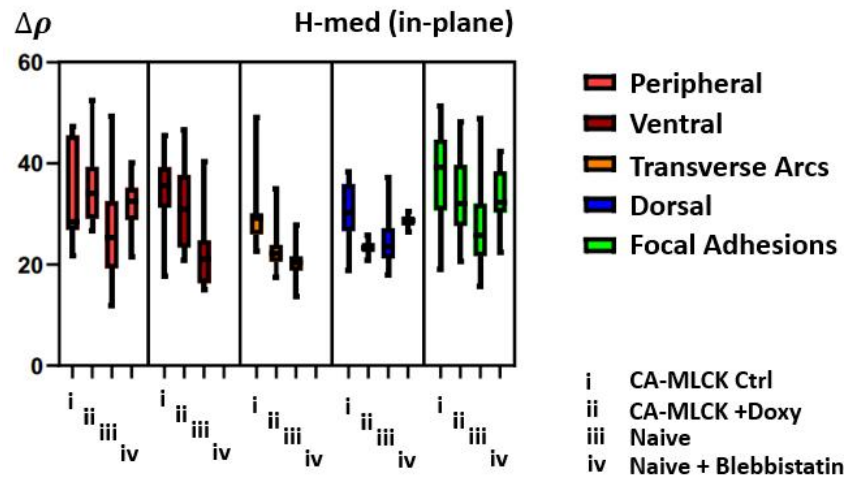


Figure 5.44 – In-plane nanoscale degree of alignment ( $\Delta\rho$ ) of different stress fibers in H-med CYTOO patterned cells upon contractility tests. The behavior of stimulating or inhibiting contractility tend to subtle disorganize F-actin nanoscale alignment in 2D. All the conditions (i, ii, and iv) yielded higher  $\Delta\rho$  for all SF types than the non-mutant and untreated cells (iii, naïve).

## V.8 Application of 4-polar dSTORM in complex and dense actin regions: cell lamellipodia

In addition to stress fibers, we noticed that 4polar-dSTORM could also be useful to analyze complex regions that presents crossed filaments, such as lamellipodia. In general, the conventional super-resolution microscopy techniques are not very suitable to probe lamellipodia, since the required resolution is still beyond their reach. However, with 4polar-



dSTORM, quantitative orientation information can still be obtained. Regions with crossed filaments such as in dorsal and transverse arcs were already been discussed in this thesis, and also represents a system that could be eventually studied (see Figure 5.45). However, lamellipodial regions, as briefly introduced in Chapter 1, are made of a dense and subdiffraction actin network at the leading edge of cells. With conventional fluorescence microscopy techniques it is not possible to predict that lamellipodial regions have specific F-actin orientation organization.

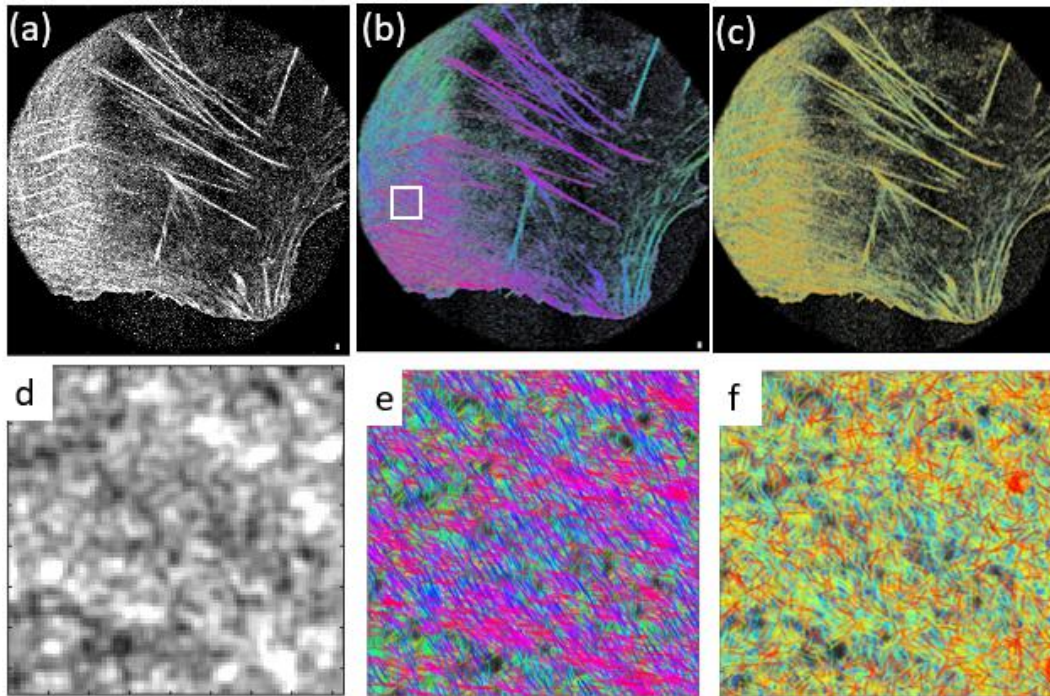


Figure 5.45 – Crossed SF regions in dSTORM (a,d, localization only), and 4polar-dSTORM (b,e – orientation map; c,f – wobbling map) in non-patterned CA-MLCK control cell (without doxy). We can see by the orientation map (b,e) that the filaments are diagonally distributed (purple orientation sticks), meanwhile in the pure dSTORM map, little information could be retrieved. The squared inset in (b) is the same for (d), (e), and (f), and it is around  $4\mu\text{m} \times 4\mu\text{m}$  size.

As we already discussed in Chapter 1, the lamellipodia has Arp2/3 protein complex that crosslinks actin filaments in a regular fashion of around  $70^\circ$ . So we expect that actin filaments to be branched with specific orientation at lamellipodial regions. To investigate lamellipodia using 4polar-dSTORM, we plated B16 melanoma (skin cancer) cells that have a pronounced lamellipodia morphology (collaboration with K. Rottner, Univ. Braunschweig Germany). The obtained results are summarized in Figure 5.46. The inset in Figure 5.46a are lamellipodial regions (1 and 2) in purely localization (dSTORM, grayscale) and with 4polar-dSTORM wobbling map. If we analyze only the orientations ( $\rho$  map) of the inner part of lamellipodia (e.g. in region 2) we can draw two main orientation vectors (yellow vectors in Figure 5.46c). We can quantify the angles by polar histogram plots of lamellipodia. We show in Figure 5.46d that the main orientations obtained are specific and separated by around  $70^\circ$  (see the yellow triangular angle). This angle reminds the observations that were reported in electron microscopy measurements in such regions, where Arp2/3 is known to impose a branching angle around this value [11].

Besides, the nanoscale alignment of other simpler structures such as filopodia (F-actin filaments protrusions trough the leading edge) could be easily evaluated (Figure 5.42e-f). Even though these results are preliminary, they show that orientational features can be detected in dense actin meshworks, that are characteristics of previous observations in electron microscopy in lamellipodia and filopodia regions [11].

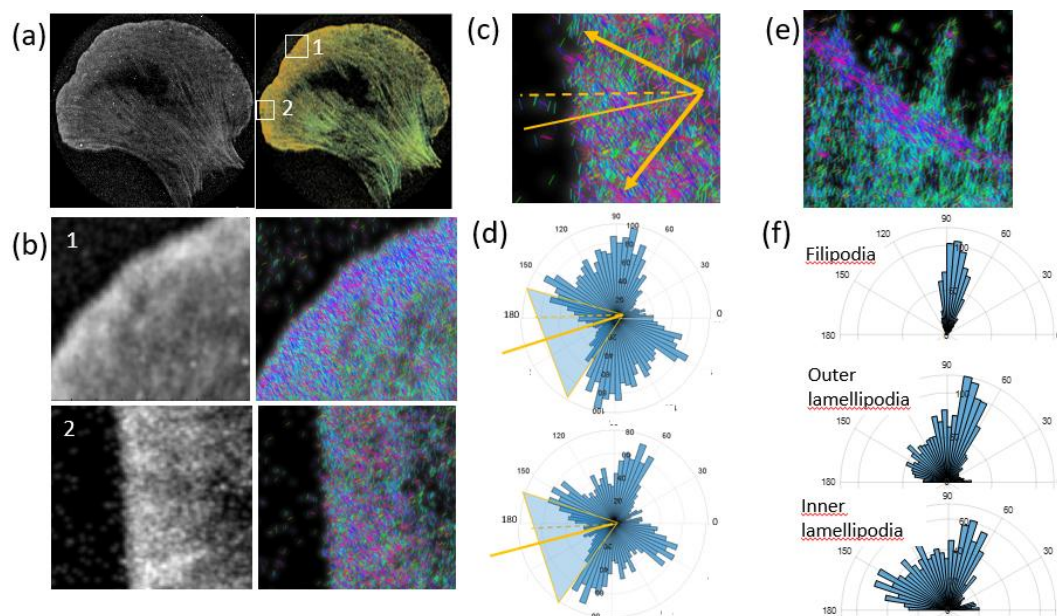


Figure 5.46 – Complex regions such as lamellipodia evaluated by 4polar-dSTORM. (a) dSTORM micrograph (gray) and 4polar-dSTORM wobbling map of B16 cell. (b) The insets lamellipodial regions 1 and 2 in purely localization (dSTORM, grayscale) and with orientational map (4polar-dSTORM). (c) The main orientation vectors in yellow of region 2. (d) Polar histogram showing the main orientations are specific and separated by around  $70^\circ$  (see the yellow triangular angle). (e) Leading edge regions with filopodial filaments (measured on another cell than the one depicted in (a)). (f) Polar histogram plots of filopodia, outer lamellipodia (border) and inner lamellipodia (like d).

## V.9 Conclusions of Chapter 5

In this chapter we introduced the main concepts and results of our novel polarized single-molecule super-resolution microscopy technique, the 4polar-dSTORM. In short, the 4polar-dSTORM is an improved version of the previously developed polar-dSTORM, with extra analyzer channels, single-molecule couplings and data processing steps. The great advantage of projecting each blinking event onto 4 analyzer channels, instead of 2, is the capacity of retrieving the mean orientation and wobbling values of each single-molecule independently in the field of view. With the latter, statistical quantification of the wobbling and estimation of the possible bias due to tilted fluorophores is possible. Therefore, the technique reaches in a qualitative manner the 3D orientation of the labels distributed on biological structures. More importantly, the acquired in-plane orientation is bias-free by theory, demonstrating that the organization of F-actin filaments or any other structure can be quantified without the influence of the wobbling behavior of the fluorophores. On the other hand, we showed that the disadvantage of splitting the detection onto 4 analyzer channels is the lower SNR that may yield a low number of localized

molecules (particularly limiting in normal incidence excitation conditions). The Total internal reflection fluorescence (TIRF) approach solves the sampling problem at expenses of probing an extra population of tilted labels, biasing the wobbling parameters. In order to circumvent such behavior we spatially filtered the emission of tilted fluorophores by reducing the detection NA to 1.20. Many experimental and processing parameters were evaluated in order to optimize the number of detected particles and reduce the possible bias in the polarimetric readout.

The 4polar-dSTORM differs from all polarimetric microscopy tools developed so far, because it can provide unbiased quantification of order (e.g., F-actin alignment) in 2D biological structures in cells at the nanoscale. Besides, it does not depend of any reference experiment to quantify the orientation and wobbling of single-fluorophores, being therefore an absolute and not relative quantitative microscopy technique. Moreover, it is an optical technique that reaches super-resolution capabilities of around 20nm localization precision in fixed cells. In fact, it goes beyond the pure localization maps: 4polar-dSTORM extract more information than typical super-resolution microscopies because it provides the structural orientation at the nanoscale, as shown in complex regions such as crossed bundles or in lamellipodia. Because it is an optical technique, in vivo analogue experiments could be eventually performed or envisioned (e.g., 4polar-PALM or 4polar-sptPALM, involving single particle tracking).

With 4polar-dSTORM we quantified the in-plane structural alignment of different stress fiber (SF) types and regions (central and close to focal adhesions). We realized that there was no striking differences in F-actin alignment on different SF types, with degrees of disorder within the range 20° to 40°. We tried to detect a correlation between F-actin alignment and actomyosin contractility by many approaches, because is an important open question in biology. First, by analyzing SF that are not contractile (dorsal) vs SF are contractile (peripheral, ventral, and transverse arcs). Later, by inducing contractility (with mutant cells +doxycycline; with different cell pattern sizes), and by inhibiting contractility (e.g., blebbistatin). In all conditions, the F-actin alignment was almost constant in all SF types, being just slightly more disorganized in the blebbistatin case (particularly more evident in peripheral SF). Actin filament alignment in stress fibers, therefore, demonstrate to be very difficult to perturb. Although such single-molecule results make sense by themselves, they are partially in contradiction to what we got with ensemble polarimetric results. With ensemble polarization resolved microscopy, we obtained more ordered structures at high contractility regions, and less ordered structures in less contractile regions (e.g., dorsal SF). Since these single-molecule measurements are less prone to bias than ensemble measurements as described in Chapter 4, we can conclude that the differences seen in ensemble measurements were likely affected by bias due to the averaging with actin background structures. In addition, single molecule measurements can reveal disorder occurring in 3D, which the ensemble measurements are less sensitive to. Ensemble vs Single molecule polarized measurements are further compared and summarized in Chapter 6.

## Chapter 6

### Conclusion and perspectives

In this last chapter we aim at making a short overview of the thesis, discussing the main concepts and results to finally address the overall conclusions. In the first three chapters, we introduced the typical biological system under investigation (actin filaments), and the typical optical systems we develop/used in this thesis to probe such structures (polarized optical microscopy methods). We detailed how actin filaments are formed and regulated within the cells to form higher ordered structures such as actin stress fibers and lamellipodia. In particular, we reviewed how the biomechanical properties of actin stress fibers can change upon different regions within bundle, among different stress fibers types, and upon different cell morphology (shape and sizes). Besides, we showed how polarized light can be used as an organization readout for biological structures, in ensemble and in single-molecule regime. In this work, we were aiming at eventually make a connection between acto-myosin contractility (forces) and actin filament alignment (structural information probed by polarized light). Importantly, we discussed in the first chapters how different excitation and emission setup schemes could affect the polarization readout. Depending on the setup scheme, one could expect to have more or less bias on the polarization readout. The bias in the orientation and order parameters depends on the setup used (e.g., excitation and detection NA), and on the relative orientation of the fluorophores (sample) in relation to the main coordinate axes of the optical system (e.g., tilted dipoles). Thus, a careful inspection of how the label binds to the structure must be performed before using a new fluorophore for polarized microscopy. Thanks to previous polarization resolved studies with phalloidin-AlexaFluor488, it is known that the orientation of this particular label is very parallel to the actin filament structure, being ideal for our cone model. Other models could be used to obtain the polarization readout if the label is oriented mainly orthogonal to the structure of interest (not discussed in this thesis).

In chapter 4, we showed the polarization resolved spinning-disk microscopy setup we built during this thesis and the respective ensemble results on actin stress fiber (SF) bundles. The concept of such ensemble polarization resolved setup is not new, but its use to investigate different stress fibers and to evaluate the possible contractility role in F-actin order in SF was. According to our ensemble results, we obtained that different SF had different F-actin order values. Surprisingly, SF were more ordered in bundles known to be contractile, such as peripheral SF, ventral SF, and transverse arcs. Dorsal SF, that in general are not decorated with myosin, are expected to not be contractile and it had the most disordered F-actin organization among all SF types. Such results seem to be in agreement with the hypothesis that acto-myosin contractility (forces) might align F-actin in SF bundles at the nanoscale. However they need to be interpreted with caution, since tilted orientation of the dorsal fibers could cause an overestimation of the measured order. Besides, we evaluated CA-MLCK mutant cells where we could trigger the contractility behavior by adding doxycycline in the medium. Such mutant cells displayed more ventral SF and thicker peripheral SF bundles in general, indicating that higher tension forces were possibly present in the system. Mutant cells in general had more ordered peripheral SF structures than naïve U2OS cells, which we correlated with their thicker SFs. An important remark is that we believe that the CA-MLCK Ctrl cell line displayed a leakage expression of the mutant gene even without the presence of doxycycline, due to similarities in the SF thickness and non-patterned cell morphology compared to naïve U2OS cells. Such similarities were also present on the polarization readout (order parameter) between CA-MLCK

Ctrl and CA-MLCK Doxy compared to naïve (not mutant) cells. While these ensemble results were informative on a relative comparison between similar samples types (for instance well isolated peripheral SFs), we noticed that possible inaccuracy in the obtained order values could occur due to the mixture of different actin organization within the diffraction limit size, or due to 3D orientations of filaments within the observed structure. This observation motivated the studies of the next chapter, dedicated to single molecule-scale orientation monitoring.

In chapter 5, we described a novel single-molecule and super-resolution polarization resolved microscopy setup, called 4polar-dSTORM. Here, both the concept of the setup and its use to investigate the nanoscale organization of F-actin in stress fibers (regions and subtypes) were new in the literature (the manuscript is in its finalization step). Importantly, this setup is the method permits to retrieve unambiguous 2D orientation readout with minimal bias, in contrast to previous studies. This is made possible thanks to instantaneous and parallel detection of two pairs of orthogonal polarized projections of the fluorescence emission ( $0^\circ$ - $90^\circ$  and  $45^\circ$ - $145^\circ$ ), which permits both the single-fluorophore orientation and single-fluorophore wobbling to be independently obtained. This is a considerable gain of information in comparison with ensemble polarization resolved microscopy. Ensemble techniques indeed average the information of mixtures of orientation populations (crossings, isotropic background), and cannot discriminate pure structural disorder from tilt-angles between the fluorophores and the proteins, as well as off-plane orientations (which overestimates wobbling). In this sense, the current available polarization resolved methods did not fully disentangle the wobbling/offset tilt angles from the mean orientation of single molecules, which is the essential parameter to evaluate structural disorder. In contrast, 4polar-dSTORM affords quantitative structural information at the nanoscale without the need of comparative (reference) studies.

We used the 4polar-dSTORM method to investigate F-actin alignment in stress fibers, in different regions of the same bundle type and at different SF subtypes. We showed that data have to be interpreted cautiously due to the presence of possible bias sources in the measured wobbling, which we attribute to possible off-plane orientations in the measured filaments. Concentrating on mostly in-plane filaments, the results obtained with 4polar-dSTORM differed from the ones obtained with the polar-spinning disk averaged method. In particular, we found that the F-actin alignment in different SF types and at different regions of the same SF bundle was rather the same within a range  $20^\circ < \Delta\rho < 40^\circ$ . This confirms that ensemble data showing more disorder in some SFs, for instance dorsal, were probably biased by the mixture of isotropic actin populations, and by off-plane orientations. Importantly, even when we tried to perturb the F-actin alignment by stimulating contractility and slightly modifying tension (mutant cells or cell size) or by using a drug (blebbistatin) that inhibits myosin contractility, the F-actin alignment did not show considerable modifications. Since the 4polar-dSTORM method is more accurate than the polar-spinning disk method, especially in dense and tilted networks of actin, we are inclined to conclude that the single-molecule results are more realistic than the ensemble averaged results. However, that does not mean that the polar-spinning disk gave us the wrong picture of F-actin alignment at the nanoscale, since well isolated in-plane bundles such as peripheral SFs can be interpreted with ensemble approaches without expected bias. Combining our single molecule and ensemble observations, we believe that when we stimulate acto-myosin contractility, actin filaments become more present in SF bundles, which is particularly clear at peripheral SF bundles which get thicker. In our ensemble measurement, the higher number of filaments translates into an average which is highly ordered, since this experiment is mostly sensitive to in-plane filaments. On the other hand, 4polar-dSTORM at TIRF excitation shows us a more realistic picture where 3D orientations within these thick bundles play also an important

role. As a result, the fact that more filaments (aligned and not aligned) are present in thick SFs creates a result which is not necessarily more ordered, since statistically, the measured behavior is a mixture of aligned and off-plane less aligned filaments. At last, 4polar-dSTORM has demonstrated its potential in very complex actin assemblies such as lamellipodia, where well defined, non-random orientation populations could be observed along the same lines as in electron microscopy images.

Finally, it is worth to give a glimpse of the possible future work with polarization resolved techniques. First, we briefly showed in Chapter 5 that 4polar-dSTORM can be used to probe complex regions such as lamellipodia or any other other region involving crossed filaments. In particular, Lamellipodia is an actin structure poorly studied at the nanoscale and the use of 4polar-dSTORM can pave a way to orientational studies of them. Second, although we aimed at studying actin filaments, we could use the technique to probe any other 2D structure of interest (e.g., cell membranes, nuclear pores, focal adhesions molecules, etc). Third, since 4polar-dSTORM setup is an optical technique, it is possible to probe living cells by changing the label for GFP tags. For example, single particle tracking PALM could be in principle performed in the same setup of 4polar-dSTORM. This possibility would open to the opportunity to study proteins orientational properties in live cells, such as the conformational changes of integrin at the adhesion sites of cells. Fourth, the polarized spinning disk and 4polar-dSTORM setups are extendable to multi-color measurements, which should permit to study different types of protein filaments, possibly interacting together such as actin and septins. At last, it is in principle possible to obtain a full 3D unbiased orientation and wobbling information of single molecules, using similar polarized microscopy tools. That is the current work of Valentina Curcio, a PhD student in the group. She is extending the 4polar-dSTORM setup to obtain quantitative 3D information of single-molecules. This extension is based on the fact that the 3D orientation of a dipole is detectable by different emission patterns in the back focal plane of a microscope. Using different detection NAs in the arms of the 4polar-dSTORM set up has thus been used to add sensitivity to the longitudinal component of single molecule's orientations.





## Appendix A:

### Sample preparation materials and protocols

#### Fibronectin coating of CYTOO chip substrates

Note: we followed the protocol described at CYTOOchip user guide, below.

1. Take enough aliquots of Fibronectin solution (Fibronectin from bovine plasma, SIGMA F1141-2MG) to prepare a 2x concentrated solution (40µg/ml in PBS-/-), the coating solution in PBS-/- buffer.
2. Transfer the CYTOOchip to a 6-well plate with micropatterned face up (sterile).
3. Cover the CYTOOchip with 2mL of PBS-/- buffer per well to completely immerge the surface (see Figure 1).
4. Add 2mL per well of 2x Fibronectin coating solution to the well (Figure A1). Adding directly the adhesion molecule on the CYTOOchip or using a small volume of solution can locally compromise the cytophobic surface and result in aberrant cell localization outside micropatterns.

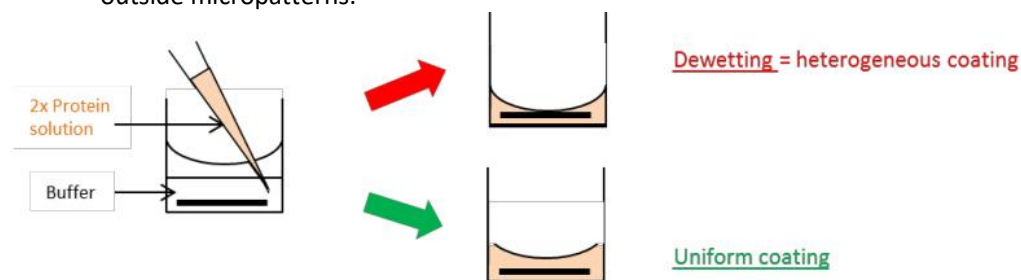


Figure A1 – Coating steps. We used PBS-/- buffer and Fibronectin (protein coating) solution. Figure taken from CYTOOchip user guide.

5. Incubate for 2h at room temperature (sterile).
6. Wash the CYTOOchips (Figure A2): make successive dilution steps in order to avoid drying during the washing steps. Never let the meniscus of the coating solution to touch the CYTOOchip surface.

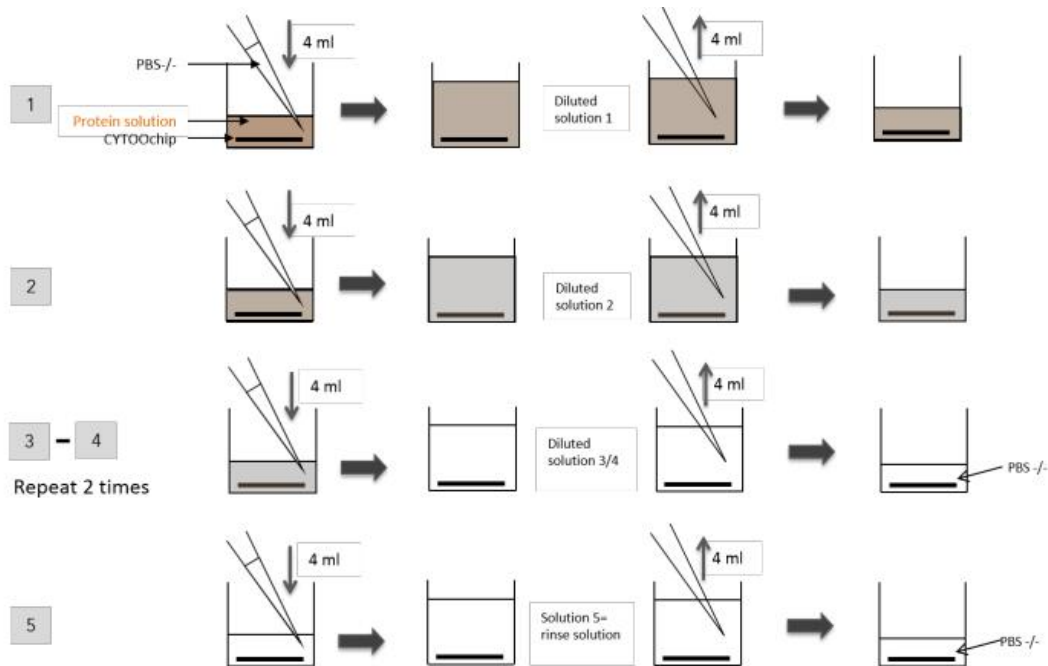


Figure A2 – Successive washing steps with the PBS-/– buffer. First add the buffer and then remove it. This procedure avoid that the meniscus touch the surface of the CYTOOchip. Figure taken from CYTOOchip user guide.

- The CYTOOchip coated with Fibronectin can be used immediately or stored in PBS-/– at 4°C for up to 3 days.

#### Permeabilization-Blocking (P/B) solution (10% BSA; 0.1% Saponin; PBS)

For 20mL P/B solution, mix in a 50mL falcon tube 200µL Saponin (10% stock), 6.666 µL Bovine Serum Albumin (30% stock), and 13.132µL PBS or DPBS -/-.

#### Cytoskeleton buffer (CB)

For 200 mL Cytoskeleton buffer, mix 10mM MES [2-(N-morpholino)ethanesulfonic acid] buffer, 150mM NaCl, 5mM EGTA (ethylene glycol tetraacetic acid), 5mM Glucose, 5mM MgCl<sub>2</sub>, adjust with NaOH to pH=6.1.

Chemical	CAS Number	Concentration (mM)	Formula Weight (D)	For 200mL
MES mohohydrate	145224-94-8	10	213,25	0,426g
NaCl	7647-14-5	150	58,44	1,75g
EGTA	67-42-5	5	380.35	0,38g
Glucose	50-99-7	5	180,16	0,18g
MgCl <sub>2</sub> hexahydrate	7791-18-6	5	203,3	0,2g
pH (NaOH for titration)	6,1			

Note: EGTA is a chelating agent more selective to Calcium ions.

## F-ACTIN staining with Formaldehyde fixation (HCHO) for Ensemble experiments

1. Thaw the number of formaldehyde aliquots you will need (based on the number of wells with coverslips) and prepare fresh two solutions: fixation and permeabilization-blocking (P/B) solutions. As soon as these solutions are ready you can bring the cells to the chemistry room. Note: paraformaldehyde was purchased from Electron Microscopy Sciences (EMS, 32% solution, catalog number 15714).
2. Aspirate the culture medium and replace with the fixation solution: 4% formaldehyde in Cytoskeleton Buffer (CB). Use 1mL for conventional coverslip (#1.5, 18mm diameter), 2 mL for storm coverslip (high precision, 24mm diameter), or 3mL for CYTOO coverslip in a 6-well dish. Incubate for 15 minutes.
3. Replace with PBS and wash by incubating 2 x 5 min. During this time prepare the humidified chambers with parafilm.
4. Remove the coverslip from the PBS solution and invert it on X  $\mu$ L drop of P/B solution onto the humidified chamber. The X  $\mu$ L volume is dependent on the coverslip size: X=100 $\mu$ L, 150 $\mu$ L or 200 $\mu$ L for conventional coverslip (18mm), storm coverslip (24mm) or CYTOO coverslip respectively. Incubate for at least 1 h.
5. Lift the coverslip by flushing gently 150  $\mu$ L of P/B under it. Transfer the coverslip to a new X  $\mu$ L drop of 1ary antibody in P/B. We mainly used rabbit-anti-phospho-FAK. In most cases 1:200 or 1:500 dilution in P/B was enough. Incubate for at least 1 h. Note: rabbit anti-P-FAK was purchased from Life technologies (Prod #44-624G, Novex<sup>TM</sup> Phospho-FAK pTyr397 antibody 10 blots, -20°C, 0,05% sodium azide).
6. Lift the coverslip by flushing gently 150  $\mu$ L of P/B under it. Transfer the coverslip to X  $\mu$ L drop of P/B solution for washing step of 10 minutes. Repeat it 3 times in total.
7. Lift the coverslip by flushing gently 150  $\mu$ L of P/B under it. Transfer the coverslip to a new X  $\mu$ L drop of 2ary antibody in P/B. We mainly used donkey-anti-rabbit-AlexaFluor647 (ThermoFisher Scientific RRID: AB\_2536183). In most cases 1:500 or 1:1000 dilution in P/B was enough. Incubate for at least 1h, protect from light with aluminium foil.
8. Lift the coverslip by flushing gently 150  $\mu$ L of P/B under it. Transfer the coverslip to X  $\mu$ L drop of P/B solution for washing step of 5 minutes. Repeat it 6 times in total, and do not forget to protect from light with aluminium foil. Prepare the phalloidin solution in P/B solution just before using (work rapidly or/and on ice to minimize methanol evaporation, put immediately the volume of phalloidin into your P/B solution otherwise the solution is dripping off the tip).
9. Lift the coverslip by flushing gently 150  $\mu$ L of P/B under it. Transfer the coverslip to X  $\mu$ L drop of phalloidin-AlexaFluor488 in P/B. For ensemble experiments, 165 nM phalloidin in P/B is enough. Incubate for at least 1h. Protect from light with aluminium foil. Note: Phalloidin-AlexaFluor488 was purchased from Invitrogen. Ref: A12379, 300u.

10. Lift the coverslip by flushing gently 150  $\mu$ L of PBS under it. Prepare 10  $\mu$ L Fluoromount on a clean slide. Take the coverslip, blot it gently and shortly against a Kimwipe to remove excess PBS and invert it on mounting medium. Protect from light and let sit for a few minutes before putting it flat in a light-tight slide box overnight at 4C.

Before imaging, make sure you rinse gently 2-3 x with water the exposed side of the coverslip to remove precipitated salt before putting it on the objective.

### **F-ACTIN staining with Formaldehyde fixation (HCHO) for STORM experiments**

1. Thaw the number of formaldehyde aliquots you will need (based on the number of wells with coverslips) and prepare fresh two solutions: fixation and permeabilization-blocking (P/B) solutions. As soon as these solutions are ready you can bring the cells to the chemistry room. Note: paraformaldehyde was purchased from Electron Microscopy Sciences (EMS, 32% solution, catalog number 15714).
2. Aspirate the culture medium and replace with the fixation solution: 4% formaldehyde in Cytoskeleton Buffer (CB). Use 1mL for conventional coverslip (#1.5, 18mm diameter), 2 mL for storm coverslip (high precision, 24mm diameter), or 3mL for CYTOO coverslip in a 6-well dish. Incubate for 15 minutes.
3. Replace with PBS and wash by incubating 2 x 5 min. During this time prepare the humidified chambers with parafilm.
4. Remove the coverslip from the PBS solution and invert it on X  $\mu$ L drop of P/B solution onto the humidified chamber. The X  $\mu$ L volume is dependent on the coverslip size: X=100 $\mu$ L, 150 $\mu$ L or 200 $\mu$ L for conventional coverslip (18mm), storm coverslip (24mm) or CYTOO coverslip respectively. Incubate for at least 1 h.
5. Lift the coverslip by flushing gently 150  $\mu$ L of P/B under it. Transfer the coverslip to a new X  $\mu$ L drop of 1ary antibody in P/B. We mainly used rabbit-anti-phospho-FAK. In most cases 1:200 or 1:500 dilution in P/B was enough. Incubate for at least 1 h. Note: rabbit anti-P-FAK was purchased from Life technologies (Prod #44-624G, Novex™ Phospho-FAK pTyr397 antibody 10 blots, -20°C, 0,05% sodium azide).
6. Lift the coverslip by flushing gently 150  $\mu$ L of P/B under it. Transfer the coverslip to X  $\mu$ L drop of P/B solution for washing step of 10 minutes. Repeat it 3 times in total.
7. Lift the coverslip by flushing gently 150  $\mu$ L of P/B under it. Transfer the coverslip to a new X  $\mu$ L drop of 2ary antibody in P/B. We mainly used donkey-anti-rabbit-AlexaFluor647 (ThermoFisher Scientific RRID: AB\_2536183). In most cases 1:500 or 1:1000 dilution in P/B was enough. Incubate for at least 1 h, protect from light with aluminium foil.
8. Lift the coverslip by flushing gently 150  $\mu$ L of P/B under it. Transfer the coverslip to X  $\mu$ L drop of P/B solution for washing step of 5 minutes. Repeat it 6 times in total, and do not forget to protect from light with aluminium foil. Prepare the phalloidin solution in P/B solution just before using (work rapidly or/and on ice to minimize methanol

evaporation, put immediately the volume of phalloidin into your P/B solution otherwise the solution is dripping off the tip).

9. Lift the coverslip by flushing gently 150  $\mu$ L of P/B under it. Transfer the coverslip to X  $\mu$ L drop of phalloidin-AlexaFluor488 in P/B. For storm experiments, use 500nM in P/B. Incubate it overnight at 4°C. Protect from light with aluminium foil. Note: Phalloidin-AlexaFluor488 was purchased from Invitrogen. Ref: A12379, 300u.
  
10. In the imaging day, prepare fresh STORM buffer and keep it on ice.
  
11. Lift the coverslip by flushing gently 150  $\mu$ L of PBS under it. Take the coverslip, blot it gently and shortly against a Kimwipe to remove excess PBS and invert it on mounting chamber (STORM or CYTOO). Fill the chamber with PBS to and close it. Check if there is any liquid leakage.
  
12. Gently clean the exposed size of the coverlip with KimWipe paper humidified with Milli-Q water, and gently dry the surface with a folded optics tissue (e.g., Thorlabs tissue).
  
13. Replace the PBS by STORM buffer just before imaging. Close the mount.

### **STORM Buffer (blinking buffer)**

Stock Materials:

- 1 M Tris-HCl, pH=8.0
- 40% Glucose (Fisher scientific G/0500/60)
- Milli-Q water
- 1M  $\beta$ -MEA in HCl, Beta-mercaptoethylamine – prepare fresh
- 100 mM Ascorbic acid (SIGMA, A7506) – prepare fresh
- 500 mM Methyl Viologen
- 200 mM COT, Cyclooctatetraene (SIGMA 138924-16T)
- 200 u/mL Pyranose oxydase (SIGMA P4234-250u)
- 230.215 u/ $\mu$ L Catalase (Merck Millipore 219001-5Mu)

Note: prepare the STORM buffer inside the chemistry hood due to toxic vapours.

1. Prepare fresh 500 $\mu$ L of  $\beta$ -MEA 1M stock solution:  
First a HCl solution 360mM with total volume 2mL to be used to solubilize 1M  $\beta$ -MEA
  - Add first 1938.2 $\mu$ L of Milli-Q water into a 2mL Eppendorf tube
  - Add 61.78 $\mu$ L of HCl concentrated onto the water very gently... total volume in the Eppendorf: 2mL. This will be used in the next step.

Solubilize  $\beta$ -MEA powder aliquots in 360mM HCl accordingly. For example: 95mg  $\beta$ -MEA /1.12mL of HCl = 1M of beta-mea stock solution. For beta-mea with N mg  $\rightarrow$  you add  $N*1.23/95$  mL of HCl.

2. Prepare fresh Ascorbic acid 100mM stock solution. Ideally: 17,6mg for 1 mL Milli-Q.

**3.** For 10mL STORM buffer, mix the following materials in the following order in a 15mL Falcon tube:

- 1) 1.0 mL of Tris-HCl 1M, pH=8,0
  - 2) 2.5 mL Glucose 40%
  - 3) 5.512 mL of Milli-Q H<sub>2</sub>O
  - 4) 500µL of β-MEA /HCl 1M (check pH after resuspension: range 8,5-9,0)
  - 5) 100µL of Ascorbic Acid 100mM
  - 6) 20,0 µL of Methyl Viologen 500mM
  - 7) 100,0 µL COT 200mM
  - 8) 250,0 µL Pyranose Oxydase 200u/mL
  - 9) 17.4 µL of Catalase 230,2 u/µL
- Total: 10 mL

Note: After mixing, STORM buffer has the following final concentrations

- |                      |                           |
|----------------------|---------------------------|
| - 100mM Tris-HCl     | - 1mM Methyl Viologen     |
| - 10% Glucose        | - 2mM COT                 |
| - 50 mM β-MEA in HCl | - 5 u/mL Pyranose oxidase |
| - 1mM Ascorbic acid  | - 400u/mL Catalase        |

**4.** Clarification (to avoid dust particles):

Equally distribute the STORM buffer volume in 1mL Eppendorf tubes. Equally oriented the tubes in the centrifuge. Centrifuge at max speed 16,100g for 2min at 25°C. As soon as it finishes, take ≈920-950µL supernatant (avoid taking pellet particles and aggregates).

**5.** Wait for 15min before using the storm buffer.

## Appendix B:

### dSTORM acquisition parameters

The typical dSTORM acquisition parameters used with Andor Ixon888 EMCCD camera

#### Camera setup:

- Acquisition mode: kinetic
- Triggering: internal
- Readout Mode: image

#### Timings:

- Exposure time: 100 ms
- Nb of accumulations: 1
- Kinetic Series Length: 20k-50k frames
- Frame Transfer: check (initial record in the RAM before the disk)

#### Vertical pixel shift

- Shift speed ( $\mu$ s): [1,13]
- Vertical clock V: normal

#### Horizontal pixel shift

- Readout rate: 30MHZ at 16bit
- Pre-amplifier gain: Gain 2
- Output amplifier: Electron Multiplying

#### Electron Multiplying (EM) gain:

- EM gain level: 300

#### Saving files:

- Format: .tiff
- Tiff format: 16bit gray





## Appendix C:

### PSI-maps of Naïve U2OS cells on CYTOO chips

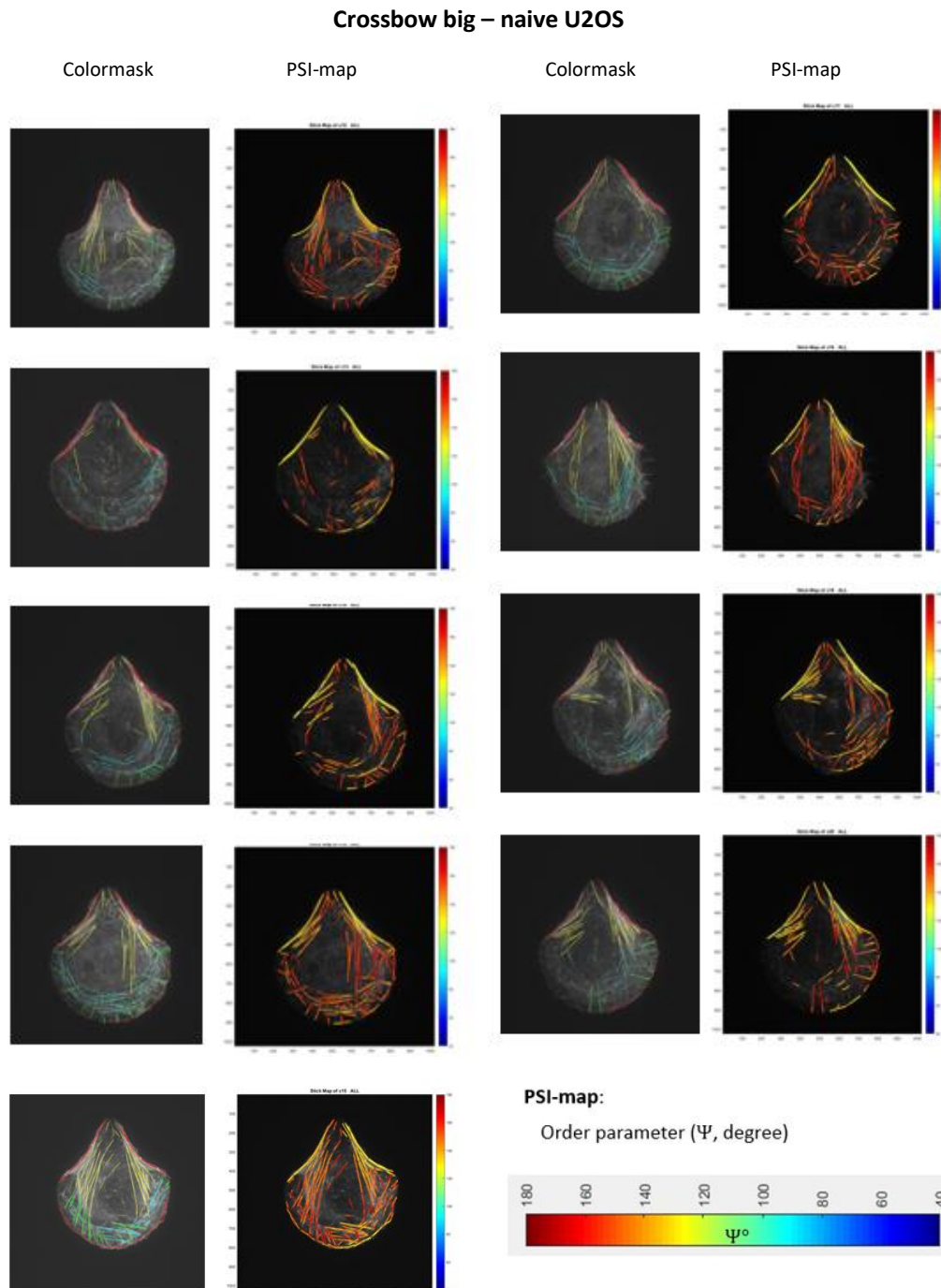


Figure C1 – Colormask and PSI-maps of **Crossbow-BIG CYTOO patterns**. On the left side, the colormask SF colors are: red (peripheral), yellow (ventral), green(dorsal), light blue(transverse arcs), dark blue(other). On the right side, the PSI-map with the ALL SF mask, the colorcode of the PSI-map is the matlab-defined “jet”, rescaled from 0-180 to 40-180.

### Crossbow medium – naive U2OS

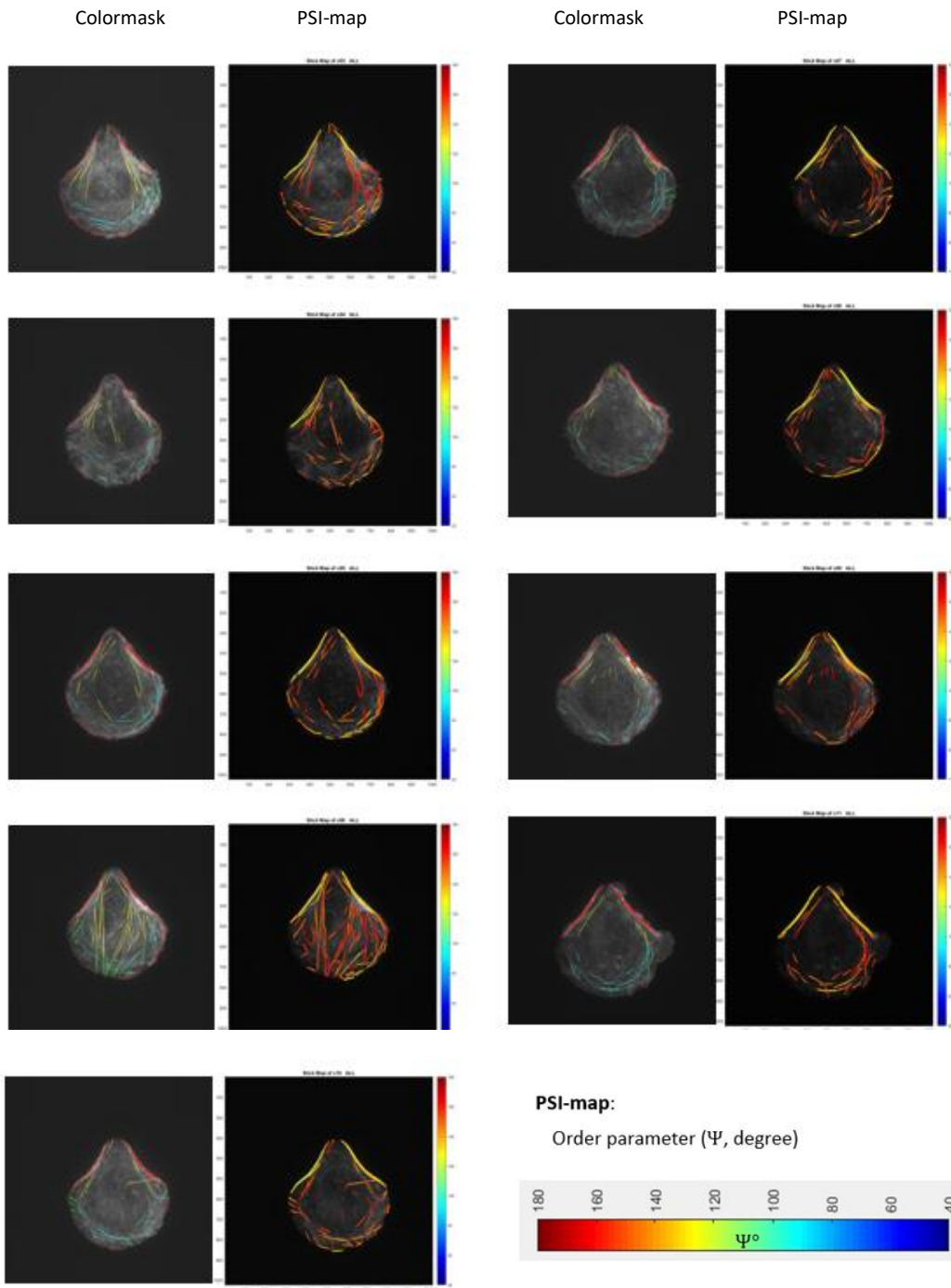


Figure C2 – Colormask and PSI-maps of **Crossbow-medium CYTOO patterns**. On the left side, the colormask SF colors are: red (peripheral), yellow (ventral), green(dorsal), light blue(transverse arcs), dark blue(other). On the right side, the PSI-map with the ALL SF mask, the colorcode of the PSI-map is the matlab-defined “jet”, rescaled from 0-180 to 40-180.

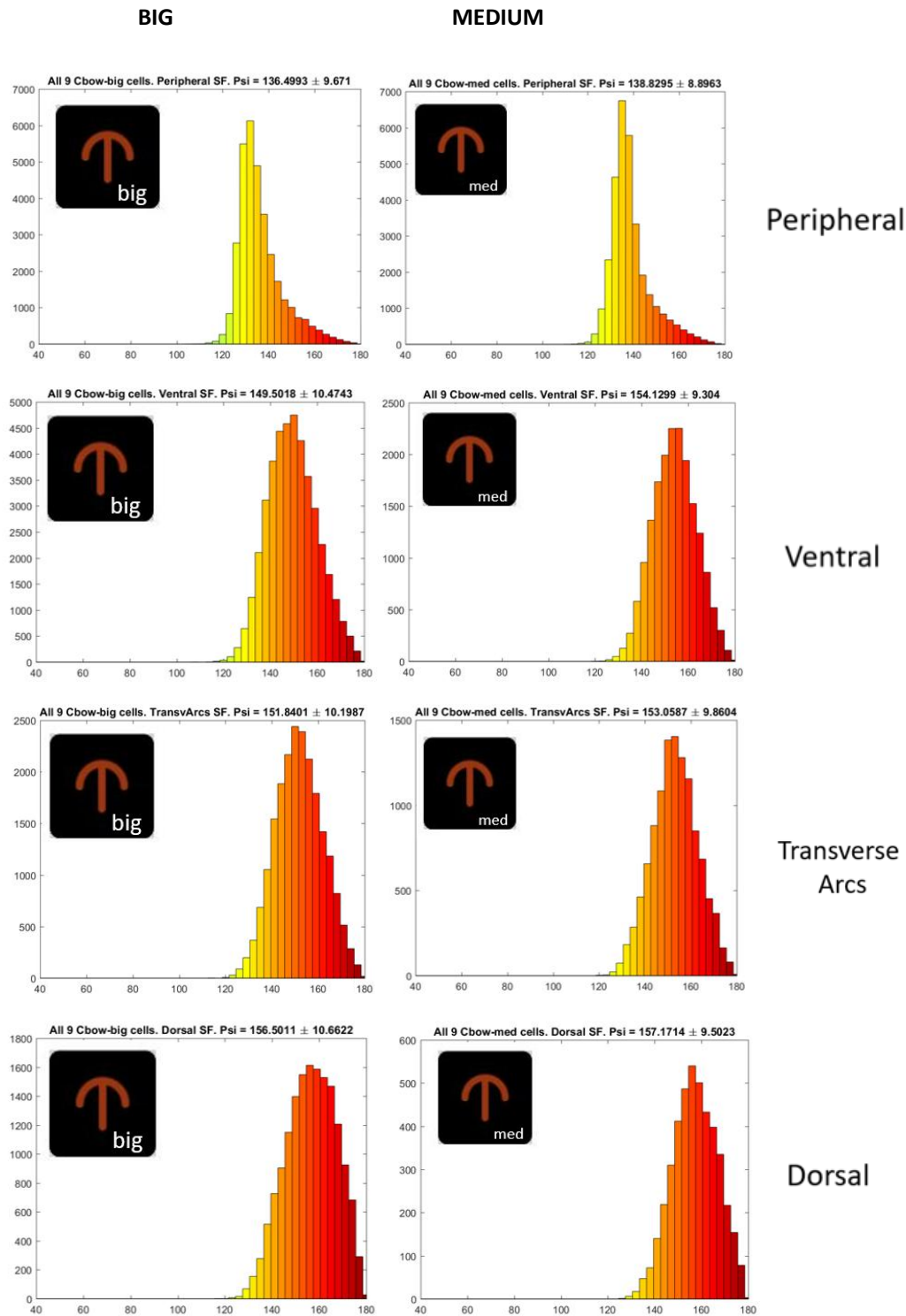


Figure C3 –  $\Psi$  histograms (counts vs psi values in between  $40^\circ < \Psi < 180^\circ$ ), comparing the SFs of big (left) and medium (right) crossbow patterned cells. The psi histogram has the same colorcode of the PSI-map (jet-40-180). Considering the psi values along these 4 SF types, we see a trend: peripheral SF bundles are more ordered than any other type of SFs. For both medium and big sizes, the trend were peripheral SF < ventral SF and/or transverse arcs < dorsal SF. Note that, among all these 4 types of SF, the dorsal SF are considered “not contractile” bundles, suggesting that contractility (i.e., the presence of NMII) might have a role in F-actin alignment in contractile bundles. Moreover,

considering the cell size, bigger crossbow cells have slightly more ordered (a shift to more ordered values less than 5°) SF bundles than medium size cells.

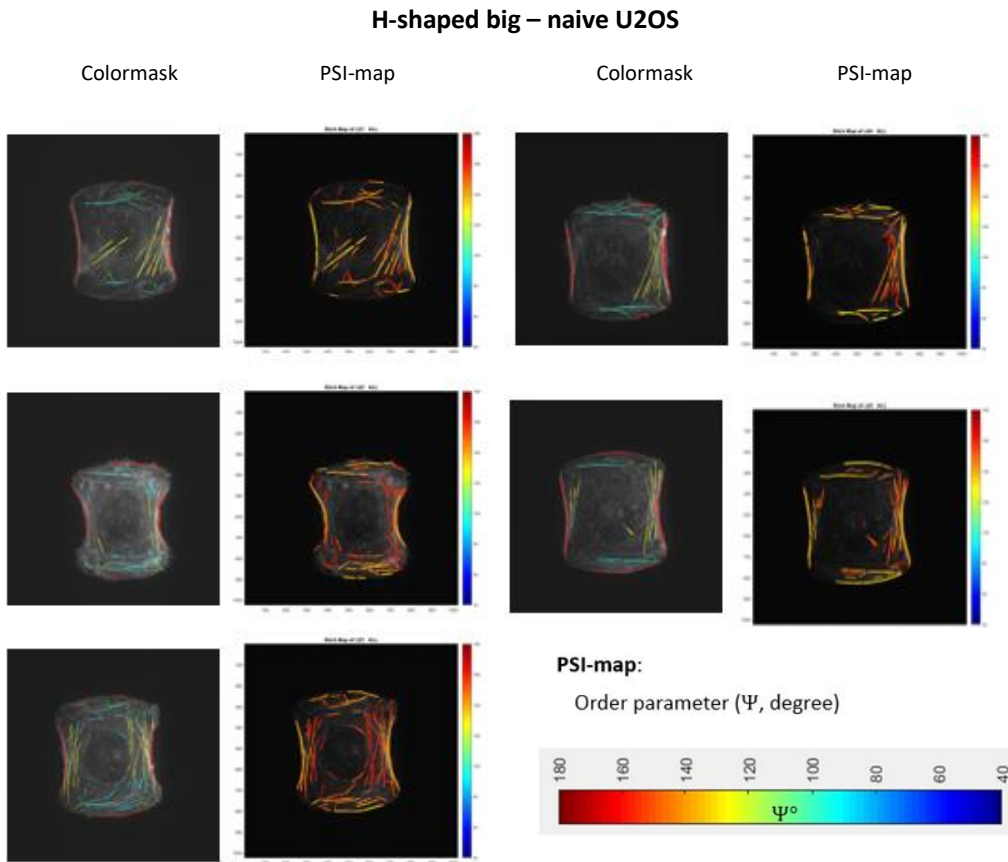
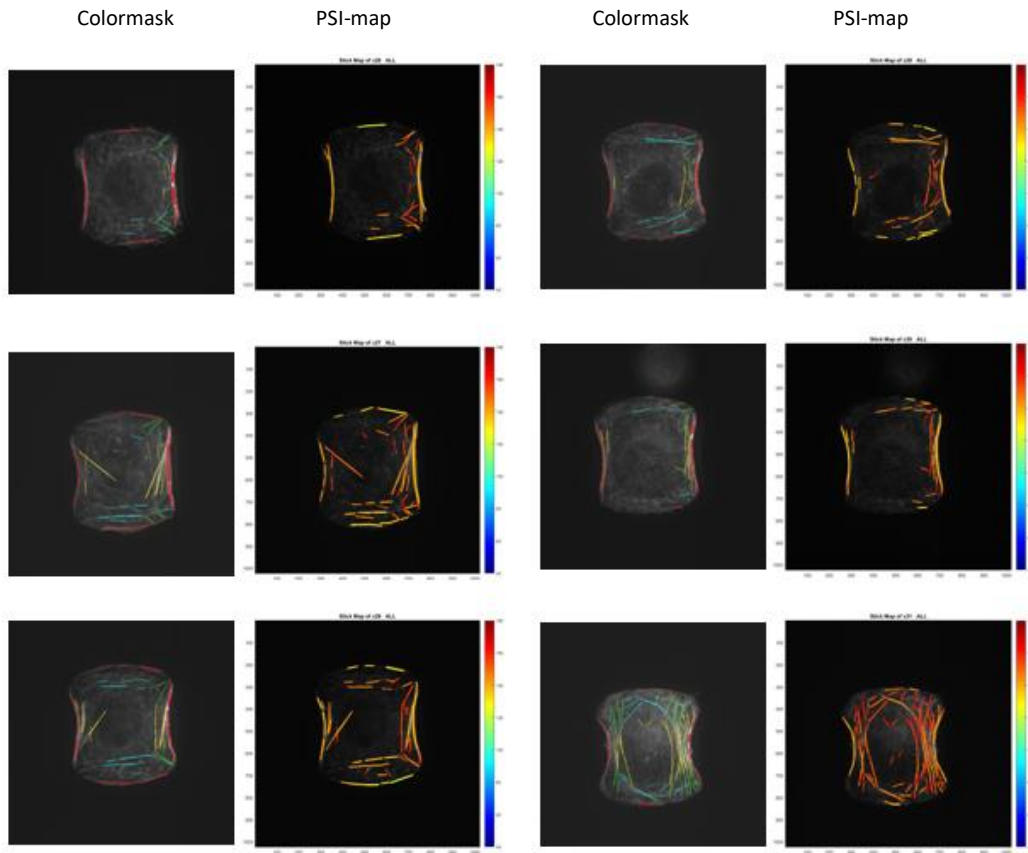


Figure C4 – Colormask and PSI-maps of **H-shaped-BIG CYTOO patterns**. On the left side, the colormask SF colors are: red (peripheral), yellow (ventral), green(dorsal), light blue(transverse arcs), dark blue(other). On the right side, the PSI-map with the ALL SF mask, the colorcode of the PSI-map is the matlab-defined “jet”, rescaled from 0-180 to 40-180.

### H-shaped medium – naive U2OS



#### PSI-map:

Order parameter ( $\Psi$ , degree)



Figure C5 – Colormask and PSI-maps of **H-shaped-medium CYTOO patterns**. On the left side, the colormask SF colors are: red (peripheral), yellow (ventral), green(dorsal), light blue(transverse arcs), dark blue(other). On the right side, the PSI-map with the ALL SF mask, the colorcode of the PSI-map is the matlab-defined “jet”, rescaled from 0-180 to 40-180.

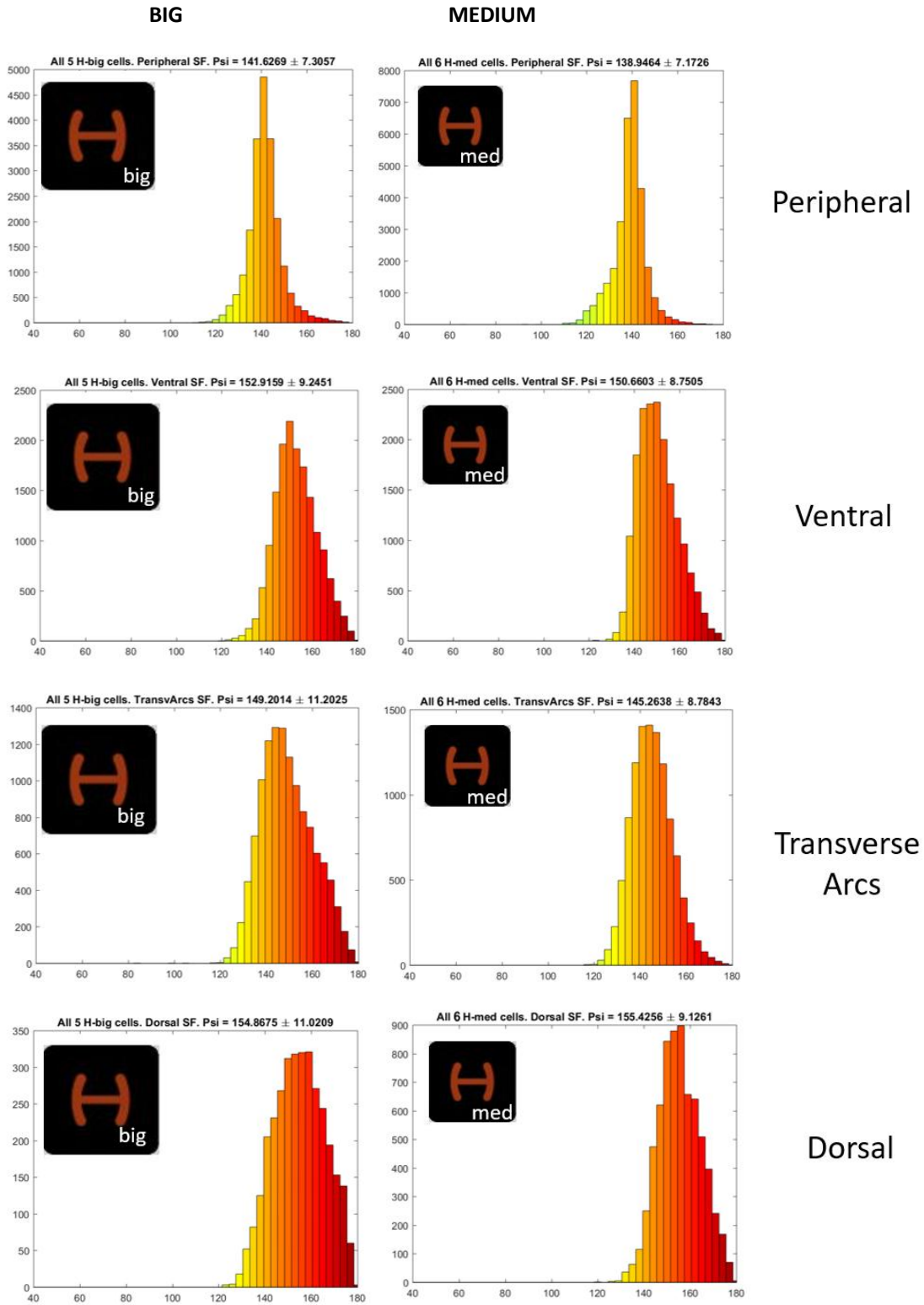


Figure C6 – PSI histograms (counts vs psi values in between  $40^\circ < \Psi < 180^\circ$ ), comparing the SFs of big (left) and medium (right) H-shaped patterned cells. The psi histogram has the same colorcode of the PSI-map (jet-40-180). Considering



the psi values along these 4 SF types, we see the same trend as in crossbow: peripheral SF bundles are more ordered than any other type of SFs. However, considering the size, it has the contrary trend seen in crossbow: the smaller H-shaped cells have slightly more ordered (a slight shift of less than 5° to narrower cone aperture values) SF bundles than big size cells.

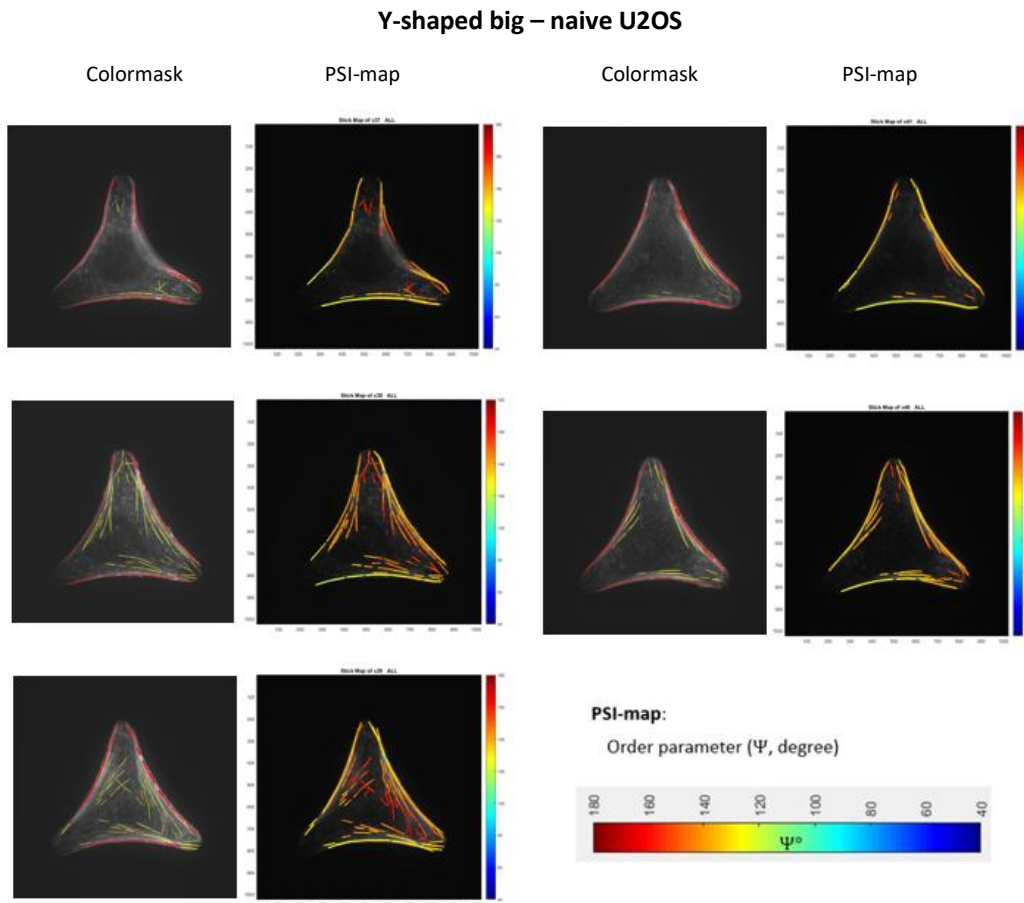


Figure C7 – Colormask and PSI-maps of **Y-shaped-BIG CYTOO patterns**. On the left side, the colormask SF colors are: red (peripheral), yellow (ventral), green(dorsal), light blue(transverse arcs), dark blue(other). On the right side, the PSI-map with the ALL SF mask, the colorcode of the PSI-map is the matlab-defined “jet”, rescaled from 0-180 to 40-180.

### Y-shaped medium – naive U2OS

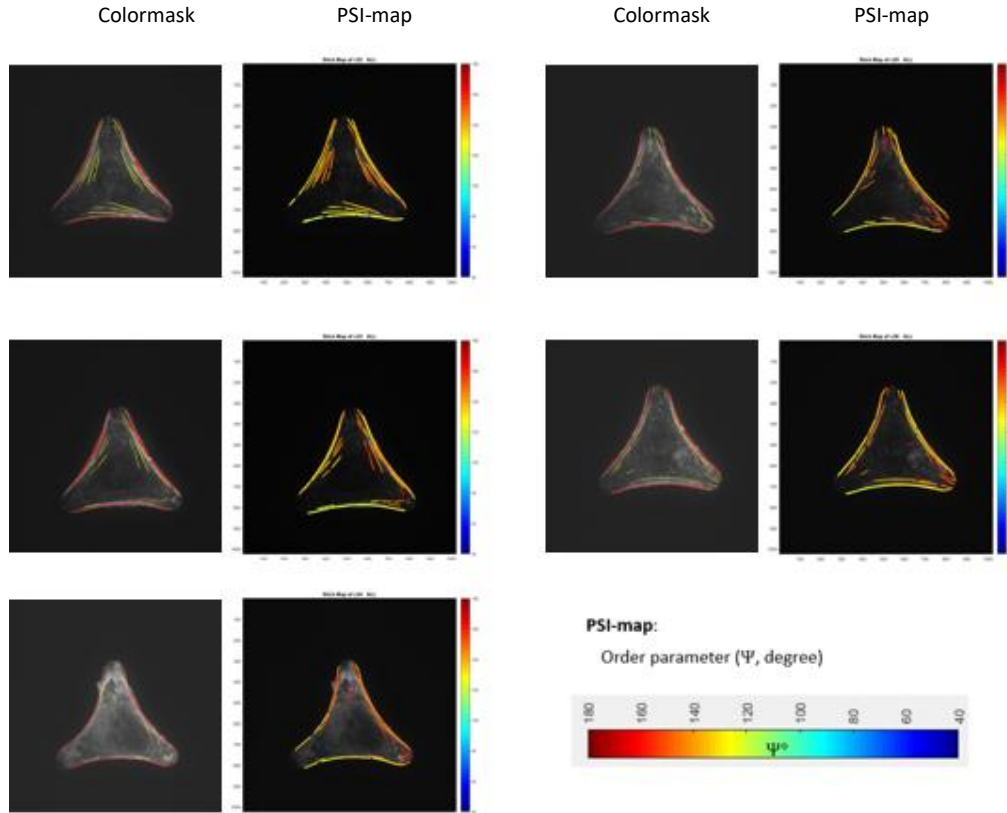


Figure C8 – Colormask and PSI-maps of **Y-shaped-medium CYTOO patterns**. On the left side, the colormask SF colors are: red (peripheral), yellow (ventral), green(dorsal), light blue(transverse arcs), dark blue(other). On the right side, the PSI-map with the ALL SF mask, the colorcode of the PSI-map is the matlab-defined “jet”, rescaled from 0-180 to 40-180.

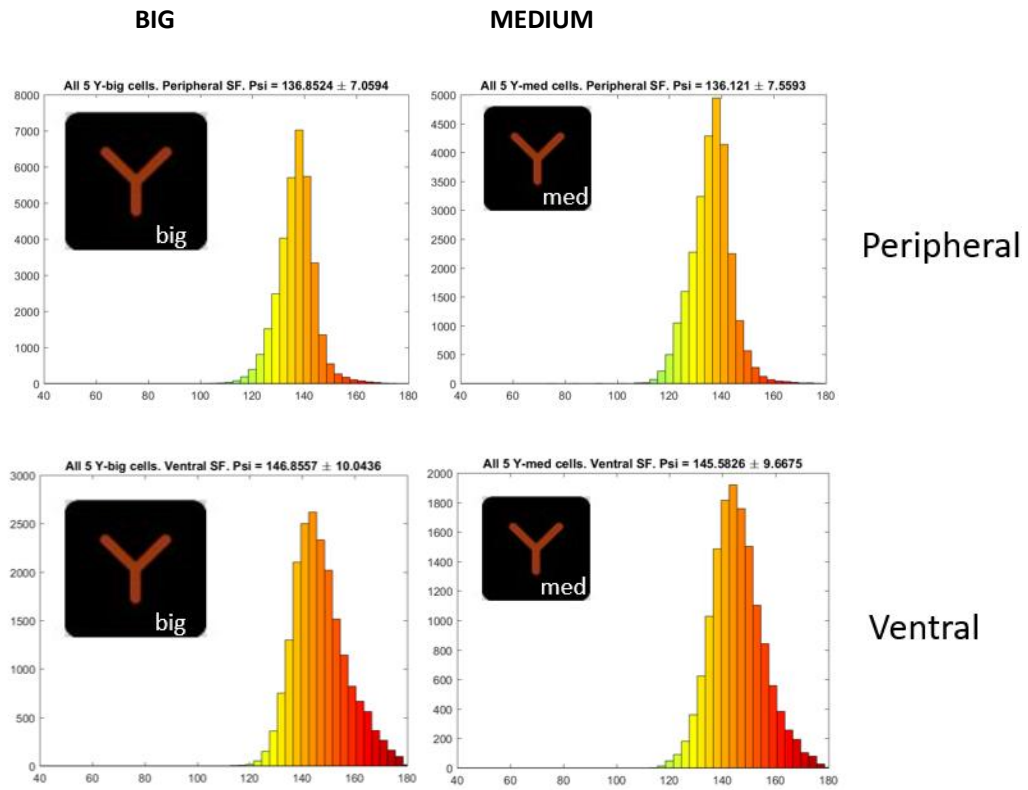


Figure C9 – PSI histograms (counts vs psi values in between  $40^\circ < \Psi < 180^\circ$ ), comparing the SFs of big (left) and medium (right) Y-shaped patterned cells. Note that size of the cell affected very little the histogram of PSIs, but the SF type



## Bibliography

- [1] Bray D. Cell movements, from molecules to motility. 2<sup>nd</sup> ed. 2001. Garland publishing group.
- [2] Alberts B, et al. Molecular biology of the cell. 7<sup>th</sup> ed. 2017. Artmed. Garland publishing group.
- [3] Jockusch BM. The actin cytoskeleton. Handbook of experimental pharmacology, vol. 235. 2017. Springer International Publishing Group. DOI 10.1007/978-3-319-46371-1
- [4] Garrels JI, Gibson W. Identification and characterization of multiple forms of actin. Cell 9:793–805 (1976).
- [5] Elzinga M, et al. Complete amino-acid sequence of actin of rabbit skeletal muscle. Proc. Nat. Acad. Sci. USA Vol. 70, No. 9, pp. 2687-2691, September 1973.
- [6] Collins, JH, Elzinga, M. The Primary Structure of Actin from Rabbit Skeletal Muscle. The journal of biological chemistry. Vol.250, No. 15. Aug 10, pp.5915-5920. (1975).
- [7] Lodish H, et al. Molecular Cell Biology. 7<sup>th</sup> edition. W. H. Freeman and Company NY. (2013).
- [8] Small J-V, Rottner K, Hahne P, & Anderson KI (1999). Visualising the Actin Cytoskeleton. Microsc. Res. Tech (Vol. 47).
- [9] Cramer LP, Siebert M, Mitchison TJ. Identification of novel graded polarity actin filament bundles in locomoting heart fibroblasts: Implications for the generation of motile force. J Cell Biol. 1997;136(6):1287–305.
- [10] Kanchanawong P, Shtengel G, Pasapera A, et al. Nanoscale architecture of integrin-based cell adhesions. Nature 468, 580–584 (2010). <https://doi.org/10.1038/nature09621>
- [11] Svitkina T. The actin cytoskeleton and actin-based motility. Cold Spring Harb Perspect Biol. 2018 Jan 1;10(1).
- [12] Vallenius T. Actin stress fibre subtypes in mesenchymal-migrating cells. Open Biol. 2013;3(JUN). <http://dx.doi.org/10.1098/rsob.130001>
- [13] Tojkander S, Gateva G, Lappalainen P. Actin stress fibers - Assembly, dynamics and biological roles. J Cell Sci. 2012;125(8):1855–64. <http://jcs.biologists.org/cgi/doi/10.1242/jcs.098087>
- [14] Pellegrin S, Mellor H. Actin stress fibers. J Cell Sci. 2007; 120(20):3491–9. <http://jcs.biologists.org/cgi/doi/10.1242/jcs.018473>
- [15] Livne A, Geiger B. The inner workings of stress fibers - From contractile machinery to focal adhesions and back. J Cell Sci. 2016;129(7):1293–304.
- [16] Hotulainen P, Lappalainen P. Stress fibers are generated by two distinct actin assembly mechanisms in motile cells. J Cell Biol. 2006;173(3):383–94. DOI: 10.1083/jcb.200511093.
- [17] Tojkander S, Gateva G, Husain A, Krishnan R, Lappalainen P. Generation of contractile actomyosin bundles depends on mechanosensitive actin filament assembly and disassembly. Elife. 2015;4:1–28.

- [18] Totsukawa G, Yamakita Y, Yamashiro S, Hartshorne DJ, Sasaki Y, Matsumura F. Distinct roles of ROCK (Rho-kinase) and MLCK in spatial regulation of MLC phosphorylation for assembly of stress fibers and focal adhesions in 3T3 fibroblasts. *J Cell Biol.* 2000;150(4):797–806.
- [19] Katoh K, Kano Y, Amano M, Kaibuchi K, Fujiwara K. Stress fiber organization regulated by MLCK and Rho-kinase in cultured human fibroblasts. *Am J Physiol - Cell Physiol.* 2001;280(6 49-6):1669–79.
- [20] Katoh K, Kano Y, Noda Y. Rho-associated kinase-dependent contraction of stress fibres and the organization of focal adhesions. *J R Soc Interface.* 2011;8(56):305–11.
- [21] Tanner K, Boudreau A, Bissell MJ, Kumar S. Dissecting regional variations in stress fiber mechanics in living cells with laser nanosurgery. *Biophys J.* 2010;99(9):2775–83. Available from: <http://dx.doi.org/10.1016/j.bpj.2010.08.071>
- [22] Kassianidou E, Hughes JH, Kumar S. Activation of ROCK and MLCK tunes regional stress fiber formation and mechanics via preferential myosin light chain phosphorylation. *Mol Biol Cell.* 2017;28(26):3832–43.
- [23] Kassianidou E, Kumar S. A biomechanical perspective on stress fiber structure and function. *Biochim Biophys Acta - Mol Cell Res.* 2015;1853(11):3065–74. Available from: <http://dx.doi.org/10.1016/j.bbamcr.2015.04.006>
- [24] Burridge K, Wittchen ES. The tension mounts: Stress fibers as force-generating mechanotransducers. *J Cell Biol.* 2013;200(1):9–19.
- [25] Lu L, Oswald SJ, Ngu H, Yin FCP. Mechanical properties of actin stress fibers in living cells. *Biophys J.* 2008;95(12):6060–71.
- [26] Kassianidou E, Brand CA, Schwarz US, Kumar S. Geometry and network connectivity govern the mechanics of stress fibers. *Proc Natl Acad Sci U S A.* 2017;114(10):2622–7.
- [27] Soiné JRD, Brand CA, Stricker J, Oakes PW, Gardel ML, Schwarz US. Model-based Traction Force Microscopy Reveals Differential Tension in Cellular Actin Bundles. *PLoS Comput Biol.* 2015;11(3):1–16.
- [28] Théry M, Pépin A, Dressaire E, Chen Y, Bornens M. Cell distribution of stress fibres in response to the geometry of the adhesive environment. *Cell Motil Cytoskeleton.* 2006;63(6):341–55.
- [29] Rigato A, Rico F, Eghiaian F, Piel M, Scheuring S. Atomic Force Microscopy Mechanical Mapping of Micropatterned Cells Shows Adhesion Geometry-Dependent Mechanical Response on Local and Global Scales. *ACS Nano.* 2015;9(6):5846–56.
- [30] Oakes PW, Banerjee S, Marchetti MC, Gardel ML. Geometry regulates traction stresses in adherent cells. *Biophys J.* 2014;107(4):825–33. Available from: <http://dx.doi.org/10.1016/j.bpj.2014.06.045>
- [31] Mandal K, Wang I, Vitiello E, Orellana LAC, Balland M. Cell dipole behaviour revealed by ECM sub-cellular geometry. *Nat Commun.* 2014;5.

- [32] Tan JL, Tien J, Pirone DM, Gray DS, Bhadriraju K, Chen CS. Cells lying on a bed of microneedles: An approach to isolate mechanical force. *Proc Natl Acad Sci U S A*. 2003;100(4):1484–9.
- [33] Peterson LJ, Rajfur Z, Maddox AS, Freel CD, Chen Y, Edlund M, et al. Simultaneous Stretching and Contraction of Stress Fibers In Vivo. *Mol Biol Cell* [Internet]. 2004 Jul;15(7):3497–508. Available from: <https://www.molbiolcell.org/doi/10.1091/mbc.e03-09-0696>
- [34] Griffiths DJ. *Introduction to Electrodynamics*. 3rd ed. Prentice Hall. January 9, 1999. ISBN-10: 013805326X
- [35] EMANIN free software. 2019. [cited 2019 Mar 07]. Software available from: <http://emanim.szialab.org>
- [36] Labman. Polarization. [Image on Internet]. 2019. [cited 2019 Mar 07]. Available from: <http://labman.phys.utk.edu/phys222core/modules/m6/polarization.html>
- [37] Frigault MM, Lacoste J, Swift JL, Brown CM. Live-cell microscopy - Tips and tools. *J Cell Sci*. 2009;122(6):753–67.
- [38] Hell SW, Sahl SJ, Bates M, Zhuang X, Heintzmann R, Booth MJ, et al. The 2015 super-resolution microscopy roadmap. *J Phys D Appl Phys*. 2015;48(44):443001. Available from: <http://dx.doi.org/10.1088/0022-3727/48/44/443001>
- [39] Manzo C, Garcia-Parajo MF. A review of progress in single particle tracking: From methods to biophysical insights. *Reports Prog Phys*. 2015;78(12):124601. Available from: <http://dx.doi.org/10.1088/0034-4885/78/12/124601>
- [40] Dempsey GT, Vaughan JC, Chen KH, Bates M, Zhuang X. Evaluation of fluorophores for optimal performance in localization-based super-resolution imaging. *Nat Methods*. 2011;8(12):1027–40.
- [41] Crivat G, Taraska JW. Imaging proteins inside cells with fluorescent tags. *Trends Biotechnol*. 2012;30(1):8–16. Available from: <http://dx.doi.org/10.1016/j.tibtech.2011.08.002>
- [42] Giepmans BNG, Adams SR, Ellisman MH, Tsien RY. The fluorescent toolbox for assessing protein location and function. *Science* (80- ). 2006;312(5771):217–24.
- [43] Lakowicz JR. *Principles of Fluorescence Spectroscopy*. 3rd ed. Springer. September 15, 2006. ISBN-10: 0387312781.
- [44] Valeur B, Berberan-Santos MN. *Molecular Fluorescence: Principles and Applications*. 2nd ed. Wiley-VCH. May 29, 2012. ISBN-10: 3527328378.
- [45] Turro NJ. *Principles of Molecular Photochemistry: An Introduction*. University Science Books January 16, 2009. ASIN: B00QCNREIU.
- [46] Lichtman JW, Conchello JA. Fluorescence microscopy. *Nat Methods*. 2005;2(12):910–9.
- [47] Hoefling M, Grubmüller H. In silico FRET from simulated dye dynamics. *Comput Phys Commun*. 2013;184(3):841–52. Available from: <http://dx.doi.org/10.1016/j.cpc.2012.10.018>



- [48] Dominik Spiegel J, Fulle S, Kleinschmidt M, Gohlke H, Marian CM. Failure of the IDA in FRET Systems at Close Inter-Dye Distances Is Moderated by Frequent Low  $\kappa_2$  Values. *J Phys Chem B*. 2016;120(34):8845–62. Available from: <http://dx.doi.org/10.1021/acs.jpcc.6b05754>
- [49] Sakurai JJ, Napolitano JJ. *Modern Quantum Mechanics*. 2nd ed. Pearson. July 14, 2010. ISBN-10: 0805382917
- [50] Forkey JN, Quinlan ME, Goldman YE. Protein structural dynamics by single-molecule fluorescence polarization. *Prog Biophys Mol Biol*. 2000;74(1–2):1–35.
- [51] Jackson, JD (1999). *Classical Electrodynamics*, 3rd Ed. Wiley. ISBN-10: 9780471309321
- [52] Wang X. Confocal angle resolved linear dichroism microscopy for structural fluorescence imaging. PhD thesis, École Centrale de Marseille, 2013.
- [53] Hecht E. *Optics*. 4th ed. Addison-Wesley. August 12, 2001. ISBN-10: 9780805385663
- [54] Axelrod D. Carbocyanine dye orientation in red cell membrane studied. *Biophys J*. 1979;26(June):557–73. Available from: <https://www.ncbi.nlm.nih.gov/pmc/articles/PMC1328570/pdf/biophysj00290-0210.pdf>
- [55] Chen RF, Bowman RL. Fluorescence polarization: Measurement with ultraviolet-polarizing filters in a spectrophotofluorometer. *Science* (80- ). 1965;147(3659):729–32.
- [56] Rusinova E, Tretyachenko-Ladokhina V, Vele OE, Senear DF, Alexander Ross JB. Alexa and Oregon Green dyes as fluorescence anisotropy probes for measuring protein-protein and protein-nucleic acid interactions. *Anal Biochem*. 2002;308(1):18–25.
- [57] Brasselet S, Ferrand P, Kress A, Wang X, Ranchon H, Gasecka A. Imaging Molecular Order in Cell Membranes by Polarization-Resolved Fluorescence Microscopy. 2012;311–37.
- [58] Kress A, Wang X, Ranchon H, Savatier J, Rigneault H, Ferrand P, et al. Mapping the local organization of cell membranes using excitation- polarization-resolved confocal fluorescence microscopy. *Biophys J*. 2013;105(1):127–36.
- [59] Cruz CAV, Shaban HA, Kress A, Bertaux N, Monneret S, Mavrikis M, et al. Quantitative nanoscale imaging of orientational order in biological filaments by polarized superresolution microscopy. *Proc Natl Acad Sci U S A*. 2016;113(7):E820–8.
- [60] Shaban HA, Valades-Cruz CA, Savatier J, Brasselet S. Polarized super-resolution structural imaging inside amyloid fibrils using Thioflavine T. *Sci Rep*. 2017;7(1):1–10. Available from: <http://dx.doi.org/10.1038/s41598-017-12864-9>
- [61] Loison O, Weitkunat M, Kaya-Çopur A, Nascimento Alves C, Matzat T, Spletter ML, et al. Polarization-resolved microscopy reveals a muscle myosin motor-independent mechanism of molecular actin ordering during sarcomere maturation. Taylor G, editor. *PLOS Biol*. 2018 Apr 27;16(4):e2004718. Available from: <https://dx.plos.org/10.1371/journal.pbio.2004718>
- [62] Mavrikis M, Azou-Gros Y, Tsai FC, Alvarado J, Bertin A, Iv F, et al. Septins promote F-actin ring formation by crosslinking actin filaments into curved bundles. *Nat Cell Biol*. 2014;16(4):322–34.

- [63] Florine-Casteel K. Phospholipid order in gel- and fluid-phase cell-size liposomes measured by digitized video fluorescence polarization microscopy. Vol. 57, Biophysical Journal. 1990. p. 1199–215.
- [64] ZEISS campus online. Introduction to spinning disk confocal microscopy. [Image on Internet]. 2019. [cited 2019 Mar 07]. Available from: <http://zeiss-campus.magnet.fsu.edu/articles/spinningdisk/introduction.html>
- [65] Zhanghao K, Gao J, Jin D, Zhang X, Xi P. Super-resolution fluorescence polarization microscopy. J Innov Opt Health Sci. 2018;11(1):1–12.
- [66] Boyd RW. Nonlinear optics. 3rd ed. Elsevier Science & Technology. April 11, 2007. ISBN-10: 8131222926
- [67] Sarri B, Chen X, Canonge R, Grégoire S, Formanek F, Galey JB, et al. In vivo quantitative molecular absorption of glycerol in human skin using coherent anti-Stokes Raman scattering (CARS) and two-photon auto-fluorescence. J Control Release. 2019;308(February):190–6. Available from: <https://doi.org/10.1016/j.jconrel.2019.07.018>
- [68] Sarri B, Poizat F, Heuke S, Wojak J, Franchi F, Caillol F, et al. Stimulated Raman histology: one to one comparison with standard hematoxylin and eosin staining. Biomed Opt Express. 2019;10(10):5378.
- [69] Gasecka A, Han TJ, Favard C, Cho BR, Brasselet S. Quantitative imaging of molecular order in lipid membranes using two-photon fluorescence polarimetry. Biophys J. 2009;97(10):2854–62. Available from: <http://dx.doi.org/10.1016/j.bpj.2009.08.052>
- [70] Hell SW. Far-field optical nanoscopy. Springer Ser Chem Phys. 2010;96(May):368–98.
- [71] Rocheleau J V., Edidin M, Piston DW. Intrasequence GFP in class I MHC molecules, a rigid probe for fluorescence anisotropy measurements of the membrane environment. Biophys J [Internet]. 2003;84(6):4078–86. Available from: [http://dx.doi.org/10.1016/S0006-3495\(03\)75133-9](http://dx.doi.org/10.1016/S0006-3495(03)75133-9)
- [72] Borejdo J, Burlacu S. Orientation of actin filaments during motion in in vitro motility assay. Biophys J [Internet]. 1994;66(5):1319–27. Available from: [http://dx.doi.org/10.1016/S0006-3495\(94\)80946-4](http://dx.doi.org/10.1016/S0006-3495(94)80946-4)
- [73] Wang X, Kress A, Brasselet S, Ferrand P. High frame-rate fluorescence confocal angle-resolved linear dichroism microscopy. Rev Sci Instrum. 2013;84(5).
- [74] DeMay BS, Noda N, Gladfelter AS, Oldenbourg R. Rapid and quantitative imaging of excitation polarized fluorescence reveals ordered septin dynamics in live yeast. Biophys J. 2011;101(4):985–94. Available from: <http://dx.doi.org/10.1016/j.bpj.2011.07.008>
- [75] DeMay BS, Bai X, Howard L, Occhipinti P, Meseroll RA, Spiliotis ET, et al. Septin filaments exhibit a dynamic, paired organization that is conserved from yeast to mammals. J Cell Biol. 2011;193(6):1065–81.
- [76] He W. Etude des propriétés structurales de cellules biologiques par microscopie optique résolue en polarisation en trois dimensions. PhD thesis, Aix-Marseille Université, 2016.

- [77] Kress, A. Probing molecular orientational order of lipid reporters and MHC Class I protein in cell membranes using polarization-resolved fluorescence imaging. PhD Thesis, Aix-Marseille Université, 2011.
- [78] Vrabioiu AM, Mitchison TJ. Structural insights into yeast septin organization from polarized fluorescence microscopy. *Nature*. 2006;443(7110):466–9.
- [79] Vrabioiu AM, Mitchison TJ. Symmetry of Septin Hourglass and Ring Structures. *J Mol Biol*. 2007;372(1):37–49.
- [80] Mattheyses AL, Kampmann M, Atkinson CE, Simon SM. Fluorescence anisotropy reveals order and disorder of protein domains in the nuclear pore complex. *Biophys J*. 2010;99(6):1706–17. Available from: <http://dx.doi.org/10.1016/j.bpj.2010.06.075>
- [81] Kampmann M, Atkinson CE, Mattheyses AL, Simon SM. Mapping the orientation of nuclear pore proteins in living cells with polarized fluorescence microscopy. *Nat Struct Mol Biol*. 2011;18(6):643–9. Available from: <http://dx.doi.org/10.1038/nsmb.2056>
- [82] Nordenfelt P, Moore TI, Mehta SB, Kalappurakkal JM, Swaminathan V, Koga N, et al. Direction of actin flow dictates integrin LFA-1 orientation during leukocyte migration. *Nat Commun*. 2017;8(1). Available from: <http://dx.doi.org/10.1038/s41467-017-01848-y>
- [83] Shroder DY, Lippert LG, Goldman YE. Single molecule optical measurements of orientation and rotations of biological macromolecules. *Methods Appl Fluoresc*. 2016;4(4):042004. Available from: <http://dx.doi.org/10.1088/2050-6120/4/4/042004>
- [84] Karedla N, Stein SC, Hähnel D, Gregor I, Chizhik A, Enderlein J. Simultaneous measurement of the three-dimensional orientation of excitation and emission dipoles. *Phys Rev Lett*. 2015;115(17).
- [85] Sick B, Hecht B, Novotny L. Orientational imaging of single molecules by annular illumination. *Phys Rev Lett*. 2000;85(21):4482–5.
- [86] Forkey JN, Quinlan ME, Shaw MA, Corrie JET, Goldman YE. Three-dimensional structural dynamics of myosin V by single-molecule fluorescence polarization. *Nature*. 2003;422(6930):399–404.
- [87] Forkey JN, Quinlan ME, Goldman YE. Measurement of single macromolecule orientation by total internal reflection fluorescence polarization microscopy. *Biophys J*. 2005;89(2):1261–71.
- [88] Backer AS, Biebricher AS, King GA, Wuite GJL, Heller I, Peterman EJJ. Single-molecule polarization microscopy of DNA intercalators sheds light on the structure of S-DNA. *Sci Adv*. 2019;5(3).
- [89] Backlund MP, Lew MD, Backer AS, Sahl SJ, Moerner WE. The role of molecular dipole orientation in single-molecule fluorescence microscopy and implications for super-resolution imaging. *ChemPhysChem*. 2014;15(4):587–99.
- [90] Ha T, Laurence TA, Chemla DS, Weiss S. Polarization spectroscopy of single fluorescent molecules. *J Phys Chem B*. 1999;103(33):6839–50.

- [91] Ha T, Enderle T, Chemla DS, Selvin PR, Weiss S. Single molecule dynamics studied by polarization modulation. *Phys Rev Lett.* 1996;77(19):3979–82.
- [92] Kaim G, Prummer M, Sick B, Zumofen G, Renn A, Wild UP, et al. Coupled rotation within single FOF1 enzyme complexes during ATP synthesis or hydrolysis. *FEBS Lett.* 2002;525(1–3):156–63.
- [93] Swaminathan V, Kalappurakkal JM, Mehta SB, Nordenfelt P, Moore TI, Koga N, et al. Actin retrograde flow actively aligns and orients ligand-engaged integrins in focal adhesions. *Proc Natl Acad Sci U S A.* 2017;114(40):10648–53.
- [94] Ohmachi VM, Komori Y, Iwane AH, Fujii F, Jin T, Yanagida T. Fluorescence microscopy for simultaneous observation of 3D orientation and movement and its application to quantum rod-tagged myosin V. *Proc Natl Acad Sci U S A.* 2012;109(14):5294–8.
- [95] Mehta SB, McQuilken M, La Riviere PJ, Occhipinti P, Verma A, Oldenbourg R, et al. Dissection of molecular assembly dynamics by tracking orientation and position of single molecules in live cells. *Proc Natl Acad Sci U S A.* 2016;113(42):E6352–61.
- [96] Van De Linde S, Sauer M. How to switch a fluorophore: From undesired blinking to controlled photoswitching. *Chem Soc Rev.* 2014;43(4):1076–87.
- [97] Van De Linde S, Krstić I, Prisner T, Doose S, Heilemann M, Sauer M. Photoinduced formation of reversible dye radicals and their impact on super-resolution imaging. *Photochem Photobiol Sci.* 2011;10(4):499–506.
- [98] Van De Linde S, Löschberger A, Klein T, Heidebreder M, Wolter S, Heilemann M, et al. Direct stochastic optical reconstruction microscopy with standard fluorescent probes. *Nat Protoc.* 2011;6(7):991–1009.
- [99] Vogelsang J, Kasper R, Steinhauer C, Person B, Heilemann M, Sauer M, et al. A reducing and oxidizing system minimizes photobleaching and blinking of fluorescent dyes. *Angew Chemie - Int Ed.* 2008;47(29):5465–9.
- [100] Sergé A, Bertaux N, Rigneault H, Marguet D. Dynamic multiple-target tracing to probe spatiotemporal cartography of cell membranes. *Nat Methods.* 2008;5(8):687–94.
- [101] Valadés-Cruz CA. Polarized super-resolution fluorescence microscopy. PhD thesis, Aix-Marseille Université, 2014.
- [102] Dickson RM, Norris DJ, Moerner WE. Simultaneous Imaging of Individual Molecules Aligned Both Parallel and Perpendicular to the Optic Axis. 1998;
- [103] Böhmer M, Enderlein J. Orientation imaging of single molecules by wide-field epifluorescence microscopy. *J Opt Soc Am B.* 2003;20(3):554.
- [104] Backlund MP, Lew MD, Backer AS, Sahl SJ, Grover G, Agrawal A, et al. Simultaneous, accurate measurement of the 3D position and orientation of single molecules. *Proc Natl Acad Sci U S A.* 2012;109(47):19087–92.

- [105] Backer AS, Backlund MP, Von Diezmann AR, Sahl SJ, Moerner WE. A bisected pupil for studying single-molecule orientational dynamics and its application to three-dimensional super-resolution microscopy. *Appl Phys Lett*. 2014;104(19).
- [106] Backer AS, Lee MY, Moerner WE. Enhanced DNA imaging using super-resolution microscopy and simultaneous single-molecule orientation measurements. *Optica* 3, 659-666 (2016).
- [107] Gould TJ, Gunewardene MS, Gudheti M V., Verkhusha V V., Yin SR, Gosse JA, et al. Nanoscale imaging of molecular positions and anisotropies. *Nat Methods*. 2008;5(12):1027–30.
- [108] Eltzner B, Wollnik C, Gottschlich C, Huckemann S, Rehfeldt F. The filament sensor for near real-time detection of cytoskeletal fiber structures. *PLoS One*. 2015;10(5):1–28.
- [109] Valentina Curcio, unpublished PhD thesis. Aix-Marseille Université.
- [110] Valadés Cruz, CA. Polarized super-resolution fluorescence microscopy. PhD Thesis, Aix-Marseille Université, 2014.
- [111] Backer AS, Backlund MP, Lew MD, Moerner WE. Single-molecule orientation measurements with a quadrated pupil. *Opt InfoBase Conf Pap*. 2013;38(9):1521–3.
- [112] Ding T, Wu T, Mazidi H, Zhang O, Lew MD. Single-molecule orientation localization microscopy for resolving structural heterogeneities within amyloid fibrils. *bioRxiv* 2020.01.22.916122 (2020).
- [113] Ding T, Wu T, Mazidi H, Zhang O, Lew MD. Single-molecule orientation localization microscopy for resolving structural heterogeneities between amyloid fibrils. *Optica*. 2020;7(6):602–7.